

Magnetic polyamide 6 nanocomposites for increasing damage tolerance through self-healing of composite structures.

GUPTA, R.

2021

The author of this thesis retains the right to be identified as such on any occasion in which content from this thesis is referenced or re-used. The licence under which this thesis is distributed applies to the text and any original images only – re-use of any third-party content must still be cleared with the original copyright holder.

**MAGNETIC POLYAMIDE 6 NANOCOMPOSITES FOR
INCREASING DAMAGE TOLERANCE THROUGH SELF-
HEALING OF COMPOSITE STRUCTURES**

RANJEETKUMAR GUPTA

PhD

2021

MAGNETIC POLYAMIDE 6 NANOCOMPOSITES FOR INCREASING
DAMAGE TOLERANCE THROUGH SELF-HEALING OF COMPOSITE
STRUCTURES

RANJEETKUMAR GUPTA

A thesis submitted in partial fulfilment of the
requirements of
Robert Gordon University
for the degree of Doctor of Philosophy

October 2021

DECLARATION

I hereby declare that the research reported in this thesis is result of my original work and have been completed independently, under the supervision of Dr Ketan Pancholi and Dr James Njuguna.

This PhD thesis has not been submitted for the award of any other degree or professional qualification.

Wherever other sources are cited/quoted, appropriate references are given.

Ranjeetkumar Gupta,

March 2021.

DEDICATION

“Let satisfaction be the basis of success, not success the basis of satisfaction”

Bhagavad-Gītā (3.35)

I dedicate this work to my beloved Lord Sri Kṛṣṇá - The Supreme Personality of Godhead. Further to this I also dedicate this work to my loving wife, supporting family and my inspiring Spiritual Mentors.

I remember the words of my late father, who always motivated me and believed that I will make him proud someday. I wish this will make him happy and proud, wherever he is watching me from.

ACKNOWLEDGEMENT

I would like to express my heartfelt thanks to my supervisor Ketan Pancholi whose encouragement, support, and guidance right from the start of my PhD journey enabled me to complete my experimental work and thesis along with other multiple RA projects and later with my full-time work. He is really a great mentor and I could not imagine my journey so far being so easy and enjoyable; especially he always supported my nascent ideas and was always there to guide me. Whenever I faced any difficulties with my research, he encouraged me and believed in me, and went out of the way to make arrangements for my smooth working. Also, I would like to thank the School of Engineering, Robert Gordon University for the part-funding scholarship towards my PhD, and my second supervisor Prof. James Njuguna for his support alongside.

I am thankful to and grateful to the support staff of the School of Engineering, Alan Mclean, David Howie, Alexander Laing, David Smith, Martin Johnstone, Alan Macpherson. Also, I thank the staff of the School of Pharmacy at Robert Gordon University for making their facility available for part of this research. From Pharmacy department I would like to thank Laurie Smith, Bruce Petrie, Carlos Fernandez, Mathew Kerr, Jenny Macaskill & Tracy Willox.

My special thanks to Dehong Huo of Newcastle University and Gavin Stenning of ISIS-STFC for their kind arrangements for my sample characterisations. Especially, I thank Gavin B Stenning for training me on using the characterisation equipment's at ISIS-STFC, Neutron and Muon Source.

Lastly, I thank my family for their continued support throughout my journey. Without their love and support, I would have not been able to reach this position today. Thank you so much.

ABSTRACT

Self-healing materials have ability to repair damages repeatedly that occur before complete failure of materials. The development of stimuli-responsive self-healing materials have been in demand recently for composites structures since their failure is relatively uncertain and can result in major expenses. Using such materials can enhance the damage tolerance leading to greater asset reliability and limits the expenditures as well as human interactions to a minimum. In this work, Fe_3O_4 magnetic polymer nanocomposites that can be used to intrinsically heal composites through thermal stimuli are investigated, followed by self-healing of glass fibre reinforced polymer (GFRP) composites which are fabricated by embedding the healable polymer nanocomposite as one of the sacrificial layered matrices.

Performance of nanocomposite, however, depends on various parameters including nanoscale dispersion of nanoparticles. Specifically, a lack of hierarchical dispersion of nanoparticles in three-dimensional polymer matrix prevents electron tunnelling and deteriorates nanocomposites' ability to conduct heat stimuli or otherwise lead to pyrolysis. To address this issue two functionalisation techniques viz. silica (Stöber method for lower silica loading and tri-phasic reverse emulsion method for higher silica loading) and oleic acid (22%, 33%, 44%, and 55% w/w of nanoparticles) variations were experimentally investigated as capable of changing hydrophobic characteristics for facilitating uniform dispersion of the Fe_3O_4 magnetic nanoparticles (MNPs).

Highlighting focus of the presented work is to understand the role of functionalisation routes in the particle-polymer interface in forming uniform dispersed and hierarchical network of MNPs in polymer matrix. Emphasis was on understanding and optimising the role of activator and initiator proportions in controlling the in-situ polymerisation of PA6, capturing the MNPs dispersion state. The resulting dispersion state due to functionalised Fe_3O_4 MNPs determined the properties of magnetic PA6 nanocomposites (PMC), to help

achieve a generic set of principles for designing desired material for stimuli-induced self-healing of GFRP composites.

The method implemented to achieve so, was on two grounds of firstly doing anionic ring opening in-situ polymerisation of PMC by experimental synthesis within the laboratory with optimised EtMgBr (activator) and NACL (initiator) proportions for improved degree of crystallinity and capturing the MNPs dispersion state attained by probe ultrasonication of the melt monomer & MNPs solution mixture. Of which the 50% EtMgBr (activator) and 30% NACL (initiator) were assessed as the optimised proportions for giving the highest possible crystallinity amongst all the prepared PMC variations. Secondly, as per the functionalisation type of the MNPs the prepared PMC samples were tested based on chemical, thermal, structural, and magnetic characterisations; to assess and present self-healing capability by microwave stimuli. The physical characterisation results were also used to train a simulation model to create the 3D dispersion state for better studying the dispersion state and interaction region defined by interaction radius (IR) of each MNP/agglomerate of the MNPs. Based on this overall comparison the most suitable PMC of 22 w/w % OA loading was selected and formed into thin films. Sandwiched tensile testing samples were then prepared using this PMC film as a sacrificial layer between GFRP tapes.

Both bare and modified Fe_3O_4 MNPs PMC exhibited paramagnetic behaviour with average particle sizes ranging from 30-60 nm. The saturation magnetisation (M_s) of the unmodified MNPs PMC was around 65% and that of the selected PMC with 22 wt/wt % OA loading was 47%. The self-healing concept was demonstrated with the prepared composite samples microwave induction heating and the efficiencies based on strength recovery were calculated as 84%, 58% and 34% after first, second and third healing, respectively. This can essentially increase the life-cycle viability of composite structure by over 175% with 60% certainty as that of an otherwise damaged structure, hence promising cost saving by extending the structural life.

KEYWORDS: Polyamide 6, magnetic nanocomposite, oleic acid, Stöber, tri-phasic reverse emulsion, functionalisation, GFRP, composites, self-healing, circular economy.

LIST OF PUBLICATIONS

I. Publication outcomes resulting from this research work.

Journal Publications:

1. **Gupta R**, De Sa R, Murray D, Huo D, Droubi G, White M, Njuguna J, Pancholi K*. Effect of Oleic Acid Coating of Iron Oxide Nanoparticles on Properties of Magnetic Polyamide-6 Nanocomposite. **The Journal of The Minerals, Metals & Materials Society (TMS)**. 2019 Sep 15;71(9):3119-28.
2. **Gupta R**, Huo D, White M, Jha V, Stenning GB, Pancholi K*. Novel Method of Healing the Fibre Reinforced Thermoplastic Composite: A Potential Model for Offshore Applications. **Composites Communications**. 2019 Dec 1; 16:67-78.
3. **Gupta R***, Stenning GB, Bucknall D, Flynn D, Pancholi K*. Role of Nanoparticle-coating Interfaces in Polyamide-6/Fe₃O₄ Magnetic Nanocomposite. **ACS Applied Materials & Interfaces**, 2021. (Submitted, Undergoing Journal Review)
4. **Gupta R***, Njuguna J, Pancholi K*. Optimising Activator and Initiator Proportions for Fe₃O₄-PA6 Magnetic Polymer Nanocomposites Rapid Prototyping. **Composites Communications**, 2021. (Submitted, Undergoing Journal Review)
5. **Gupta R**, Gupta P, Stenning GB, Darr J*, Pancholi K*. Tunable Ferroelectric and Ferromagnetic Dispersed Magnetite in Polyamide Nanocomposites. **Scientific Reports**, 2021. (Under Submission)

Patent Application:

Submitted an Invention Disclosure form with RGU innovation on "Remote Structural Health Monitoring with Autonomous Self-Healing Capability of Composite Structures". Formalisation of Patent still pending.

Conference Publications:

1. **Gupta R**, Prabhu R, Pancholi M, Huo D, Jha V, Latta J, Pancholi K*. Integrated self-healing of the composite offshore structures. In **Oceans 2017-Aberdeen** 2017 Jun 19 (pp. 1-4). IEEE.
2. **Gupta R**, Staknevicus R, Pancholi K*. Rapid Multifunctional Composite Part Manufacturing using Controlled In-situ Polymerization of PA6 Nanocomposite. **Procedia CIRP**. 2019 Jan 1; 85:61-5.

Poster Publications:

1. **Gupta, R.**, Huo, D., Pancholi, M., Njuguna, J. and Pancholi, K*, 2017. Self-Healing Polymer Nanocomposite for Composite Structures. **Defense and Doctoral Symposium**, Cranfield University, Swindon 2017.
2. **Gupta, R.**, De Sa, R., Droubi, G. and Pancholi, K*, 2018. Magnetic Polymer Nanocomposite Preparation using in-situ Polymerisation of ϵ -Caprolactam. **Advanced Materials for Environmental Protection, UK-Thai Link**, Thailand.

II. Publication outcomes related with this research work.

Journal Publications:

1. **Gupta R**, Smith L, Njuguna J, Deighton A, Pancholi K*. Insulating MgO-Al₂O₃-LDPE Nanocomposites for Offshore Medium Voltage DC Cable. **ACS Applied Electronic Materials**. 2020 Jun 3.
2. **Gupta R***, Badel B, Gupta P, Bucknall D, Flynn D, Pancholi K*. Flexible Low-Density Polyethylene-BaTiO₃ Nanoparticle Composites for Monitoring Leakage Current in High-Tension Equipment. **ACS Applied Nano Materials**. 2021 March 2.
3. **Gupta R***, Mitchell D, Blanche J, Harper S, Pancholi K, Baines L, Bucknall D, Flynn D. A Review of Sensing Technologies for Non-Destructive Evaluation of Structural Composite Materials. **Journal of Composites Science**. 2021. (Submitted Reviewed Manuscript, Undergoing 2nd Journal Review)
4. **Gupta R***, Baines L, Flynn D, Bucknall D. Epoxy Resin and its Composites: A Comprehensive Review of their Synthesis techniques, Properties, Applications with Market Trends, and Circular Economy Perspectives. **Materials & Design**. (Under Submission)
5. Mitchell D*, Blanche J, Harper S, Kong L, Lim T, **Gupta R**, Zaki O, Tang W, Robu V and Flynn D. A Review: Challenges and Opportunities for Artificial Intelligence and Robotics in the Offshore Wind Sector. **Energy and AI**. (Under Submission)
6. Harper S*, Kong L, Cole D, Lim T, Flynn D, Mitchell D, Blanche J, **Gupta R**, Roe J, and Tang W. Digital Technologies and Edge Analytics for Operational Decision Support in Energy Systems. **IEEE Access**. (Under Submission)

Conference Publications:

1. **Gupta R**, Huo D, Pancholi M, Njuguna J, Pancholi K*. Insulating Polymer Nanocomposites for High Thermal Conduction and Fire Retarding Applications. **Defense and Doctoral Symposium**, Cranfield University, Swindon 2017.
2. Blanche J*, Mitchell D, **Gupta R**, Tang A, Flynn D. Asset Integrity Monitoring of Wind Turbine Blades with Non-Destructive Radar Sensing. **IEEE IEMCON 2020**.
3. Mitchell D*, Harper S, Osama Z, Blanche J, Roe J, Tang W, **Gupta R**, Flynn D. Autonomy and Me: Working together for a better future, **MMLDT-CSET 2021**. September 26-29, 2021. San Diego, CA.
4. Tang W*, Blanche J, Mitchell D, **Gupta R**, Flynn D. Machine Learning Analysis of Non-Destructive Evaluation Data from Radar Inspection of Wind Turbine Blades, **IEEE International Conference on Sensing, Diagnostics, Prognostics, and Control (SDPC 2021)**. August 13-15. Weihai, China.

CONTENTS

DECLARATION	I
DEDICATION	II
ACKNOWLEDGEMENT	III
ABSTRACT	IV
LIST OF PUBLICATIONS	VII
1. INTRODUCTION	1
1.1 OUTLINE.....	1
1.2 PROBLEM STATEMENT.....	2
1.2.1 Overview.....	2
1.2.2 Research Questions/Hypothesis.....	3
1.3 AIM AND OBJECTIVES.....	4
1.3.1 Aim	4
1.3.2 Objectives	4
1.7 THESIS STRUCTURE	7
2. LITERATURE REVIEW	8
2.1 DAMAGE TOLERANCE BY SELF-HEALING	8
2.1.1 Self-healing Synthetic Materials	9
2.1.2 Self-healing Techniques	11
2.1.2.1 Microcapsules based.....	11
2.1.2.2 Hollow fibres or Microvascular Network based	12
2.1.2.3 Reversible Covalent Bonding and Supramolecular Noncovalent Interactions	13
2.1.2.4 Photochemically Induced	14
2.1.2.5 Self-healing using Polymer Nanocomposites.....	14
2.2 MAGNETIC POLYMER NANOCOMPOSITES FOR SELF-HEALING.....	17
2.2.1 Magnetic Materials and their Applications	17
2.2.2 Concept of Magnetism.....	19
2.2.3 Concept of Superparamagnetic iron oxide nanoparticles (SPIONs)	23
2.2.4 Concept of Polymer Magnetic Nanocomposites (PMC).....	24
2.3 DISPERSION OF NANOPARTICLES IN PMC.....	26
2.3.1 Functionalisation of Magnetic Nanoparticles (MNPs)	27
2.3.2 Silica Functionalisation of MNPs.....	30
2.3.2.1 Stöber Method.....	31

2.3.2.2 Microemulsion Method	31
2.3.3 Oleic Acid Functionalisation of MNPs	32
2.4 PA6 POLYMERISATION	33
2.4.1 Hydrolytic Polymerisation	33
2.4.2 Cationic Polymerisation	33
2.4.3 Anionic Polymerisation	34
2.5 REVIEW OF RELEVANT METHODS OF CHARACTERISATION	35
2.5.1 Fourier transform infrared spectroscopy (FTIR)	35
2.5.2 Differential scanning calorimetry (DSC) and Thermogravimetric Analysis (TGA)	37
2.6 PROPOSED SELF-HEALING TECHNOLOGY USING PMC	43
3. FUNCTIONALISATION EFFECT ON MAGNETIC PROPERTIES OF MNPS.....	49
3.1 MATERIALS	49
3.2 EXPERIMENTAL SECTION.....	49
3.2.1 Silica Functionalisation	49
3.2.1.1 Stöber Method.....	49
3.2.1.2 Tri-Phasic Reverse Emulsion Method	51
3.2.2 Oleic Acid Functionalisation.....	52
3.3 FUNCTIONALISED MNP CHARACTERISATION METHODS.....	53
3.3.1 Transmission electron microscopy (TEM)	53
3.3.2 Scanning Electron Microscopy/Energy-Dispersive X-Ray Analysis (SEM/EDX)	53
3.3.3 Superconducting Quantum Interference Device (SQUID)	54
3.4 RESULTS & DISCUSSIONS	54
3.4.1 Quantitative Analysis of TEM Micrographs for Coating Thickness.....	55
3.4.1.1 Coating Thickness of Silica Functionalised MNPs.....	55
3.4.1.2 Coating Thickness of Oleic Acid Functionalised MNPs	56
3.4.2 Surface Elemental Identification using SEM-EDX.....	57
3.4.2.1 Surface Elemental Identification of Silica Functionalised MNPs	57
3.4.2.2 Surface Elemental Identification of Oleic Acid Functionalised MNPs	58
3.4.3 Magnetic Moment Ratio using SQUID Measurement	59
3.4.3.1 Magnetic Moment Ratio of Silica Functionalised MNPs	59
3.4.3.2 Magnetic Moment Ratio of Oleic Acid Functionalised MNPs.....	61
4. OPTIMISATION OF PA6 PMC SYNTHESIS.....	65
4.1 MATERIALS	65
4.2 SYNTHESIS METHOD.....	65

4.2.1 Concentration & Calculation	65
4.2.2 Polymerisation Process	67
4.3 CHARACTERISATION METHODS FOR POLYMERISED SAMPLES	67
4.3.1 Fourier transform infrared spectroscopy (FTIR)	67
4.3.2 Differential Scanning Calorimetry (DSC)	68
4.3.3 Thermogravimetric analysis (TGA)	68
4.4 OPTIMISING ACTIVATOR AND INITIATOR CONCENTRATIONS	68
4.4.1 Effect of Varying Proportion of Initiator (EtMgBr)	70
4.4.2 Effect of Varying Proportion of Activator (NACL)	78
4.4.3 Effect of Varying Proportion of Initiator (EtMgBr) and Activator (NACL) both .	84
4.5 SELECTION OF OPTIMUM PROPORTION	90
5. PMC SYNTHESIS WITH FUNCTIONALISED MNPS	92
5.1 EXPERIMENTAL METHOD	92
5.2 PMC CHARACTERISATION METHODS	94
5.2.1 Fourier transform infrared spectroscopy (FTIR)	94
5.2.2 X-Ray diffraction (XRD)	94
5.2.3 Transmission electron microscopy (TEM)	95
5.2.4 Differential Scanning Calorimetry (DSC)	95
5.2.5 Small & Wide-angle X-ray scattering (SAXS/WAXS)	95
5.2.6 Superconducting Quantum Interference Device (SQUID)	96
5.3 RESULTS AND DISCUSSION	96
5.3.1 Functional Group Study of synthesised samples	96
5.3.1.1 Silica-functionalised samples	96
5.3.1.2 OA-functionalised samples	98
5.3.2 Functionalisation effect on dispersion of MNPs	100
5.3.2.1 Silica-functionalised samples	100
5.3.2.2 OA-functionalised samples	104
5.3.3 Degree of crystallinity and crystallite size	109
5.3.3.1 Silica-functionalised samples	109
5.3.3.2 OA-functionalised samples	113
5.3.4 Determination of Interaction Radius using Simulation	117
5.3.5 SQUID Characterisation	124
5.3.5.1 Silica-functionalised samples	124
5.3.5.2 OA-functionalised samples	126
5.4 CORELATION OF DISPERSION STATE WITH OTHER KEY FINDINGS	129

6. COMPOSITE STRUCTURE APPLICATION	135
6.1 MATERIALS	135
6.2 STANDARD DOG BONE SAMPLE PREPARATION	135
6.3 TENSILE TESTING AND SELF-HEALING.....	137
6.3.1 Tensile Test Characterisation Method	137
6.3.2 Results and Discussion	138
6.4 DETERMINATION OF SELF-HEALING EFFICIENCY	140
7. CONCLUSION AND FUTURE SCOPE.....	143
7.1 CONCLUSION	143
7.2 FUTURE SCOPE	148
7.2.1 Underwater Self-Healing Capability.....	148
7.2.2 Remote Structural Health Monitoring	148
7.2.3 Self-healing Insulation Materials for HVDC Cables.....	149
7.2.4 PMC for Microscale Magnetic Components.....	150
7.2.5 Hydrogen Generation with Functionalised MNPs.....	150
REFERENCES	152
APPENDIX A: MATLAB CODE	166
APPENDIX B: INITIATOR & ACTIVATOR VARIATION DATA	169
B.1 VARYING PROPORTION OF INITIATOR (EtMgBr).....	169
B.2 VARYING PROPORTION OF ACTIVATOR (NaCl)	170
B.3 VARYING PROPORTION OF INITIATOR (EtMgBr) AND ACTIVATOR (NaCl) BOTH	172
APPENDIX C: SIMULATED MODELS GENERATED	174
APPENDIX D: EDX & MAGNETIC MEASUREMENTS	176
APPENDIX E: COMPOSITE SAMPLE PREPARATION.....	181

List of Figures

Chapter 1. Introduction

Figure 1.1. Thesis methodology overview showing knowledge gap and known knowledge	5
Figure 1.2. Sequence of research workflow showing PMC synthesis, film preparation, dogbone sample preparation, various characterisation methods followed and tensile testing with subsequent microwave stimuli-based healing.	6

Chapter 2. Literature Review

Figure 2.1. Various self-healing systems employed till date: (a) Classification based on self-healing ability, (b) Autonomic self-healing systems, and (c) Non-autonomic systems (10).	10
Figure 2.2. Microcapsule based self-healing demonstration [Top: Progression of crack, Middle: Rupture of Microcapsule carrying healing agent, and Bottom: Crack filled by the polymerised healing agent] (11).	11
Figure 2.3. Self-healing with (a) hollow fibres, (b) compartmented fibres and (c) microvascular network [In all Cases - Top: Progression of crack, Middle: Rupture of Microfibre carrying healing agent, and Bottom: Crack filled by the polymerised healing agent] (16).	12
Figure 2.4. Supramolecular ionomer based self-healing caused upon by a ballistic impact (17).	13
Figure 2.5. Self-healing functionality representation in nanocomposites (a) undamaged sample and (b) nanoparticle migration towards a microcrack for arresting further damage (23).	15
Figure 2.6. Graphical review of the four major application areas of Magnetic Nanoparticles and the synthesised Polymer Magnetic Nanocomposites.	18

Figure 2.7. Hysteresis ($M-H$) response of an ideal ferromagnet material.....	22
Figure 2.8. Variation of Magnetic coercivity with respect to particle (size) diameter (58). (Keys: SD = Single-Domain; MD = Multiple-Domain; SP = Superparamagnetic). (Reproduced with permission, copyright 2011 Wiley.)	23
Figure 2.9. Layout of risers used in deep-sea oil explorations. Conventional Riser(left) & GE Hybrid Design(right) (86).	44
Figure 2.10. (a) Crack on the region of interest. Inset image shows propagation of crack on the bending layer and (b) Delaminated area highlighted in blue and cracks represented in red (186).....	45
Figure 2.11. Crack initiation with the increased compressive loading and the pattern of subsequent failures observed in composite materials (186).	45
Figure 2.12. Schematic of automated tape placement method for placing GFRP/CFRP tapes on the structures like composite riser, using laser heat source (187).	46
Figure 2.13. Proposed method of damage control by self-healing of PMC nanocomposites. Top-Left: Shows original sample state, Top-Right: Exposed PMC surface due to the microcrack/delamination, Bottom-Right: The MNPs absorb the microwave stimuli and fill the microcrack.	47

Chapter 3. Functionalisation of Magnetic Nanoparticles

Figure 3.1. Experimental scheme that was followed for the Stöber method functionalisation of MNPs and the subsequent characterisation methods followed.	50
Figure 3.2. Experimental scheme that was followed for the TPPE functionalisation of MNPs and the subsequent characterisation methods followed.	51
Figure 3.3. Experimental scheme that was followed for the Oleic Acid (OA) functionalisation of MNPs and the subsequent characterisation methods followed.	52

Figure 3.4. TEM micrographs of MNP samples with (a) uncoated MNPs and (b) & (c) MNPs with varying proportions of silica coating (Stöber and TPRE respectively). (Scale bar shown is of 100 nm).....	55
Figure 3.5. TEM micrographs of MNP samples with (a) 22 w/w% OA-Fe ₃ O ₄ MNPs, (b) 33 w/w% OA-Fe ₃ O ₄ MNPs, (c) 44 w/w% OA-Fe ₃ O ₄ MNPs and (d) 55 w/w% OA-Fe ₃ O ₄ MNPs. (Scale bar shown is of 100 nm).....	56
Figure 3.6. EDX spectra demonstrate the Fe peaks are observed in all samples, and the silica peak is observed in the Stöber and TPRE method functionalised samples.	57
Figure 3. 7. EDX spectra demonstrate the Fe peaks are observed in all oleic acid functionalised samples, and the oleic acid's (carbon and oxygen) group are overlapping with that of iron oxide.....	58
Figure 3.8. Magnetisation hysteresis loops for the MNPs functionalised by Stöber and TPRE method, measured at (a) 100 K and (b) 400 K.	59
Figure 3.9. Magnetisation hysteresis loops for the MNPs functionalised by oleic acid, measured at (a) 100 K and (b) 400 K.	61
Figure 3.10. Summarised comparison plot of the magnetic moment ratio (M_r/M_s) both at 100K and 400K for uncoated and all the functionalised MNP samples.	63

Chapter 4. Anionic In-situ Polymerisation

Figure 4.1. DSC plot for variable proportions of initiator (EtMgBr) concentrations.	72
Figure 4.2. DSC plot for the initiator (EtMgBr) – 10% concentration - Boiled water sample (to remove unreacted monomer).	74
Figure 4.3. TGA plot depicting weight loss for variable proportions of initiator (EtMgBr) concentrations.	75
Figure 4.4. FTIR plot for variable proportions of initiator (EtMgBr) concentrations.....	78
Figure 4.5. DSC plot for variable proportions of activator (NAACL)	79

Figure 4.6. TGA plot depicting weight loss for variable proportions of activator (NACL) concentrations.	81
Figure 4.7. FTIR plot for variable proportions of activator (NACL) concentrations.....	83
Figure 4.8. DSC plot for variable proportions of initiator (EtMgBr) and activator (NACL) both.	85
Figure 4.9. TGA plot depicting weight loss for variable proportions of initiator (EtMgBr) and activator (NACL) both.	87
Figure 4.10. FTIR plot for variable proportions of initiator (EtMgBr) and activator (NACL) both.	88
Figure 4.11. Comparison of degree of crystallinity achieved by each sample with varying the proportions of EtMgBr, NACL and EtMgBr+NACL.	90

Chapter 5. Characterisation of PMC Samples

Figure 5.1. Experimental method followed for the polymer magnetic nanocomposite synthesis and the subsequent list of characterisation methods followed.	93
Figure 5.2. ATR-FTIR Spectra of pristine polymer (PA6), sample with uncoated MNPs and samples with varying proportions of silica coatings (Stöber and TPPE) on the MNPs.....	96
Figure 5.3. ATR-FTIR Spectra of Pristine PA6, sample with uncoated MNPs and polymer samples with varying proportions of OA coatings on the MNPs.	98
Figure 5.4. TEM micrographs showing dispersion of nanoparticles in microtome section of the prepared PMC samples with (a) uncoated MNPs and (b) & (c) MNPs with varying proportions of silica coatings (Stöber and TPPE respectively). (Scale bar shown is of 100 nm).....	100
Figure 5.5. Background corrected SAXS ($0.005-0.3 \text{ \AA}^{-1}$) and WAXS ($0.3-4.17 \text{ \AA}^{-1}$) intensities $I(q)$ as a function of the scattering vector 'q' for the pristine polymer (PA6), sample with uncoated MNPs and samples with varying proportions of silica coatings (Stöber and TPPE) on the MNPs.	101

Figure 5.6. (a) Guinier plot for the pristine polymer (PA6), sample with uncoated MNPs and samples with varying proportions of silica coatings (Stöber and TPRE) on the MNPs and (b) with the region fitting highlighted.	103
Figure 5.7. TEM image shows dispersion of nanoparticles with (a) 22 w/w%, (b) 33 w/w%, (c) 44 w/w% and (d) 55 w/w% OA in microtome section of the prepared PMC. (Scale bar shown is of 50 nm).....	105
Figure 5. 8. Background corrected SAXS (0.005-0.3 Å ⁻¹) and WAXS (0.3-4.17 Å ⁻¹) intensities I(q) as a function of the scattering vector 'q' for Pristine PA6, sample with uncoated MNPs and polymer samples with varying proportions of OA coatings on the MNPs.	106
Figure 5.9. (a) Guinier plot for Pristine PA6, sample with uncoated MNPs and polymer samples with varying proportions of OA coatings on the MNPs and (b) with the region fitting highlighted.	107
Figure 5.10. DSC curves of the Pristine PA6 sample, sample with uncoated MNPs and samples with varying proportions of silica coatings (Stöber and TPRE) on the MNPs...	109
Figure 5.11. XRD patterns of the Pristine PA6 sample, sample with uncoated MNPs and samples with varying proportions of silica coatings (Stöber and TPRE) on the MNPs...	111
Figure 5.12. DSC curves of the Pristine PA6 sample, sample with uncoated MNPs and samples with varying percentages of OA loading on the MNPs.....	113
Figure 5.13. XRD patterns of the Pristine PA6 sample, sample with uncoated MNPs and samples with varying percentages of OA loading on the MNPs.....	115
Figure 5.14. Flowchart for the developed MATLAB code for the simulated PMC model generation.....	119
Figure 5.15. Simulated model representation of the PMC samples with 1 wt% MNPs and included with the interaction radius (IR) of the individual nanoparticle/agglomerate regions (1 cubic micron size) for (a) Uncoated-Fe ₃ O ₄ PMC; samples with varying proportions of	

silica coatings i.e. (b) Stöber-Fe₃O₄ PMC & (c) TPRE-Fe₃O₄ PMC; and samples with varying percentages of OA loading on the MNPs viz. (d) 22 w/w% OA-Fe₃O₄ PMC, (e) 33 w/w% OA-Fe₃O₄ PMC, (f) 44 w/w% OA-Fe₃O₄ PMC, and (g) 55 w/w% OA-Fe₃O₄ PMC. (Herein, solid Black spheres represent Fe₃O₄ MNPs or agglomerates and the faint black region/sphere around it represents their interaction region/range.) 122

Figure 5.16. Magnetisation hysteresis loops for the Pristine PA6 sample, sample with uncoated MNPs and samples with varying percentages of silica coatings (Stöber and TPRE) on the MNPs at (a) 100 K and (b) 400 K 124

Figure 5.17. Magnetisation hysteresis loops for the Pristine PA6 sample, sample with uncoated MNPs and samples with varying percentages of OA loading on the MNPs at (a) 100 K and (b) 400 K..... 126

Figure 5. 18. Summarised comparison plot of the magnetic moment ratio (Mr/Ms) both at 100K and 400K for PMC samples with uncoated MNPs and samples with varying percentages of silica and OA loading on the MNPs. 129

Chapter 6. Composite Structure Application

Figure 6.1. Tensile testing specimen dimensions, with grip length 30 mm and the specimen width 25 mm. 135

Figure 6.2. Standard dog bone samples prepared, showing different layers of the composite sample in CAD representation. (Arrangement of the layers are shown more clearly in the inset image; wherein the grey layer represents the Glass Fibre Tape, and the dark layer is the nanocomposite film.) 136

Figure 6.3. An example of the prepared samples (a) without and (b) with the induced crack. 137

Figure 6.4. Load-displacement curves measured during tensile testing of virgin sample without and with crack, and the subsequent healings..... 138

Figure 6.5. Stress-Strain curves measured during tensile testing of virgin sample without and with crack, and the subsequent healings. 139

List of Tables

Chapter 2. Literature Review

Table 2.1: Various self-healing approaches developed and tested for structural composites with their associated key features and limitations.	16
Table 2.2: Summary of different types of magnetism depicted by materials.	20
Table 2.3: Various functionalisation techniques tested in literatures for improving the stability of MNPs.	28

Chapter 3. Functionalisation of Magnetic Nanoparticles

Table 3.1: Summarised magnetic results at 100 K for Uncoated MNPs, and MNPs with varying percentages of silica coatings (Stöber and TPRE).	60
Table 3.2: Summarised magnetic results at 400 K for Uncoated MNPs, and MNPs with varying percentages of silica coatings (Stöber and TPRE).	60
Table 3.3: Summarised magnetic results at 100 K for Uncoated MNPs, and MNPs with varying percentages of OA loading.	62
Table 3.4: Summarised magnetic results at 400 K for Uncoated MNPs, and MNPs with varying percentages of OA loading.	62

Chapter 4. Anionic In-situ Polymerisation

Table 4.1: Variable proportions of initiator (EtMgBr)	70
Table 4.2: Calculation of glass transition temperature, melting temperature, and degree of crystallinity from DSC plot for EtMgBr variation samples.....	73
Table 4.3: Variable proportions of activator (NACL)	79
Table 4.4: Calculation of glass transition temperature, melting temperature, and degree of crystallinity from DSC plot for NACL variation samples.	80
Table 4.5: Variable proportions of initiator (EtMgBr) and activator (NACL) both.	84

Table 4.6: Calculation of glass transition temperature, melting temperature, and degree of crystallinity from DSC plot for samples with variation of initiator (EtMgBr) and activator (NACL) both.	85
---	----

Chapter 5. Characterisation of PMC Samples

Table 5.1: Size calculation of the MNPs for each sample types from Guinier plot.	104
---	-----

Table 5.2: Size calculation of the MNPs for each sample types from Guinier plot.	108
---	-----

Table 5.3: A list of degree of crystallinity, Glass transition (T_g) and Melting temperature (T_m) from DSC results for Pristine PA6 sample, sample with uncoated MNPs and samples with varying proportions of silica coatings (Stöber and TPPE) on the MNPs.	110
--	-----

Table 5.4: Crystallite sizes of MNPs calculated from FWHM of intense peaks observed in XRD patterns for sample with uncoated MNPs and samples with varying proportions of silica coatings (Stöber and TPPE) on the MNPs.	112
---	-----

Table 5.5: A list of degree of crystallinity, Glass transition (T_g) and Melting temperature (T_m) from DSC results for Pristine PA6 sample, sample with uncoated MNPs and samples with varying percentages of OA loading on the MNPs.	114
---	-----

Table 5.6: Crystallite sizes of MNPs calculated from FWHM of intense peaks observed in XRD for sample with uncoated MNPs and samples with varying percentages of OA loading on the MNPs.	116
---	-----

Table 5.7: Estimated ferret diameters of MNP or their agglomerate regions identified from TEM micrographs, SAXS (Guinier plot) analysis and XRD peak study.	120
--	-----

Table 5.8: Summarised magnetic results at 100 K for Pristine PA6 sample, sample with uncoated MNPs and samples with varying percentages of silica coatings (Stöber and TPPE) on the MNPs.	125
--	-----

Table 5.9: Summarised magnetic results at 400 K for Pristine PA6 sample, sample with uncoated MNPs and samples with varying percentages of silica coatings (Stöber and TPPE) on the MNPs.	125
--	-----

Table 5.10: Summarised magnetic results at 100 K for Pristine PA6 sample, PMC sample with uncoated MNPs and PMC samples with varying percentages of OA loading on the MNPs.	128
Table 5.11: Summarised magnetic results at 400 K for Pristine PA6 sample, PMC sample with uncoated MNPs and PMC samples with varying percentages of OA loading on the MNPs.	128
Table 5.12: Summary of key findings from all the characterisation results.....	131

Chapter 6. Composite Structure Application

Table 6.1: Some concepts of self-healing composites proposed for structural applications.	140
--	-----

Abbreviations and Symbols

MNPs	Magnetic Nanoparticles
PMC	Polymer Magnetic Nanocomposites
nm	Nanometre
Fe ₃ O ₄	Iron (II, III) oxide or Magnetite
Fe ₂ O ₃	Ferric/iron (III) oxide
CNTs	Carbon Nanotubes
PA-6	Polyamide-6
EM	Electromagnetic
SCF	Self-consistent Field
GFRP	Glass Fibre Reinforced Polymer
HGF	Hollow Glass Fibre
HVDC	High-Voltage DC Cables
FR	Flexible Risers
GE	General Electric
3-D X-Ray CT	3-Dimensional X-Ray Computed Tomography
PVA	Polyvinyl Acetate
H	Magnetic Field Strength
M_s	Saturation Magnetisation
M_r	Remnant Magnetisation
M_r/M_s	Magnetic Moment Ratio
H_c	Coercivity
H^+	Coercivity measured only on Positive axis
H^-	Coercivity measured only on Negative axis
SD	Single-Domain
MD	Multiple-Domain
SP	Superparamagnetic
D_s	Critical Diameter

D_p	Superparamagnetic Diameter
T_c	Curie temperature
CONH	Carbonamide Group
ACO	Acridine orange
PLA	Polylactic acid
PMMA	Polymethyl methacrylate
PAA	Polyacrylic acid
PEG	Polyethylene glycol
CA	Citric acid
LA	Lauric acid
OA	Oleic Acid
TEOS	Tetraethyl Orthosilicate
TPRE	Tri-phasic Reverse Emulsion
CL	ϵ -Caprolactam (99% purity)
EtMgBr	3.0 M Ethyl Magnesium Bromide solution in diethyl ether
H+	Free Proton
TEM	Transmission electron microscopy
SEM/EDX	Scanning Electron Microscopy/Energy-Dispersive X-Ray Analysis
SQUID	Superconducting Quantum Interference Device
FTIR	Fourier transform infrared spectroscopy
XRD	X-Ray diffraction
TEM	Transmission Electron Microscopy
DSC	Differential Scanning Calorimetry
TGA	Thermogravimetric Analysis
SAXS/WAXS	Small & Wide-Angle X-Ray Scattering
UTM	Universal Tensile Testing Machine
IR	Interaction Radius/Region
APTES	(3-Aminopropyl)triethoxysilane

DI	De-ionised Water
NH ₃	Aqueous Ammonia
w/v	Weight per Volume Ratio
v/v	Volume per Volume Ratio
w/w	Weight per Weight Ratio
ca.	Approximately
<i>Uncoated-Fe₃O₄ MNPs</i>	Uncoated Fe ₃ O ₄ MNPs
<i>Stöber- Fe₃O₄ MNPs</i>	Fe ₃ O ₄ MNPs functionalised by Stöber Method
<i>TPRE- Fe₃O₄ MNPs</i>	Fe ₃ O ₄ MNPs functionalised by TPPE Method
<i>22 w/w% OA-Fe₃O₄ MNPs</i>	Fe ₃ O ₄ MNPs functionalised with 22 w/w% OA
<i>33 w/w% OA-Fe₃O₄ MNPs</i>	Fe ₃ O ₄ MNPs functionalised with 33 w/w% OA
<i>44 w/w% OA-Fe₃O₄ MNPs</i>	Fe ₃ O ₄ MNPs functionalised with 44 w/w% OA
<i>55 w/w% OA-Fe₃O₄ MNPs</i>	Fe ₃ O ₄ MNPs functionalised with 55 w/w% OA
<i>minFeret</i>	Minimum Feret Diameter
<i>maxFeret</i>	Minimum Feret Diameter
K	Kelvin
°C	Celsius
Oe	Oersted
<i>M</i>	Molar Concentration
<i>m</i>	Molarity
<i>mol %</i>	Mole percentage or Molar percentage
NACL	N-Acetyl Caprolactam (99% purity)
<i>V</i>	Volume
<i>ρ</i>	Density
<i>% Crystallinity</i>	Degree of Crystallinity (%)
ΔH_f^{obs}	Observed Heat of Fusion from the DSC plot
ΔH_f^o	Heat of Fusion of 100% crystalline polymer
T _g	Glass Transition Temperature

T_m	Melt Peak or Melting Temperature
J/g	Joule/gram
UV	Ultraviolet Radiation
kHz	Kilohertz Frequency Range
<i>Pristine PA6</i>	Virgin PA6 sample having no MNPs
<i>Uncoated-Fe₃O₄ PMC</i>	PMC with Uncoated Fe ₃ O ₄ MNPs
<i>Stöber-Fe₃O₄ PMC</i>	PMC with Fe ₃ O ₄ MNPs functionalised by Stöber Method
<i>TPRE-Fe₃O₄ PMC</i>	PMC with Fe ₃ O ₄ MNPs functionalised by TPRE Method
<i>22 w/w% OA-Fe₃O₄ PMC</i>	PMC with Fe ₃ O ₄ MNPs functionalised with 22 w/w% OA
<i>33 w/w% OA-Fe₃O₄ PMC</i>	PMC with Fe ₃ O ₄ MNPs functionalised with 33 w/w% OA
<i>44 w/w% OA-Fe₃O₄ PMC</i>	PMC with Fe ₃ O ₄ MNPs functionalised with 44 w/w% OA
<i>55 w/w% OA-Fe₃O₄ PMC</i>	PMC with Fe ₃ O ₄ MNPs functionalised with 55 w/w% OA
$I(q)$	Background corrected SAXS intensity
D	Diameter of MNPs assumed as perfect sphere
R_g	Radius of Gyration
G	Guinier Prefactor
B	Peak Width
K	Machine Constant (XRD)
λ	Incident wavelength
θ	Angular Position
L	Crystallite Size
CAD	Computer Aided Design
kN	Kilo Newtons
W	Watts

1. INTRODUCTION

1.1 Outline

The emphasis on the self-healing materials research has recently increased in this decade because all the structural composites are vulnerable to high probability of sudden damage and degradation due to micro failures (at matrix phase, realised as crack initiation and propagation; or at reinforcing phase, observed as fibre breakage/fracture; or at interface, wherein fibre detaches from base matrix, ideally referred to as debonding) or degradation over time by various (thermal, mechanical, UV radiation, chemical, etc.) factors (1,2). The self-healing property is tempting particularly for composites and polymer structures because such materials are frequently used in large-scale applications and the ability to (remotely) repair damaged parts in situ would be invaluable for increasing the structural life. For instance, if a wind turbine blade which is made up of fibre reinforced polymer (FRP) composites is damaged, then heat-induced healing process can be employed to heal the damage without any part removal if self-healing material is used in its fabrication and this would successfully delay its decommissioning. Such self-healing materials can as well be used in space where the repair operations are adversely affected by environment. The service life and cost effectiveness of parts can be essentially increased by integrating self-healing materials (3).

The design of such self-healing composite materials involve selection of suitable composite additives as nano-inclusions. Magnetic nanoparticles (MNPs) are promising material to use for such self-healing of composites structures because the versatility in their surface modifications provides benefits for the development of effective and thermally responsive polymer nanocomposites. They can be functionalised effortlessly with different types of modifying agents, like polymer, organic acid, and silanes, depending on their usage. Furthermore, the explicitly functionalized MNPs having

combination of higher magnetic reaction level and magnetic inductive behaviour, can perform encapsulations, sensing, delivery, entrapments and adsorption of various materials such as heavy metal, drug, protein, DNA, enzymes, etc (4). The property of such MNPs is tuneable, for example the control of their curie temperature can switch the magnetic domain on and off, making them the right candidate for the development of magnetic stimuli based responsive polymer nanocomposite materials. For such materials the heating response can hence be modified as per the application requirement, since the curie temperature response for the stimuli like electromagnetic induction are directly dictated in presence of the MNPs in terms of their proportion and also their dispersion state.

Such behaviour of MNPs included in polymer nanocomposites, make them magnetically responsive and can be extended to polymeric composite structures as a means for structural health monitoring and self-healing of micro-damages. These materials exhibit property combinations with unique possibilities for design applications and are rapidly perceived as the materials for the demanding engineering applications. Since the MNPs are having substantial surface area, they influence the interfaces of nanoparticles dictating the properties of the final nanocomposite. The polymerisation techniques of such nanocomposites demand controlled mixing, achieving stabilised dispersion, orienting the dispersed phase with the concept of blending polymers. Though a key requirement for achieving the desired function, is the uniform dispersion of MNPs in the polymer matrix, which still remains a major challenge.

1.2 Problem Statement

1.2.1 Overview

Effectively tackling the issues of agglomeration and uniform dispersion are the key requirements for enhancing the mechanical, electrical, etc. properties of the designed nanocomposite (5). Upon achieving such to an acceptable limit, there are various possibilities of inducing self-healing characteristics by engineering the phase interfaces,

to design application driven specific properties-based nanocomposite materials. One of such high mechanically yielding and lightweight materials is sought to solve the major challenge faced by the oil and gas industry in the areas of ultra-deep-water environments for solving the fatigue life concerns of the flexible risers. These are current areas of research by various flexible riser manufacturer. Flexible riser pipes design is one of the important considerations, as they are prone to various harsh loadings, including tensile, bending, blow, collapse, and torsion. Inducing stresses far greater than what traditional material are capable to withstand. The harsh deep-sea environment present engineering challenges where the self-weight of pipe, compression and bending loads are too extensive for current designs and materials to address effectively (6). Therefore, it is proposed to combine the traditional metallic layers with reinforcing layers made of composite materials. The idea of utilising reinforcing layers of composite material would address the concerning issue of self-weight. It has been proposed that by utilising this technique 32% reduction in weight is possible (7). And, with the advanced possibilities of self-healing with magnetic polymer nanocomposites; the newer avenues of detection and limiting induced damages, due to the harsh environmental conditions, is rapidly emerging.

1.2.2 Research Questions/Hypothesis

The research question that are addressed in this work are:

- Remotely operated self-healing capability for arresting of crack/delamination in composite structures, by dispersing the damage energy and increasing tolerance.
- Silica and oleic acid method for functionalisation of MNPs for synthesis of magnetic PA6 polymer nanocomposites, addressing the dispersion issue while bringing marginal effect on their magnetic moment ratio response.
- Achieving 45% or maximum possible degree of crystallinity (facilitating the desired thermo-mechanical properties) and uniform MNPs distribution with in-situ polymerisation technique, by selecting optimised activator and initiator proportions.

- Validating self-healing capabilities and assess its efficiency, with selected magnetic PMC for composite structural application.

The major research areas that are addressed by this work is shown in terms of the methodology overview in Fig. 1.1.

1.3 Aim and Objectives

1.3.1 Aim

The aim of this thesis is to analyse the dispersion state effect of MNPs by applying probe ultrasonication to monomer and MNPs solution, controlling the polymerisation rate hence capturing the dispersed state of MNPs by varying the initiator (EtMgBr) and activator (NaCl) proportions for in-situ polymerisation of the PMC. Also, to test two varying methods (silica and oleic acid) of MNPs functionalisation to improve the dispersion state further for avoiding local response or pyrolysis. The overall aim is to develop an effective magnetic polymer nanocomposite for achieving self-healing capabilities for various applications, and in particular to test it in GFRP composite structures for offshore applications. The entire research workflow is represented in Fig. 1.2.

1.3.2 Objectives

- Develop the research methodology based on self-healing capabilities and present self-healing of composite sample by microwave stimuli using magnetic polymer nanocomposite.
- Tuning the polymer nanocomposites degree of crystallinity during in-situ polymerisation process and to capture the MNPs ultrasonicated dispersed state by controlling initiator and activator proportions.
- Investigating role of functionalisation and chemical composition of functionalised nanoparticles in determining the dispersion-state and in turn properties of nanocomposite.

- Investigate the chemical, thermal, structural, and magnetic response of the prepared PMC samples.
- Correlate hierarchical dispersion of nanoparticles in three-dimensional polymer matrix with interaction radius and interrelate their magnetic response by using simulated model.
- Validate self-healing abilities with magnetic PA-6 PMC in damage arresting of composite structures.

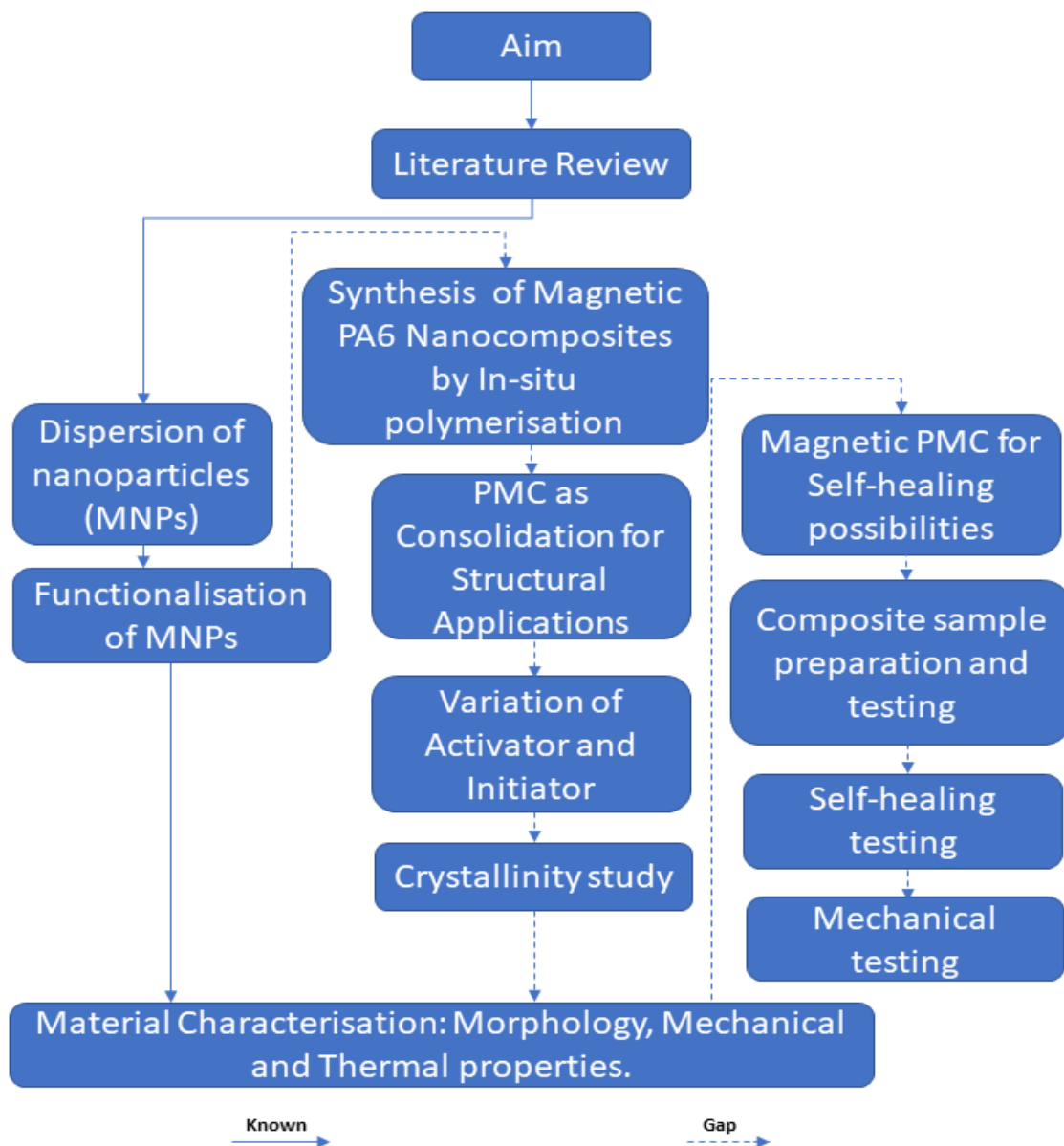


Figure 1.1. Thesis methodology overview showing knowledge gap and known knowledge

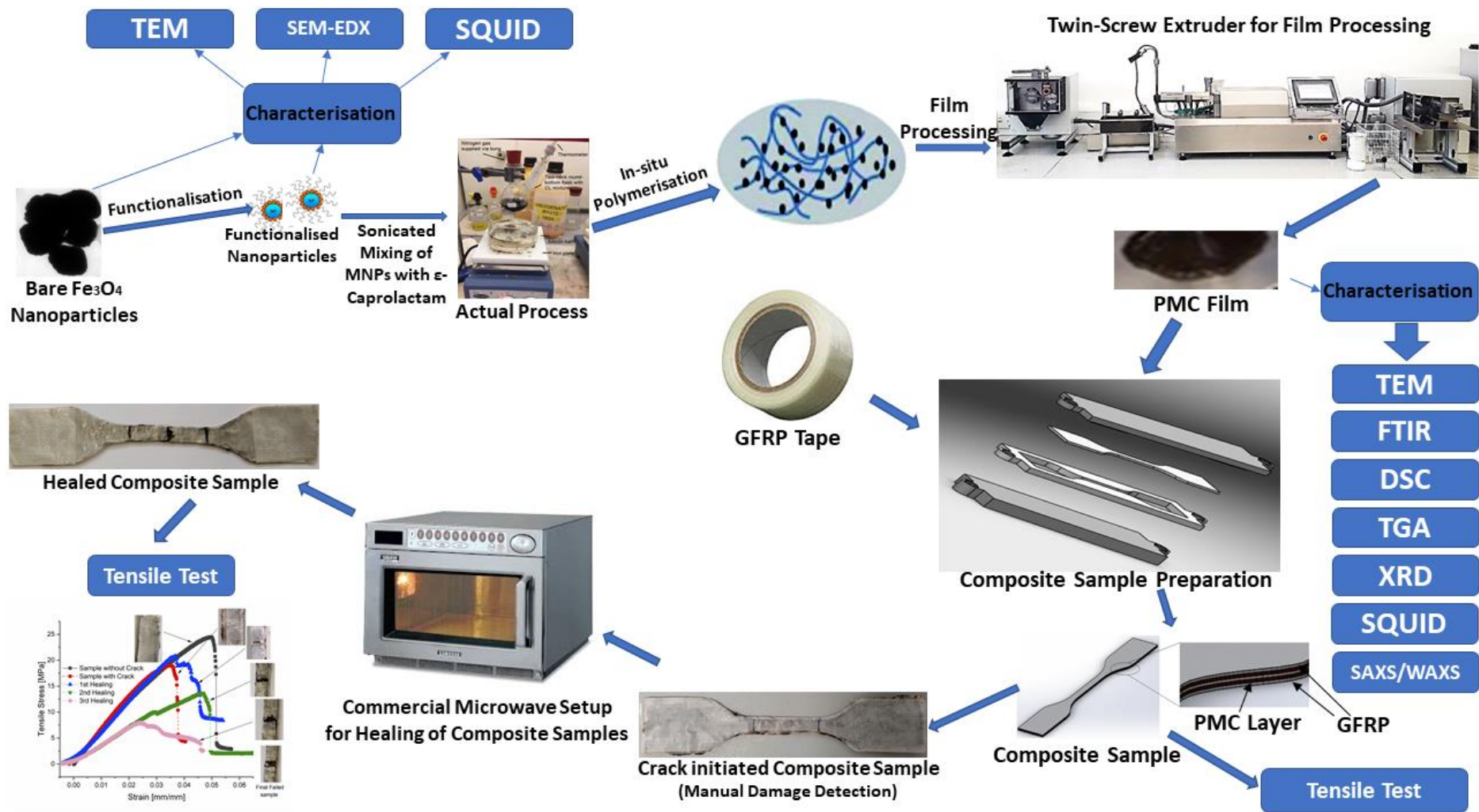


Figure 1.2. Sequence of research workflow showing PMC synthesis, film preparation, dogbone sample preparation, various characterisation methods followed and tensile testing with subsequent microwave stimuli-based healing.

1.7 Thesis Structure

Chapter 1 - Introduction: Provides a brief overview of the thesis and the concept of self-healing materials. Also outlines the aims and objectives of this thesis, with methodology overview and the research workflow chart.

Chapter 2 - Literature Review: Investigates the current research on self-healing materials using both extrinsic and intrinsic methods to provide healing capabilities for CFRP test samples. Also develops the background theory and concepts of magnetism, magnetic polymer nanocomposites, PA6 polymerisation and suitable characterisation methods, which have been used within this thesis.

Chapter 3,4 & 5 – Discusses experimental method of Functionalisation of MNPs and In-situ Polymerisation. Describing the processes which have been undertaken to achieve the desired MNPs dispersion state and the degree of crystallinity. Various functionalisation techniques and the effect of variation of activator and initiator is discussed.

Characterization results of both the functionalised MNPs and the synthesised PMC samples is discussed in depth; MNPs dispersion state, degree of crystallinity and magnetic response of the PMC samples study are essentially focussed. For selecting the suitable candidate PMC for preparing the composite sample.

Chapter 6 – This chapter discusses the sample preparation of composite GFRP, for structural application with the selected PMC, various mechanical characterisation and the experimental results which have been generated from experiments. An extensive discussion of the self-healing experimentation results is included, and suitability of the method discussed with the achieved efficiency.

Chapter 7 - Highlights the conclusions from the work undertaken and highlights the future scope and suggestions.

2. LITERATURE REVIEW

In this chapter various concepts of stimuli-based self-healing are discussed, and the basis is laid out for incorporating PMC for composites structure application. Further magnetic materials like MNPs and their nanocomposites are discussed herein which have been developed and tested for multiple applications, and specifically Fe_3O_4 superparamagnetic nanocomposites are discussed. The surface modification, and their specific application for synthesis of PMC leading to improved dispersion with in-situ polymerisation technique is also discussed in detail. Lastly, to substantiate the appropriate characteristics of the synthesised polymer nanocomposite samples for the targeted application, various characterisation techniques that can be used are briefly introduced. Towards the end the proposed method is included to address the key objectives of this thesis based on the review.

2.1 Damage Tolerance by Self-healing

The features of lightweight, easy processability and efficacy in adverse environmental scenarios have made polymers and fibre-reinforced polymers (FRPs) the most popular choice for structural applications. But the lack of elastic deformation is the limiting factor of polymer composites and hence under impact they are adversely influenced by a drop in their stiffness and mechanical strength, as well as dimensional instability. Such scenarios involve the dissipation of impact energy in the matrix, leading to micro-cracks. These micro-cracks inevitably degrade the polymer and its progression results in sudden failure. Hence, it becomes essential to identify and repair such micro-failure sites before it reaches catastrophic damage. For thermoset plastics various patch layup repair methods are employed and for thermoplastics fusion bonding repair method is employed. However, these methods are very complicated and time consuming, even very costly for some cases when demanding expert

operators. In such cases self-healing techniques can be the best possible solution to detect the damage at an early stage and even to repair automatically well in time.

2.1.1 Self-healing Synthetic Materials

The ability of self-healing of synthetic materials autonomously is a rapidly evolving field of smart materials (8). Inspired by various naturally occurring materials, their research is driven by the need of developing multifunctional materials with the ability to recover their basic properties such as conductivity, fracture toughness, mechanical strength, corrosion resistance, etc., subsequent to any partial damage (9). Based on the self-healing ability of these materials, there are two main categories of these materials: (i) autonomic and (ii) non-autonomic self-healing materials (Fig. 2.1(a)–(c)) (10). These materials are developed specially in terms of the technique or stimuli that is to be followed for the self-healing method. Like those used for autonomic self-healing, as the name suggests, automatically get activated for self-healing response upon the damage propagation. And those used for non-autonomic self-healing, require an external stimulus in terms of heat, light, etc. to bring about the self-healing effect. And each one of them have a unique application for themselves. Though some of these self-healing materials (for example ionomers) cannot be effectively used in composite structure applications due to limitation of their physical properties, hence the need for the synthesis of self-healing capable materials that possess the in-built structural strength. Since these materials are used in various methods of self-healing, based on the technique that is employed for bringing about the self-healing effect, so there can be many ways of categorising them. The main methods of self-healing employed based on numerous techniques are reviewed in the following 2.1.2 section.

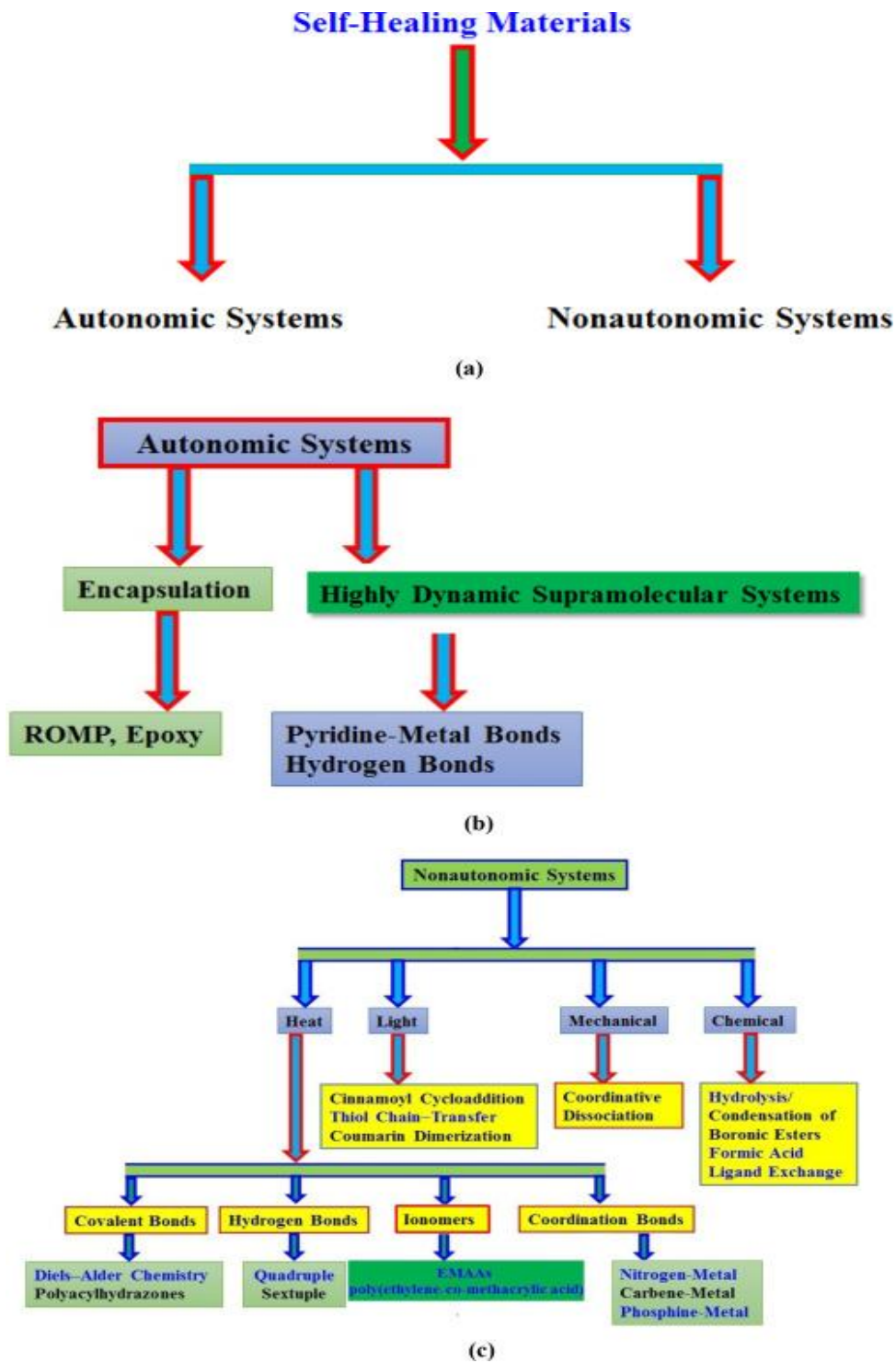


Figure 2.1. Various self-healing systems employed till date: (a) Classification based on self-healing ability, (b) Autonomic self-healing systems, and (c) Non-autonomic systems (10).

2.1.2 Self-healing Techniques

The various self-healing techniques that are developed and tested are discussed in this section as follows.

2.1.2.1 Microcapsules based

In the microencapsulation method of self-healing the healing is brought about by the reactive constituents that are preloaded and dispersed in the form of microcapsules in the polymer matrix. A healing agent is generally filled in microcapsules and reactive catalyst is dispersed alongside the microcapsules. Whenever there is a propagation of crack, the damage ruptures the microcapsule in path leading to the flow of the healing agent that polymerises coming in contact with the catalyst present around. The mechanism of microcapsule based self-healing is shown in the Fig. 2.2.

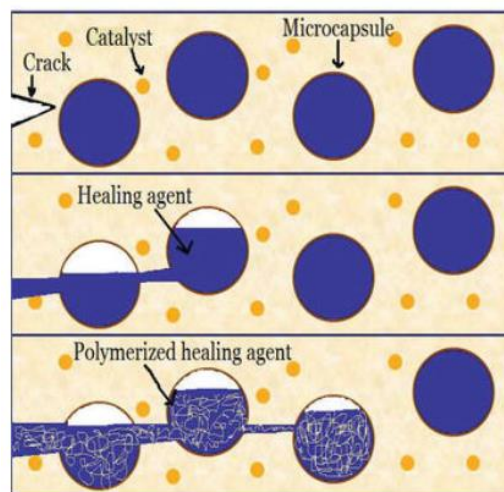


Figure 2.2. Microcapsule based self-healing demonstration [Top: Progression of crack, Middle: Rupture of Microcapsule carrying healing agent, and Bottom: Crack filled by the polymerised healing agent] (11).

The reaction mechanism can occur in various ways as cycloaddition (12), cycloreversion (13), catalytic activation (14), crosslinking (15), or ring opening metathesis polymerisation (ROMP) (11). The damage here acts as an impetus for the healing to occur, which occurs by the gradual capillary flow of the healing agent to the damaged site. The polymerising mixture of the healing agent covers the crack faces

by the virtue of surface tension, hence making the choice of the healing material quite critical and limited in number. The key features and limitations of this method are summarised in Table 2.1.

2.1.2.2 Hollow fibres or Microvascular Network based

The concept of involving hollow fibres for the supply of higher volume of healing agent, overcomes the limitations of the limited amount of healing agent that can be carried by microcapsules. The hollow fibres can be of a prefilled standalone type or of a continuous supply vascular type, and can be arranged either in 1D, 2D or even 3D. The vascular type of arrangement of the fibres can supply healing agent continuously, until the hollow fibre faces an issue of accidental blockage. The mechanism of healing for the hollow fibres, compartmented fibres and microvascular network arrangement is represented in Fig. 2.3.

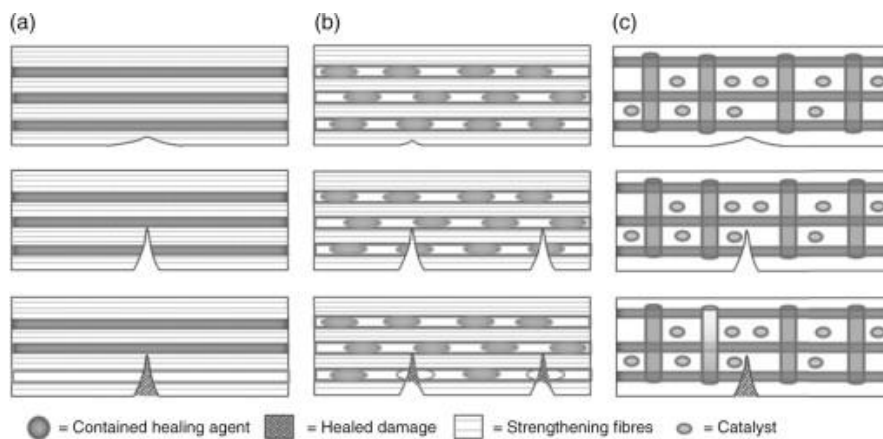


Figure 2.3. Self-healing with (a) hollow fibres, (b) compartmented fibres and (c) microvascular network [In all Cases - Top: Progression of crack, Middle: Rupture of Microfibre carrying healing agent, and Bottom: Crack filled by the polymerised healing agent] (16).

Similar to the microcapsule method, here also damage acts as the impetus for the healing to occur. In some cases, if the base polymer is damaged in such a way that none of the fibres are affected or ruptured, then healing cannot happen in such scenarios. Which implies that there should be a dense network of hollow fibres (carrying the healing agent) to ensure that any damage is effectively affecting the hollow fibre in the vicinity, for bringing about the flow of healing agent. The key

features and limitations of this method are further summarised in Table 2.1 for comparison with other methods.

2.1.2.3 Reversible Covalent Bonding and Supramolecular Noncovalent Interactions

In this method the restructuring of molecular architecture happens by the interaction of dynamic bonds due to an external stimulus. Here the covalent and non-covalent interactions (reversible bonding chemistry) or supramolecular interactions are used to synthesise structurally active polymer structures, that respond to any macroscopic changes. Due to their make, they can heal under damage for an infinite number of damage cycles. Though in most of the cases the healing can only occur when the polymeric chains mobility is enhanced by certain external intervention.

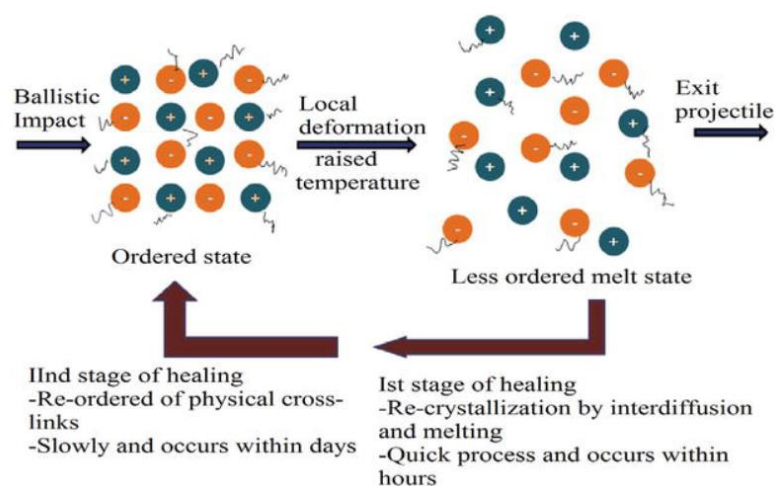


Figure 2.4. Supramolecular ionomer based self-healing caused upon by a ballistic impact (17).

Since they involve certain mode of energy for the healing to begin, they are categorised as passive self-healing technique. Though modes of energy can be mechanical (e.g. static load), heat, light (e.g. UV irradiation), chemical, etc., but in all cases macroscale healing is quite slow (sometimes even taking days) (17). Various methods of supramolecular interactions are involved based on their chemistry and they are listed in Table 2.1 along with the key features and limitations of this type of self-healing.

2.1.2.4 Photochemically Induced

The self-healing brought about by an incidence of light irradiation is specifically categorised as photochemically induced self-healing. This can involve various techniques like reversible cleavage (18), light-induced isomerisation (19), UV-triggered polymerisation (20), photoinduced reaction (21), or even photoabsorbing microcapsules (22). This technique has advantages that it doesn't require any external healing material supply or catalyst. Though it specifically requires photo stimuli to activate and undergo the self-healing process.

2.1.2.5 Self-healing using Polymer Nanocomposites

Computer simulations have shown that on addition of suitable nanoparticles to polymer resulted in such nanocomposites wherein the particles aligned themselves in proximity of any initiated nanoscale cracks. It concluded that various mechanical properties could be restored up to 75-100%, as compared to that of pristine nanocomposite material (10). Though modelling and computational design tools give some insight, but their usage is still limited on understanding the self-healing mechanism.

Another theoretical approach is also proposed for the synthesis of refined nanocomposites, that exhibit "nacre-like" patterned structural arrangement of the nanoparticles (23). Such arrangement results in suitability of self-healing ability. Also, the analytical study based on self-consistent field (SCF) theory of "Self-assembly of polymer-grafted nanoparticle/diblock copolymer" blends, presented that different components can be made to assemble in hierarchical structures with nanosized mineral bridges, which resulted in self-healing functionality.

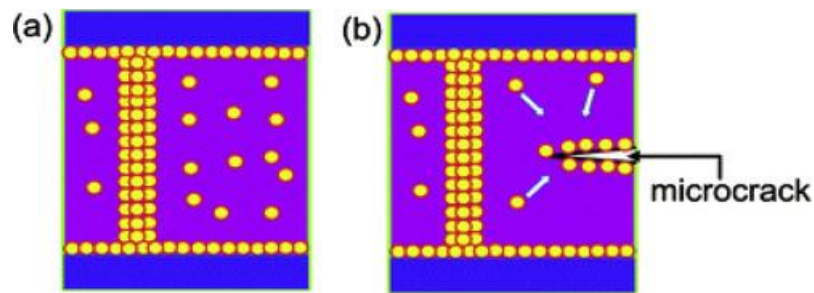


Figure 2.5. Self-healing functionality representation in nanocomposites (a) undamaged sample and (b) nanoparticle migration towards a microcrack for arresting further damage (23).

Figure 2.5 schematically represents the self-healing mechanism of the nanocomposites. The migration of the nanoparticles with defined quantity around the microcrack surface is evident, and forms an interphase layer between the organic and inorganic phases. Though the migration of the nanoparticles is much dictated by the viscosity of the base polymer, which is usually quite high for having a such unified response.

Various approaches for self-healing of structural composites have been developed and tested till date, some of the prominent of which are discussed in Table 2.1 below. The Table 2.1 summarises the method as well the associated key features and limitations of each of them.

Table 2.1: Various self-healing approaches developed and tested for structural composites with their associated key features and limitations.

	Self-healing Method	Strategies involved	Key features	Limitations	References
1	Passive self-healing based on extrinsic methods	Microcapsules	Here the self-healing is created by the inclusion of a foreign healing material in the core matrix.	The healing efficiency can be as low as 20% (24). Distribution of microcapsules is very challenging and so is the fabrication of hollow fibre networks. The microvascular network face issue of getting blocked. The consumption of catalyst after every heal cycle and the blockage of network imply that this system cannot give repetitive healing effects. The efficiency of the healing depends on the activation of catalyst agents brought about by the progress of defect.	(11,24-30)
		Hollow Fibres			(31-37)
		Microvascular network			(16,38-42)
2	Active self-healing based on intrinsic methods	Reversible covalent bonding	Here the reorganization of the molecular arrangement based on an applied stimulus happens by the dynamic bonds, which undergo selective reversible bonding and de-bonding.	In most cases it requires external/human involvement for bringing about the healing. Various modes of energies like UV irradiation, static load, heat, etc. are necessary and crucial for the polymer chains movability. Intrinsic methods are not suitable for healing larger defects, due to the limited capacity of microcapsules or complexity of vascular networks involved. Suitable mostly for microscopic damages only.	(43-45)
		Supramolecular noncovalent interaction i. H-bonding ii. Metal-ligand polymers iii. π - π interaction iv. Ionomers			(46-53)
3	Photochemically induced self-healing	Photo cis-trans isomerisation	Here self-healing is induced by strong light irradiation. It's a rapid and eco-friendly concept. It doesn't demand any external healing implants, catalyst, or external temperature rise to bring about the damage healing.	Systems like photo absorbing microcapsules cannot give sufficient efficiency (22). This method cannot be used effectively in composites thicker than 5 mm thickness and is mostly limited to surface visible defects, where light irradiation can reach.	(12,19)
		UV-induced polymerisation			(20)
		Photo reaction			(21)
		Photo absorbing microcapsules			(22)

As summarised in this Table 2.1, it is noted that most of the existing methods of self-healing are limited in the number of cycles of healing that can be successively accomplished, or they can only work for a limited size of defects. These limitations demand a renewed material development, that can work effectively for structural applications and even can work seamlessly for situations of multiple repair cycles. It is also worth highlighting that majority of the proposed and tested methods of self-healing are applicable for thermoset polymer composites only. Hence, the usage of PMC for stimuli based self-healing can address majority of the limitations of the techniques listed in Table 2.1 and it can also be seamlessly used for thermoplastic FRP composites self-healing. Specifically, magnetic polymer nanocomposites can address these issues, proving to be a suitable choice as discussed in the following sections.

2.2 Magnetic Polymer Nanocomposites for Self-healing

2.2.1 Magnetic Materials and their Applications

Magnetic materials or specifically magnetic nanoparticles are widely used for many applications such as drug delivery, biosensing, catalysis, bio-separation, data storage and medical imaging (4). Iron (II, III) oxide (Fe_3O_4) or ferric/iron (III) oxide (Fe_2O_3) MNPs impart magnetic and catalytic properties onto the traditional polymer materials, resulting in efficient and recyclable new-gen nano-adsorbents nanocomposites (54). This has initiated an entire new category of conductive and magnetically responsive polymer nanocomposites to be formed (55,56).

A review of various possible and tested applications of magnetic nanoparticles and their derived polymer magnetic nanocomposites in the listed four major areas are summarised in Figure 2.6.

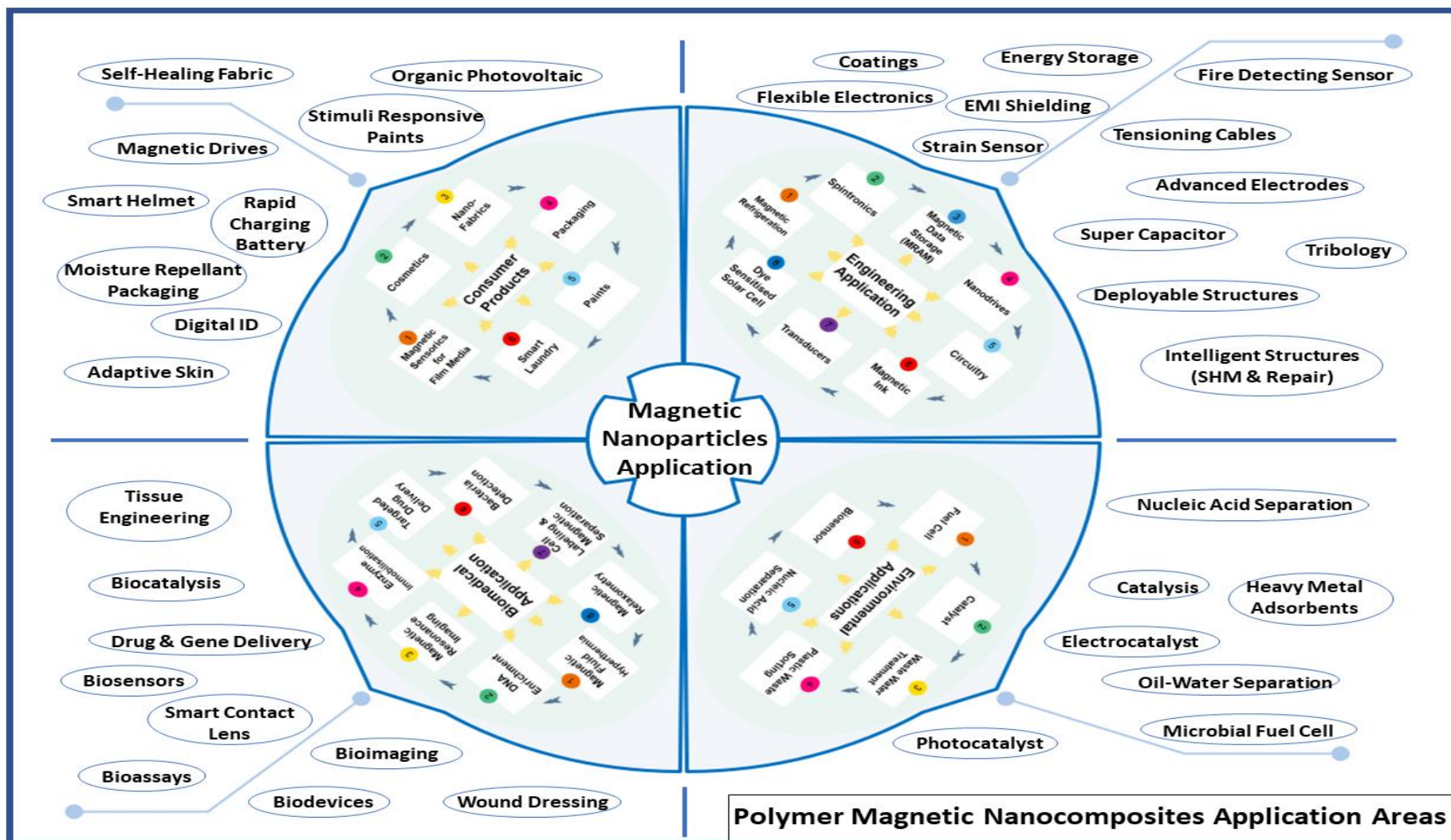
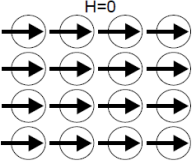
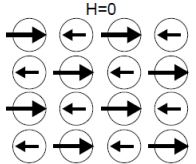
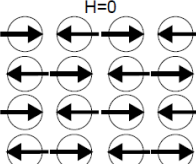
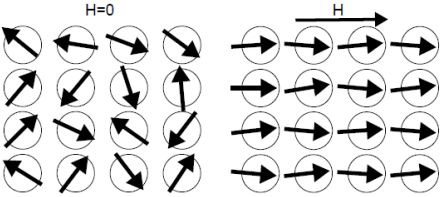


Figure 2.6. Graphical review of the four major application areas of Magnetic Nanoparticles and the synthesised Polymer Magnetic Nanocomposites.

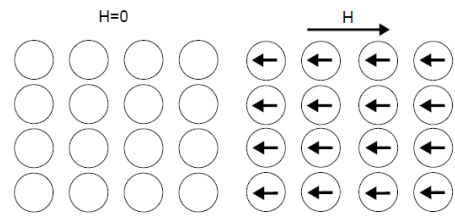
2.2.2 Concept of Magnetism

Ideally, all materials exhibit magnetic response to an extent. This exhibition of magnetism is an intrinsic physical phenomenon resulting from the atomic-level movement of electrons. The grasp on magnetism can be perceived by understanding the response of magnetic materials due to the applied magnetic field influence. Those that are magnetically ordered in response to an externally applied magnetic field are categorised as ferromagnetic, ferrimagnetic and antiferromagnetic based on how their spins are oriented in response. And some types that depict very small positive or negative response are termed as paramagnets and diamagnets, respectively. Table 2.2 summarises the basic concepts of different types of magnetism depicted by materials (57).

Table 2.2: Summary of different types of magnetism depicted by materials.

Magnetism Type	Schematic presentation	Characteristics
Ferromagnetism		<p>The spin orientation is aligned in a single direction depending on the crystal structure. They show spontaneous magnetisation despite of presence or absence of the external magnetic field. Exhibit permanent magnetic behaviours at the macroscopic scale.</p>
Ferrimagnetism		<p>The weaker magnetic dipoles are located antiparallel to adjoining stronger dipoles; therefore, the net magnetisation effect is reduced.</p>
Antiferromagnetism		<p>These comprise of two magnetic sublattices, and both have ferromagnetic atomic moments. However, the magnetic moment of sublattice is in antiparallel direction to adjacent sublattice. Hence, the net magnetising effect is zero.</p>
Paramagnetism		<p>Magnetic dipoles align a bit parallel to the applied external magnetic field, and when absent, make the dipoles orientation random. These dipoles have very weak magnetic response with positive magnetic susceptibility.</p>

Diamagnetism



When the external magnetic field is absent these are characterised with no magnetic dipoles and during its presence as oppositely induced weak dipoles. They show very small magnetic response with negative susceptibility.

Further, the magnetic response of the variety of magnetic materials are examined by analysing their response under a varying external magnetic field termed as hysteresis loops or simply called as $M-H$ plot. Fig. 2.7 shows the hysteresis response of an ideal ferromagnet. The magnetic dipoles gradually align along the large, applied DC magnetising field and reach a saturation level called as the saturation magnetisation M_s . After the applied field is reduced to zero, the spins relax and do not follow the field anymore, herein the residual magnetisation is only prominent which is termed as remnant magnetisation M_r . To reach absolute zero magnetisation a reverse magnetic field is applied, the magnitude of which depends on various structural factors like grain boundaries, shape, size, vacancies or impurities and intrinsic crystalline anisotropy, etc. of the material. This required reverse field is termed as coercivity H_c which is estimated from the $M-H$ plot using the following relation:

$$H_c = \frac{(H^+ - H^-)}{2}$$

where H^+ and H^- are the positive and negative coercivities measured from the $M-H$ plot.

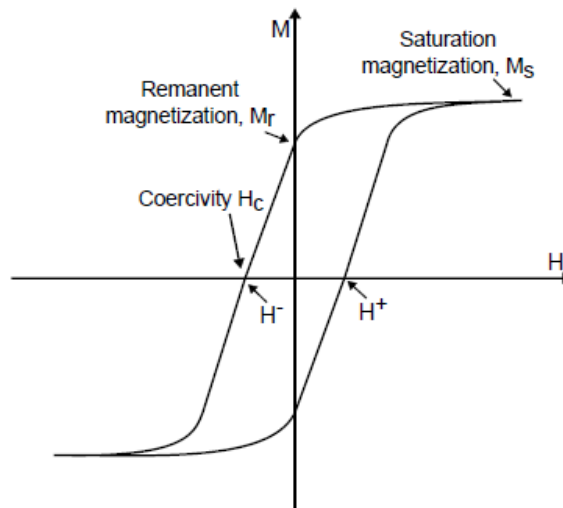


Figure 2.7. Hysteresis ($M-H$) response of an ideal ferromagnet material.

2.2.3 Concept of Superparamagnetic iron oxide nanoparticles (SPIONs)

Magnetite (Fe_3O_4) materials when reduced to nanoparticles, commonly called as magnetic nanoparticles (MNPs), exhibit superparamagnetic behaviour. These materials fall under a special category wherein each magnetite particle acts as a single-domain crystal (58). At elevated temperature, the thermal fluctuation gradually overcomes the energy barrier posed by the magnetic anisotropy, resulting in rapid spin fluctuations and unstable magnetisation akin to paramagnetic model (57). Since here a group of moments are induced in a single particle with comparably higher net magnetic moment than a paramagnet's atomic moment, it is termed as superparamagnetic (59).

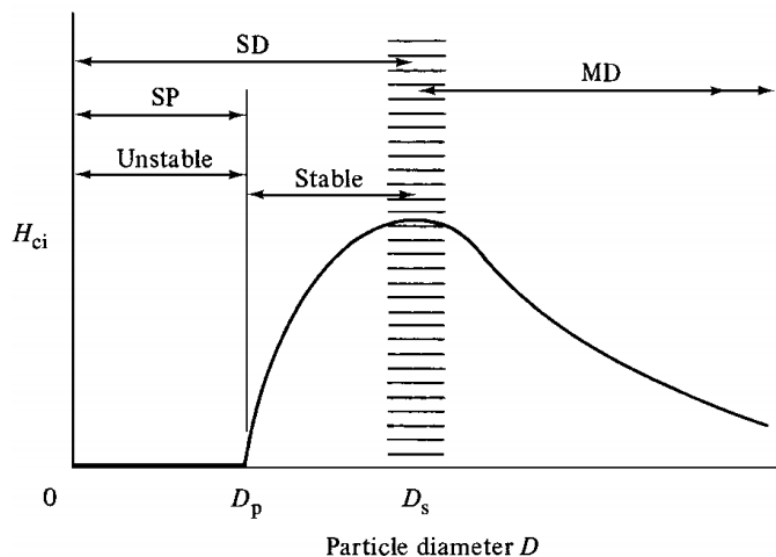


Figure 2.8. Variation of Magnetic coercivity with respect to particle (size) diameter (58). (Keys: SD = Single-Domain; MD = Multiple-Domain; SP = Superparamagnetic). (Reproduced with permission, copyright 2011 Wiley.)

Figure 2.8 illustrates the change of domain state and magnetism type with respect to the particle size. Below a critical diameter (D_s) single magnetite behaves as single domain site and a further reduction causes drop in the H_c which reaches zero value at superparamagnetic diameter (D_p) limit, implying there is no M_r on the $M-H$ plot. The critical diameter limit of MNPs for exhibiting superparamagnetic response is *ca.* 6-8

nm for very hard magnets and about 40 nm for soft magnets (60). The superparamagnetism exhibited by MNPs is temperature dependent with much lower Curie temperature (T_c) than their bulk counterpart. Though this MNPs do not possess any permanent magnetic moment, but quickly respond to an externally applied magnetic field. Major advantage of using such MNPs is that they can display superparamagnetic behaviour even at room temperature and are quite cheaper to synthesise at a commercial scale. These properties of MNPs are vital to act as a suitable receptor for the electromagnetic stimuli response demanded for targeted self-healing applications, when sequentially embedded within a host polymer matrix. Hence, the choice of using Fe_3O_4 MNPs in this study.

2.2.4 Concept of Polymer Magnetic Nanocomposites (PMC)

For preparing polymer magnetic nanocomposites, the MNPs like magnetite (Fe_3O_4 and its oxidised form maghemite, Fe_2O_3), nickel, cobalt, etc. are blend mixed in the polymer solution or melt, followed by drying, precipitation or solvent recovery (61,62). Other routes involve dispersing the MNPs in melt monomer, pre-polymers, or resins and then the mixture is subjected to polymerisation, crosslinking, or curing (63). And there are variable choices of thermoplastic polymer for structural applications, like polyamide-6 (PA6), polyamide-12 (PA12), polyethylene, etc. But the laboratory synthesis of PA6 is much easier as compared to others and even the tuning of initiator and activator proportions gives much control on the properties of the resulting polymer. Though the major challenge faced in PA6 nanocomposite preparation is that the MNPs can settle down due to self-weight or phase separation can occur during the precipitation or polymerisation process itself (64).

To achieve efficient properties with nanocomposites, the uniform spatial distribution of MNP clusters in polymer matrix is essential. Increasing MNP loading reduces the inter-particle distances allowing formation of the agglomerates due to short range Van der Waals or hydrogen bonds. As in at air-liquid interface in bubbles, the particles tend to

agglomerate at interfaces such as solid-solid, solid-liquid or air-liquid (65,66).

Presence of MNP agglomerates in polymer matrix cause an uneven response to the applied stimulus as the agglomerated particles region will absorb much of the stimulus energy and will melt excessively or undergo pyrolysis (67). Hence, the concept of using ultrasonication (68), adjusting curing temperature (69), and suitable MNP surface modification (70), serves the purpose of effectively controlling the improved dispersion of MNPs.

The level of interaction and bonding strength between phases are vital in determining the dispersion of MNPs in a polymer matrix. Further, to achieve uniform dispersion and to break agglomerates, the most widely applied techniques such as melt compounding by twin-screw extrusion (71), high shear mixing (72) or three roll mills (73), solution blending (74) are being used in research. However, these methods do not promote a strong enough interaction between phases so that the agglomerates break down to a required nanometre size, as for example the solution blending method still faces a major shortcoming due to the need to find an appropriate polymer/solvent pair for each nanofiller-polymer system (9). Modifying MNP surfaces using ionic charge, polymer coating (brushes), small molecules, and core-shell arrangement is more efficient way to promote dispersion in the hydrophobic polymer through an electrostatic or steric mechanism. These techniques enhance the polymer-nanocomposite interactions at nanoscale to avoid formation of agglomerates. Many studies have analysed the effect of MNP functionalisation on its adhesion with the base polymer matrix (75-78). The in-situ polymerisation method of dispersion is found useful for polyamide (79) as it enhances covalent bonding between the base polymer matrix and the MNP surfaces (73). However, a high viscosity and non-Newtonian rheology of the melted polymer still poses a challenge in dispersing MNPs homogenously. In the in-situ polymerisation (75) method, the MNPs can be added in a low viscosity monomer melt to achieve dispersion. Additionally, an in-situ polymerisation method presents many opportunities for attaining rapid and controlled

cross-linking density and hence, it allows rendering new properties to the polymer nanocomposite. The methods such as an interfacial polymerisation, free radical polymerisation, anionic ring-opening polymerisation, frontal polymerisation, micellar copolymerisation, and network polymerisation have already been used for in-situ polymerisation (80). Though anionic ring-opening polymerisation is suitable to be used, for it allows much control on the polymerisation process by varying either the activator-initiator combination or their proportions itself (81). Hence it is also chosen as one of the objectives of this study to investigate the resulting effect on the resulting property of the synthesised PMC, specifically its degree of crystallinity.

2.3 Dispersion of Nanoparticles in PMC

Engineering polymer interfaces play a vital role in modifying their thermo-mechanical properties. The polymer region surrounding the nanoparticles surface are called as interface, which behave differently than the rest of polymer mass depending on the volume fraction that is altered by the addition in the overall nanocomposite. This specific behaviour can be tuned and utilised for bespoke response, for example the magnetic nature of such PMC can be exploited as a melt response under induced electromagnetic (EM) field or application with targeted EM or more specifically microwaves. Such response of designed PMC can be usefully involved in limiting crack propagation or even delaying damage in composite structures.

Though polymer nanocomposites have incredible market potential, but the biggest challenge is how to develop the technologies for their processing–manufacturing in lieu of commercialisation. For example, the dispersion of nanoparticles or its chemical compatibility within the polymer matrix is a popular research topic. It is very difficult to achieve hierarchical dispersion by incorporating existing/traditional polymerisation techniques, due to the nature of the nanoparticles to agglomerate (82,83). The way the nanoparticles are aligned in the polymer matrix is crucial to maximize the unidirectional material properties (84). And namely two categories of issues related to

the interfacial dynamics are faced: (i) Local Interfacial Properties: The effect of interface size and how does enthalpic and entropic interactions affect nanoparticle wettability, and (ii) Effectiveness to Macroscopic properties: The effect on the nanoparticle dispersion in the polymer matrix and their concluding effect on the magnetic and thermo-mechanical behaviour. Suitable advanced techniques for scaling the production of such nanocomposites are sought and driven by manufacturing needs for specialised applications (85). However, achieving hierarchical dispersion and improved interfacial bonding between nanoparticles and polymer matrix has been hard. Currently, not much supporting research is available to effectively conclude on the best solution. Further, achieving suitable degree of crystallinity and the improved MNPs dispersion is the main aim for having an optimised PMC that can be presented for the commercial application of stimuli induced composite-structure self-healing.

For the synthesis of polymer nanocomposites with organic–inorganic nanoparticles, the level of interaction or bonding strength across phases is also a vital concern. Conventional mixing does not lead to a very strong phase interaction, i.e. only Van der Waals forces and hydrogen bonding come into action. Hence, high affinity covalent or ionic–covalent bond forming techniques across the phases or sol gel method, melt-blend followed by in-situ polymerisation, etc are the distinctive techniques followed for preparation of organic–inorganic nanocomposites (76). But to further improve the dispersion of MNPs, in various studies the functionalisation of MNPs is vividly analysed relating their effect on base polymer matrix, nanoparticle–matrix adhesion, etc (75-77,86).

2.3.1 Functionalisation of Magnetic Nanoparticles (MNPs)

Significant research progress in the synthesis of MNPs with variable size, structure and properties has been recently observed for addressing the agglomeration issue and protecting them against erosion or oxidation by acidic or basic mediums. Hence to improve the chemical stability of MNPs efficient strategies for coating the MNPs with

protective layer and providing end functional groups for targeting ligands and small molecules conjugation. The tested end groups have been of variable kinds and provide a basis for suitably latching the MNPs to the polymer chains in the polymer matrix. The tested functionalisation categories are of two kinds: (i) organic – consisting of polymers and surfactants (87-90) and (ii) inorganic – covering silica (91-96) and metals (89,97-100). The most common surfactants for the surface modifications of MNPs are alkane sulphonic acid, oleic acid, alkane phosphonic acid, citric acid and lauric acid (101-103). The hydrocarbon chains of these surfactants form a protective shell around the MNPs rendering them hydrophobic nature, which are most suitable for interlinking with the polymer chains, and are also hydrophobic in nature; hence a major contender for resulting in improved dispersion. Though other functionalisation techniques involving polymers, chitosan, liposomes, and silica are also been tested considering their individual advantages (104-106); specifically, the silica based MNPs have shown superior colloidal stability. The following Table 2.3 summarises various functionalisation techniques tested for improving the stability, and hence important to be considered for the dispersion behaviour of MNPs.

Table 2.3: Various functionalisation techniques tested in literatures for improving the stability of MNPs.

Surface Functionalisation	Advantages	Applications	References
Acridine orange (ACO)	Strong fluorescence useful in tracking intracellular movement of MNPs.	Intracellular tracking	(107)
Poly(lactic acid) (PLA)	Hemocompatible, biocompatible and biodegradable; ability to act carry drug loadings for targeted applications	MR imaging media, magnetic cell separation and cell labelling, hyperthermia, and tissue repair	(108,109)
Polymethyl methacrylate (PMMA)	Improves stability, useful as media for automating improved throughput identification of single nucleotide polymorphisms	Amplification and separation of DNA	(110,111)

Polyacrylic acid (PAA)	Increased stability, biocompatibility, and bio-adhesion of MNPs. Helped overcome particle size limitation in orientation, assisting nucleation and growth of lyotropic liquid crystal grains	Regulated placement of lyotropic liquid crystal; Pursuing drug resistance for mycobacteria	(112-114)
Polyethylene glycol (PEG)	Enhances biocompatibility, circulation through blood and absorption efficiency of MNPs.	Contrast agent for MR imaging	(115,116)
Lipids mixture	Magnetic cationic liposomes were readily taken by retinal pigment epithelium cells and helped build its sheet in vitro by using magnetic force.	Tissue engineering	(117)
Citric acid (CA)	Enhances biocompatibility and stability.	Magnetic Hyperthermia, cellular cataloguing	(118-120)
Lauric acid (LA)	Improves colloidal stability and lower concentration promotes biocompatibility.	Imaging agents for MR, cellular cataloguing, and enzyme immobilization for processed food.	(101,121)
Oleic Acid (OA)	Enhances thermosensitivity and biodegradability of magnetite micelles; MRI capabilities; tumour targeting and controlled drug release; Water dispersible agents.	Targeted drug release and imaging agents for MR	(122-125)
Carboxydextran	Targeted heating by magnetic induction stimuli destroying heat sensitive tumour tissues with no adverse side effects on healthy cells.	Magnetic Hyperthermia	(126)
Mesoporous silica	High pore volume and even pore size with high surface area.	Mercury removal from industrial emission; enzyme immobilisation in bio-catalysis; drug delivery;	(127-131)

		fluorescent imaging	
Amorphous silica	Useful in vacuum filtrates and column separators; Eliminates the requirement of multiple centrifuge cycles.	Separation, isolation, and purification of DNA strands from soil, ultrapure plasma DNA from microbial samples; separation of phenolic complexes from ecological water.	(132-134)

Other studies suggest that not just the functionalisation material but the coating thickness, surface charge and the degree of hydrophobicity influences the properties of MNPs in various ways (104,135,136). For instance, some researchers have reported an increase in saturation magnetisation from 0.067 emu/cm³ of water based MNPs to 0.335 emu/cm³ for OA-kerosene based MNPs (137). On the other hand, decreased saturation magnetisation for polymer coated MNPs (138) and similar reduction with silica coated MNPs (127) have been reported. This suggests that the chosen functionalisation category will have combinatorial effects on the final properties of the synthesised magnetic PMC. Two main categories of functionalisation stand out from the above discussion, viz. oleic acid: that has been proven for favouring hydrophobic nature and silica: that has shown superior colloidal stability. Since both these properties can help dictate superior dispersion in the synthesis of PA-6 PMC by in-situ polymerisation techniques as discussed earlier, hence these were chosen for investigation and further application for this research work.

2.3.2 Silica Functionalisation of MNPs

Being biocompatible, silica coating has been reported favourable for improving chemical stability and protecting MNPs against agglomeration at considerable pH ranges and oxidation (89). Also, since having silanol group at surface, silica coating

promotes reaction with silane coupling agents and various chemicals, facilitating conjugation with other biomolecules and ligands for specific targeting and delivery of drugs (139). Furthermore, by nature silica is hydrophilic and silica coated core-shell MNPs in aqueous/colloidal suspensions are reported to show superior dispersion (104).

The varying levels of silica functionalisation were tested by employing two most frequently used and proven methods for preparation of silica functionalised MNPs, viz.: (i) Stöber method (140,141) and (ii) microemulsion method (93,142,143). The former is widely implemented for water soluble MNPs synthesis and the latter for non-polar solvent based MNPs (104). These two separate methods were followed for testing the increasing levels of silica functionalisation, because employing Stöber method with higher silica proportions leads to agglomeration of the MNPs during functionalisation stage itself, with a complete thick glass coating being formed on them. But the emulsion method, ensures that Stöber coated MNPs are further dispersed uniformly in a non-polar solvent while having a further silica functionalisation. Hence, the choice of two separate methods.

2.3.2.1 Stöber Method

The standard procedure involves the formation of silica shells on MNPs surface by polycondensation and hydrolysis of silica content, like mixture of ethanol and tetraethyl orthosilicate (TEOS) in the presence of ammonia water as catalyst (140,144,145). Multiple methods as a modification of the original Stöber method have been presented for improving the MNPs properties (146). Some researchers have reported the effect of varying reaction parameters of alcohol type, alcohol to water volume ratio and precursor & catalyst proportions on the MNPs structure formation; with the synthesised MNPs showing superparamagnetic property (145).

2.3.2.2 Microemulsion Method

This is another popular method for uniform silica layer functionalisation of MNPs. It involves interaction of three medias: oil, water, and an amphiphilic surfactant. Based

on the prominent affinity of the surfactant (hydrophilic or hydrophobic) used, micelles or reverse micelles are formed surrounding the MNPs which dictates the thickness of silica layer deposition. The confined nano-droplet shaped nano-reactors formed by the reverse micelle yield extremely monodisperse MNPs. Furthermore, the thickness of the silica shell deposited can be controlled by tuning the nano-droplet environment, selecting an appropriate molar ratio of water to surfactant used. Hence, the tri-phasic reverse emulsion (TPRE) method can possibly produce 1 nm ultra-thin silica shells (147,148). Apart from the control over reactant concentration, aging time, and molar ratio for dictating the resulting particle size and dispersity, TPRE is found to give low yield (139,149). The low yield is due to the requirement for excessive centrifuge and washing involved due to the multi-phase interaction. But the use of probe ultrasonication method for breaking down the colloid with excessive power at micro-scale can be a desirable technique for stabilising the multi-phase emulsion quickly and hence upscaling the yield process.

2.3.3 Oleic Acid Functionalisation of MNPs

The hydrophobic coating layer can be achieved using oleic acid as the functionalising material, as the MNP surface attract the polar end groups and develop a firmly attached protective monolayer, this aide the uniform and hierarchical arrangement of MNPs (150). By nature, OA has very small molecule which easily complements with magnetite MNPs, making it very popular for *in vivo* applications. Such hydrophobic OA-MNPs are proven to improve the efficiency of localised hyperthermia treatments and targeted drug release upon subjected to a magnetic stimulus (151). In other study the hydrophobic core was found to act as contrasting MRI agents and the hydrophilic tail segment derivatised with other polymer ligand bestows them with targeting motility (152,153). Variable coating thickness can be achieved by seed-mediated growth, wherein MNPs act as the seed base; hence eliminating the fractionation method for even size distribution and can be easily scaled up for bulk

production. Mixing with bipolar surfactant can even transform the hydrophobic MNPs into hydrophilic ones, allowing aqueous dispersion capabilities (154).

The molecular structuring of OA consists of carboxylic acid based polar head and hydrocarbon based non-polar tail. The two oxygen atoms from the carboxylate anion presumably interact with the iron atoms of the magnetite surface (122). This forms the basis for the polar head group to latch over magnetite surface and the non-polar tail free floats, rendering the MNPs hydrophobic in nature. This makes them a suitable choice for applications into polymer media.

2.4 PA6 Polymerisation

Varieties of techniques are being employed for synthesis of polymer nanocomposites as listed earlier. The role of chosen polymerisation technique on the properties of the resulting polymer nanocomposite is discussed in the following section along with the various parameters involved.

2.4.1 Hydrolytic Polymerisation

The name itself suggests that this polymerisation process is associated with presence of water or more specifically water releasing materials. It is mostly suitable to for large scale industrial production of PA6 as it requires sophisticated setup, and the polymerisation of monomer CL happens between 215 – 260 °C. In this method the majority of monomer gets converted into PA6 by polyaddition and the remaining small proportion follows conversion by polycondensation method (155). Employing this method for lab-based testing may involve uneconomical and elaborate setup expense.

2.4.2 Cationic Polymerisation

Polymerisation of monomer CL under the presence of anion-rich protonic acids, strong acidic salts, or Lewis acids (156), and which is promoted under such anhydrous mixtures is termed as cationic polymerisation. They also involve complicated arrangements and demand robust setup with cautious handling due to the

involvement of several active elements (acids), which define the monomer conversion rate. Also, the conversion happens at elevated temperatures between 220 – 260 °C (157). With this discussion it is suitable not to involve such complicated method for lab-based experiments, hence it is not discussed in detail further.

2.4.3 Anionic Polymerisation

Anionic polymerisation as the name suggests, is a proton (anion) controlled reaction. It is one of the polymerisation methods that provides versatile control on the PA6 synthesis with defined structures and uniform chain length & functionality. It also enhances the polymer property by promoting stable chain growth and providing control over their transfer reaction or termination. The control is easily administered by selecting the appropriate activator-initiator combination. With such versatility and ease of control, anionic polymerisation becomes the prominent choice for lab-based experimentation and study.

In this process, if the polymer is formed below its melting point then simultaneous crystallisation and polymerisation occurs (158). Herein, the anionic proportion involved with the activation of monomer dictates the rate of conversion (159), and due to presence of free protons the reaction is quite rapid. Again, the rate of reaction can be modified by suitable choice of the activator that also matches with the initiator involved. This rapid nature of polymerisation is very favourable for capturing the MNPs in their uniform dispersed state in the melt CL.

The cycle of anionic monomer formation follows when the N-acetylated monomer caprolactam growing chain contacts the activated monomer (160). The choice of catalyst, unlike Grignard reagent EtMgBr or MgBr⁺ plays the critical role in capturing the free proton (H⁺) from the activated monomer; this also supports in preserving the basicity of the mixture (161). Often the Grignard reagent is utilised in situ with the monomer caprolactam, forming the catalyst; this aids in setting the site for the

activator. Activators, like N-acetyl caprolactam fits compatibly with the EtMgBr initiator and aids the simultaneous growth of PA6 chains.

With the polymerisation of CL, the MNPs can be as well dispersed in the melt monomer with ease and the whole mixture polymerised to form the PMC. The main idea behind using MNPs is to test their effective response in the resulting PMC to applied excitations, such as Magnetic induction or Electrical current. If they can effectively absorb such excitations then by the virtue of their physical property there will be rise in their temperature, leading to the melting of the polymer matrix in their proximity. And such behaviour is desirable for having self-healing capability in composite structures, as in the case of micro cracks they will get filled up easily by the melt flow.

Hence, the highlighting focus of this thesis is to effectively utilise the anionic in-situ polymerisation technique for the synthesis of PMC. Since it benefits in synthesising polymer nanocomposites with be-spoke properties, utilising the ease of dispersion of the functionalised MNPs in the melt monomer and also the ability of tuning the thermo-mechanical properties by controlling the activator-initiator proportions.

4.5 Review of Relevant Methods of Characterisation

In this section the basics behind the suitable methods of MNP and PMC characterisations are briefly discussed, setting the basic idea. The specific discussions of the exact methods followed are included with the respective characterisation sections where the characterisation results of MNPs and PMC samples respectively are discussed.

2.5.1 Fourier transform infrared spectroscopy (FTIR)

The Fourier transform infrared spectroscopy (FTIR) is a well-known method for polymer characterisation (162) and is very popular for polyamides. The sharp IR peaks associated with hydrogen bonded N-H stretch is observed at 3300 cm^{-1} , that for

amide I C=O stretch bond at 1640 cm^{-1} and associated C-N stretch plus CONH bend with amide II at 1545 cm^{-1} . These characteristic peaks confirm the trans planar amide group presence (163). The differences in intensity of (sharp) crystalline bands from (broader) amorphous phase allow identifying the type of PA6 and even helps in determining the sample crystallinity.

The highly prominent band in the spectra of PA6 is usually the amide I band. This occurs at 1640 cm^{-1} in the solid state and correspond with the C=O double bond stretching mode. It is susceptible to intermolecular interactions, like contributing to H-bond formation and other differences like variation in crystal type or variation between the amorphous and crystal forms. The amide II band includes participations from in-plane N-H bending modes and central amide -N-CO- stretching modes. The amide II band is relatively susceptible to the PA chain packing details and the amide groups interactions due to different contribution sources and the coupling between them. A pattern is observed when both the amide I and amide II bands are studied collectively, wherein the amide I band moves upfield when the amide II moves downfield (164). These moves are related to the degree of sample's disorder; the sample with higher disorder show lower amide II and higher amide I band (165).

IR spectroscopy can be utilised in different polymer analysis fields and areas (162) like:

1. Recognition and determination of additives (166).
2. End group investigation (167).
3. Investigation of oxidation and degradation reactions (168), and molecular interactions (166).
4. Identification of crystallinity (169).

2.5.2 Differential scanning calorimetry (DSC) and Thermogravimetric Analysis (TGA)

For the analysis of polymer samples, it is crucial to assess their degree of crystallinity, because physical properties like density, melting point, permeability, and storage modulus are affected by crystallinity (170). The method of differential scanning calorimetry (DSC) is used to measure the exchange of heat from the sample in relation with temperature or time. DSC can be utilised to measure the polymer crystallinity by measuring the heat of fusion (related to melting) of the sample.

The DSC analysis can be done to investigate various thermodynamic properties of the synthesised polymers; in particular, the glass transition temperature (T_g), melt onset temperature, the melt peak temperature (T_m), and calculation of the degree of crystallinity by the melting endothermic peak measurement. Most of the parameters can be automatically processed and identified using the TA software that accompanies the TA DSC instrument. And the degree of crystallinity can be calculated using the following standard formula (170):

$$\% \text{ Crystallinity} = \frac{\Delta H_f^{obs}}{\Delta H_f^o} \times 100\% \quad \text{Eqn 2.1}$$

where, ΔH_f^{obs} = Observed Heat of Fusion from the DSC plot

and ΔH_f^o = Heat of Fusion of 100% crystalline polymer.

Thermogravimetric Analysis (TGA) is a method used to monitor variation in weight in a sample with the change of temperature and provides a feasible substitute to oven aging (171). In the TGA practice, different heating rates are given to material through its decomposition area. From the resultant thermal graphs, the temperatures are determined for a constant decomposition level. The kinetic activation energy is then identified from the graph of heating rate logarithm as a function of reciprocal of the temperature of constant decomposition level (171). This activation energy can be

utilised to evaluate estimated lifetime at maximum working temperature or any given temperature for a provided estimated lifetime.

To study the presence of unreacted monomer content in all the samples, the TGA can be done to quickly pick the weight loss at lower temperatures pertaining to the monomers melting. This also gives a quick insight on the crystallisation instances and various phases present in the synthesised polymer, that melt at different temperatures.

2.5.3 Transmission electron microscopy (TEM)

While the setup and proficiency are not as common as must be for essential scanning probe methods, the transmission electron microscope (TEM) is conceivably the highest quality imagery equipment for organic polymer composites currently (172). These modern techniques permit 3-dimensional plot of blend morphologies at nanometre scale with sharp material classification abilities. Though, appropriate and representative electron transparent blend layer sample are mandatory.

The basic of all TEM-based methods is the same fundamental notion of high energy electron beam (~ 100 keV) projection by an electron-transparent specimen (a fully blend film, or a prefabricated film cross-section), and producing a micrograph by transmitted electrons. The simplest method is bright-field TEM (BF-TEM), in which an image is formed after the transmission from sample along the optical axis of the electron beam (173). The brightest area of a BF-TEM image represents least scattered beam by the sample and the darkest area represents highly scattered beam far from its initial incident angle. In this way, when the nanocomposite blend film image is formed, the transmitted electron beam is scattered by various blend components to different levels and forms contrast in the resultant micrograph. This difference in scattering strength is originated from the various polymer densities (174), though these are often little because of predominantly carbon-based blend components (175). Large, crystalline characteristics like polymer 'fibrils' and nano-inclusions can thus be often distinguished quite easily, though identifying these by amorphous areas

or from mixed phase areas in polymer are very hard by BF-TEM image (176). Incident beam defocusing can improve image contrast on definite length scales to form visible BF-TEM image (177), nevertheless this can reduce resolutions, and any new feature identified in a defocused image are certainly an outcome of morphological characteristics (174).

Hence, the TEM micrographs of PMC samples can be taken to quantify the dispersion state of the MNPs within the polymer matrix, with the aim of interrelating with the other properties. Also, the details of the MNPs or agglomerates diameter range to be used for generating the simulated model can be picked by processing the micrographs. Since TEM micrographs can only help in estimating the information on dispersion state of the MNPs for few micron regions effectively, but SAXS data can give an advantage in evaluating dispersion state on a bulk scale (*ca.* hundreds of micron). Hence, the dispersion state of the PMC can additionally be characterised using the SAXS/WAXS techniques.

2.5.4 Small Angle X-Ray Scattering (SAXS)

The X-Ray scattering is a popular method for analysing the microstructural arrangements and presence or size distribution of nano-inclusions within the polymer matrix (178). This technique follows the interaction of a focused monochromatic X-ray beam with the sample electrons, wherein the scattered X-ray beams are recorded with a detector. The electron density distribution present within a crystal unit cell is presented as a Fourier transform in the form of the detected diffraction pattern (179). This scattering phenomenon can be easily described by Bragg's law:

$$n\lambda = 2d \sin \theta \quad \text{Eqn 2.2}$$

here n is a positive integer, λ is the wavelength of the incident wave, d is the repeating structure spacing, and θ is the scattering angle.

As per the Bragg's law, the observed diffraction peaks are proportional with the material's repeating unit and the analysis of the scattering pattern can give the details on the microstructural scale (179).

Generally, a wave vector \vec{q} is defined when analysing the scattering pattern, as:

$$\vec{q} = \vec{k}_0 - \vec{k}_1 \quad \text{Eqn 2.3}$$

where \vec{k}_0 is the incident X-rays wave vector and \vec{k}_1 is the scattered X-rays wave vector due to the influence of the scattering angle θ . Since, in the case of elastic scattering $|\vec{k}_0| = |\vec{k}_1| = 2\pi/\lambda$ for having the energy and wavelength similar for both the incident and scattered wave. Hence, the resulting wave vector can be written as:

$$|\vec{q}| = q = \frac{4\pi}{\lambda} \sin \frac{\theta}{2} \quad \text{Eqn 2.4}$$

Interrelating Eqn. 2.2 and 2.4, gives the relation between structure spacing and the wave vector as:

$$d = \frac{2\pi}{q} \quad \text{Eqn 2.5}$$

With this relation it can be concluded that bigger structural aspects correlate to a smaller q-value and hence a smaller scattering angle. Therefore, SAXS is widely used for characterising relatively larger structural aspects, of the range within few to hundreds of nanometres (180). This feature is hence widely used for studying the particle distribution in the polymer nanocomposites, using the derived methods of Guinier plot.

The Guinier plot obtained from SAXS/WAXS data can be used to calculate the slope of the chosen region that dictates the value of radius of gyration (R_g) of the polymer chain, from which the diameter D for the MNP/agglomerate size can be calculated qualitatively. The SAXS profile of the Guinier type plot shows two vivid regions, one which is flat region due to the base polymer response and second, a very steep sloped curve that is observed related to the response from the MNPs. Hence, the SAXS/WAXS

data is a tool for qualitative analysis of the MNP/agglomerate regions present in the samples.

The scattering intensity $I(q)$, plotted as a function of the scattering vector q can be represented with the following relation (181):

$$I(q) = G \exp\left(-\frac{q^2 R_g^2}{3}\right) \quad \text{Eqn. 2.6}$$

herein, G is the Guinier prefactor and R_g the radius of gyration.

The Guinier plot represented as $\ln I(q)$ vs q^2 , is further used to calculate the slope of the chosen region that dictates the value of R_g , giving out the MNP/agglomerate size qualitatively. The MNPs are assumed as perfect sphere and the diameter D is calculated using the following equation (181):

$$D = 2 \times (5/3)^{1/2} R_g \quad \text{Eqn. 2.7}$$

The slope of regions in the Guinier plot were calculated to give the R_g estimate (182), this was used to calculate the diameters of the MNP/agglomerate using Eqn. 2.4.

2.5.5 X-ray diffraction (XRD)

Wide-angle X-ray diffraction or simply called as X-ray deflection (XRD, $2\theta > 3^\circ$) is utilised to determine the phase composition, crystallinity, orientation and crystallite size and perfection. It is widely used for detecting features at sub-nanometre scale (180). The intensity of diffracted beams is affected by the crystallite size and perfection. The heating effects on a material are usually led to crystallites growth and simultaneously relieve any strain in material. The peak intensity is increased by heating and decrease the width at half maximum due to the significant growth of crystallite that has occurred. X-ray diffraction is most commonly used method to investigate crystalline structure.

The normal semicrystalline PA is typically considered as two-phase system consisted of amorphous and crystalline areas. The fully amorphous PA has diffraction pattern of broad diffuse radiance with maximum 22° 2θ intensity. The fully crystalline PA will

have diffraction pattern of a series of strong peaks, associated with diffraction from different crystalline planes. The size of the crystals is inversely proportional to the width of a crystalline peak. The presence of defects and distortions in crystal lattice additionally broaden the crystalline reflections in polymers. The crystallite size and perfection (L) measurement can be identified by the following Debye-Scherrer equation (183):

$$L = \frac{k\lambda}{\beta \cos \theta} \quad \text{Eqn 2.8}$$

This equation gives the relation between the peak width (β) and the crystallite size (L). It states that peak width is inversely proportional to crystallite size. (Here K is the machine constant, λ the incident wavelength and θ the angular position)

Crystallite size can be a most practical approach in many cases than crystallinity and the higher crystallite size in a sample usually implies the brittle nature of material. The higher crystallite size in many polymers is related to the greater crystal density. For usual measurement, the variation in PA unit cell volume can be eagerly followed by identifying position of the different crystalline reflections.

2.5.6 Superconducting Quantum Interference Device

Superconducting Quantum Interference Device (SQUID) is a receptive magnetometer utilized to determine very small magnetic field. It is a flux voltage converter and changes a little, hardly noticeable, flux difference into an assessable voltage change (184). The output voltage is related periodically with the applied flux, with period ϕ_0 (the magnetic flux quantum) and the output signals are detected corresponded with flux much smaller than ϕ_0 . SQUIDs can, therefore, determine any physical quantity which can be transferred into the flux, like magnetic field or its variant, displacement, voltage, current, or magnetic susceptibility. SQUIDs unite two physical phenomena, Josephson effect and flux quantization in a superconducting ring (185).

There are two kinds of SQUIDs: radio frequency (RF) SQUID which consists of only one Josephson junction (Josephson junction consist of two superconductors, separated

by a thin insulating layer, through which electrons can pass through), mounted on a superconducting ring. In an external circuit, an oscillating current is applied, and its voltage varies as a result of interactions between it and the ring. With this the magnetic flux is determined. Another one is a direct current (DC) SQUID, which is more sensitive and consists of two Josephson junctions utilized in parallel, to tunnel the electrons through the junctions showing quantum interference, depending on the magnetic field strength within the loops. DC SQUIDs show resistance in reaction of every minute changes in a magnetic field, which is the characteristic used for enabling the detection of these tiny variations.

Even though RF SQUIDs are more commonly used, DC SQUIDs are more sensitive. These are capable to determine lower fields of almost 5 aT (5×10^{-18} T), within a few days of averaged detections with much sensitivity. They have noise levels of as low as $3 \text{ fHz}^{-1/2}$. A normal refrigerator magnet generates 0.01 Tesla (10^{-2} T), and for comparison, a polymer nanocomposite sample can generate very tiny magnetic fields between 1 fT and 1 μ T.

The magnetic (SQUID) measurement technique at variable temperatures hence can be used for comparing the effect of functionalisation and the resulting dispersion state of the MNPs/agglomerates. The properties like coercivity, magnetic remanence, magnetic saturation and most importantly the derived value of magnetic moment ratio of the MNPs and the PMCs can be discussed to analyse the resulting effect. This study gives a basis to compare the other characterisation results with the magnetic response based on the resulting dispersion state of the MNPs/agglomerates in the prepared samples.

2.6 Proposed Self-healing Technology Using PMC

Considering the feasible and the upcoming trend of combining the benefits of in-situ polymerisation with alongside inculcating self-healing characteristics in the developed PMC; the possibilities of attending smart materials is assured. Such material can fulfil

much of the expected properties demanded by the rapidly advancing engineering applications as that of electrical insulation of high-voltage DC cables (HVDC), flexible risers (FR), umbilicals, etc.

Considering the current design restrictions of flexible risers, particularly the self-weight constraint, there are innovative designs of flexible risers for ultra-deep sea suitability (86). These quantifying measures are inspired by safe working needs, while reaching to ultra-deep operations. A variety of proposed configurations for hybrid-FR are presented till date, considering both composite and metal materials. One of the optimally engineered (86) combination is shown in Fig. 2.9. This design provided a baseline, which was considered to create a concept design and placed it under analysis (75).

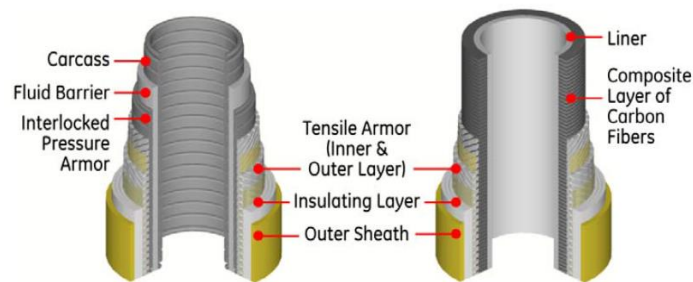


Figure 2.9. Layout of risers used in deep-sea oil explorations. Conventional Riser(left) & GE Hybrid Design(right) (86).

Even with the replacement of the metallic layer with composite carbon fibre layer, the problem is not completely addressed. As there is another issue of bending and delamination of even the reinforced composite layers, ultimately leading to crack propagation. Fig. 2.10 (a) & (b) depicts the phenomenon of delamination and crack propagation.

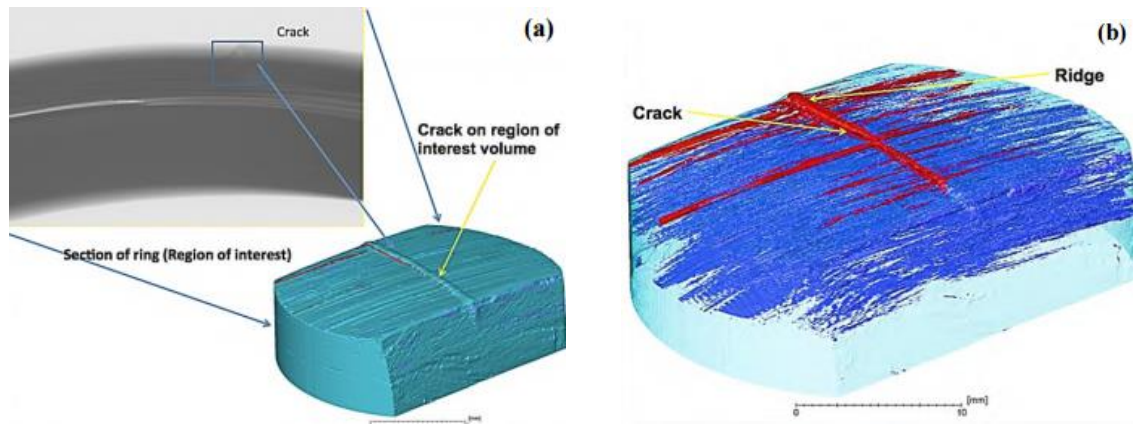


Figure 2.10. (a) Crack on the region of interest. Inset image shows propagation of crack on the bending layer and (b) Delaminated area highlighted in blue and cracks represented in red (186).

Also, further it has been noted that progressive delamination caused the further crack propagation with increased compression loads suffered on the layers. The relationship obtained by 3-D X-Ray CT (186) as shown in Fig. 2.11, present an interesting phenomenon that cracks are initiated in the elastic region of the nanocomposite material itself; hence suggesting an idea that if it is predicted in time and responded with self-healing while in the elastic region then the damage of crack propagation can be limited from further progression and even assuring healing of the nanocomposite layer back to its somewhat original state.

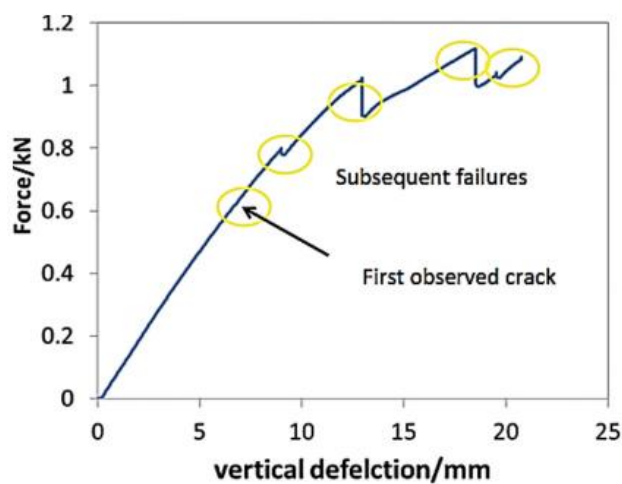


Figure 2.11. Crack initiation with the increased compressive loading and the pattern of subsequent failures observed in composite materials (186).

So, the major challenge to be carried out, is to incorporate suitable polymer based metallic nanocomposites for this application. This can be effectively addressed by designing the interfaces in polymer nanocomposites to replicate self-healing capability. Polymers like PA-6 or PVA are suitable to be used here as they can melt easily and way earlier than the other reinforcing layers, hence serving the means of filling the initiated cracks by the melt. Particularly PMC can be activated to melt the polymer matrix, by absorbing induced energy (stimuli) which can be given in the either form of wave propagation, ultra-sound, magnetic induction, or high voltage electrical signals. This concept seems quite clear and straight forward, but its implementation and specifically controlling the interfacial design for fulfilling specific applications' is the crucial research challenge ahead.

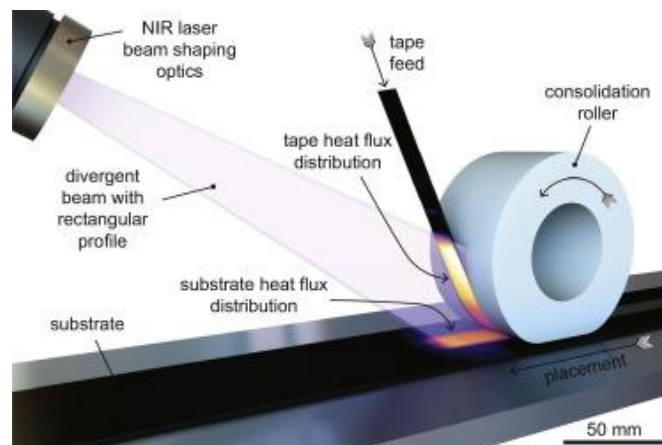


Figure 2.12. Schematic of automated tape placement method for placing GFRP/CFRP tapes on the structures like composite riser, using laser heat source (187).

The designed PMC material can be incorporated within the existing composite manufacturing process of the automated tape placement (ATP) type, as shown in Fig. 2.12, wherein the layers are placed together using a heat source (either a heat gun or laser source). The designed PMC can be placed as a consolidation or sacrificial layer between the fibres placed by the ATP method.

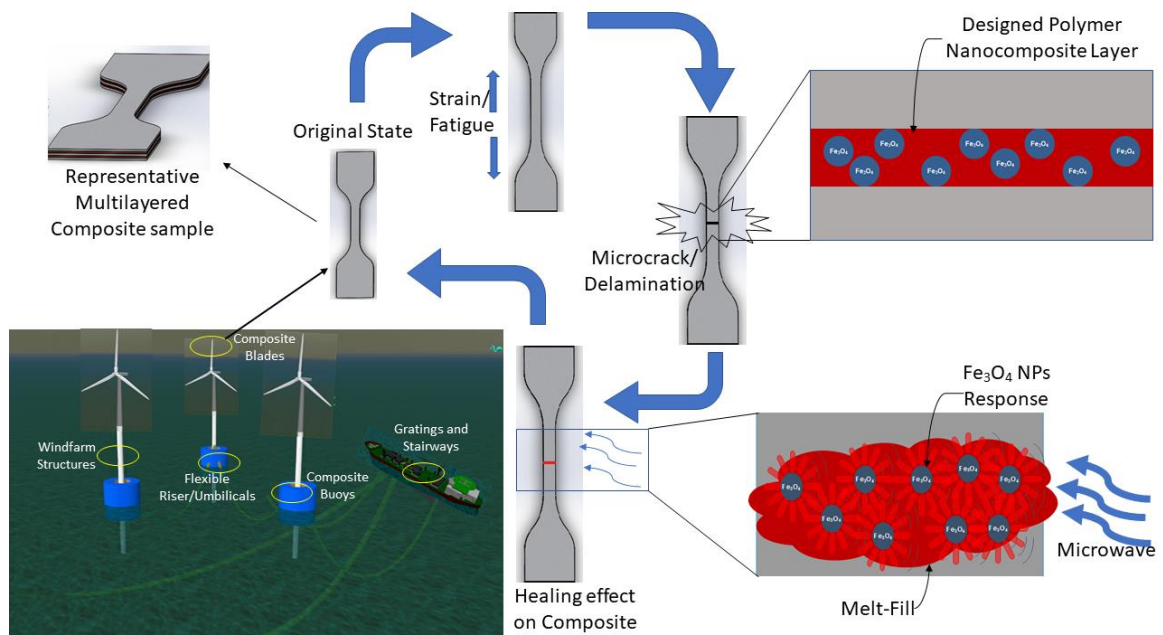


Figure 2.13. Proposed method of damage control by self-healing of PMC nanocomposites. Top-Left: Shows original sample state, Top-Right: Exposed PMC surface due to the microcrack/delamination, Bottom-Right: The MNPs absorb the microwave stimuli and fill the microcrack.

The proposed method for this study is to test with an experimental sample, the effectiveness of the designed PMC by subjecting it to purposeful failure and then implement microwave stimuli for the sample's recovery by self-healing. The efficiency of this method for damage tolerance by self-healing is then estimated by repetitive cycles of failure and subsequent healing. The overall proposal is graphically summarised in the Fig. 2.13.

Chapter Conclusion: This chapter discussed the basic required concepts of self-healing of composites, magnetism, magnetic nanoparticles, polymer nanocomposites, magnetic polymer nanocomposites, polymerisation of PA6 polymer, functionalisation of nanoparticles. The issues related with the dispersion state of nanoparticles was critically analysed for the polymer nanocomposite synthesis and the possible solutions to address those were cited from literatures. The following chapters addresses the selected method for functionalisation of MNPs and the experimental procedure for

optimising the magnetic polymer nanocomposite synthesis and its application in the composite sample preparation for self-healing demonstration by microwave stimuli.

3. FUNCTIONALISATION EFFECT ON MAGNETIC PROPERTIES OF MNPS

In this chapter the silica (Stöber and TPPE) and oleic acid functionalisation methods of the MNPs are discussed. The effect due to the functionalisation on MNPs is characterised and the characterisation results are discussed herein.

3.1 Materials

Iron(II, III) oxide MNPs (<50nm particle size) and OA (99% purity), (3-Aminopropyl)triethoxysilane (APTES) (99% purity) and Span-85 were purchased from Sigma-Aldrich Company Ltd. Dorset, UK; and used as received. The deionized water with 18 MO conductivity was used throughout the experiment.

3.2 Experimental Section

3.2.1 Silica Functionalisation

3.2.1.1 Stöber Method

The as-received MNPs weighing 2.0 g were added to 65 mL of aqueous citric acid (0.5 g/mL concentration), associated with rigorous stirring. For effective adsorption, the pH value was adjusted to 5.2 by adding aqueous ammonia solution, which resulted in dissociation of two carboxylic groups of each of the citric acid molecules. Further adsorption was enhanced by heating to 80 °C and rigorous stirring continued for 90 min. After that, the pH was increased to 10.1, wherein the third carboxylic group of the adsorbed citric acid, was dissociated (188). The resulting nanoparticles' have higher surface charge aiding electrostatic inter-particle repulsion and preventing agglomeration. The MNPs were separated and excess solvent was removed by centrifuging at 5000 rpm for 5 min and the collected nanoparticles were dispersed in clean DI water.

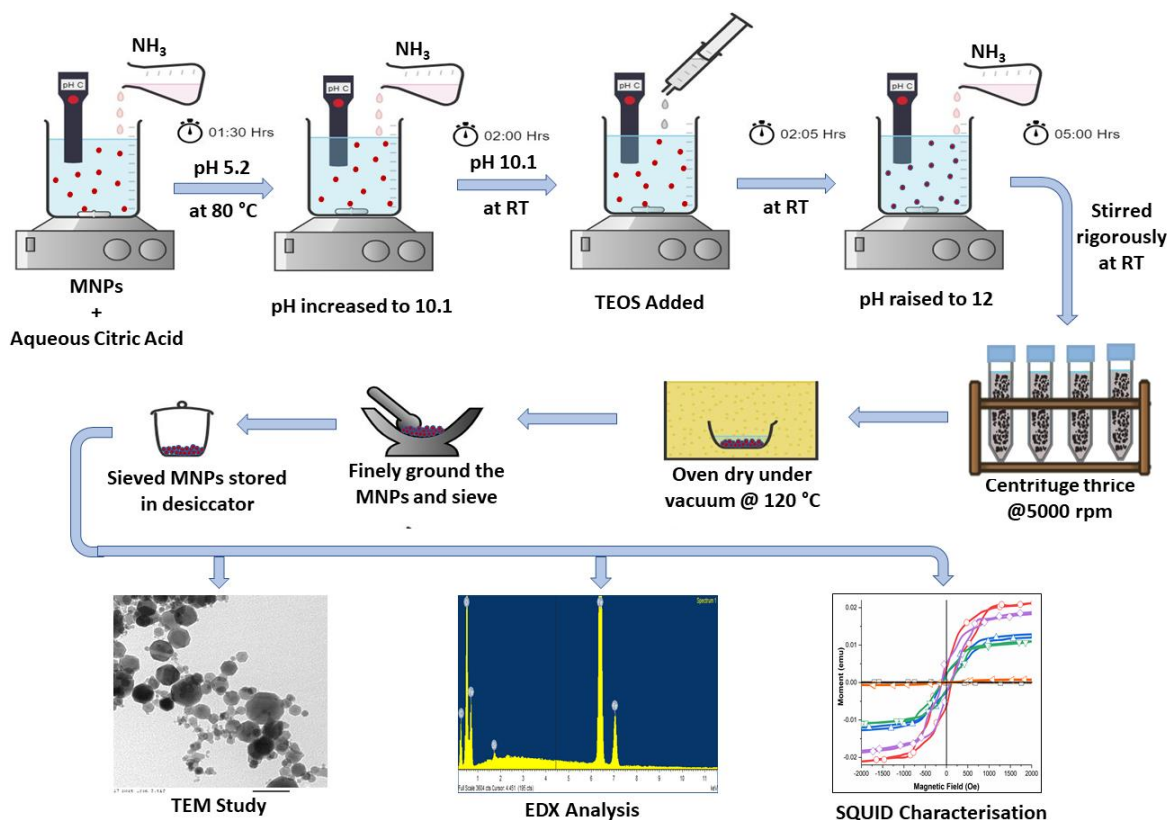


Figure 3.1. Experimental scheme that was followed for the Stöber method functionalisation of MNPs and the subsequent characterisation methods followed.

The Stöber functionalisation method was used to nucleate a silica layer on the MNPs surfaces by first hydrolysis and then polycondensation based deposition of TEOS. It's a well-known fact that the hydrolysis reaction can be catalysed using acid or alkaline solvent media, whereas it is very slow in neutral conditions (189); so aqueous NH_3 as an alkaline catalyst was used herein. The amount of TEOS to be added was calculated considering 2.4 mass ratio of MNP to TEOS. 0.85 g of TEOS dissolved in ethanol was added to the prepared suspension of magnetite MNPs; considering that the average diameter of coated MNPs are 30 nm and the used mass ratio resulted in a functionalised layer of *ca.* 2 nm (based on the surface area estimation). The pH was then stabilised at 12.0 by adding aqueous NH_3 which triggered the Stöber functionalisation reaction. The mixture was rigorously stirred for 3 hr at room temperature (RT) with probe-type 150-Watt sonicator (Soniprep 150; MSE., UK), giving the MNPs a rough silica-functionalised

coating. The MNPs were centrifuged at 5000 rpm for 5 min and then washed thoroughly three times with DI water. Collected MNPs were dried in oven at 120 °C under vacuum and further sieved. The summary of the processing technique is presented in Fig. 3.1.

3.2.1.2 Tri-Phasic Reverse Emulsion Method

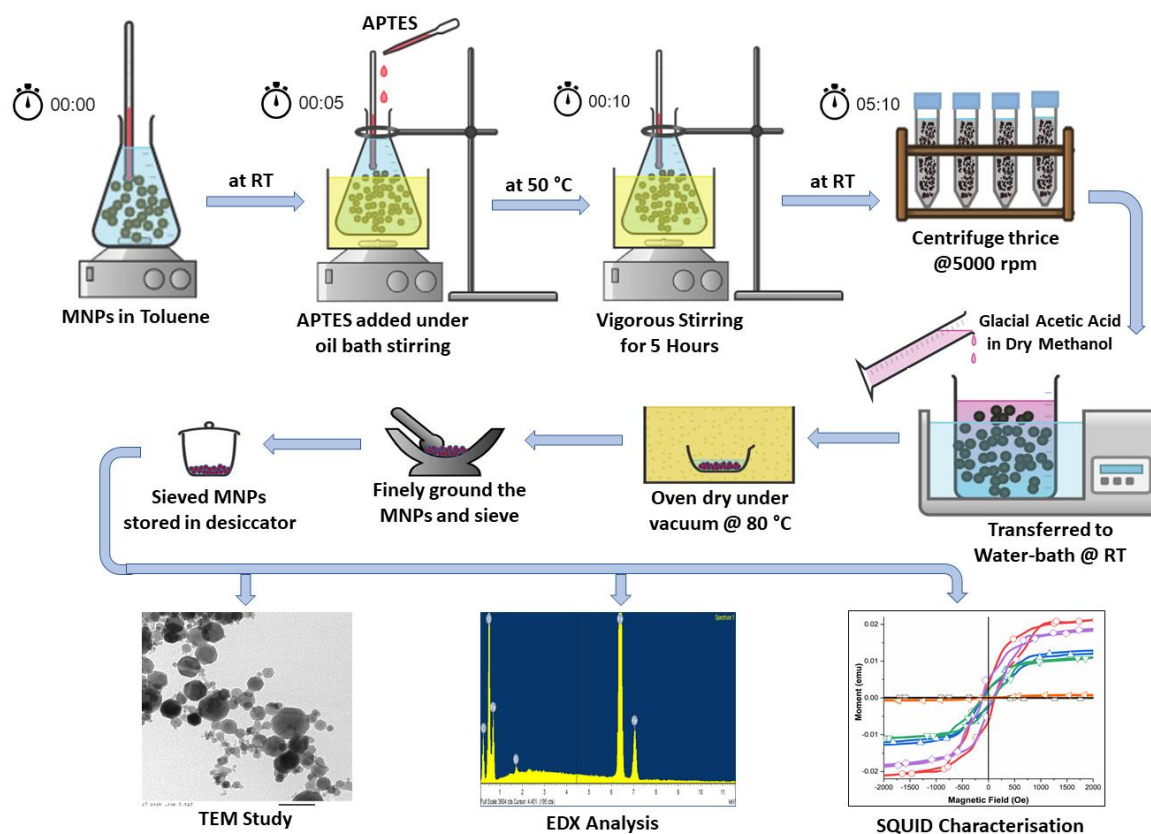


Figure 3.2. Experimental scheme that was followed for the TPRES functionalisation of MNPs and the subsequent characterisation methods followed.

Diamagnetic silica spheres were synthesized following standard Stöber method (140). Then, 150 mg of diamagnetic silica spheres was introduced into a mixture of 30ml toluene and 5gm of span-85; the mixture was shaken to form a tri-phasic reverse emulsion. APTES was added to a final concentration of 2% w/v and the mixture was left to react in condenser at 50 °C in an oil bath for 5 hrs with constant stirring. The nanoparticles were separated using decantation and washed with coupling solution of

0.8% (v/v) glacial acetic acid in dry methanol, three times and was stored in the same solution at RT. The summary of the processing technique is presented in Fig. 3.2.

3.2.2 Oleic Acid Functionalisation

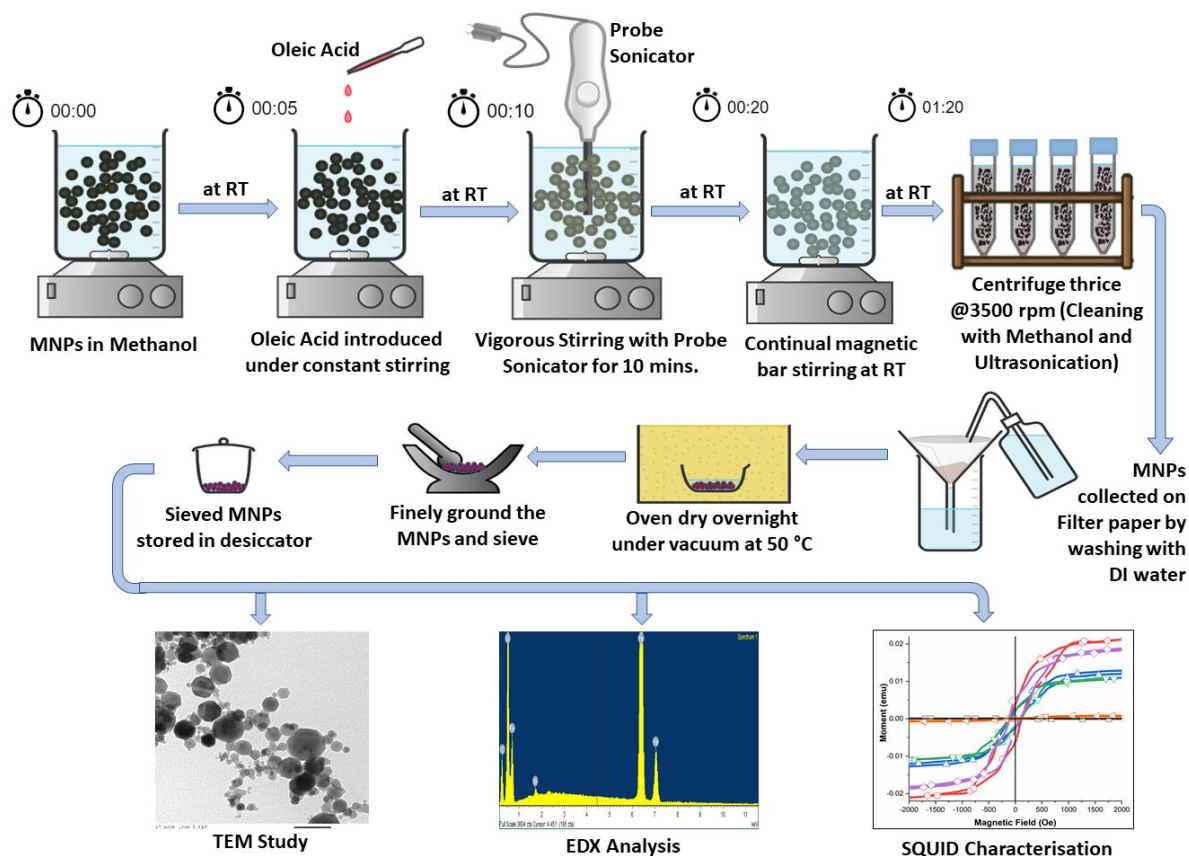


Figure 3.3. Experimental scheme that was followed for the Oleic Acid (OA) functionalisation of MNPs and the subsequent characterisation methods followed.

The Fe_3O_4 MNPs were taken in four batches of 0.225 g each and dispersed in 10 ml of methanol. Subsequently, the OA was added to individual batch to make up 22%, 33%, 44% and 55% w/w solution. Resulting solution was then mixed thoroughly using probe type sonicator (150 Watts for 10 minutes). After an hour, the mixture was centrifuged at 3500 rpm for 8 minutes and the supernatant was decanted. In remaining MNPs, the fresh methanol equivalent to discarded supernatant was added and cycle of ultrasonication and centrifugation was repeated three times to remove excess OA from the surface of iron oxide MNPs. Finally, the OA coated Fe_3O_4 MNPs were filtered using

filter paper no.1 and washed with deionized water. Later, the collected functionalised MNPs were dried overnight in oven at 50° C under vacuum. The summary of the processing technique is presented in Fig. 3.3.

3.3 Functionalised MNP Characterisation Methods

The MNPs were analysed to differentiate the morphological effect with and without the employed functionalisation method. Further, the effect on the magnetic response of the MNPs due to the involvement of functionalisation method is to be also enunciated. The description of various characterisation methods employed for the study of MNP samples are discussed as follows:

3.3.1 Transmission electron microscopy (TEM)

TEM images were used to determine the morphology and mean diameter in the MNP agglomerates, especially to measure the thickness of the functionalised layer formed on the MNPs sample. TEM imaging was conducted at an accelerating voltage of 100 kV, with a spot size of 10 nm. The exposure time was varied from 0 to 50 s. The images of all samples were obtained using a Philips CM100 TEM at different direct magnifications, ranging from x7900 to x245000. For MNPs imaging, the nanoparticles were first dispersed in isopropyl alcohol and a droplet from this was placed on gilder grid of 400 mesh. Five set of TEM images for each sample was recorded for the functionalisation thickness study.

3.3.2 Scanning Electron Microscopy/Energy-Dispersive X-Ray Analysis (SEM/EDX)

The MNP samples, both uncoated and functionalised, were firstly dispersed in isopropyl alcohol and a droplet from this was placed on the SEM stub already having carbon film on it. Once all the alcohol evaporated the MNPs were sputter coated with gold film under vacuum. The samples were then analysed with Zeiss EVO MA10 SEM & Oxford INCA X-ray microanalysis setup, having magnification range of x20 – x50,000 and resolution of

~ 20 nm. The EDX analysis was done with SEM images with focussed areas of ca. 500 μm^2 with the processing option of all elements analysed with a total of 5 iterations, on randomly selected regions. The spectrum plot was auto generated by the Oxford processing software, that is pre-loaded with the setup. Such analysis gave the quantitative results for the comparison of functionalisation employed (190,191).

3.3.3 Superconducting Quantum Interference Device (SQUID)

Magnetization loops of the functionalised MNP samples were measured at $T = 100\text{K}$ and 400K on Quantum Design MPMS XL-7, integrated with Superconducting Quantum Interference Device (SQUID) detection system and precision temperature control unit. The instrument had temperature range of 1.8 to 400 K and applied maximum field strength of ± 7 Tesla with field uniformity of 0.01% over 4 cm. Total 3 set of measurements were done for each sample type. The magnetic flux results of all the samples were plotted in terms of emu/g while analysing, hence the variations of sample weight has been accordingly considered.

3.4 Results & Discussions

The processed MNPs were analysed for the functionalisation, firstly by comparing the TEM micrographs of the bare uncoated MNPs with the processed one's. Though TEM does not gives an exact estimation, but the functional groups were exactly picked by the SEM-EDX analysis to confirm the presence of the functionalising groups. Further, the SQUID study was done to estimate the effect on the magnetic response suppression due to the functionalisation approach.

3.4.1 Quantitative Analysis of TEM Micrographs for Coating Thickness

3.4.1.1 Coating Thickness of Silica Functionalised MNPs

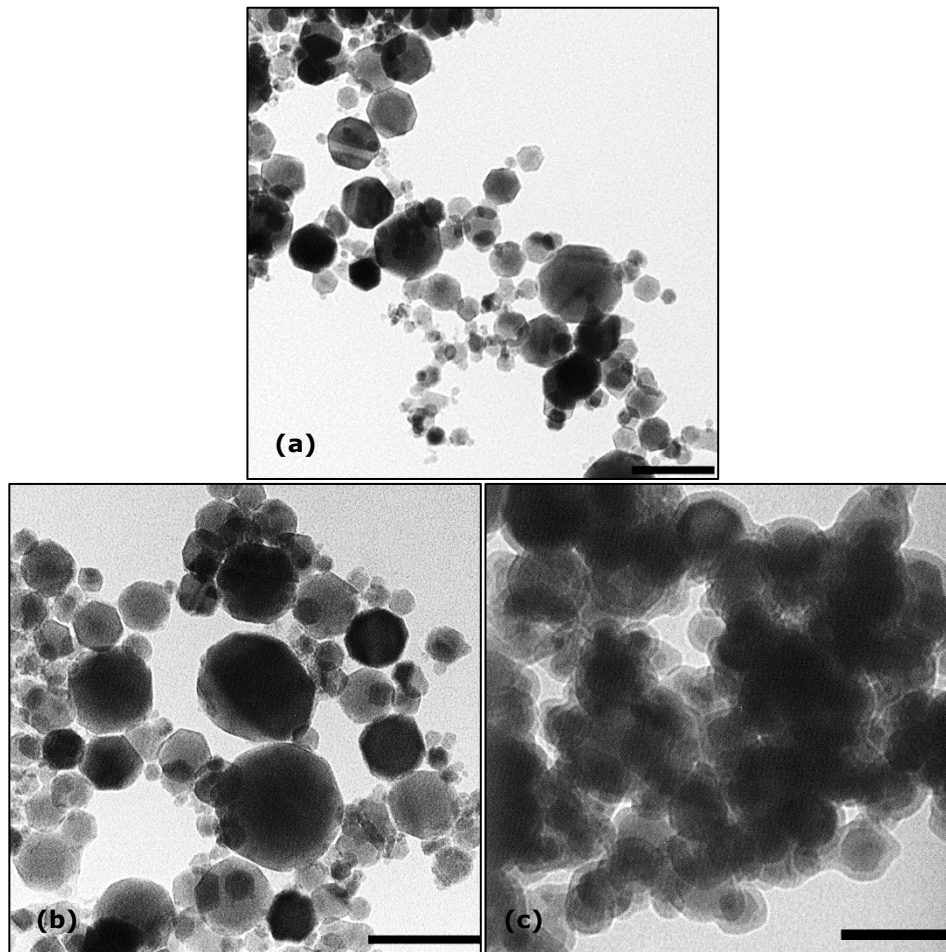


Figure 3.4. TEM micrographs of MNP samples with (a) uncoated MNPs and (b) & (c) MNPs with varying proportions of silica coating (Stöber and TPRE respectively). (Scale bar shown is of 100 nm)

In order to measure the average diameter of nanoparticles using TEM images, the obtained TEM images were first converted to 8-bit images and subsequently, the particle analysis was performed to identify the approximated area of particles assuming them to be circular. The diameters of the particles calculated using relation $\sqrt{4 \times Area/\pi}$ were compared with the measured ferret diameters and the average difference between two values were found to be 7.52% with ferret diameters being always smaller. Results show that the uncoated Iron oxide MNPs are highly agglomerated with region sizes in range of

35-50 nm, whilst the Stöber coated MNP had diameters in the range of 30-60 nm and that for TPPE coated MNP was 30-50 nm with the coating thickness of silica layer on the functionalised MNPs being *ca.* 2-3 nm and *ca.* 7-9 nm respectively. The thick silica layer formed in the TPPE functionalisation is clearly visible in the Fig. 3.4(c), hinting the higher silica loading. The original geometry of MNPs was retained even after the surface modification.

3.4.1.2 Coating Thickness of Oleic Acid Functionalised MNPs

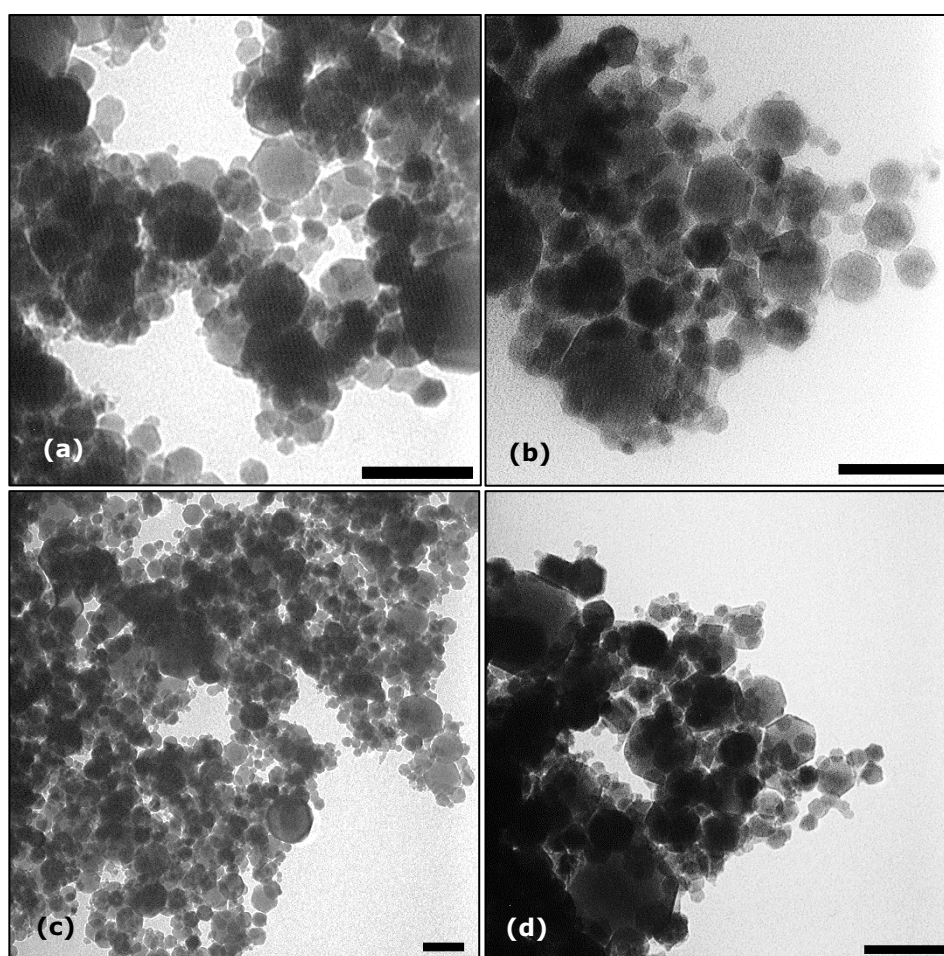


Figure 3.5. TEM micrographs of MNP samples with (a) 22 w/w% OA-Fe₃O₄ MNPs, (b) 33 w/w% OA-Fe₃O₄ MNPs, (c) 44 w/w% OA-Fe₃O₄ MNPs and (d) 55 w/w% OA-Fe₃O₄ MNPs. (Scale bar shown is of 100 nm)

The ferret diameters were calculated using the relation; $\sqrt{(minFeret \times maxFeret)}$. Results show that the OA coated MNP diameters were found to be in range of 25-40 nm for 22 wt% OA and 30-60 nm for 55 wt% OA loading. The hydrophobic nature of the organic

OA layer on the MNP surfaces restricted the interaction during sample preparation and thus small mean diameter of the MNP agglomerates in the PMC matrix is also expected (23). The thickness of the formed OA layer (Fig. 3.5) on the MNP surfaces was *ca.* 2-3.5 nm, 2.5-4 nm, 3.5-5 nm, and 4-6 nm for 22, 33, 44 and 55 wt% OA loading, respectively. Here also the original geometry of MNPs was retained even after the surface modification. The adsorption of OA on the MNPs surface are less transparent to electron beam and therefore, the coating on MNP was observed as a thick opaque layer.

3.4.2 Surface Elemental Identification using SEM-EDX

3.4.2.1 Surface Elemental Identification of Silica Functionalised MNPs

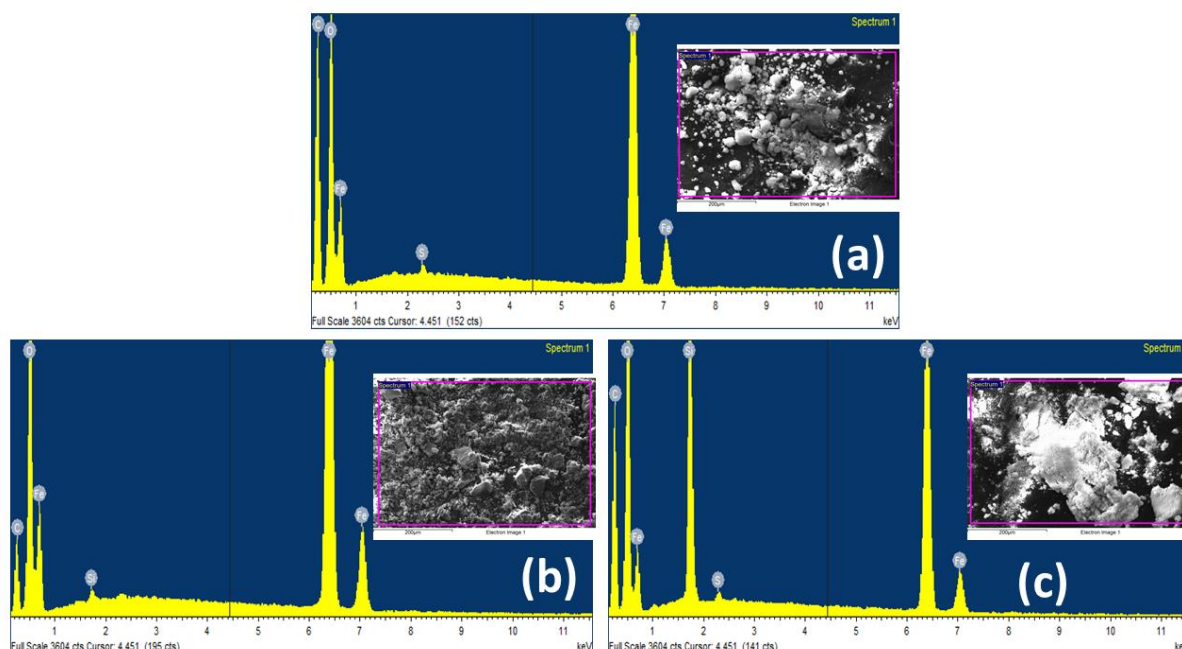


Figure 3.6. EDX spectra demonstrate the Fe peaks are observed in all samples, and the silica peak is observed in the Stöber and TPPE method functionalised samples.

EDX analysis (Fig. 6) was carried to confirm the presence of the functionalisation components in the synthesised MNP samples, since while comparing the TEM images of the uncoated Iron oxide MNPs and Stöber coated MNPs, both looked almost similar with the latter showing very faint surface coating. Hence, to distinguish and confirm the functionalisation difference between the two of them, the EDX results are purposeful

(190,191). The analysis was done on the recovered functionalised nanoparticles, hence ruling out the presence of excess silica content. The EDX spectra clearly mentions the presence of silica in the Stöber coated MNPs confirming the functionalisation, which is not observed in the uncoated Iron oxide MNPs sample. Interestingly, the silica peak is much magnified in the TPRE coated MNPs sample; wherein quantitative analysis (detailed result table included in Appendix D) showed the silica peak was 1.2 and 5.82 wt% for the *Stöber-Fe₃O₄ MNPs* and *TPRE-Fe₃O₄ MNPs* respectively which confirms the higher silica loading on the *TPRE-Fe₃O₄ MNPs* as observed in the TEM images of Fig. 3.6 (c).

3.4.2.2 Surface Elemental Identification of Oleic Acid Functionalised MNPs

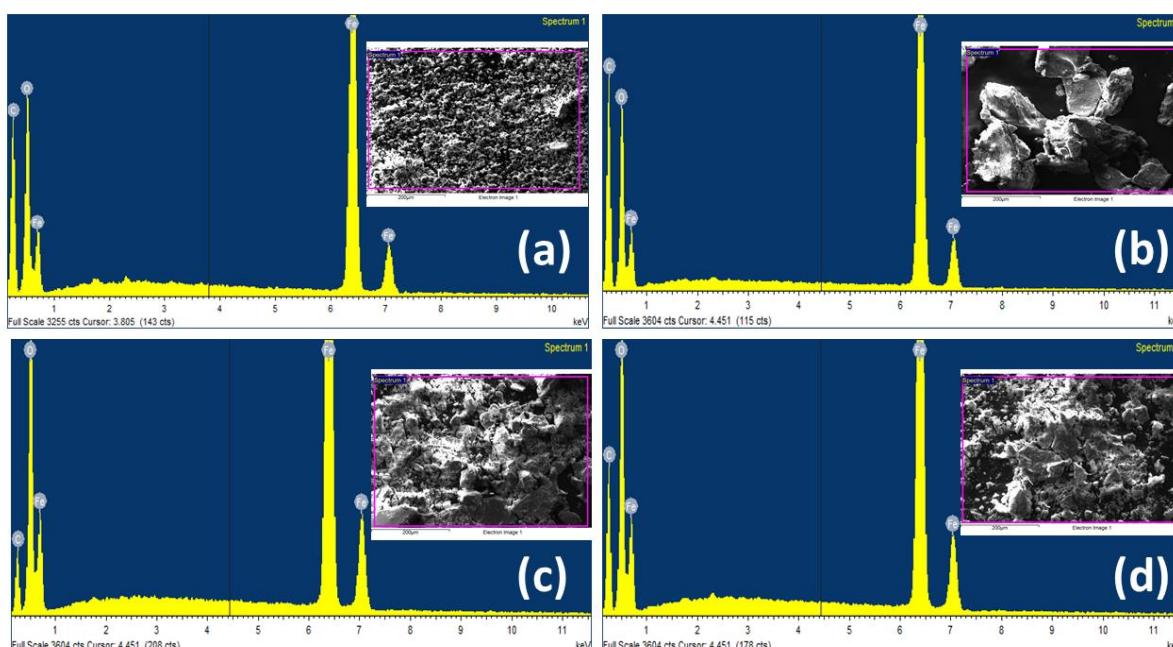


Figure 3. 7. EDX spectra demonstrate the Fe peaks are observed in all oleic acid functionalised samples, and the oleic acid's (carbon and oxygen) group are overlapping with that of iron oxide.

The EDX spectra of the OA functionalised samples (Fig. 3.7) also confirmed the functionalisation effect as compared with the uncoated Iron oxide MNPs. As expected, increasing contents of the oleic acid compounds (C and O) are observed with the sequence of 22, 33, 44 and 55 w/w % OA loading, respectively. The quantitative analysis (detailed result table included in Appendix D) showed the increasing wt% content for the C and O peaks with 48.93%, 51.15%, 54.43%, and 57.38% for the 22, 33, 44 and 55

w/w % OA loaded MNPs respectively. This confirms the increasing coating thickness as the observed pattern in the TEM images in Fig. 3.5.

3.4.3 Magnetic Moment Ratio using SQUID Measurement

3.4.3.1 Magnetic Moment Ratio of Silica Functionalised MNPs

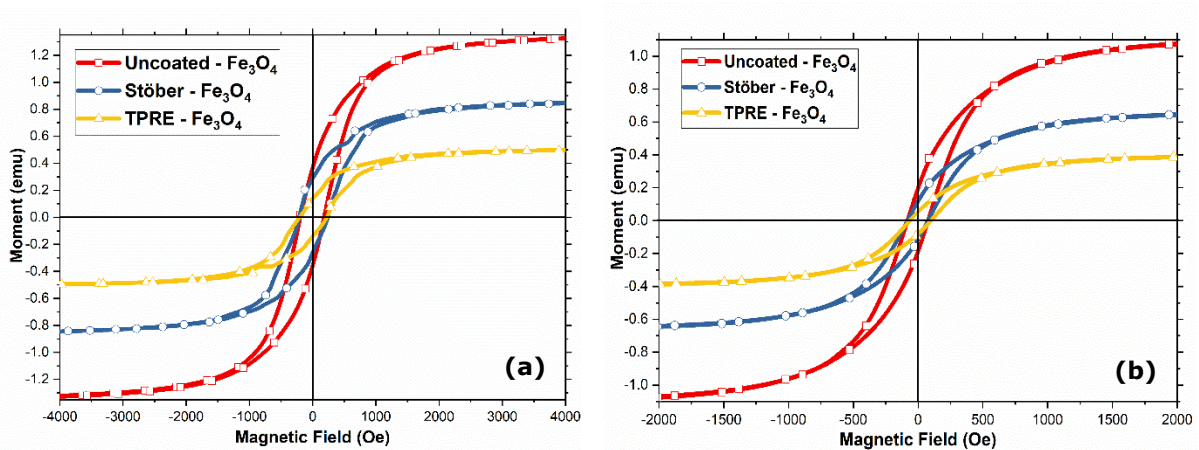


Figure 3.8. Magnetisation hysteresis loops for the MNPs functionalised by Stöber and TPRE method, measured at (a) 100 K and (b) 400 K.

The effect on the magnetic response suppression due to the silica-functionalisation is evaluated and discussed herein. The magnetic properties of the MNPs with and without functionalisation were assessed by magnetization curves at 100 and 400 Kelvin temperatures. The hysteresis loops were attained as standard, though the variation due to the silica functionalisation of MNPs clearly distinguishable in Fig. 3.8 (a) and (b). On application of homogeneous magnetic field of 50000 Oe (full scale plots included in Appendix D), at 100K the MNPs showed magnetic moment ratio (M_r/M_s) of remanence magnetisation (M_r) to saturation magnetisation (M_s) of 27.73 % for *Uncoated-Fe₃O₄* MNPs sample; and for *Stöber-Fe₃O₄* MNPs and *TPRE-Fe₃O₄* MNPs it was 33.14 % and 27.03 % respectively. And at 400K the ratio was 12.13 % for *Uncoated-Fe₃O₄* MNPs, 15.74 % and 13.42 % for *Stöber-Fe₃O₄* MNPs and *TPRE-Fe₃O₄* MNPs, respectively. The key measured response at 100K and 400K are summarised in following Table 3.1 and Table 3.2, respectively.

Table 3.1: Summarised magnetic results at 100 K for Uncoated MNPs, and MNPs with varying percentages of silica coatings (Stöber and TPRE).

Sample	Coercivity (H _c) (Oe)	Magnetic Remanence (M _r) (emu/g)	Magnetic Saturation (M _s) (emu/g)	Magnetic Moment Ratio (M _r /M _s) (%)
Uncoated-Fe ₃ O ₄ MNPs	166	3682 × 10 ⁻⁴	13280 × 10 ⁻⁴	27 ± 5
Stöber- Fe ₃ O ₄ MNPs	209	2811 × 10 ⁻⁴	8482 × 10 ⁻⁴	33 ± 3
TPRE- Fe ₃ O ₄ MNPs	210	1370 × 10 ⁻⁴	5069 × 10 ⁻⁴	27 ± 6

Table 3.2: Summarised magnetic results at 400 K for Uncoated MNPs, and MNPs with varying percentages of silica coatings (Stöber and TPRE).

Sample	Coercivity (H _c) (Oe)	Magnetic Remanence (M _r) (emu/g)	Magnetic Saturation (M _s) (emu/g)	Magnetic Moment Ratio (M _r /M _s) (%)
Uncoated-Fe ₃ O ₄ MNPs	84	2013 × 10 ⁻⁴	6600 × 10 ⁻⁴	12 ± 4
Stöber- Fe ₃ O ₄ MNPs	81	1025 × 10 ⁻⁴	6512 × 10 ⁻⁴	15 ± 3
TPRE- Fe ₃ O ₄ MNPs	81	0509 × 10 ⁻⁴	3792 × 10 ⁻⁴	13 ± 5

The combination of higher coercivity with smaller magnetic moment ratio is suitable for having higher superparamagnetic response, as discussed in the Fig. 2.7 in Chapter 2. With this observation the *Uncoated-Fe₃O₄ MNPs* and *TPRE-Fe₃O₄ MNPs* are the suitable candidates, though the *TPRE-Fe₃O₄ MNPs* has quite lower magnetic remanence than all other samples. Here, the drop in the magnetic remanence is observed with the presence and increased silica functionalisation on the MNPs, which are suppressing the magnetic response due to the magnetically dead silica layer formation. The very thick silica layer in the case of *TPRE-Fe₃O₄ MNPs*, drastically reduces their magnetic response.

3.4.3.2 Magnetic Moment Ratio of Oleic Acid Functionalised MNPs

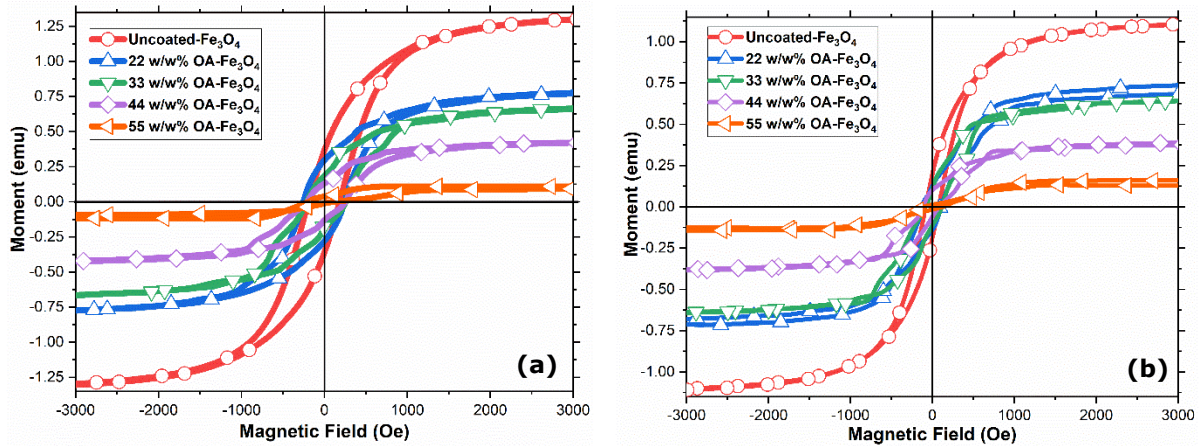


Figure 3.9. Magnetisation hysteresis loops for the MNPs functionalised by oleic acid, measured at (a) 100 K and (b) 400 K.

The effect with the varying OA functionalisation on the magnetic response of the MNPs is noted herein. It is observed that the increasing functionalisation loading proportionally reduces the magnetic response. Being organic content, the coating layer suppresses the magnetic response of the core MNPs. Here as well the magnetic response of the MNPs with and without OA functionalisation were assessed by magnetization curves at 100 and 400 Kelvin temperatures. The hysteresis loops were attained as standard, and the variation with the OA functionalisation is clearly distinguishable in Fig. 3.9 (a) and (b). With the application of homogeneous magnetic field of 50000 Oe (full scale plots included in Appendix D), at 100K the MNPs showed magnetic moment ratio (M_r/M_s) of 28 % for Uncoated-Fe₃O₄ MNPs sample; and 38 %, 34 %, 36 %, and 33 % for increasing percentages of OA loading on the MNPs, viz. 22 w/w%, 33 w/w%, 44 w/w%, and 55 w/w%, respectively. And at 400K the ratio was 12 % for *Uncoated-Fe₃O₄* MNPs and for increasing percentages of OA loading it was 24 %, 25 %, 28 %, and 22 %, respectively. The key measured response at 100K and 400K are summarised in following Table 3.3 and Table 3.4, respectively.

Table 3.3: Summarised magnetic results at 100 K for Uncoated MNPs, and MNPs with varying percentages of OA loading.

Sample	Coercivity (H _c) (Oe)	Magnetic Remanence (M _r) (emu/g)	Magnetic Saturation (M _s) (emu/g)	Magnetic Moment Ratio (M _r /M _s) (%)
Uncoated-Fe ₃ O ₄ MNPs	166	3682 × 10 ⁻⁴	13280 × 10 ⁻⁴	27 ± 5
22 w/w% OA-Fe ₃ O ₄ MNPs	249	2998 × 10 ⁻⁴	7837 × 10 ⁻⁴	38 ± 3
33 w/w% OA-Fe ₃ O ₄ MNPs	221	2285 × 10 ⁻⁴	6725 × 10 ⁻⁴	33 ± 4
44 w/w% OA-Fe ₃ O ₄ MNPs	244	1560 × 10 ⁻⁴	4286 × 10 ⁻⁴	36 ± 3
55 w/w% OA-Fe ₃ O ₄ MNPs	329	775 × 10 ⁻⁴	2361 × 10 ⁻⁴	32 ± 6

Table 3.4: Summarised magnetic results at 400 K for Uncoated MNPs, and MNPs with varying percentages of OA loading.

Sample	Coercivity (H _c) (Oe)	Magnetic Remanence (M _r) (emu/g)	Magnetic Saturation (M _s) (emu/g)	Magnetic Moment Ratio (M _r /M _s) (%)
Uncoated-Fe ₃ O ₄ MNPs	84	2013 × 10 ⁻⁴	16600 × 10 ⁻⁴	12 ± 4
22 w/w% OA-Fe ₃ O ₄ MNPs	109	1594 × 10 ⁻⁴	6715 × 10 ⁻⁴	23 ± 2
33 w/w% OA-Fe ₃ O ₄ MNPs	127	1644 × 10 ⁻⁴	6483 × 10 ⁻⁴	25 ± 4
44 w/w% OA-Fe ₃ O ₄ MNPs	108	1080 × 10 ⁻⁴	3854 × 10 ⁻⁴	28 ± 5
55 w/w% OA-Fe ₃ O ₄ MNPs	109	329 × 10 ⁻⁴	1500 × 10 ⁻⁴	21 ± 4

As discussed earlier the combination of higher coercivity with smaller magnetic moment ratio is desirable here, and the 22 w/w% OA-Fe₃O₄ MNPs comes as the suitable candidate. But in this case the 22 w/w% OA-Fe₃O₄ MNPs have quite good magnetic remanence as compared with all other samples. Again, the drop in the magnetic remanence with increasing OA loading is observed because of the magnetically inactive layer formed on the MNP surfaces. The higher the OA loading the lower is the magnetic response, as is clear with the 55 w/w% OA-Fe₃O₄ MNPs response.

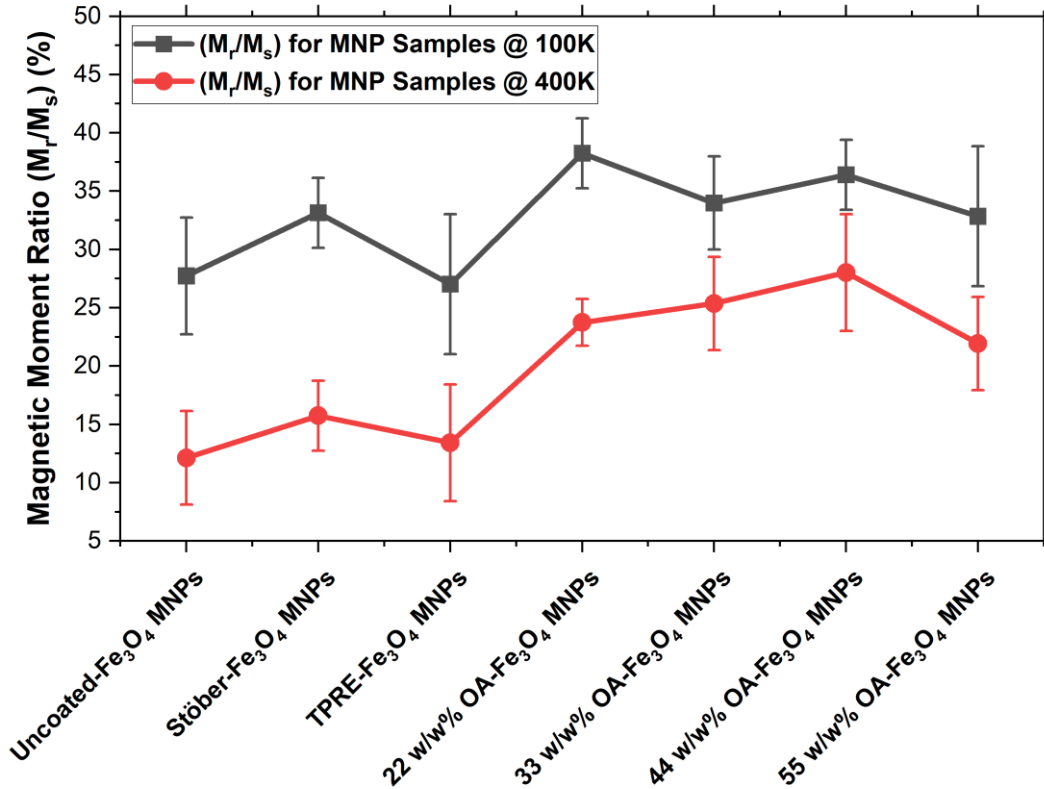


Figure 3.10. Summarised comparison plot of the magnetic moment ratio (M_r/M_s) both at 100K and 400K for uncoated and all the functionalised MNP samples.

The comparison of the uncoated and all the functionalised MNPs is summarised in Fig. 3.10, from where it can be concluded that the 22 w/w% OA- Fe_3O_4 MNPs stands out as the best performing functionalised MNP sample, in terms of the magnetic moment ratio (M_r/M_s) both at 100K and 400K. Though the effectiveness of all the functionalised MNPs is yet to be estimated based on their response when dispersed within the polymer matrix and importantly the dispersion state which they will follow. This discussion will continue in Chapter 5, wherein the PMC samples are characterised, and a suitable candidate will be selected based on the overall criteria.

Chapter Conclusion: In this chapter the variable proportions of silica and oleic acid functionalisation methods was discussed and implemented for analysing their effects on the magnetic response of the MNPs. The comparison of the magnetic response was taken

as main criteria for the selection of the most suitable technique. The functionalisation effectiveness was also analysed using the EDX and TEM method for confirming and comparing the functionalisation, wherein the EDX confirmed the elemental deposition on the MNPs surfaces and the TEM micrographs confirmed the varying functionalised coating thickness formed on the MNPs surface due to each method. The final comparison of the magnetic moment ratio (M_r/M_s) both at 100K and 400K for uncoated and all the functionalised MNP samples concluded that the 22 w/w% OA-Fe₃O₄ MNPs stands out as the best performing functionalised MNP sample. Though the main decision of selecting the best performing MNP is to be done based on their performance when dispersed in the polymer matrix. This will be assessed in the Chapter-5, as the next Chapter-4 discusses the optimisation of the polymerisation process.

4. OPTIMISATION OF PA6 PMC SYNTHESIS

This chapter discusses the effect of the activator and initiator proportions on the properties of the polymerised PA6 PMC containing 1 wt% of the uncoated MNPs. The focus herein is to tune the degree of crystallinity of the prepared PA6 PMC for the optimum response for stimuli based self-healing. The study is divided in three parts of studying the (i) initiator variation, (ii) activator variation, and (iii) both initiator and activator varied simultaneously. Based on the comparison of the results of these variation study, an optimum initiator and activator proportion is elected.

4.1 Materials

The ϵ -Caprolactam (CL) (99% purity), 3.0 M Ethyl Magnesium Bromide (EtMgBr) solution in diethyl ether, N-Acetyl Caprolactam (NACL) (99% purity), Iron(II, III) oxide MNPs (<50 nm particle size), were purchased from Sigma-Aldrich Company Ltd. Dorset, UK; and used as received. The deionized water with 18 MO conductivity was used throughout the experiment.

4.2 Synthesis Method

4.2.1 Concentration & Calculation

Following are various terms that we need to be clear of before embarking on the polymerisation calculations:

- i. Molar concentration: It is the measure of the solute concentration in a solution for a given volume. It is also referred to as substance concentration or amount concentration or even molarity. And is denoted as " M ".
- ii. Molarity: Specifically defining it, as we are calculating the proportions in terms of this. It denotes the total number of solute moles in a unit mass (kilogram) of solvent. Ideally, its denoted as " mol/kg " or molar, or simply as ' m '.
- iii. Molar solution: Molar solution refers to a solution containing one mole solute in a unit mass (kilogram) of solvent, also referred to as "one molar".

- iv. Mole fraction or Molar fraction: It represents the number of solute moles out of the total number of moles present in a solution. It is a dimensionless quantity.
- v. Mole percentage or Molar percentage: It equals to the percentage representation of mole fraction and is denoted as "mol %". It is often used in replacement for mole fraction.

The calculations for 5 g of CL polymerisation, with 1:1 volume ratio of EtMgBr and NACL and weight percentage of 2.5 % is shown as follows. This ratio and weight percentage (81) is taken as the reference for the crystallinity study of the PMC herein.

Firstly, calculating the 2.5 % equivalent of the CL's molar concentration as shown below in Equation 4.1:

$$\text{Molecular weight of CL } (M_{w-CL}) = 113.16 \text{ g/mol}$$

$$\text{Polymerisation Mass of CL } (m) = 5 \text{ g}$$

$$\text{Molar concentration, } M = \frac{m}{M_{w-CL}} \quad \text{Eqn 4.1}$$

$$M_{CL} = \frac{5}{113.16} = 0.0442 \text{ mol}$$

$$M_{CL} = 0.0442 \text{ mol}$$

$$2.5\% \text{ of CL} = 0.025 \times 0.0442 = 1.105 \times 10^{-3} \text{ mol}$$

Now, the proportional weight of 2.5 % EtMgBr can be estimated in g first and then converted into ml, as shown below in Equation 4.2:

$$\text{Molecular weight of EtMgBr } (M_{w-EtMgBr}) = 133.27 \text{ g/mol}$$

$$\text{Molar Equivalent Mass of EtMgBr} = 1.105 \times 10^{-3} \times 133.27 = 0.1472 \text{ g}$$

$$\text{Density of EtMgBr } (\rho_{EtMgBr}) = 1.02 \text{ kg/m}^3$$

$$\text{Volume } (V) = \frac{\text{Mass } (m)}{\text{Density } (\rho)} \quad \text{Eqn 4.2}$$

$$V_{EtMgBr} = \frac{0.1472}{1.02}$$

$$V_{EtMgBr} = 0.143 \text{ mL}$$

Similarly, doing the calculations for NACL:

$$\text{Molecular weight of NACL } (M_{w\text{-NACL}}) = 155.19 \text{ g/mol}$$

$$\text{Molar Equivalent Mass of NACL} = 1.105 \times 10^{-3} \times 155.19 = 0.1715 \text{ g}$$

$$\text{Density of NACL } (\rho_{\text{NACL}}) = 1.094 \text{ kg/m}^3$$

$$V_{\text{NACL}} = \frac{0.1715}{1.094}$$

$$V_{\text{NACL}} = 0.16 \text{ mL}$$

4.2.2 Polymerisation Process

The first step in the polymerisation process was to melt 30 g of CL at 60°C. MNPs were introduced into the melted monomer to prepare a 1 wt.% iron oxide nanocomposite. The mixture of MNPs and melt monomer was sonicated at 20 kHz for 30 min to ensure effective dispersion of the MNPs. The temperature of the mixture was then raised to 150°C and EtMgBr as per the calculated proportion (at a concentration of calculated mol.% mol⁻¹ CL) was introduced under an inert gas atmosphere. To complete the polymerisation, calculated proportion of NACL was added at 160°C. The mixture was left for polymerisation and time was noted with stopwatch. Before characterisation, the nanocomposite samples were thoroughly washed with deionized water (18 MΩ cm) at 100°C to remove any unreacted monomer, activator, and initiator. Total three PMC samples for each proportion type was prepared for the variation study.

4.3 Characterisation Methods for Polymerised Samples

4.3.1 Fourier transform infrared spectroscopy (FTIR)

The nanocomposite samples were characterized using Perkin-Elmer ATR-FTIR (Attenuated Total Reflection- Fourier Transmission Infrared Spectroscopy) Spectrum Gx system containing DGS-KBr sensor to identify phases and structural changes after

addition of the iron oxide MNPs. To scan each sample, the nanocomposite films of approximately 0.1 mm thickness were prepared and total 30 scans in range of 525-4000 cm^{-1} wavelength were carried out at a resolution of 4 cm^{-1} . The gain was set to 2 whereas the optical velocity was fixed to 0.4747 m/s.

4.3.2 Differential Scanning Calorimetry (DSC)

DSC was performed using a TA Instruments DSC Q100 at a heating rate of 10°C/min under a nitrogen environment with a temperature range of 20 to 270°C using a sample mass of 9 mg. The Heat/Cool/Heat standard cycle type analysis was selected for accurately depicting the behaviour and T_g and T_m for the samples prepared. The running segment consisted of a ramp heating at 10 °C/min to 250 °C, then ramp cooling at 5 °C/min to -90 °C and finally ramp heating at 10 °C/min to 250 °C. The glass transition temperature (T_g) and melting temperature (T_m) were determined from the DSC traces obtained, where the first small endothermic peak represents the glass transition temperature, and the second larger endothermic peak represents the melting temperature of the nanocomposite sample.

4.3.3 Thermogravimetric analysis (TGA)

TGA was performed using TA Instruments TGA Q500 using a sample mass of 7-12 mg. The heating rate was 10 °C/min and the 100% weight reduction mode was selected for the analysis.

4.4 Optimising Activator and Initiator Concentrations

The PA-6 finds various applications, being a semi-crystalline thermoplastic with rapid crystallisation during the polymerisation process, it depicts very good formability and mechanical properties (192). Since the inclusions of MNPs have been very popular for the means of incorporating multi-functionality in the otherwise limited-applicability polymers. Though the interface adhesion and the MNPs dispersion affect and control such attempts

(192-195); but also, the degree of crystallinity and the crystalline structure within the polymer, dictate the properties of the final synthesised PMC.

In this thesis various functionalisation techniques are studied and implemented, that were pursued to improve the dispersion of MNPs. Hence, improving the local heating effect and the physical properties of the PMC itself. One of the key findings that raised a scientific question with the reference proportions used, was the stiff behaviour of the synthesised samples. They were often very hard and stiff and could not be formed into a flexible composite structure's sacrificial layer, hence raising a challenge in its applicability for such applications. This led to the further investigation of the properties of the synthesised PMC, as to whether the properties of synthesised sample can be improved for the suitability of the application. And the first most significant parameter of the study is the crystallinity of the PMC, as that plays an important role in delivering the desired output for the application at hand. This section of study focusses on what effects it would have if the proportions of the initiator and the activator are varied in the in-situ polymerisation; and as it is obvious that the MNPs inclusion would definitely alter the PMC crystallinity under quiescent crystallisation and the resulting morphology due to huge surface area introduced by the nano-inclusions (196), though the phase transformations based on the wt% of MNPs inclusions and the resulting controlled parameterisation for growing specific crystals/crystalline phases, haven't been uncovered by any study yet. The inclusions act as nucleating sites hence inducing the crystallisation process. Also, the investigation will be whether the functionalisation plays any role in dictating the crystallisation behaviour.

The purpose of this whole study is to investigate whether any parametric control is achievable by controlling the proportions of activator & initiator, limiting wt% of MNPs inclusion to 1 wt%. Though the effect due to the designed functionalisation of MNPs is discussed separately in the following Chapter 5, along with other characterisation results for overall comparison.

Whilst investigating the effect of the above parameters on the semi crystalline morphologies; more relevantly the interested part is in finding how would the spatial distribution of MNPs be affected by crystallisation of these polymers, as that would dictate the macroscopic properties of the PMC (197,198).

Since the in-situ polymerisation process depends upon a suitable combination of initiator and activator to bring about the polymerisation of the monomer, it is obvious to comment that the rate of polymerisation will affect the crystal growth and also the variable phase transformation. In this study Ethyl Magnesium Bromide (EtMgBr) is used as the initiator. Since it is an efficient anionic initiator i.e. it gives out a lot of free protons for the reaction, hence considered as a quick-initiator. NACL was used as activator for its suitable match with EtMgBr.

In this study, each one was varied at a time first, and both together at the end. This gives an idea on the optimised usage of the proportions for getting a semi-crystalline structure of flexible thermoplastic nature, that can aid in the effective dispersion of MNPs and be easily mendable for composite structure applications.

4.4.1 Effect of Varying Proportion of Initiator (EtMgBr)

On varying the proportions of EtMgBr in this study, the initial proportion that was calculated previously, was taken here to be as being the 50% amount. So, that the proportion can be changed as higher and lower around this value. And hence the effect of the variable proportion on the synthesised PMC characteristic's is studied. The following Table 4.1 lists the parameters set for each run.

Table 4.1: Variable proportions of initiator (EtMgBr)

Sample	Proportion	EtMgBr (ml)	NACL (ml)
1	10%	0.03	0.16
2	30%	0.09	0.16
3	50%	0.14	0.16
4	70%	0.20	0.16

5	100%	0.29	0.16
----------	------	------	------

The observed time here is an approximate estimation, as some part of the monomers, especially the ones which were on the top polymerised instantly. But the measured time was for until the whole volume is polymerised or visibly solidified. The trend clearly implies that the polymerisation happens very quick as the proportion of EtMgBr is increased. This is because more protons are readily available at hand for the polymerisation reaction. Though it was also visibly observed that in the case of higher proportion of EtMgBr there were some volume of it remaining unreacted in the polymerisation. Indicating that it was wasted and hence it is not desirable to have a higher proportion of EtMgBr for polymerisation. Since that can also degrade the mechanical properties of the prepared composite samples.

Further, the DSC analysis was done to investigate various thermodynamic properties of the synthesised polymers; in particular, the glass transition temperature, melt onset temperature, the melt peak temperature, and calculation of the degree of crystallinity was investigated. The degree of crystallinity was calculated using the standard formula as given by Eqn. 2.1.

The DSC plots for all the samples of EtMgBr variations (for each % variation, there were 3 sample run with standard ramp heating at the rate of 10 °C/min (up to 250 °C) and 1 complete heat-cool-heat cycle run, wherein cooling rate was set as 5 °C/min). The detailed experimental result plots are included in Appendix B and the summary plots are presented as follows:

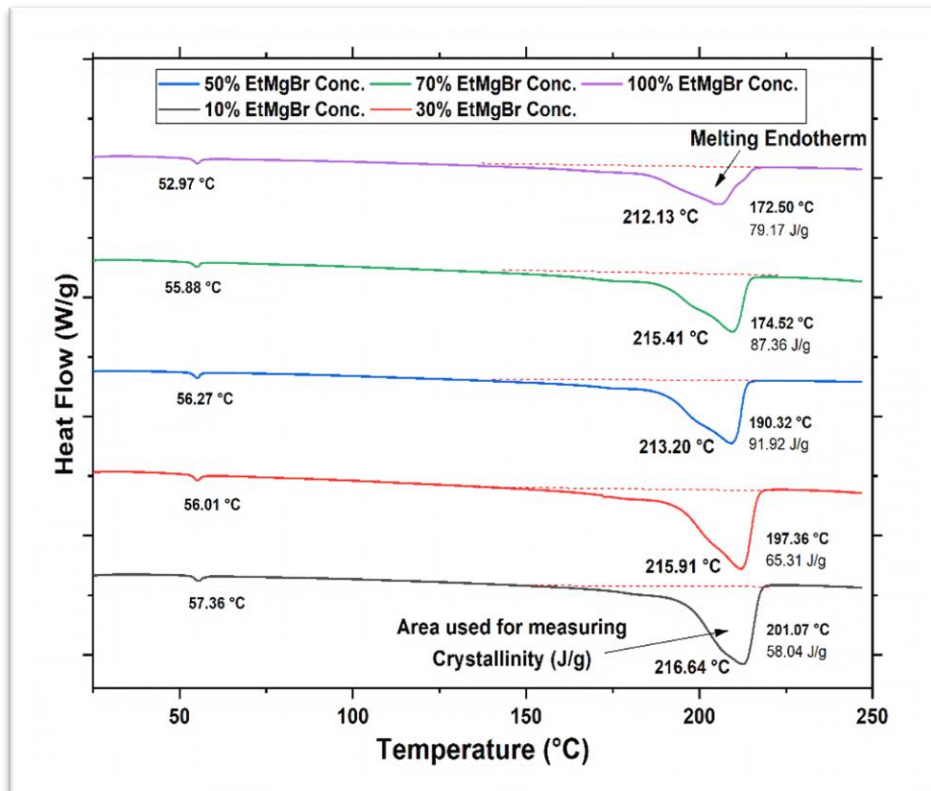


Figure 4.1. DSC plot for variable proportions of initiator (EtMgBr) concentrations.

The heat of fusion was taken from the DSC plot using the TA software functionality; and the area used is shown in Fig. 4.1.

The glass transition temperature (T_g) is reached when a polymer in its molten state is cooled. At this point, with variations in chain mobility the mechanical properties transition from elastic to brittle. The transition does not occur at a particular fixed temperature, rather is acted over a range of temperatures. And the average temperature during this transition is taken as the T_g . It is observed that the heat capacity of the sample increases after the T_g , as per the norm. Beyond T_g there is high mobility of the polymer chains and require sufficient energy for undergoing ordered patterning and finally crystallisation. The endothermic melting process lets loose, if any, ordered arrangements that were existing of the polymer chains. Hence, the heat energy absorbed now, does not adds to the increase of the chain's Kinetic energy, rather is fed to melting

of the crystalline regions. This melt peak temperature; T_m is the peak temperature of the melting curve.

These properties give the detailed characterisation on the formed crystalline phases and their transitions in the synthesised PMC samples, and hence will be giving a concluding idea on the suitability of the PMC that can suit the composite application.

Hence, the endothermic heat is calculated using this melting peak, and using the standard reference value of heat of fusion for 100% crystalline PA6 as 230 J/g (199), the calculated crystallinity values for all the samples of EtMgBr variations are summarised in Table 4.2 below. (The detailed noted values for each case are included in Appendix B)

Table 4.2: Calculation of glass transition temperature, melting temperature, and degree of crystallinity from DSC plot for EtMgBr variation samples.

EtMgBr Variation	Glass Transition Temperature (°C)	Crystallizing Temperature (°C)	Melt Peak Temperature (°C)	Enthalpy (J/g)	Crystallinity (%)
10%	57 ± 2	201 ± 2.5	216 ± 3	58 ± 1.5	30 ± 1.5
30%	56 ± 3	197 ± 4.5	215 ± 1	65 ± 2	34 ± 2
50%	56 ± 3	190 ± 5	213 ± 1.5	91 ± 1.5	48 ± 1.5
70%	55 ± 2.5	174 ± 8	215 ± 1	87 ± 2.5	45 ± 2.5
100%	52 ± 1	172 ± 10	212 ± 4	79 ± 3	41 ± 3

The above observations suggest that the crystallinity is steadily increasing with the increase in the EtMgBr proportions but drops after the 50% limit as is seen from the crystallinity values from the Table 4.2. Alongside, with the DSC plots it can be said that for higher % of EtMgBr, considerable melting and annealing occurred prior to final melting. This can be due to the crystal reorganisation and maybe part occurrence of crystallisation. Also, the presence of glass transition is observed with a steep peak gradually rising as the % of EtMgBr is increased, as the trend seen in the progression from the samples of 10% EtMgBr to 50% EtMgBr. Though there is a high possibility that

the peak observed at around 50-60 °C was because of the melting out of the unreacted monomer. Especially, the distinguishingly huge peak for 10% sample suggests that most monomers were unreacted in this case, and the melting peak for this sample is barely visible in Fig. 4.1. This also explains why the crystallinity first increased and then dropped, because there was no uniform polymer composite formation at the higher proportions level. Suggesting that 50% EtMgBr is the optimum usage for this case.

To justify this, a part of the 10% sample was taken and soaked in boiling water; and the monomers which have melting point of around 55 °C dissolved in it and were discarded with the boiling water. Further, single ramp heated DSC study was done of this treated sample. The DSC plot is as follows in Fig. 4.2:

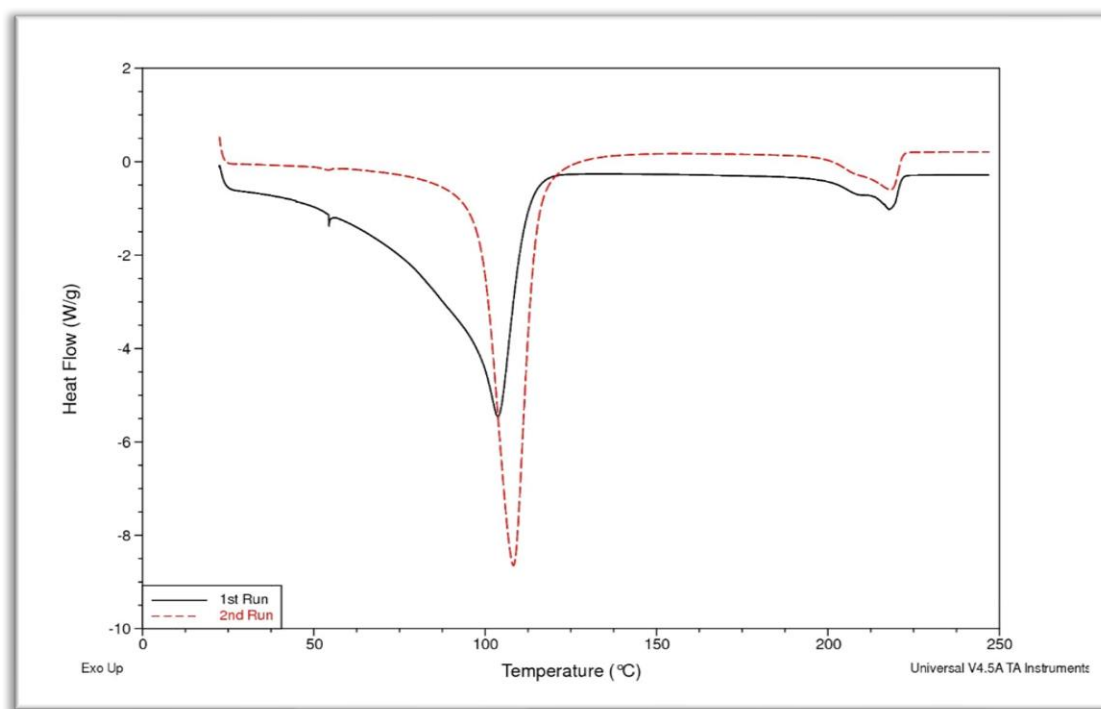


Figure 4.2. DSC plot for the initiator (EtMgBr) – 10% concentration - Boiled water sample (to remove unreacted monomer).

From the above DSC plot for two samples, it is seen that the endothermic heat peak is around 100 °C itself, which should obviously be corresponding to the water content loss from the samples, which was there due to the boiling water treatment. The 1st run gradually started forming the peak, as it had bit more water content since being the first

one; whilst the second run showed exact peak around boiling point of water temperature, also here the sample got much time to evaporate the moisture content by the passage of time. Later, a comparably smaller endothermic peak at the regular expected temperature of 215 °C is observed, which is obviously for the PMC. And the smaller peak, can also hint towards the smaller content of polymer that is present in the sample.

Also, to study the presence of such unreacted monomer content in all the samples, the thermogravimetric analysis (TGA) was done to quickly pick the weight loss at lower temperatures pertaining to the monomers melting. The maximum temperature was fixed to 800 °C, and the standard heat cycle was run for the study. This gave a quick insight of all the samples (Fig. 4.3), on the crystallisation instances and various phases present in the synthesised polymer, that melt at different temperatures.

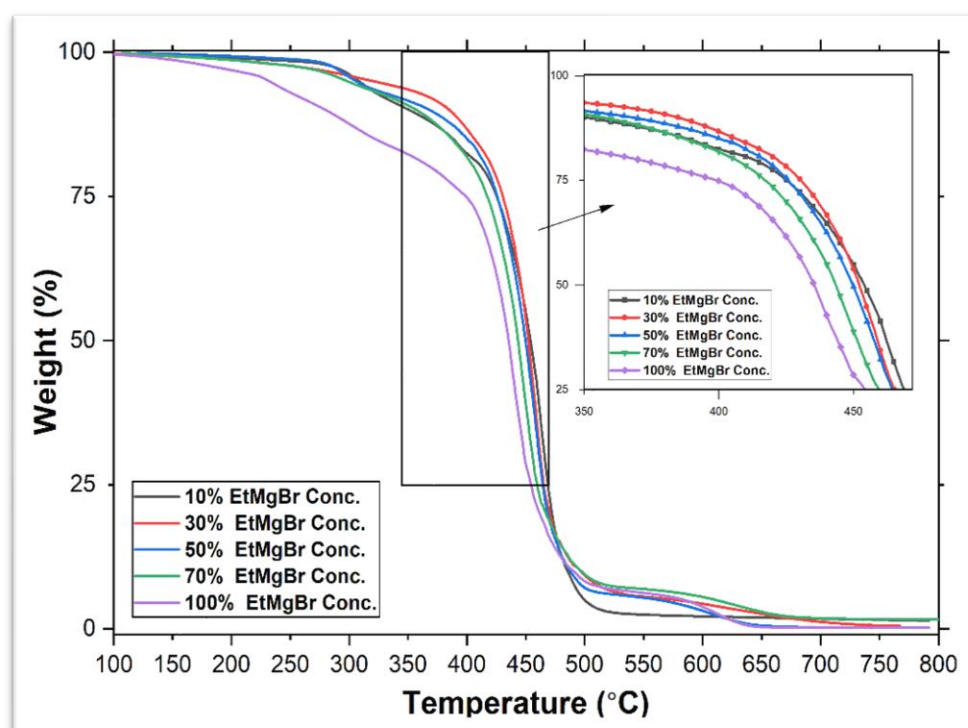


Figure 4.3. TGA plot depicting weight loss for variable proportions of initiator (EtMgBr) concentrations.

For most of the samples there was a total mass loss of 99% at the max temperature since the residue of nanoparticles remained, with around 0.15% inert residue. Though

references suggest the thermal degradation of nylon starts around 480 °C (200), but amongst all the synthesised samples the degradation for the lower % EtMgBr samples starts earlier possibly due to the agglomeration of MNPs, and then gradually rises. Since PA-6 is prone to absorb moisture, hence the plot evolves from around 150-160 °C, but this can be attributed to the most suspected monomer content and as well the absorbed moisture. Though the variations are between 1.5 % - 35 %, so here the higher value hints toward the only possibility of excess monomer presence.

The characterisation of the successful synthesis of PA6-PMC samples with varying EtMgBr proportions are assessed by analysing their FTIR spectra as shown in Fig. 4.4. The strong IR bands of commercial PA6 (163) at 3300 cm^{-1} , 1640 cm^{-1} , and 1545 cm^{-1} , conforming the hydrogen inclusive N-H stretch, the characteristic trans-planar match for amide chain of C=O stretch with amide-I, and C-N stretch with CONH bend of amide-II correspondingly are seen to be shifted slightly to 3293 cm^{-1} , 1633 cm^{-1} , and 1538 cm^{-1} respectively. This is partly due to the unreacted monomer and otherwise due to the inclusion of 1 wt% MNPs. Of the amide I and II and N-H stretch bands, the amide II band is especially sensitive to crystalline structure and hence appears to be shifted with the nano-inclusions (MNPs) and is observed around 1539 - 1537 cm^{-1} (α -phase). The IR bands for out-of-plane bends of the N-H (amide V) and C=O (amide VI) groups ideally appear as relatively sharp bands at 690 cm^{-1} and 580 cm^{-1} for the α -phase, but due to the MNPs inclusions they have shifted to around 685 cm^{-1} and 575 cm^{-1} respectively. Samples with 10%, 30%, and 100% EtMgBr proportions are observed with far wider bands close to the individual frequencies associated with the amide group, indicating that the amorphous phase consists of a wider distribution of structures α -like and γ -like. This in turn suggests that they have higher amorphous content (unlike the monomer), which is undesirable for the characteristic mechanical property built-up for the concerned composites application in this study.

The strong IR bands for CH₂ bands adjoining the NH bend and CO bend in the α -phase were herein identified at 1461 cm^{-1} and 1410 cm^{-1} respectively; instead of their regular

occurrence at 1475 cm^{-1} and 1415 cm^{-1} , respectively. The amorphous and γ -phases both are represented by bands at 1460 cm^{-1} (for some samples it appeared at 1461 cm^{-1}) and 1440 cm^{-1} (for some samples it appeared around $1436\text{-}1435\text{ cm}^{-1}$), respectively and the former is generally observed as sharp peak in the γ -phase. The two peaks between 1200 cm^{-1} (one of the samples has its appearance at 1205 cm^{-1}) and 1170 cm^{-1} is specifically indicative in all samples. The higher band (1200 cm^{-1} to 1190 cm^{-1}) appears only in the α -phase while the lower band (1189 cm^{-1} to 1170 cm^{-1}) indicates amorphous components. The wide band at 1120 cm^{-1} (appearing at 1123 cm^{-1} and 1118 cm^{-1} in most of the samples) is also helpful in examining the amorphous proportion; but the turn to sharp peaks at this band in 50%, 70% and 100% EtMgBr proportion samples reveals that they have more crystalline contents. The sharp bands observed in the synthesised samples between 980 cm^{-1} (appearing at $979, 978, 976$ or 972 cm^{-1} for the prepared samples) and 920 cm^{-1} (appearing at 918 cm^{-1} only for the 30%, 50% and 70% EtMgBr proportion samples) can identify the α - and γ - crystalline phases respectively (201). Again, indicating that the 30%, 50% and 70% EtMgBr proportion samples have higher crystalline contents. The peak near 686 cm^{-1} corresponds to the Fe-O bond stretching of iron oxide (202), confirming the presence of MNPs presence; and even relates to the amide V (α and β) content of the pristine PA6.

proportion can be changed higher and lower around this value (Table 4.3) to study its effect on the degree of crystallinity of the prepared samples.

Table 4.3: Variable proportions of activator (NACL)

Sample	Proportion	EtMgBr (ml)	NACL (ml)
1	10%	0.14	0.03
2	30%	0.14	0.10
3	50%	0.14	0.16
4	70%	0.14	0.22
5	100%	0.14	0.32

The DSC plots for all the samples of NACL variations (for each % variation, there were 3 sample run at standard ramp heating (up to 250 °C) and 1 complete heat-cool-heat cycle run) are included in the Fig. 4.5.

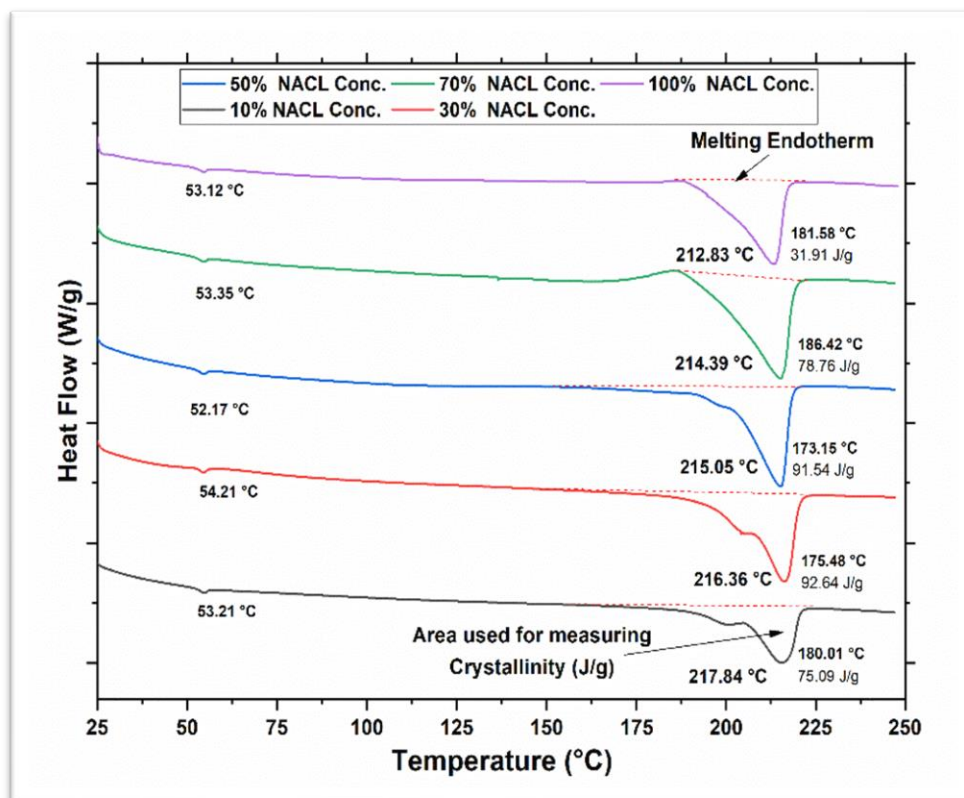


Figure 4.5. DSC plot for variable proportions of activator (NACL)

The endothermic heat is evaluated by the melting peak and standard reference value of heat of fusion as 230 J/g is used for 100% crystalline PA6 (199), the calculated crystallinity values for all the specimens of NACL variations are summarised in Table 4.4:

Table 4.4: Calculation of glass transition temperature, melting temperature, and degree of crystallinity from DSC plot for NACL variation samples.

NACL Variations	Glass Transition Temperature (°C)	Crystallizing Temperature (°C)	Melt Peak Temperature (°C)	Enthalpy (J/g)	Crystallinity (%)
10%	53 ± 1	180 ± 4	217 ± 2	75 ± 8	39 ± 8
30%	54 ± 2	175 ± 0.5	216 ± 1	92 ± 1.5	48 ± 1.5
50%	52 ± 1.5	173 ± 6	215 ± 1	91 ± 4	48 ± 4
70%	53 ± 1.5	186 ± 1.5	214 ± 0.5	78 ± 2	41 ± 2
100%	53 ± 1	181 ± 8	212 ± 0.5	73 ± 1	31 ± 1

As per the observation documented in above Table 4.4, it presents that the crystallinity steadily increases at first with the increase of NACL proportions, but gradually drops after the proportion crosses the 30% limit. Here as well considerable melting and annealing occurred prior to the final melting due to the crystal reorganisation and possible part occurrence of crystallisation. Though the higher proportion of activator made the polymerisation reaction faster, but the resulting settlement of crystals is not uniform. Hence, the resulting lower degree of crystallinity at higher NACL proportions. As per the results tabulated, it is suggested that either the proportion of 30% or 50% NACL be used as optimum value, to give the highest level of degree of crystallinity. Also, at higher proportions there was unreacted NACL remaining at the surface of the samples. Though the polymerisation reaction was rapid, which is good for capturing the dispersed state of the nanoparticles, but the polymerisation reaction was non-uniform and polymer chains could not propagate and interlink together due to unreacted monomers. This is what resulted in the lower degree of crystallinity.

To study the presence of unreacted monomer content in all the samples, the thermogravimetric analysis (TGA) was done to quickly pick the weight loss at lower temperatures pertaining to the monomers melting. The maximum temperature was fixed to 800 °C, and the standard heat cycle was run for the study.

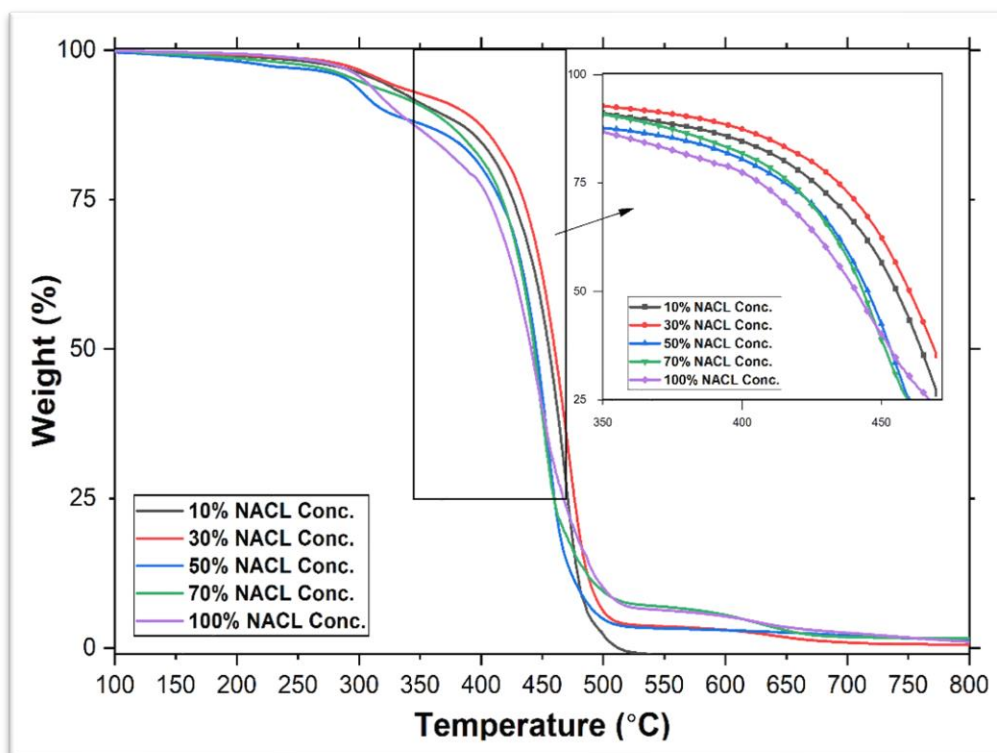


Figure 4.6. TGA plot depicting weight loss for variable proportions of activator (NACL) concentrations.

Here also at maximum temperature, the total mass loss was 99% with nanoparticles residue and with inert residue of 0.15% for all samples. All the samples thermally degraded (Fig. 4.6) as almost like the standard nylon sample and the degradation trend follows from the lower to higher % NACL samples. The plot evolves from around 150-160 °C as in previous case, but main variations were observed in the range of 350 to 500 °C. The highest thermal resistance is illustrated by 30% NACL proportion sample as compared to all other samples; overall, it performed better against thermal degradation.

FTIR spectra were used to analyse the successful synthesis of PA6-PMC samples with different NACL proportion as depicted in Fig. 4.7. The strong IR bands of commercial PA6

(163) were around 3300 cm^{-1} for hydrogen bonded N-H stretch, 1640 cm^{-1} corresponding to amide group's trans-planar presence for the amide-I C=O stretch, and 1545 cm^{-1} , corresponding to amide-II C-N stretch with CONH bend were all observed to be partly shifted to 3296 cm^{-1} , 1634 cm^{-1} , and 1538 cm^{-1} , respectively. This is partly because of unreacted monomer and otherwise due to 1 wt% MNPs inclusion. The amide II band of the amide I & II and N-H stretch bands is particularly responsive to crystalline structures and therefore appears to be shifted with the nano-inclusions (MNPs) and was observed around $1539 - 1537\text{ cm}^{-1}$ (α -phase). The IR bands at 690 cm^{-1} for off-the-plane stretch of N-H (amide V) and at 580 cm^{-1} for C=O (amide VI) groups for the α -phase ideally appeared as comparatively sharp bands, however, these have shifted to around 685 cm^{-1} and 577 cm^{-1} respectively because of the MNPs inclusions. The samples with 10% and 100% EtMgBr proportion were observed to have much wider bands close to every frequency related with the amide group and showed that the amorphous phase is consisted of broader distributions of α -like and γ -like structures. This signifies that unlike monomers, they have greater amorphous proportion which is undesirable for general mechanical properties.

The CH_2 bends adjoining the NH and CO in the α -phase are herein detected as sharp IR bands around 1461 cm^{-1} and $1415/1416\text{ cm}^{-1}$ respectively, instead of their regular occurrence at 1475 cm^{-1} and 1415 cm^{-1} , respectively. The amorphous and γ -phases both are represented by peaks at 1461 cm^{-1} (for 50% NACL proportion sample it appeared at 1460 cm^{-1}) and 1440 cm^{-1} (for 30% NACL proportion sample it appeared at 1441 and for 50% and 70% NACL proportion samples it appeared at 1440 cm^{-1} itself), respectively and the former is generally observed as sharp peak in the γ -phase. The 10% and 100% NACL proportion samples did not showed the 1440 cm^{-1} peak, indicating their lower crystalline content. The two peaks between 1200 cm^{-1} (the samples have its appearance around $1205\text{-}1199\text{ cm}^{-1}$) and 1170 cm^{-1} (some samples showed its presence at 1169 cm^{-1}) is exclusively present in all samples, though the 1170 peak is quite sharp in only 30%, 50% and 70% NACL proportion samples. Herein the higher band (1200 cm^{-1} to 1190 cm^{-1}) appears only in the α -phase while the lower broad peak (1189 cm^{-1} to 1170 cm^{-1})

C=O double bond stretching mode and appeared around 1635-1633 cm^{-1} for all the prepared NACL samples. Regarding the shifts associated with disordering level of the samples; more disordered samples imply higher amide I and lower amide II bands (164). In this case, disorder is seen with the variation in proportions of NACL in samples which had unreacted monomer because of either insufficient NACL (10% NACL proportion sample) or which had higher NACL content (100% NACL proportion sample) that formed polymerisation of the monomer+EtMgBr solution rapidly by contacting with activator (NACL). The sample with 100% NACL proportion, also had noteworthy concentration of NACL remaining as unreacted, because of unbalanced mixtures resulting from rapid polymerisation of the top surface monomer+EtMgBr solutions.

4.4.3 Effect of Varying Proportion of Initiator (EtMgBr) and Activator (NACL) both

Like mentioned earlier, the initial proportion as calculated previously, was taken here to be as being 50%. So, that the proportions of initiator (EtMgBr) and activator (NACL) both can be changed higher and lower around the calculated value.

Table 4.5: Variable proportions of initiator (EtMgBr) and activator (NACL) both.

Sample	Proportion	EtMgBr (ml)	NACL (ml)
1	10%	0.03	0.03
2	30%	0.09	0.10
3	50%	0.14	0.16
4	70%	0.20	0.22
5	100%	0.29	0.32

The DSC plots for all the sample variations (for each % variation sample there were three standard ramp heating (up to 250 °C) sample run and 1 complete heat-cool-heat cycle run and are included in the Appendix B) is included in the following Fig. 4.8.

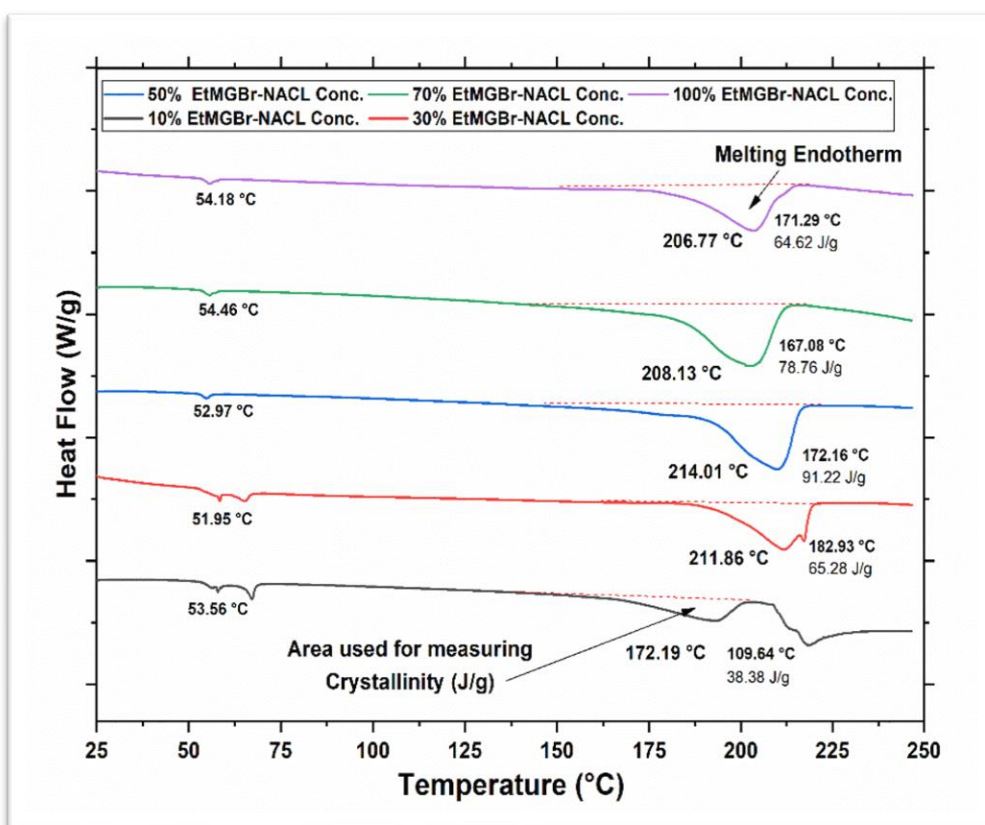


Figure 4.8. DSC plot for variable proportions of initiator (EtMgBr) and activator (NACL) both.

Like previous, the endothermic heat is calculated using this melting peak, and using the standard reference value of heat of fusion for 100% crystalline PA6 as 230 J/g (199), the calculated crystallinity values for all the sample variations are summarised in Table 4.6 below. (The detailed noted values for each case are included in Appendix B)

Table 4.6: Calculation of glass transition temperature, melting temperature, and degree of crystallinity from DSC plot for samples with variation of initiator (EtMgBr) and activator (NACL) both.

EtMgBr & NACL Variations	Glass Transition Temperature (°C)	Crystallizing Temperature (°C)	Melt Peak Temperature (°C)	Enthalpy (J/g)	Crystallinity (%)
10%	53 ± 1	109 ± 9	172 ± 12	38 ± 9	20 ± 9
30%	51 ± 1.5	182 ± 4	211 ± 2	65 ± 5	34 ± 5
50%	52 ± 2	172 ± 8	214 ± 2.5	91 ± 1.5	48 ± 1.5

70%	54 ± 2	167 ± 4.5	208 ± 2.5	81 ± 1.5	42 ± 1.5
100%	54 ± 3	171 ± 11	206 ± 3	64 ± 3.5	34 ± 3.5

As per the observation documented in above Table 4.6, the degree of crystallinity steadily increases till the proportions of 50% for both EtMgBr & NaCl, but again gradually drops after that limit. Again, considerable melting & annealing occurred prior to the final melting due to the crystal reorganisation and possible part occurrence of crystallisation. The lowest proportion, i.e. 10% of both initiator and activator made the polymerisation reaction incapable, hence clearly confirming that both need to be at least used at 50% proportion values for successful polymerisation. The lowest proportion sample had most part as unreacted monomers, since the lack of protonating members led to limited polymerising sites. On the other hand, the higher proportion values of initiator and activator can rapidly capture the dispersed nanoparticle state, but the resulting polymer nanocomposite sample lacks the degree of crystallinity due to non-uniform polymerisation caused by the rapid reaction. Also, there are losses due to unreacted activator remaining, in case of higher proportions samples.

The results of this variation study present that both activator and initiator, if used at the 50% proportion value, can give the highest degree of crystallinity. Otherwise, the resulting samples lack the required mechanical properties (degree of crystallinity) as desirable for composite sample preparations. An excess of this proportion leads to non-uniform polymerisation, wastage of activator and even lower degree of crystallinity.

Likewise, to study the volume of unreacted monomer content in all the samples, the thermogravimetric analysis (TGA) was done to quickly pick the weight loss at lower temperatures pertaining to the monomers melting. The maximum temperature was fixed to 800 °C, and the standard heat cycle was run for the study.

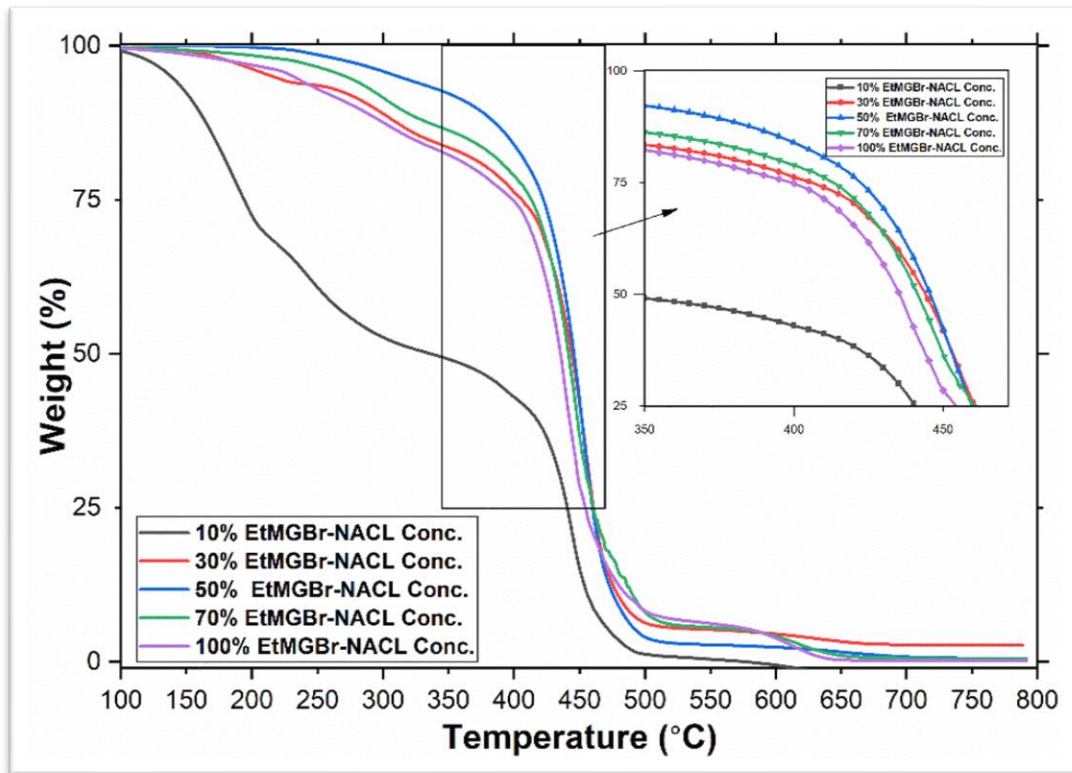


Figure 4.9. TGA plot depicting weight loss for variable proportions of initiator (EtMgBr) and activator (NACL) both.

Here also the total mass loss was 99% at the max temperature with the residue of nanoparticles and with around 0.15% inert residue for all the samples. The thermal degradation of all the samples (Fig. 4.9) are almost like that of a standard nylon sample. And the degradation trend follows from the lower to higher % NACL samples. Unlike the previous case, here as well the plot evolves from around 150-160 °C and major changes are observed in the 350 to 500 °C region, except for the 10% EtMgBr-NACL sample which showed drastic degradation in sample weight. The TGA result confirms the higher unreacted monomer content in this sample and its unsuitability for any mechanical application. And the superior performance against thermal degradation is shown by the 50% EtMgBr-NACL proportion value polymer composite sample, amongst all the samples.

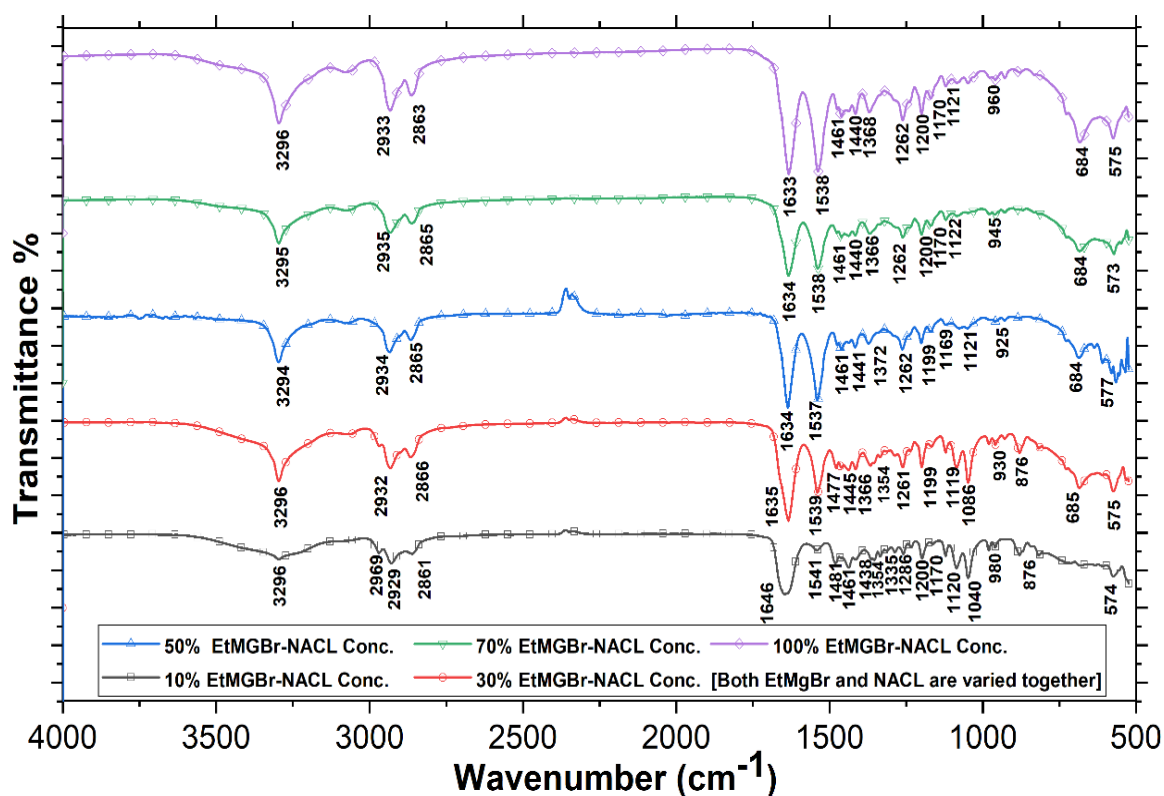


Figure 4.10. FTIR plot for variable proportions of initiator (EtMgBr) and activator (NACL) both.

The characterisation of the successful synthesis of PA6-PMC samples with varying EtMgBr & NACL proportions are assessed by analysing their FTIR spectra as shown in Figure 4.10. The prominent IR bands of commercial PA6 (163) are seen to be shifted slightly to 3296-3294 cm⁻¹, 1646-1633 cm⁻¹, and 1541-1537 cm⁻¹ respectively; partly due to the unreacted monomer and otherwise due to the inclusion of 1 wt% MNPs. The amide II band appears to be shifted with the nano-inclusions (MNPs) and is observed around 1541 - 1537 cm⁻¹ (α -phase). The out-of-plane bends of the N-H (amide V) and C=O (amide VI) groups ideally appear as relatively sharp bands at 690 cm⁻¹ and 580 cm⁻¹ for the α -phase, but due to the MNPs inclusions they have shifted to around 685 cm⁻¹ and 575 cm⁻¹ respectively. Samples with 10%, 30%, and 100% EtMgBr & NACL proportions are observed with much broader bands associated with the amide group, indicating that the amorphous phase consists of a wider distribution of structures α -like and γ -like, suggesting that they have higher amorphous content (unlike the monomer).

The CH₂ bends adjoining the NH and CO in the α-phase for these samples are detected as sharp IR bands around 1461 cm⁻¹, instead of its regular occurrence at 1475 cm⁻¹. The amorphous and γ-phases both are represented by the stretch at 1461 cm⁻¹ and 1440 cm⁻¹ (for some samples it appeared around 1445-1441 cm⁻¹), respectively and the former is generally observed as sharp peak in the γ-phase. The peaks between 1200 cm⁻¹ appeared for all samples (some of the samples has its appearance at 1199 cm⁻¹) but the peak at 1170 cm⁻¹ was seen only for the 10%, 30%, and 100% EtMgBr & NACL proportion samples. The higher band (1200 cm⁻¹ to 1190 cm⁻¹) appears only in the α-phase while the lower band (1189 cm⁻¹ to 1170 cm⁻¹) indicates amorphous components, hence indicating that the 10%, 30%, and 100% EtMgBr & NACL proportion samples had higher amorphous contents. The wide band at 1120 cm⁻¹ (also appearing as 1121 cm⁻¹ and 1119 cm⁻¹) appeared only for the 50%, 70%, and 100% EtMgBr & NACL proportion samples and gives hint on their amorphous content. But the turn to sharp peaks at this band in 10%, and 30% EtMgBr & NACL proportion samples reveals that they have more crystalline contents; but since the 10% sample wasn't properly formed, so this only applies to the 30% EtMgBr & NACL proportion sample. The peak near 685-684 cm⁻¹ corresponds to the Fe-O bond stretching of iron oxide (202), confirming the presence of MNPs presence; and even relates to the amide V (α and β) content of the pristine PA6. The 1640 cm⁻¹ amide I band corresponding to the C=O double bond stretching mode is observed around 1646-1633 cm⁻¹ for the prepared samples. Observing the shifts in the amide I and amide II bands the disorder is observed (164) herein with the varying proportions of EtMgBr & NACL proportion in samples those had either unreacted monomer due to insufficient EtMgBr & NACL (10% EtMgBr & NACL proportion sample) or the one's with high content of EtMgBr & NACL proportion (70% and 100% EtMgBr & NACL proportion samples) that created very rapid polymerisation of the monomer+EtMgBr solution after contacting the activator (NACL). In this case also excess/unreacted NACL was left above the prepared samples, due to insufficient mixing arising due to very quick polymerisation reaction.

4.5 Selection of Optimum Proportion

Based on the FTIR study from the proportion variations of EtMgBr, NACL and EtMgBr+NACL it is observed that most of the samples (except the 10% EtMgBr+NACL proportion sample) were mostly following the PA6 backbone; though with varying amorphous/crystalline contents. Hence confirming that most of them were synthesised almost to the level of commercial PA6 nanocomposite. And the thermal degradation study also showed fairly similar response from all the samples (except the complete distinguishing and degraded performance by the 10% EtMgBr+NACL proportion sample). So, the main criteria of comparison can be taken as that of the highest degree of crystallinity level achieved by any individual sample, as studied by the DSC results. This criterion would also ensure the best candidate is selected fulfilling the better mechanical property of film formability, crucial for the composite film preparation to prepare the composite samples. Following Fig. 4.11 compares the degree of crystallinity achieved by the samples of varying proportions of EtMgBr, NACL and EtMgBr+NACL.

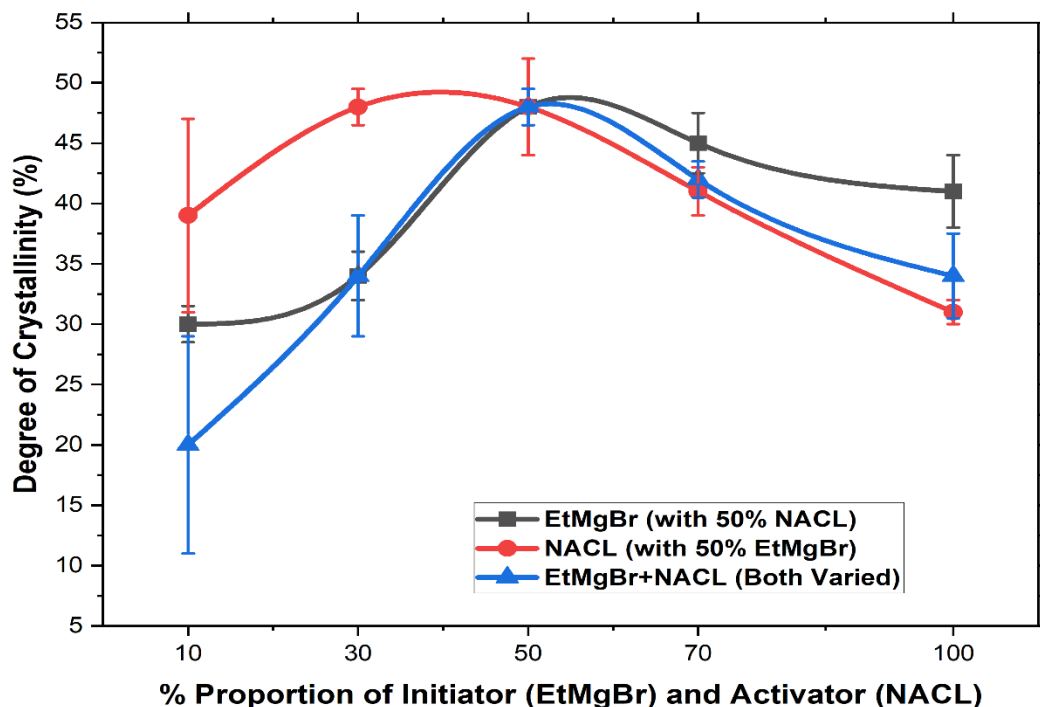


Figure 4.11. Comparison of degree of crystallinity achieved by each sample with varying the proportions of EtMgBr, NACL and EtMgBr+NACL.

The comparison plot clarifies that the samples with 50% EtMgBr proportion or in other words with 50% NACL proportion or also termed as 50% EtMgBr + 50% NACL had all similar degree of crystallinity (%); which is obvious as they all were practically the same samples, just prepared in slightly different manner. Though the highest degree of crystallinity (%) was noted for the sample with 30% NACL proportion (with 50% EtMgBr proportion) amongst all the samples. But it was almost comparable to what was observed in the 50% samples mentioned before. So, as a matter of choice either one could be selected as the optimum proportion for giving the highest degree of crystallinity (%). However, to ensure the efficient utilization of resources the 30% NACL proportion (with 50% EtMgBr proportion) should be selected as the optimum proportion; this would ensure that no excess/unreacted NACL is left during the polymerisation process.

Furthermore, the inferences from this variation study are taken and applied on the crucial part of the further study, i.e., to synthesise the final magnetic PA6 nanocomposite samples and elect the best one out of them to form into thin films for preparing the sandwich composite GFRP samples.

Chapter Conclusion: In this chapter the PA6 polymerisation process is discussed with the inclusion of MNPs. The variation of the initiator and activator is discussed in detail, with their variation effects discussed on the resulting composite properties. The FTIR spectra was used to analyse the resulting composite samples chemical backbone, DSC analysis was utilised to study their resulting degree of crystallinity and TGA analysis was used to assess their thermal degradation. The degree of crystallinity achieved by each sample with varying the proportions of EtMgBr, NACL and EtMgBr+NACL was plotted for comparison and the sample with 30% NACL proportion (with 50% EtMgBr proportion) showed highest degree of crystallinity (%) amongst all the samples. This sample is hence chosen for making the composite dogbone samples for further testing.

5. PMC SYNTHESIS WITH FUNCTIONALISED MNPS

This chapter discusses the preparation of the PMCs with the optimised proportions of the activator and initiator but involving the silica (Stöber and TPPE) and oleic acid functionalised MNPs. The effect of the functionalised MNPs on the prepared PMCs properties in terms of the interrelation of the MNPs/agglomerates dispersion state, degree of crystallinity, crystallite size, and the magnetic moment ratio response is discussed. The simulated model generation is also presented including the interaction radius discussion. It concludes with an overall comparison of all the studied/observed parameters and suggesting the selection of the most suitable PMC for the composite sample preparation on this basis.

5.1 Experimental Method

Prior to the polymerisation process, all MNPs used were exposed to UV radiation (36 Watts, 368 nm (peak wavelength)) for 30 minutes to remove any moisture. Separately, 30 g of CL was weighed in a beaker and heated to 90°C on a hot plate. Once monomer was fully melted in the beaker, the MNPs were added and resulting mixture was sonicated at 20 kHz for 30 minutes to ensure uniform dispersion of the MNPs.

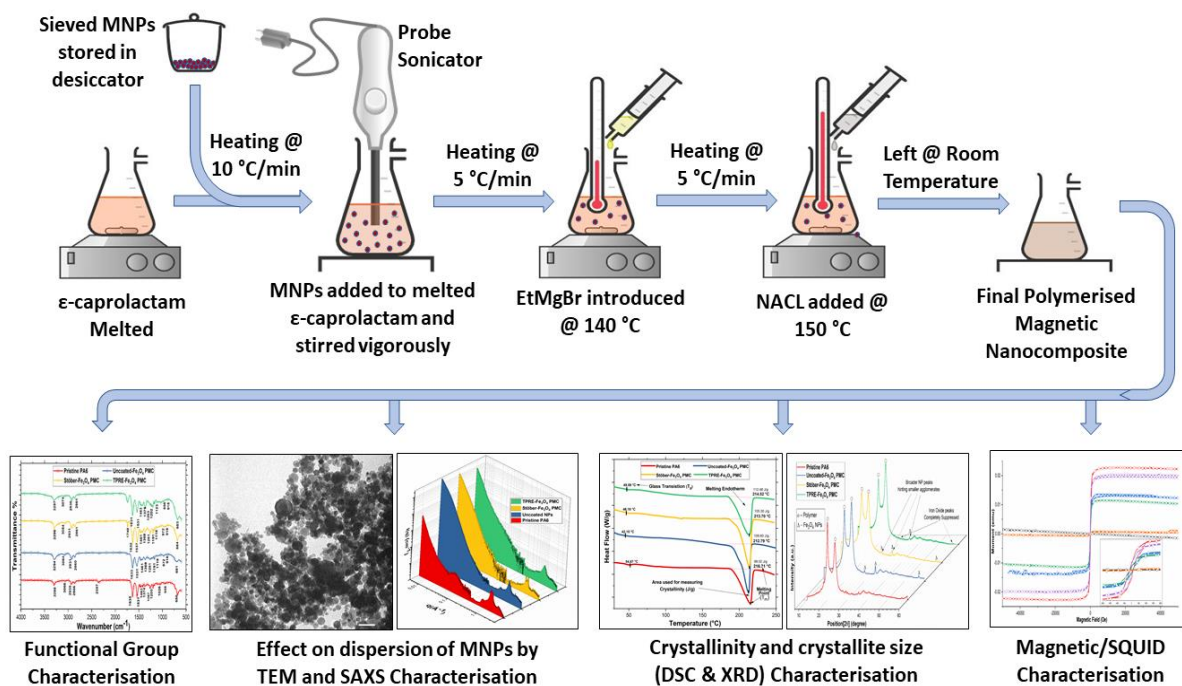


Figure 5.1. Experimental method followed for the polymer magnetic nanocomposite synthesis and the subsequent list of characterisation methods followed.

The mixture was then transferred to two-necked flask and heated until 150°C. The flask was continuously flushed with nitrogen to avoid moisture and its volatile reaction with catalyst EtMgBr. Now, here the optimised contents of activator and initiator were used for the polymerisation process. EtMgBr measuring 0.86 mL was extracted from the stock bottle using syringe while stock bottle was nitrogen flushed. Subsequently, EtMgBr was injected through rubber stopper fixed on two-necked flask. Next, 0.576 mL of NACL was introduced as an initiator to the mixture kept at 150°C. As soon as NACL was introduced, the mixture was instantly polymerized. Once the nanocomposite was cool, then boiling water was used to wash recover nanocomposite from the glassware. Three PMC samples of each type was prepared for the characterisation study. The nanocomposite samples were prepared and thoroughly washed with alcohol for further characterisations. The entire process is summarised in Fig. 5.1.

5.2 PMC Characterisation Methods

The descriptions of various characterisation methods followed for the PMC sample study are described in this section. Though, specific results and inferences from them on the property of the samples are summarised in Chapter 5.

5.2.1 Fourier transform infrared spectroscopy (FTIR)

The nanocomposite samples were characterized using Perkin-Elmer ATR-FTIR (Attenuated Total Reflection- Fourier Transmission Infrared Spectroscopy) Spectrum Gx system containing DGS-KBr sensor to identify phases and structural changes after addition of the iron oxide MNPs. To scan each sample, the nanocomposite films of approximately 0.1 mm thickness were prepared and total 30 scans in range of 525-4000 cm^{-1} wavelength were carried out at a resolution of 4 cm^{-1} . The gain was set to 2 whereas the optical velocity was fixed to 0.4747 m/s.

5.2.2 X-Ray diffraction (XRD)

A PANalytical X'Pert Pro MPD, powered by a Philips PW3040/60 X-ray generator and fitted with an X'Celerator detector was used. Diffraction data is acquired by exposing samples to Cu-K α X-ray radiation, which has a characteristic wavelength (λ) of 1.5418 Å. X-rays were generated from a Cu anode supplied with 40 kV and a current of 40 mA. The data were collected over a range of 0 to 80° (2θ) with a step size of 0.117° (2θ) and nominal time per step of 1099.82, using the scanning X'Celerator detector. Fixed anti-scatter and divergence slits of 0.38 mm were used together with a beam mask of 10mm and all scans were carried out in a continuous mode. Phase identification was carried out by means of the X'Pert-PRO accompanying software program PANalytical High Score Plus in conjunction with the JCPDS card.

5.2.3 Transmission electron microscopy (TEM)

TEM imaging was conducted at an accelerating voltage of 100 kV, with a spot size of 10 nm. The exposure time was varied from 0 to 50 s. The images of all samples were obtained using a Philips CM100 TEM at different direct magnifications, ranging from x7900 to x245000. An ultrathin section of nanocomposite obtained using microtome were placed on gilder grid of 400 mesh to obtain all images. For MNPs imaging, the particles were dispersed in isopropyl alcohol and droplet were placed on TEM grid.

5.2.4 Differential Scanning Calorimetry (DSC)

DSC was performed using a TA Instruments DSC Q100 at a heating rate of 10°C/min under a nitrogen environment with a temperature range of 20 to 270°C using a sample mass of 9 mg. The Heat/Cool/Heat standard cycle type analysis was selected for accurately depicting the behaviour and T_g and T_m for the samples prepared. The running segment consisted of a ramp heating at 10 °C/min to 250 °C, then ramp cooling at 5 °C/min to -90 °C and finally ramp heating at 10 °C/min to 250 °C. The glass transition temperature (T_g) and melting temperature (T_m) were determined from the DSC traces obtained, where the first small endothermic peak represents the glass transition temperature, and the second larger endothermic peak represents the melting temperature of the nanocomposite sample.

5.2.5 Small & Wide-angle X-ray scattering (SAXS/WAXS)

SAXS and WAXS scattering patterns were obtained on Xenocs Nano-inXider, equipped with microfocus sealed tube: Cu, 30W point focus. With Dectris Pilatus 3 hybrid photon counting (two fixed) detectors for continuous and simultaneous SAXS and WAXS acquisition up to $2\theta=60^\circ$. The beam path was windowless beam path, entirely under vacuum from beam delivery system to detector sensor. The SAXS patterns were obtained over a scattering vector length within the range of $0.008 \text{ \AA}^{-1} < q < 0.18 \text{ \AA}^{-1}$ and WAXS patterns with the range of $0.18 \text{ \AA}^{-1} < q < 0.24 \text{ \AA}^{-1}$. One-dimensional (1D) fitting of

the scattering curves was obtained by an azimuthal binning and averaging of corresponding two-dimensional scattering patterns using the XSACT (X-Ray Scattering Analysis and Calculation Tool) supplied with the instruments.

5.2.6 Superconducting Quantum Interference Device (SQUID)

Magnetization loops of the synthesised PMC samples were measured at $T = 100\text{K}$ and 400K on Quantum Design MPMS XL-7, integrated with Superconducting Quantum Interference Device (SQUID) detection system and precision temperature control unit. The instrument had temperature range of 1.8 to 400 K and applied maximum field strength of ± 7 Tesla with field uniformity of 0.01% over 4 cm.

5.3 Results and Discussion

5.3.1 Functional Group Study of synthesised samples

5.3.1.1 Silica-functionalised samples

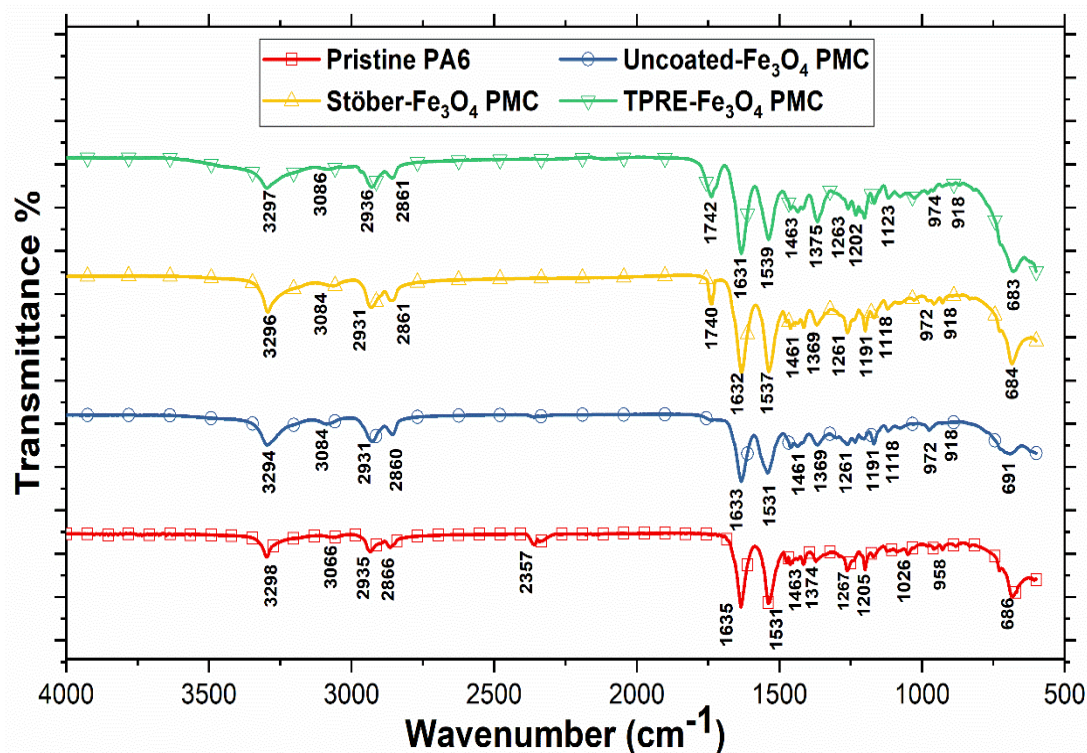


Figure 5.2. ATR-FTIR Spectra of pristine polymer (PA6), sample with uncoated MNPs and samples with varying proportions of silica coatings (Stöber and TPRE) on the MNPs.

The FTIR peaks confirm the synthesis unlike commercial polyamide 6 (PA6), matching with standard template chemical groups (23). From Fig. 5.2, the N-H stretching absorbance band and hydrogen bonding as observed in PA6 is seen around 3294-3298 cm^{-1} . Major absorbance peaks relating to methylene (CH_2) symmetric and asymmetric stretching vibrations band related to PA6 are also observed around 2860-2866 cm^{-1} and 2931-2936 cm^{-1} confirming the successful synthesis of PA6 (23,203). Additionally, these absorbance bands also confirmed the presence of amide II band of primary amides, which occurred due to the stretching vibration of C=O double bond, that in turn attributed to the functionality of the amide I band. Additional peaks relating to amide I and II bands were also seen around 1531-1537 cm^{-1} , of the primary nature but led to the vibration due to stretching of the C-N bond, which further resulted in vibration due to bending of the N-H bond and the CO-NH bend (204).

From the observed trend in Fig. 5.2 the level of crystallinity is seen increasing with the involvement of silica functionalisation, which can be confirmed by the shift observed in the peaks from 1531 cm^{-1} (*Uncoated-Fe₃O₄ PMC*) to 1537 cm^{-1} (*Stöber-Fe₃O₄ PMC*) and 1539 cm^{-1} (*TPRE-Fe₃O₄ PMC*) (203). The degree of crystallinity is generally dictated by the position and intensity of these crystalline bands, as well as the broader bands from the amorphous phase (205). It is inferred that the degree of crystallinity is moderately high in the polymer samples with the functionalised MNPs, as the amide II band, sensitive to the crystalline structure, appeared around 1531 cm^{-1} in the spectrum of *Uncoated-Fe₃O₄ PMC* sample. The wavelength fingerprint for silica is typically around 1700 cm^{-1} , however, the closest corresponding absorbance band is observed as a sharp peak at ca. 1740 cm^{-1} and 1742 cm^{-1} for *Stöber-Fe₃O₄ PMC* and *TPRE-Fe₃O₄ PMC* sample, respectively (206).

5.3.1.2 OA-functionalised samples

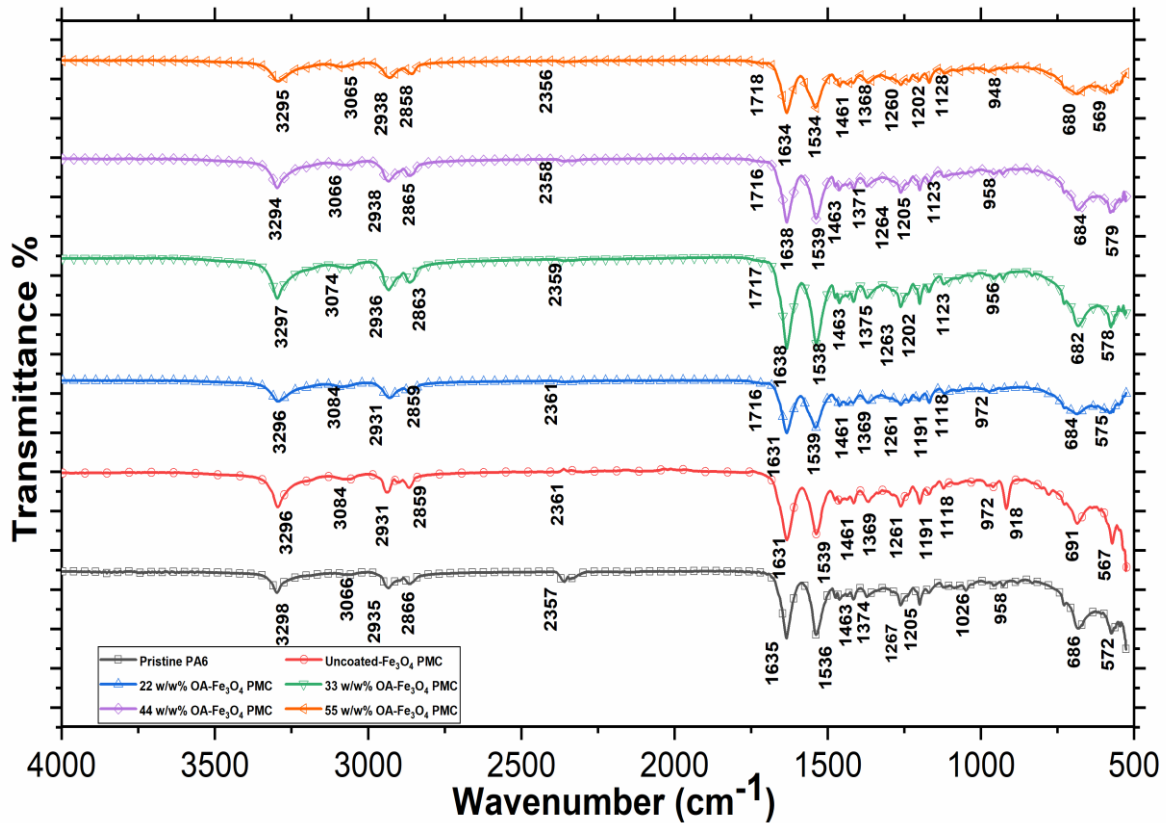


Figure 5.3. ATR-FTIR Spectra of Pristine PA6, sample with uncoated MNPs and polymer samples with varying proportions of OA coatings on the MNPs.

Here as well, the FTIR peaks confirmed successful synthesis of polyamide 6 (PA6), matching with template standard chemical groups associated with commercial grade PA6 (23). As observed in Fig. 5.3, the absorbance band corresponding to N-H stretching and hydrogen bonding as found in the PA6 was observed at 3296 cm⁻¹. Prominent peaks related to methylene (CH₂) asymmetric and symmetric stretching vibrations absorbance band related to PA6 were also observed at 2935 cm⁻¹ and 2861 cm⁻¹ confirming formation of PA6 (23,203). In addition, this absorbance band also confirmed the presence of the amide II band of primary amides, which occurred due to stretching vibration of the C=O double bond, which further attributed to the functionality of the amide I band. Peaks were also seen around 1540 cm⁻¹, which were additional peaks relating to the previously mentioned amide I and II bands of the primary type but also

the vibration due to stretching of the C-N bond, which then resulted in a vibration due to bending of the N-H bond and the CO-NH bend (204).

As observed in Fig. 5.3, the levels of crystallinity was seen decreasing with increase in OA concentration in coating, which was confirmed by observation of shift in the peaks from 1538 cm^{-1} to 1539 cm^{-1} , 1537 cm^{-1} , 1537 cm^{-1} , to 1531 cm^{-1} for increasing proportion of OA coating (203). The degree of crystallinity is generally dictated by the position and intensity of these crystalline bands, as well as the broader bands from the amorphous phase (205). It is inferred that the degree of crystallinity is moderately high in the polymer samples with low concentration of OA, as the amide II band, sensitive to the crystalline structure, appeared around 1540 cm^{-1} in spectrum of uncoated PA6. The carboxylic end group present at the end of OA fatty acid chain coating that interacted with NH_2 of the polyamide chain and reduced polymer chain mobility and therefore, slow formation of crystals and crystallinity (207). The wavelength fingerprint for OA is typically around 1700 cm^{-1} , however the closest absorbance band of OA was observed at a small broad peak near the end of the 1633 cm^{-1} peak and are noted around $1716\text{-}1718\text{ cm}^{-1}$. (208).

Level of crystallinity in PMC affects the melting temperature. For self-healing functionality, the PMC film was required to melt in response to microwave stimuli. It is, therefore, necessary to select PMC with lowest melting temperature. Secondly, PMC film should not contain agglomeration to avoid pyrolysis during heating. Therefore, FTIR results suggest that PMC with lowest proportion of OA, i.e. 22% OA concentration is best selection for the self-healing purpose.

5.3.2 Functionalisation effect on dispersion of MNPs

5.3.2.1 Silica-functionalised samples

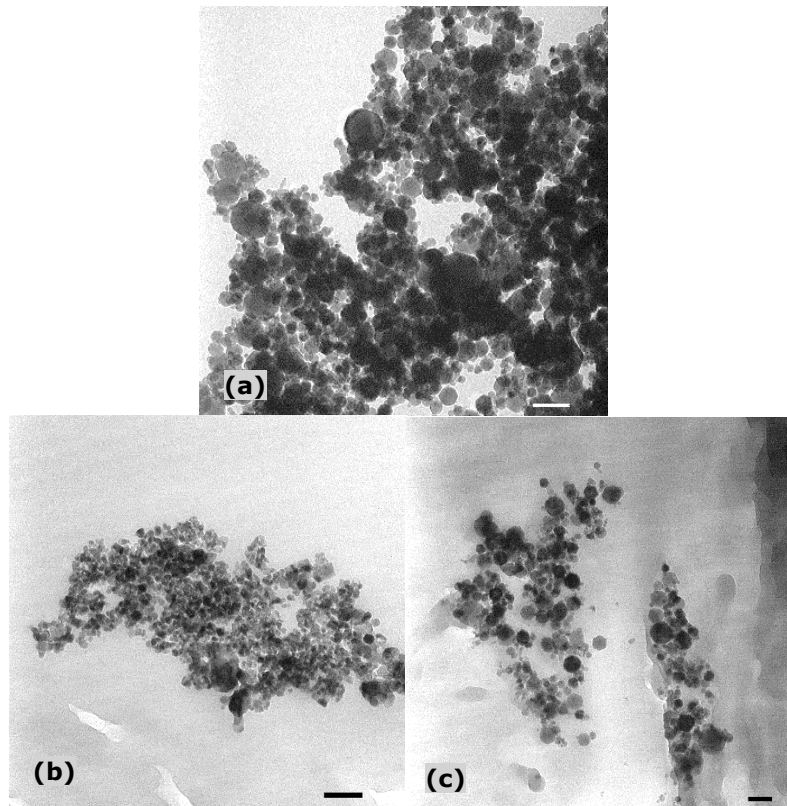


Figure 5.4. TEM micrographs showing dispersion of nanoparticles in microtome section of the prepared PMC samples with (a) uncoated MNPs and (b) & (c) MNPs with varying proportions of silica coatings (Stöber and TPPE respectively). (Scale bar shown is of 100 nm)

Uniform dispersion of MNPs is very important to achieve desired properties of the PMC. Further, a uniform dispersion state with small agglomerates in PMC, will ensure high polymer crystallinity with small crystallite size and uniform magnetic saturation. Hence, to achieve uniform dispersion of the MNPs, involving the silica functionalisation was the main aim. To quantify the dispersion state of the MNPs with the aim of interrelating with the other properties, TEM micrographs were taken. The TEM micrographs of microtome PMC samples show that the dispersion state of MNPs (or agglomerates) improves with the silica functionalisation. As observed in Fig. 5.4, the Uncoated MNPs sample, and to some extent the *Stöber-Fe₃O₄* PMC sample formed agglomerated MNPs state in the composites due to high dipole-dipole interparticle attraction. And uniform dispersion

state of MNPs was observed in *TPRE-Fe₃O₄ PMC* sample, which is due to the limited interparticle interactions prevailing due to the thick silica coating been formed. This uniform dispersion is leading to the higher degree of crystallinity phase of the composite, which was slightly observed in the FTIR results and is confirmed by the DSC and XRD results that follow this section.

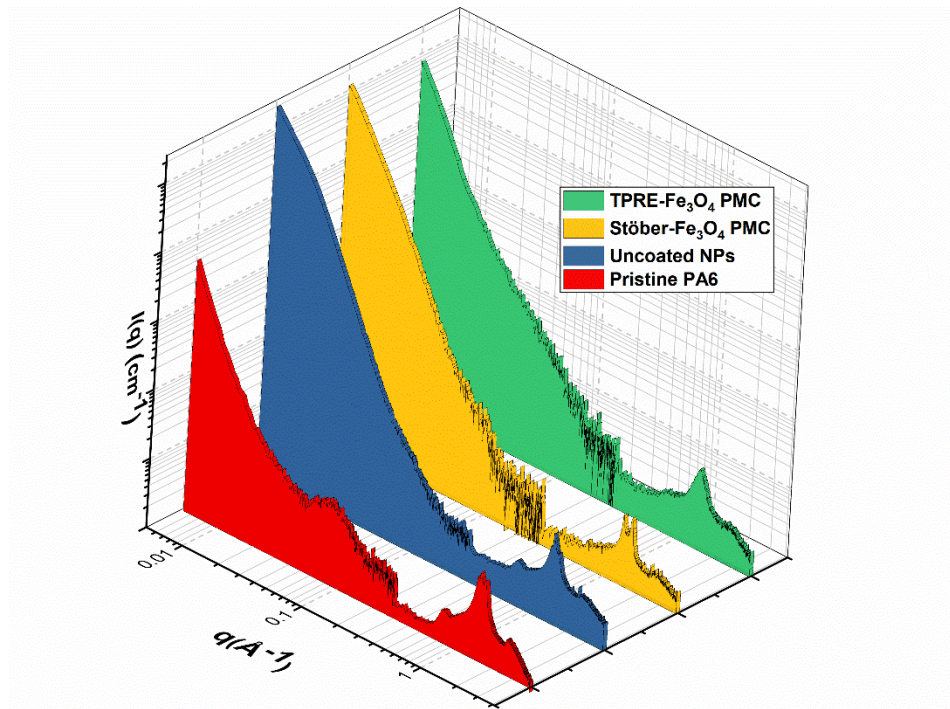


Figure 5.5. Background corrected SAXS ($0.005\text{-}0.3 \text{ \AA}^{-1}$) and WAXS ($0.3\text{-}4.17 \text{ \AA}^{-1}$) intensities $I(q)$ as a function of the scattering vector ' q ' for the pristine polymer (PA6), sample with uncoated MNPs and samples with varying proportions of silica coatings (Stöber and TPRE) on the MNPs.

TEM micrographs can only help in estimating the information on dispersion state of the MNPs for 2-3 micron regions effectively, however, SAXS data have an advantage in evaluating dispersion state on a bulk scale (*ca.* area of $2\text{-}10 \text{ mm}^2$). Hence, the dispersion state of the PMC was characterised using the SAXS/WAXS techniques. The MNP filler structure and polymer chain structures inside a PMC have been previously studied with scattering techniques such as XRD, SAXS/WAXS, etc (209). Statistical mechanical theories have related the dispersion state (dictating the space configuration of the nano-inclusions, such as the MNPs in PMCs) to stress within the composite (210), and this gives an better insight into how the orientations at the nanoscale, dictate the overall

mechanical properties at macro scale. Herein, it also helps in identifying the MNP sizes, including for complex agglomerates of the MNPs (211).

Figure 5.5 represents the scattering intensity $I(q)$, plotted as a function of the scattering vector q . All obtained spectra were corrected for background scattering before any further analysis with the Eqn. 2.6. And the Guinier plot represented in Fig. 5.6, of $\ln I(q)$ vs q^2 , is used to calculate the slope of the chosen region that dictates the value of R_g , giving out the MNP/agglomerate size qualitatively using Eqn. 2.7.

The SAXS profile of the Guinier type plot in Fig. 5.6, shows two vivid regions. One which is flat region, which is due to the base polymer response (as is clear from the Pristine PA6 data plot); second, a very steep sloped curve is observed that is related to the response from the MNPs in the prepared samples.

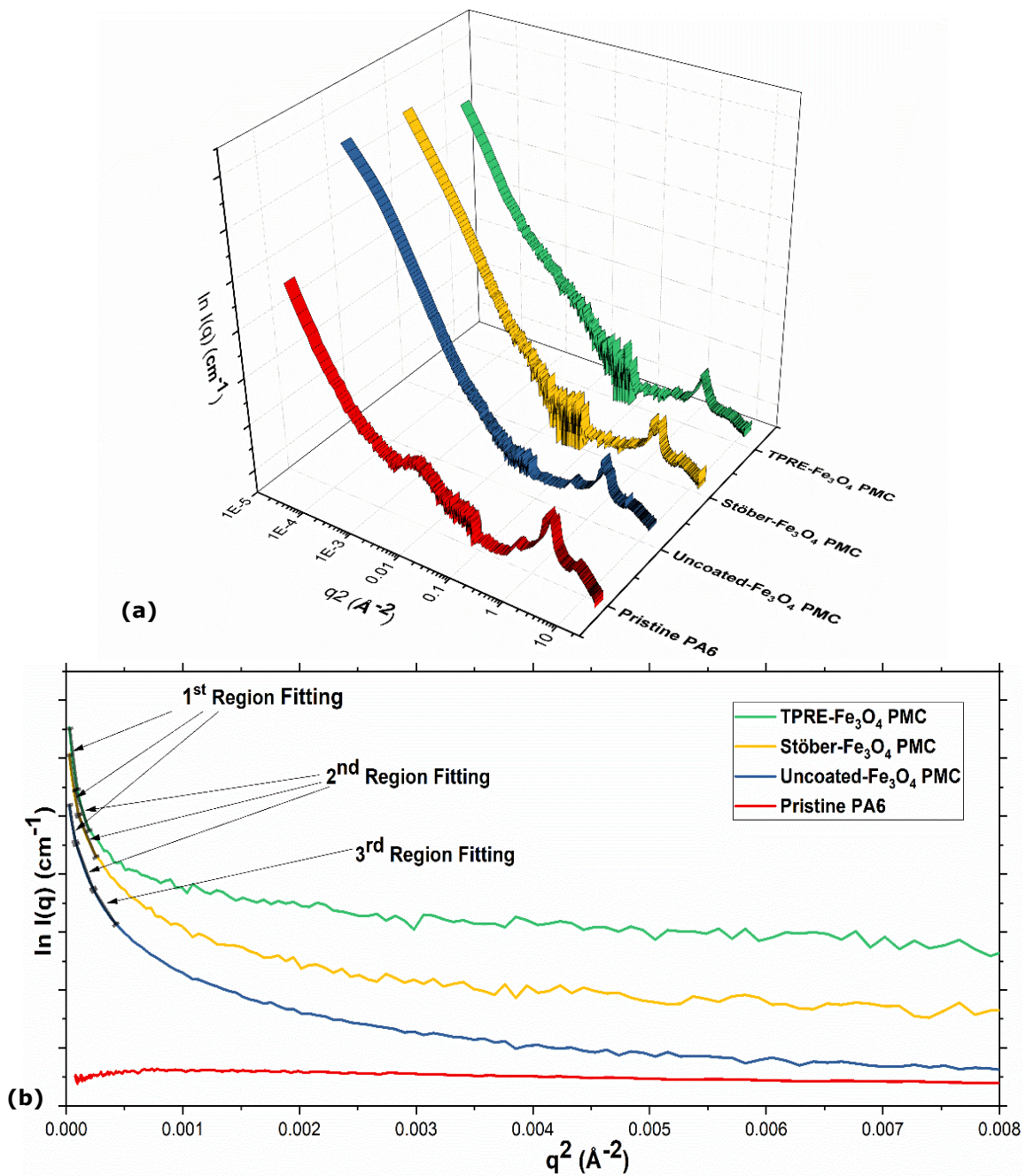


Figure 5.6. (a) Guinier plot for the pristine polymer (PA6), sample with uncoated MNPs and samples with varying proportions of silica coatings (Stöber and TPRE) on the MNPs and (b) with the region fitting highlighted.

The cumulatively slope-dropping region in Fig. 5.6 is a characteristic of the Porod scattering response from the MNPs (212). Here, the Guinier region precedes the Porod region, wherein the scattering of the former reflects the radius of gyration of the MNPs present in the observed PMC sample as per Guinier's law. By calculating the radius of

gyration, the average diameter of MNPs in a volume of PMC, were calculated and are summarised in Table 5.1.

The average diameter of the MNPs calculated from the SAXS data as listed in Table 5.1 are in broad agreement with the values obtained from the TEM micrographs, as discussed earlier in this Section 5.2.2.1. The measured values from TEM and SAXS/WAXS study confirms that the *TPRE-Fe₃O₄ PMC Sample* has the lowest average diameter of MNP/agglomerates. Furthermore, the WAXS curves suggests that some of the peaks associated with the crystalline lattices of PA6, become sharper for *Stöber-Fe₃O₄ PMC* and *TPRE-Fe₃O₄ PMC Samples*, which conforms that the degree of crystallinity changed due to functionalisation. Also, peak height decreases for *Uncoated-Fe₃O₄ PMC Sample* in comparison to the pristine PA6, highlighting the drop in crystallinity due to MNPs nano-inclusion.

Table 5.1: Size calculation of the MNPs for each sample types from Guinier plot.

		<i>Uncoated-Fe₃O₄</i> <i>PMC</i>	<i>Stöber- Fe₃O₄</i> <i>PMC</i>	<i>TPRE- Fe₃O₄</i> <i>PMC</i>
1 st Region Fitting	<i>I(q)</i> Range	0.009-0.012	0.009-0.014	0.009-0.013
	<i>R_g</i>	196	162	186
	<i>D(nm)</i>	50	40	46
2 nd Region Fitting	<i>I(q)</i> Range	0.012-0.018	0.014-0.021	0.013-0.021
	<i>R_g</i>	143	96	146
	<i>D(nm)</i>	37	24	38
3 rd Region Fitting	<i>I(q)</i> Range	0.018-0.022	-	-
	<i>R_g</i>	97	-	-
	<i>D(nm)</i>	25	-	-
Observed Range	<i>D(nm)</i>	38 ± 13	32 ± 8	42 ± 4

5.3.2.2 OA-functionalised samples

Dispersion of MNPs is important to achieve desired properties of the PMC. A good dispersion with small agglomeration diameter in PMC ensures high degree of crystallinity, small crystallite size and uniform magnetic saturation. To achieve better dispersion of the

MNPs, OA concentration in coating was varied. TEM images were obtained to quantify the dispersion state of the MNPs. The TEM images of microtome nanocomposite slices show that the dispersion of particles improves with coating. Although samples with OA concentration greater than 33 w/w % were seen promoting agglomeration due to excessive amount of OA. At lower concentration, OA coating promotes the dispersion of MNPs in the polymer matrix of PA6 as it imparts hydrophobic properties to MNPs (122). When hydrophobic properties of polymer and MNPs are similar, a homogenous dispersion can be achieved.

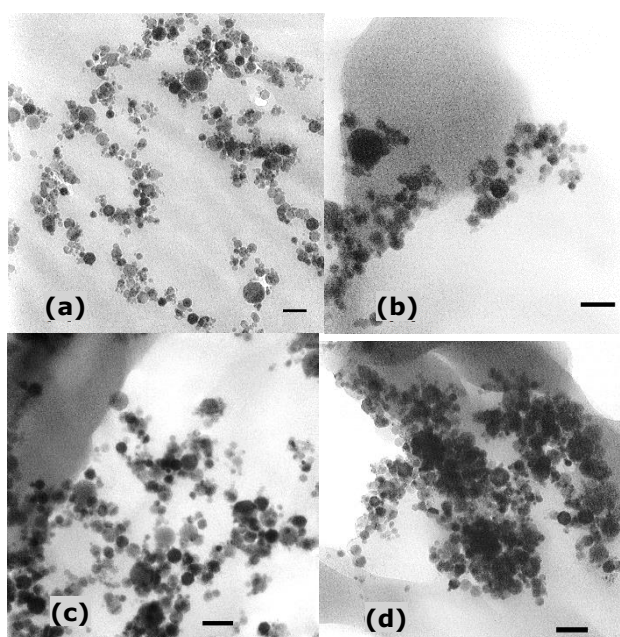


Figure 5.7. TEM image shows dispersion of nanoparticles with (a) 22 w/w%, (b) 33 w/w%, (c) 44 w/w% and (d) 55 w/w% OA in microtome section of the prepared PMC. (Scale bar shown is of 50 nm)

As observed in Fig. 5.7, the increased concentration of OA in the MNP coating formed the agglomeration due high OA adsorption. Homogenous dispersion is responsible for smallest crystallite size and degree of crystallinity in 22 w/w% OA- Fe_3O_4 PMC sample, which is also confirmed by the XRD results later.

TEM only provides the information on dispersion state of MNPs at point scale. However, SAXS can determine dispersion state on broader scale (large-area wise distribution) than

TEM. To determine the dispersion, the PMC samples were characterized using SAXS/WAXS technique.

The filler structure and their dispersivity amongst the conformations of polymer chains inside a PMC is widely studied with scattering techniques. Measurement of hard particle dispersivity in the soft polymer using a small angle scattering is based on the variation of the X-ray scattering length density across the sample. The scattering density depicted by the scattering intensity $I(q)$ is sensitive to density variation and hence, allows determination of statistics of hard particle dispersion. The small angle ensures absence of scattering due to sample surface roughness (210). This helps in identifying numerical values of the MNPs radius of gyration and complex agglomerates (211).

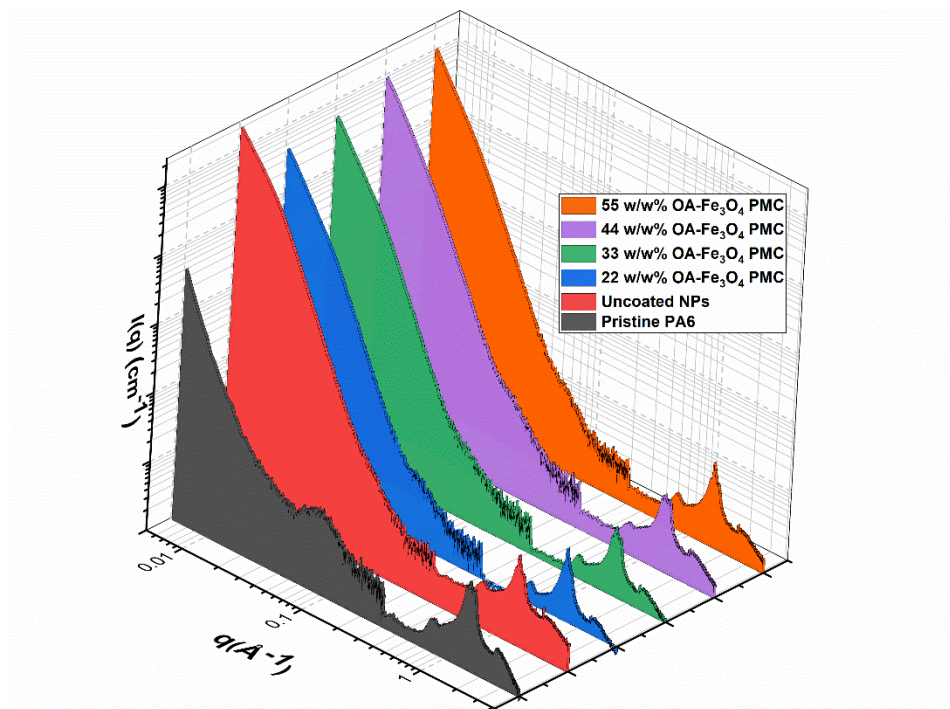


Figure 5. 8. Background corrected SAXS ($0.005\text{-}0.3 \text{ \AA}^{-1}$) and WAXS ($0.3\text{-}4.17 \text{ \AA}^{-1}$) intensities $I(q)$ as a function of the scattering vector 'q' for Pristine PA6, sample with uncoated MNPs and polymer samples with varying proportions of OA coatings on the MNPs.

Figure 5.8 represents the scattering intensity $I(q)$, plotted as a function of the scattering vector "q" for all the samples studied herein. The Guinier profile here also shows two regions, the one which is flat, that is due to the polymer response, as is very clear from the Pristine PA6 data plot alone; second is the very high slope curve pertaining to the

response of the nanoparticles in the samples. Absence of diffraction peaks at lower OA concentration confirms good dispersion and low interaction between MNPs.

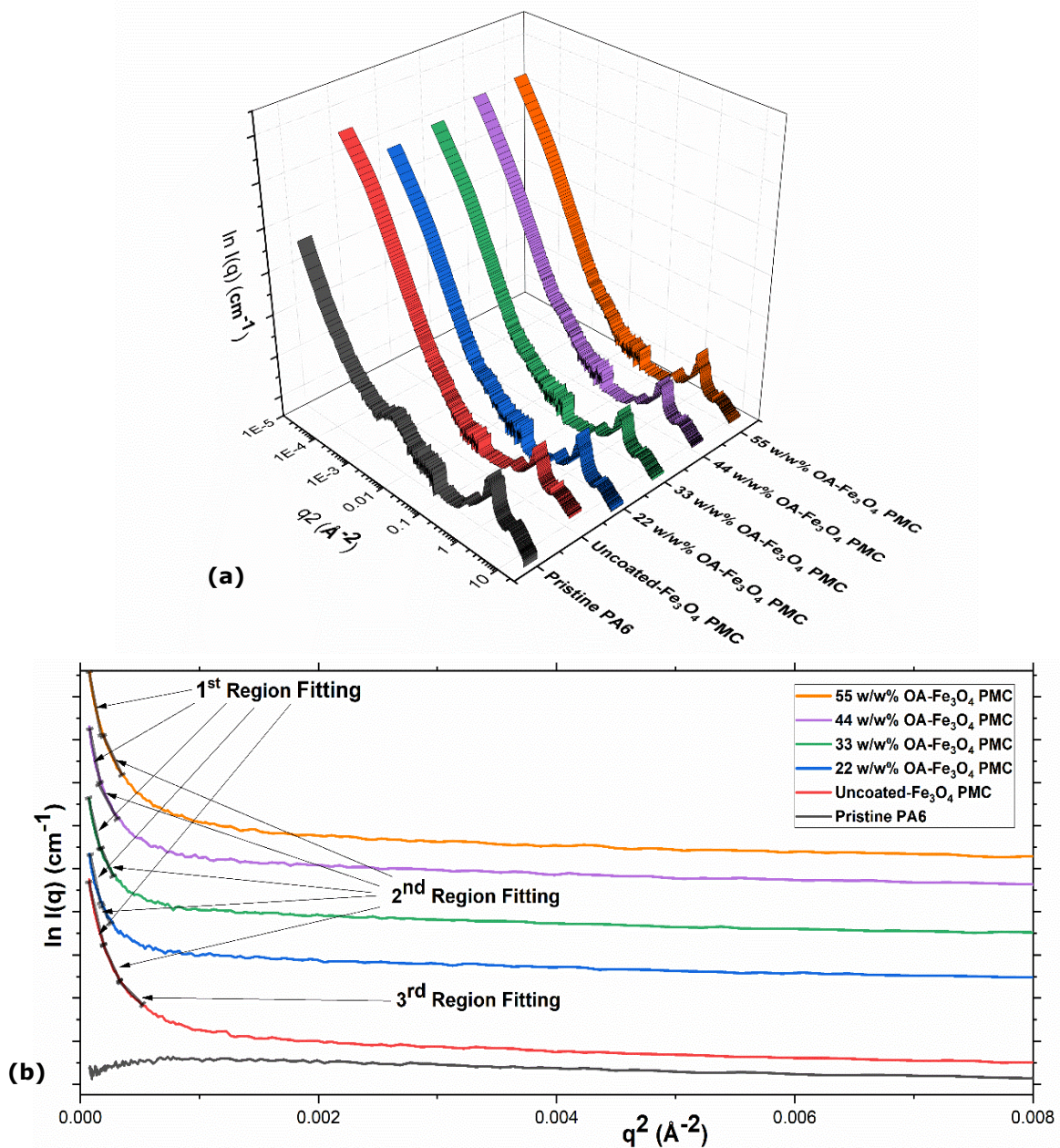


Figure 5.9. (a) Guinier plot for Pristine PA6, sample with uncoated MNPs and polymer samples with varying proportions of OA coatings on the MNPs and (b) with the region fitting highlighted.

In the Fig. 5.9 the cumulatively slope-dropping region is a characteristic of Porod scattering response from the MNPs (212). And the Guinier region precedes the Porod region, wherein the scattering of this region reflects the radius of gyration of the MNPs as per the Guinier's law. By calculating the radius of gyration, the average diameter of

MNPs in a volume of PMC were calculated using Eqn. 2.3 and 2.4, which are summarised in the Table 5.2 below.

Table 5.2: Size calculation of the MNPs for each sample types from Guinier plot.

		<i>Uncoated- Fe₃O₄ PMC</i>	<i>22 w/w% OA-Fe₃O₄ PMC</i>	<i>33 w/w% OA-Fe₃O₄ PMC</i>	<i>44 w/w% OA-Fe₃O₄ PMC</i>	<i>55 w/w% OA-Fe₃O₄ PMC</i>
1st Region Fitting	<i>I(q) Range</i>	0.009-0.012	0.009-0.014	0.009-0.013	0.009-0.012	0.009-0.012
	<i>R_g</i>	196	151	166	196	185
	<i>D(nm)</i>	50	39	42	58	47
2nd Region Fitting	<i>I(q) Range</i>	0.012-0.018	0.014-0.021	0.013-0.021	0.012-0.021	0.012-0.019
	<i>R_g</i>	143	94	116	145	121
	<i>D(nm)</i>	37	24	29	36	31
3rd Region Fitting	<i>I(q) Range</i>	0.018-0.022	-	-	-	-
	<i>R_g</i>	97	-	-	-	-
	<i>D(nm)</i>	25	-	-	-	-
Observed Range	<i>D(nm)</i>	38 ± 13	31 ± 8	36 ± 6	48 ± 11	39 ± 9

The average diameter of MNPs calculated with the SAXS data are listed in Table 5.2 and lie in proximity of that obtained with TEM above. This confirms that the 22 w/w% OA-Fe₃O₄ PMC sample has the lowest average diameter of MNPs and even has the least agglomerates. Further, the WAXS curves for nanocomposites shows that some of the peaks associated to the crystalline lattices of PA6 become sharper for PMC sample containing 22 w/w% OA-Fe₃O₄ and peak height decreases for samples with OA concentration more than 22 w/w% in comparison to the pristine PA6. The increase of intensity of peaks corresponding to PA6 reflection planes of (010) and (012) for these nanocomposites was observed. Based on these results, it can be concluded that the large crystals in PMC can be formed with a presence of thick lamellae produced by excessive OA concentration in coating (122), as seen with higher OA loading samples. Again, 22 w/w% OA-Fe₃O₄ PMC sample emerges as a favourable choice for self-healing application as aggregates of MNPs can induce local heating and subsequently, pyrolysis when they interact with electromagnetic wave such as microwave.

5.3.3 Degree of crystallinity and crystallite size

5.3.3.1 Silica-functionalised samples

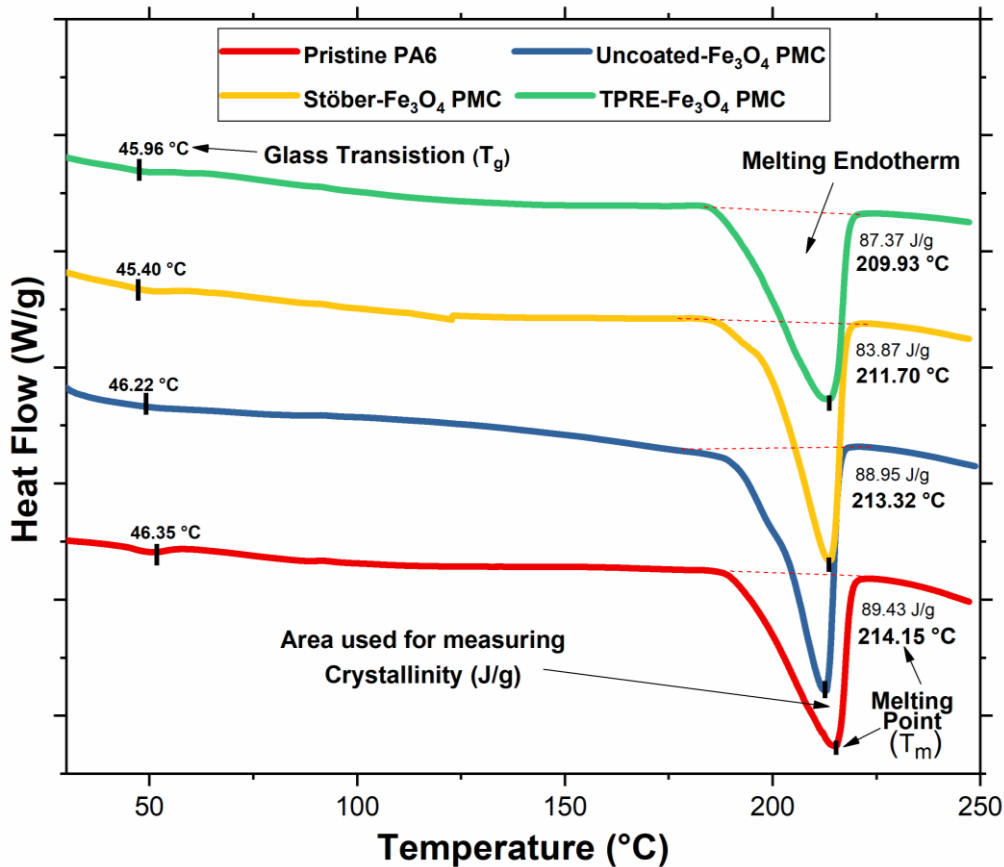


Figure 5.10. DSC curves of the Pristine PA6 sample, sample with uncoated MNPs and samples with varying proportions of silica coatings (Stöber and TPRE) on the MNPs.

The DSC results (Fig. 5.10) exhibit a noticeable melting endothermic peaks and highlights the glass transition temperature of all the PMC samples. The results of the thermal analysis represent the glass transition temperature (T_g) occurrence of the pristine polymer at ca. 46 °C, which is in alignment with the previously reported values (213). Though the melting temperature (T_m) observed was slightly lower than the published values of PA6, at ca. 220 °C (213). Additionally, from the summarised values in Table 5.3, the T_m of the PMC samples was observed to increase in the functionalised MNP samples. Also, the T_g showed linear increase in the functionalised samples; herein the increased wetting of the surface modified MNPs by polymer is also known to decrease crystallinity of the nanocomposite and hence, it increases T_g and T_m amongst the

functionalised samples, but decreases the T_m as compared to the Pristine PA6 sample due to the presence of MNPs itself.

Table 5.3: A list of degree of crystallinity, Glass transition (T_g) and Melting temperature (T_m) from DSC results for Pristine PA6 sample, sample with uncoated MNPs and samples with varying proportions of silica coatings (Stöber and TPPE) on the MNPs.

Sample	T_g (°C)	T_m (°C)	Enthalpy (J/g)	Degree of Crystallinity (%)
Pristine PA6	46 ± 1	214 ± 2	89 ± 2	47 ± 2
Uncoated-Fe ₃ O ₄ PMC	46 ± 4	213 ± 4	89 ± 5	47 ± 5
Stöber- Fe ₃ O ₄ PMC	45 ± 2	212 ± 2	84 ± 4	44 ± 4
TPPE- Fe ₃ O ₄ PMC	46 ± 1	210 ± 2	87 ± 3	46 ± 3

In the DSC results when comparing with the Uncoated-Fe₃O₄ sample, it was confirmed that the wetting of MNPs by the polymer melt was increased in the functionalised samples as a result of the silica functionalisation; by the eventual increase in T_g and T_m . With no coating on surface of MNPs, this promoted strong attraction between the MNPs themselves and in turn with surrounding polymer chains, which led to reductions in cooperative segmental mobility in the polymer and an increase in T_g (214-216).

Further study on the crystallinity of synthesised PMCs was done by XRD analysis. As seen in Fig. 5.11, the main characteristic XRD peaks for the PMCs gave a good match to those in the reference pattern JCPDS file number 82-1533; peaks were observed for (hkl) values of (220), (311), (400), (511) and (440) at 2 theta values of 30.3°, 35.4°, 43.1°, 57.3° and 62.7° respectively, as observed in the reference (122).

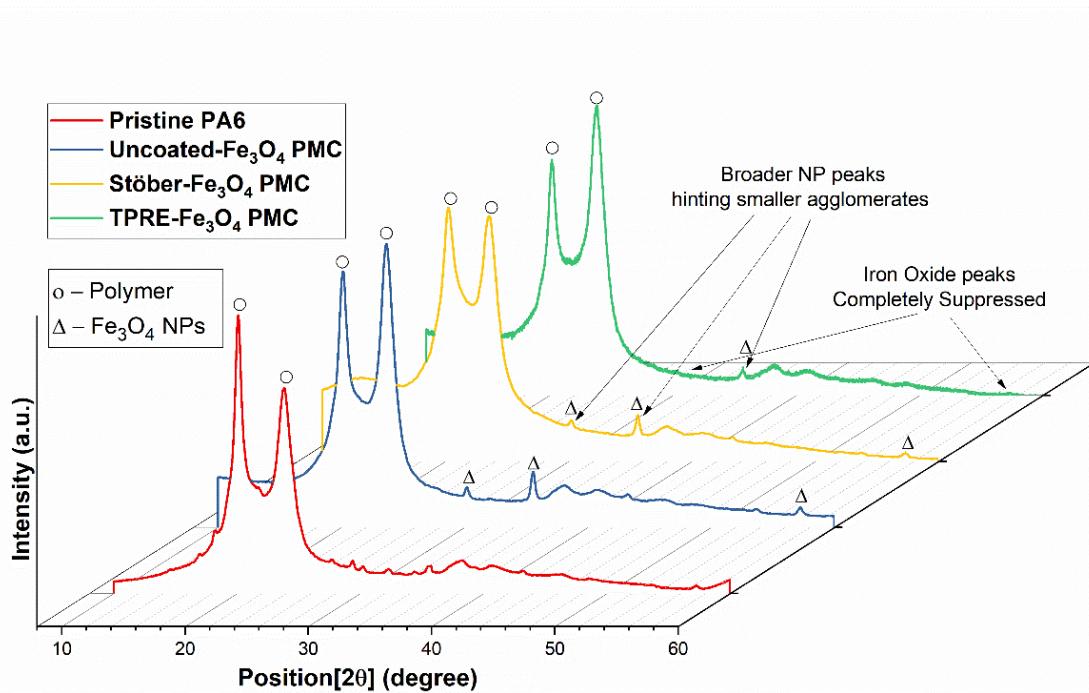


Figure 5.11. XRD patterns of the Pristine PA6 sample, sample with uncoated MNPs and samples with varying proportions of silica coatings (Stöber and TPRE) on the MNPs.

The crystallite sizes of MNPs were calculated from FWHM of the most intense peaks using the Debye–Scherrer formula as listed in Eqn. 2.8. The matrix crystallization behaviour significantly influences the mechanical and physical properties of the designed nanocomposites. The pristine PA6 shows a sharp crystallization peak as compared with that of the nanocomposite samples. The broader peaks resulting due to the MNP inclusions, as shown by the nanocomposite samples are hinting towards non-uniform crystal phases. The crystallite sizes of MNPs were calculated from FWHM of the most intense peaks using the Debye–Scherrer formula (183) as shown in Eqn. 2.8.

The two broad crystalline peaks associated with crystalline to amorphous ratio, decreased for *Stöber-Fe₃O₄ PMC* and *TPRE-Fe₃O₄ PMC Samples*, showing decrease in crystallinity as compared to the *Pristine PA6* and *Uncoated-Fe₃O₄ PMC samples*. Also, as observed in Fig. 5.11 the silica-functionalisation somewhat suppressed the MNP peaks in *TPRE-Fe₃O₄ PMC Sample*, as were observed in *Uncoated-Fe₃O₄ PMC* and *Stöber-Fe₃O₄ PMC Samples*, showing maximum broadening with minimum intensity. The XRD peak broadening hints that the MNP agglomerate sizes were reduced in the sequence of

Uncoated-Fe₃O₄ PMC, Stöber-Fe₃O₄ PMC and TPRE-Fe₃O₄ PMC Samples. This again confirms that uncoated MNPs tend to agglomerate, due to strong magnetic dipole–dipole interaction and therefore they may appear as larger agglomerates. In the functionalised MNPs samples, the non-magnetic silica layer formed on the surface of MNPs partially limits the strong MNP-MNP interactions and hence, the mean crystallite size or agglomerates reduced. The summarised observations for all these samples are listed in Table 5.4. The calculated values confirm that *TPRE-Fe₃O₄ PMC sample* has the lowest crystallite/agglomerate size.

Table 5.4: Crystallite sizes of MNPs calculated from FWHM of intense peaks observed in XRD patterns for sample with uncoated MNPs and samples with varying proportions of silica coatings (Stöber and TPRE) on the MNPs.

Sample Type	Absolute Crystallite Size	
	Size(A)	Size(nm)
Uncoated-Fe ₃ O ₄ PMC	418 ± 3	42 ± 3
Stöber- Fe ₃ O ₄ PMC	365 ± 5	37 ± 5
TPRE- Fe ₃ O ₄ PMC	331 ± 4	33 ± 4

5.3.3.2 OA-functionalised samples

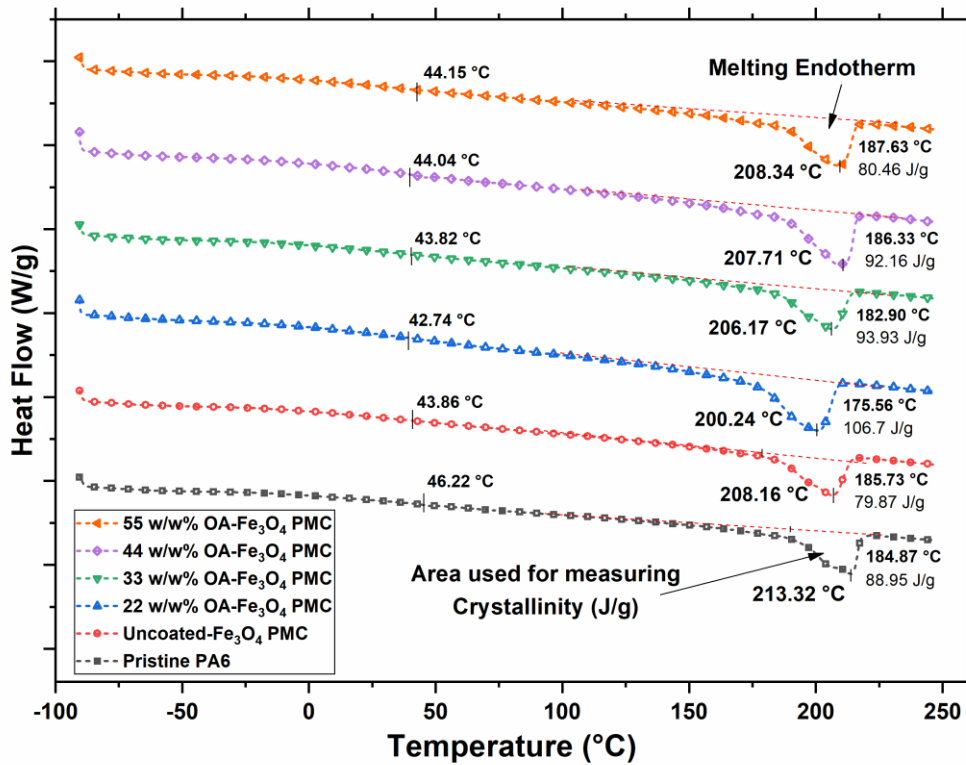


Figure 5.12. DSC curves of the Pristine PA6 sample, sample with uncoated MNPs and samples with varying percentages of OA loading on the MNPs.

The DSC results for all the samples, as seen in Fig. 5.12, exhibit the noticeable melting endothermic peaks and clearly depicting the glass transition temperature of all polymer samples. The results of the thermal analysis represent the glass transition temperature (T_g) occurrence of the pristine polymer at around 46°C that matches roughly the previously reported values (213). The melting temperature (T_m) observed in DSC results were found to be slightly lower than the published values, at around 220°C (213). The MNPs act as impurities which affect the crystal growth during the polymerisation process, this is observed to reduce the T_m and even responsible for the corresponding reduction in degree of crystallinity as compared to the pristine PA6 sample.

The enthalpy of all the samples were calculated using the Universal Analysis software that comes along with the DSC instrument control package. By quantifying the heat associated with the melting endotherm. This heat was then reported in terms of percent

crystallinity by normalizing the observed heat of fusion with that of the 100% crystalline PA6 polymer. The area used for the enthalpy (crystallinity) calculation as identified using the "Integrate Peak" functionality of the TA Universal Analysis 2000 software (170), which is recreated in the plots in Fig. 5.12. The same analysis also helped identify the "Melt Peak Temperature" of the endotherm peak, which was the melting point T_m of the samples and listed in the Table below. Adding to the discussion, the Glass transition temperature T_g was also identified using the "Glass/Step transition" functionality available in the same software.

The degree of crystallinity for all the samples was calculated from the Eqn. 2.1, using the standard reference value of PA6.

Table 5.5: A list of degree of crystallinity, Glass transition (T_g) and Melting temperature (T_m) from DSC results for Pristine PA6 sample, sample with uncoated MNPs and samples with varying percentages of OA loading on the MNPs.

Sample	T_g (°C)	T_m (°C)	Enthalpy (J/g)	Degree of Crystallinity (%)
Pristine PA6	46 ± 1	214 ± 2	89 ± 2	47 ± 2
Uncoated-Fe ₃ O ₄ PMC	46 ± 4	213 ± 4	88 ± 5	46 ± 5
22 w/w% OA-Fe ₃ O ₄ PMC	42 ± 2	200 ± 3	107 ± 4	56 ± 4
33 w/w% OA-Fe ₃ O ₄ PMC	43 ± 2	206 ± 3	94 ± 6	49 ± 6
44 w/w% OA-Fe ₃ O ₄ PMC	44 ± 1	207 ± 2	92 ± 3	48 ± 3
55 w/w% OA-Fe ₃ O ₄ PMC	44 ± 1	208 ± 2	80 ± 2	42 ± 2

Additionally, as seen in Table 5.5, the melting temperature of the PMCs was found to be increasing with the increase in OA concentration of the coating. However, the T_g also showed linear relation with OA concentration, which is result of decrease in degree of crystallinity. Decrease in degree of crystallinity in high OA concentrations PMC was responsible for increases in the melting temperature.

The DSC results also show that the wetting of the MNPs by the polymer melt was increased because of the OA coating on MNPs, by comparing them with the *Uncoated-Fe₃O₄ PMC* sample. The fatty acid chain in OA coating rendered hydrophobicity to the surface of MNPs and promoted wetting by the hydrophobic polymer at interface. With

increased OA concentration, the denser fatty acid chain on surface of MNPs promoted strong attractive interaction with surrounding polymer chain, leading to reductions in cooperative segmental mobility in the polymer and an increase in Tg (214-216).

Though the decrease in the degree of crystallinity observed with the increased OA concentration can be attributed to the MNPs inclusion which restricts the movement and limit the growth of PA6 crystals, but the excessive OA assisted formation of agglomeration in the 55 w/w% OA-Fe₃O₄ PMC sample showed lowest degree of crystallinity, even lower than the sample containing uncoated MNPs. Such decrease in degree of crystallinity due to agglomerates was also observed in previously reported works when increase in the wt% of nano-inclusions was responsible for formation of agglomerates (217).

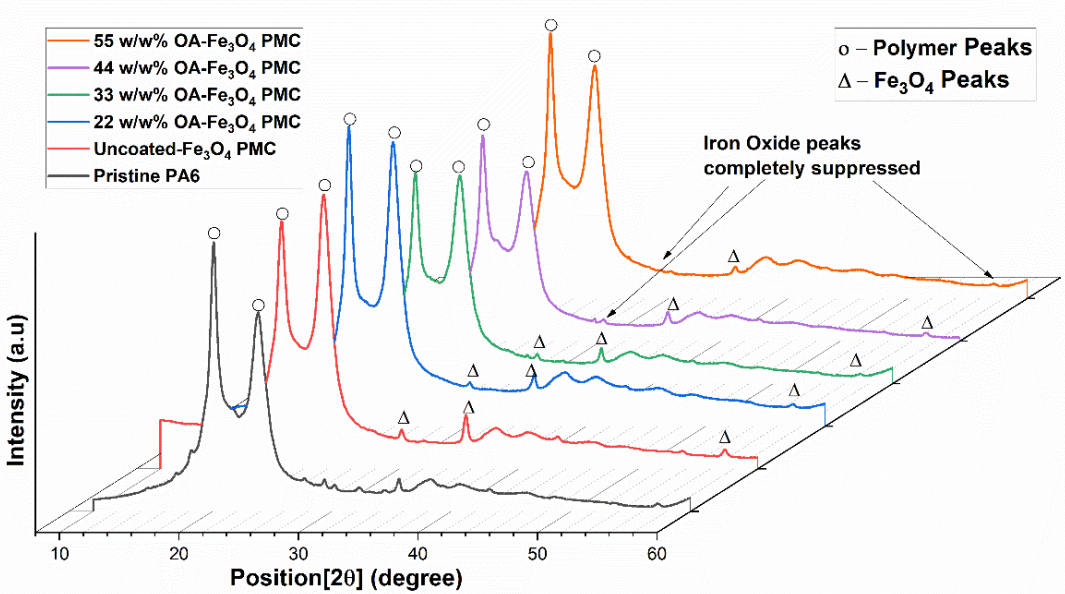


Figure 5.13. XRD patterns of the Pristine PA6 sample, sample with uncoated MNPs and samples with varying percentages of OA loading on the MNPs.

Furthermore, the results on degree of crystallinity of PMC were confirmed by the XRD results. As seen in Fig. 5.13, the main characteristic peaks were obtained by the XRD matches with the (hkl) values of (220), (311), (400), (511) and (440) when compared with the reference (122). These were then matched with the JCPDS file number 82-1533, which corresponded to Fe₃O₄ phase.

Table 5.6: Crystallite sizes of MNPs calculated from FWHM of intense peaks observed in XRD for sample with uncoated MNPs and samples with varying percentages of OA loading on the MNPs.

Sample Type	Absolute Crystallite Size	
	Size(A)	Size(nm)
Uncoated-Fe ₃ O ₄ PMC	418 ± 3	42 ± 3
22 w/w% OA-Fe ₃ O ₄ PMC	300 ± 3	30 ± 3
33 w/w% OA-Fe ₃ O ₄ PMC	365 ± 4	37 ± 4
44 w/w% OA-Fe ₃ O ₄ PMC	476 ± 11	48 ± 11
55 w/w% OA-Fe ₃ O ₄ PMC	424 ± 13	42 ± 13

Ideally, PA6 contains two dominant monoclinic crystalline phases that are usually referred to as the α -phase and γ -phase. In the α -phase, which is known to be the most stable phase in terms of thermodynamics, the hydrogen bonds appear in between adjacent antiparallel chains, with the entirety of the phase attaining a trans-chain conformity (218). This, however, is not the case in the γ -phase, as chains are seen to appear twisted to enable the formation of hydrogen bonds between parallel chains (218). Two broad peaks were seen to appear around 4.2 Å^o (21° 2 θ) and 3.7 Å^o (24° 2 θ) corresponds to α -crystalline phase form in PA6. The α crystalline phase dominated the crystalline structure of prepared PA6. The line at 4.2 Å^o referred to α_1 and originated from (200) plane whereas 3.7 Å^o originated from (002) plane (122). The peaks observed at 11°, 22° and 23° can be identified as the γ -phase of the of PA6 with the corresponding indexes of (020), (001) and (200)/(201) (81).

The number of unit cells (N) along their respective directions, define the broadening of the diffraction peaks. Though independent of the N , the peak area remains constant. Therefore, the peak broadening in XRD results was accompanied by decrease in the maximum peak height. However, as seen in Fig. 5.13 the peaks were broadened, and intensity was decreased when OA content in MNP coating was set to 22% (22 w/w% OA-Fe₃O₄ PMC sample). After increasing OA loading on the MNPs, the crystallite size has started increasing up to 55 w/w% OA-Fe₃O₄ PMC sample.

There were many factors contributing to the observed peak profile. In essence, the peak profile shown in Fig. 5.13 was a deconvolution of the peak from other contributions such as instrumental peak profile, crystallite size, microstrain, solid solution inhomogeneity, and temperature factors.

The two broad crystalline peaks associated with crystalline to amorphous ratio, decreased for 22 w/w% OA-Fe₃O₄ PMC sample showing increase in crystallinity as compared to pristine and uncoated sample and further with increase in OA loading there is gradual amorphous sites development. Also, as observed in Fig. 5.13 the increased OA loading suppressed the intense Fe₃O₄ peaks in 55 w/w% OA-Fe₃O₄ PMC sample, showing maximum broadening and minimum intensity.

Moreover, the reduction in crystal size justifies the enhanced mechanical response as observed in similar study (219). These can help conclude, bare MNPs tend to agglomerate upon drying due to strong magnetic dipole–dipole interaction and therefore, they appear as agglomerates. Once coating was applied, the non-magnetic hydrophobic oleic acid layer formed on the surface of each particles that prevented or partially hindered magnetic interaction and hence, the mean crystallite size or agglomerates reduced as highlighted in Table 5.6; especially the 22 w/w% OA-Fe₃O₄ PMC sample showed the least crystallite/agglomerate size.

5.3.4 Determination of Interaction Radius using Simulation

The TEM micrographs were used as an input for building the simulated 3D model using MATLAB® platform. The micrographs were processed in Photoshop® software; wherein they were cropped, rotated, and enlarged, for removing their edges and any distorted background. Further, they were digitally enhanced using filters for several purposes, such as removing the background noise and their artefacts or improving upon the definition and sharpness of the image. All grayscale images were corrected for the brightness and contrast to achieve correct black and white tonalities, which helped distinguishing the polymer matrix represented by the grayscale region and the pure

black entities representing the nanoparticles. Then the final toned images were saved as high quality 8-bit TIFF format and loaded in ImageJ image processing software for estimating the MNP/agglomerate sizes of all the sample variations. This size data was then added as input to the designed MATLAB[®] code, to be used as a basis for generating the random MNPs/agglomerates in the simulated 3D model of the nanocomposite. The code was able to generate the model with the required concentration of 1 wt% of MNPs and sizes within the input diameter range. Image tone colours allocated in the simulated model was, black colour spheres represented Fe₃O₄ MNPs/agglomerates, and faint region around them represented their interaction radius/region (IR).

The code followed the logic as described by the following flowchart and the main code blocks are included in Appendix A.

The flowchart highlights the algorithm followed by the developed MATLAB Code for generating the simulated 3D model of the PMC samples with 1% weight of MNPs as compared to the PMC weight for the volume of 1-micron cube.

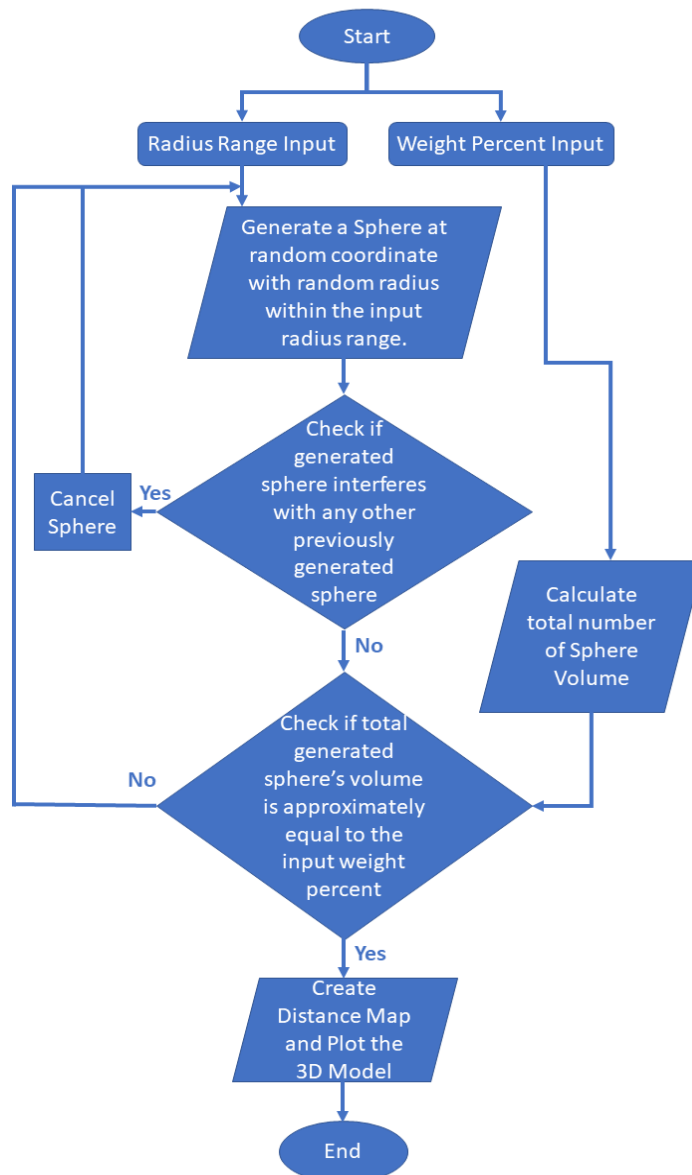


Figure 5.14. Flowchart for the developed MATLAB code for the simulated PMC model generation.

The dispersion state and IR are two main parameters that dictate the transfer of charged electrons (220) or in other words the electromagnetic properties of the synthesised sample; hence, the dispersion state of the MNPs in the nanocomposite was simulated. The purpose of the simulated modelling is to visualise and interpret the dispersion state of the synthesised samples with the uncoated and various functionalised MNPs, which is quite challenging to attain with the physical methods of sample characterisation. Using

the distance between the nearest neighbours (spheres) in a simulated volume of the PMC, the interaction radius (IR) of each MNP/agglomerate region were calculated.

The TEM micrographs of all the samples were analysed using ImageJ image processing software and the ferret diameter measurement tool, which approximates each selected region of MNP/agglomerate as an ellipsoidal entity, was used to calculate the agglomerate diameter based on relation $\sqrt{(minFerret \times maxFerret)}$. Final estimated diameter data from this calculation, SAXS (Guinier plot) calculation and from XRD peak calculations for each synthesised sample are summarised in Table 5.7. The values in Table 5.7 were then used as an input diameter range for the developed MATLAB® code to generate the spherical nanoparticles in the simulated 3D model. The diameter ranges from SAXS and XRD analysis are almost matching, as expected. Though the TEM values are quite varying, especially the upper range, since it is considered over a broader area in perspective.

Table 5.7: Estimated ferret diameters of MNP or their agglomerate regions identified from TEM micrographs, SAXS (Guinier plot) analysis and XRD peak study.

Sample	TEM estimation of MNP/ agglomerate size range (nm)		SAXS calculation for MNP/ agglomerate size range (nm)	XRD calculation For MNP/ agglomerate size range (nm)
	Smallest	Largest		
Uncoated-Fe ₃ O ₄ PMC	25 ± 5	195 ± 10	38 ± 13	42 ± 3
Stöber-Fe ₃ O ₄ PMC	30 ± 5	80 ± 15	32 ± 7	37 ± 5
TPRE-Fe ₃ O ₄ PMC	30 ± 5	60 ± 10	36 ± 6	33 ± 4
22 w/w% OA-Fe ₃ O ₄ PMC	25 ± 5	70 ± 10	31 ± 8	30 ± 3
33 w/w% OA-Fe ₃ O ₄ PMC	25 ± 5	90 ± 10	36 ± 6	37 ± 4
44 w/w% OA-Fe ₃ O ₄ PMC	30 ± 5	110 ± 20	48 ± 11	48 ± 11
55 w/w% OA-Fe ₃ O ₄ PMC	25 ± 5	100 ± 10	39 ± 9	42 ± 13

To keep the complexity of the simulated model to a minimum, all the entities are generated as spherical MNP/agglomerate regions. The simulated models for all the PMC samples are generated with 1 wt% of MNPs and is shown in Appendix C. Wherein

smallest spheres represent the individual MNPs or agglomerates and the large spheres particularly correspond to agglomerates itself.

Since, having the largest sized agglomerates (as summarised in Table 5.7 above), the *Uncoated-Fe₃O₄ PMC* sample also showed the highest IR value. This is due to one of the reasons of bigger agglomerates present, as discussed previously. Hence, the presence of little higher sized agglomerates present in this sample, is in fact occasionally aiding the magnetic performance of this sample in certain measurements and viz. confirmed by the SQUID measurements that are discussed in the following Section 5.2.5.

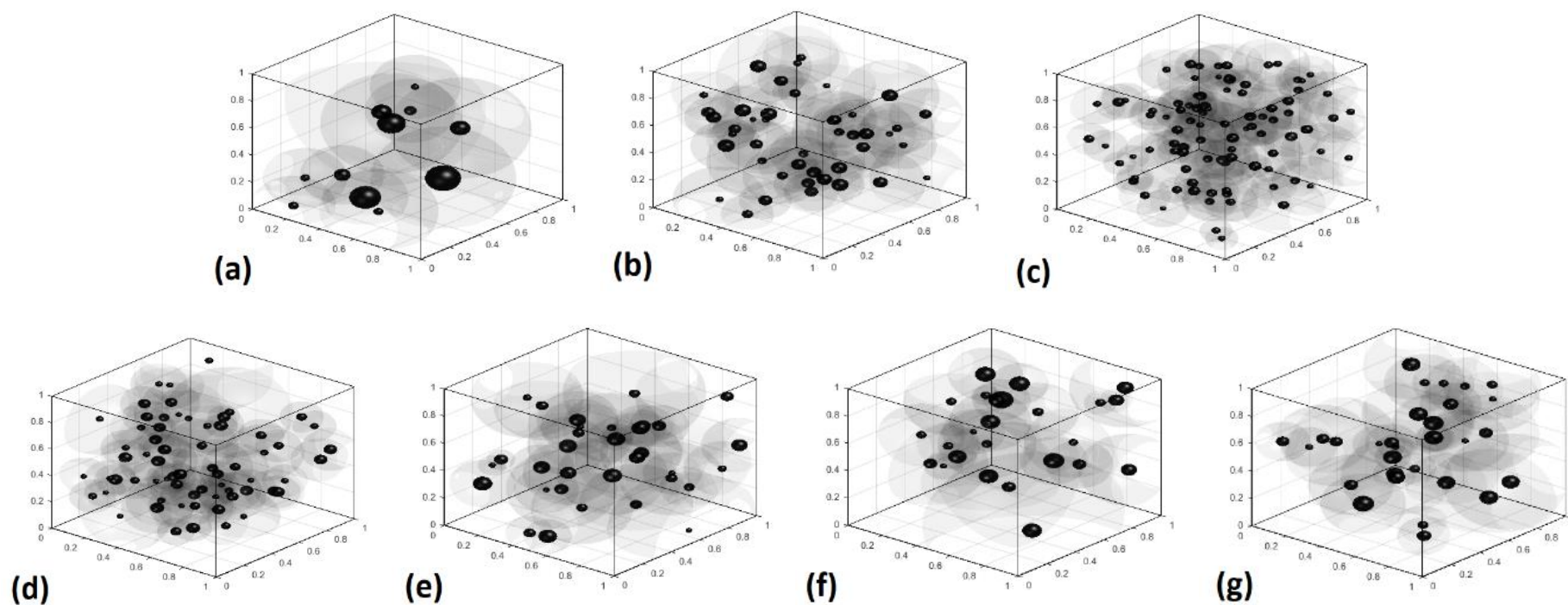


Figure 5.15. Simulated model representation of the PMC samples with 1 wt% MNPs and included with the interaction radius (IR) of the individual nanoparticle/agglomerate regions (1 cubic micron size) for (a) Uncoated- Fe_3O_4 PMC; samples with varying proportions of silica coatings i.e. (b) Stöber- Fe_3O_4 PMC & (c) TPPE- Fe_3O_4 PMC; and samples with varying percentages of OA loading on the MNPs viz. (d) 22 w/w% OA- Fe_3O_4 PMC, (e) 33 w/w% OA- Fe_3O_4 PMC, (f) 44 w/w% OA- Fe_3O_4 PMC, and (g) 55 w/w% OA- Fe_3O_4 PMC. (Herein, solid Black spheres represent Fe_3O_4 MNPs or agglomerates and the faint black region/sphere around it represents their interaction region/range.)

The simulated models (Figure in Appendix C and Fig. 5.15 above both) give a clear perception on the dispersion of the MNPs or agglomerates in the synthesised samples and having matching details with the previous characterisation results of showing improved dispersions in the TPRE-Fe₃O₄ PMC and 22 w/w% OA-Fe₃O₄ PMC samples. The IR values for each region containing the individual sphere of variable sizes (Figure in Appendix C) helped determine the influencing region or the interaction region of each MNP or agglomerates in the simulated model. The values of the IR generated by the designed MATLAB® code is summarised in Table included in Appendix C, and this data was used for graphically representing the interaction region as shown in Fig. 5.15 (interaction region is shown as faint spheres around each solid sphere of MNP/agglomerate). According to the definition, the variable IR values are dependent on the size of the MNP/agglomerate and its nearest neighbours. The IR values are found to be varying between ca. 55 nm to 475 nm considering all the PMC samples simulated. The associated error with the generated IR values is also calculated as the standard deviation error and is summarised in the same table with the IR values (Appendix C). Finally, this data is correlated with the measured magnetic response of all PMC samples in the following Section 5.3.5.

5.3.5 SQUID Characterisation

5.3.5.1 Silica-functionalised samples

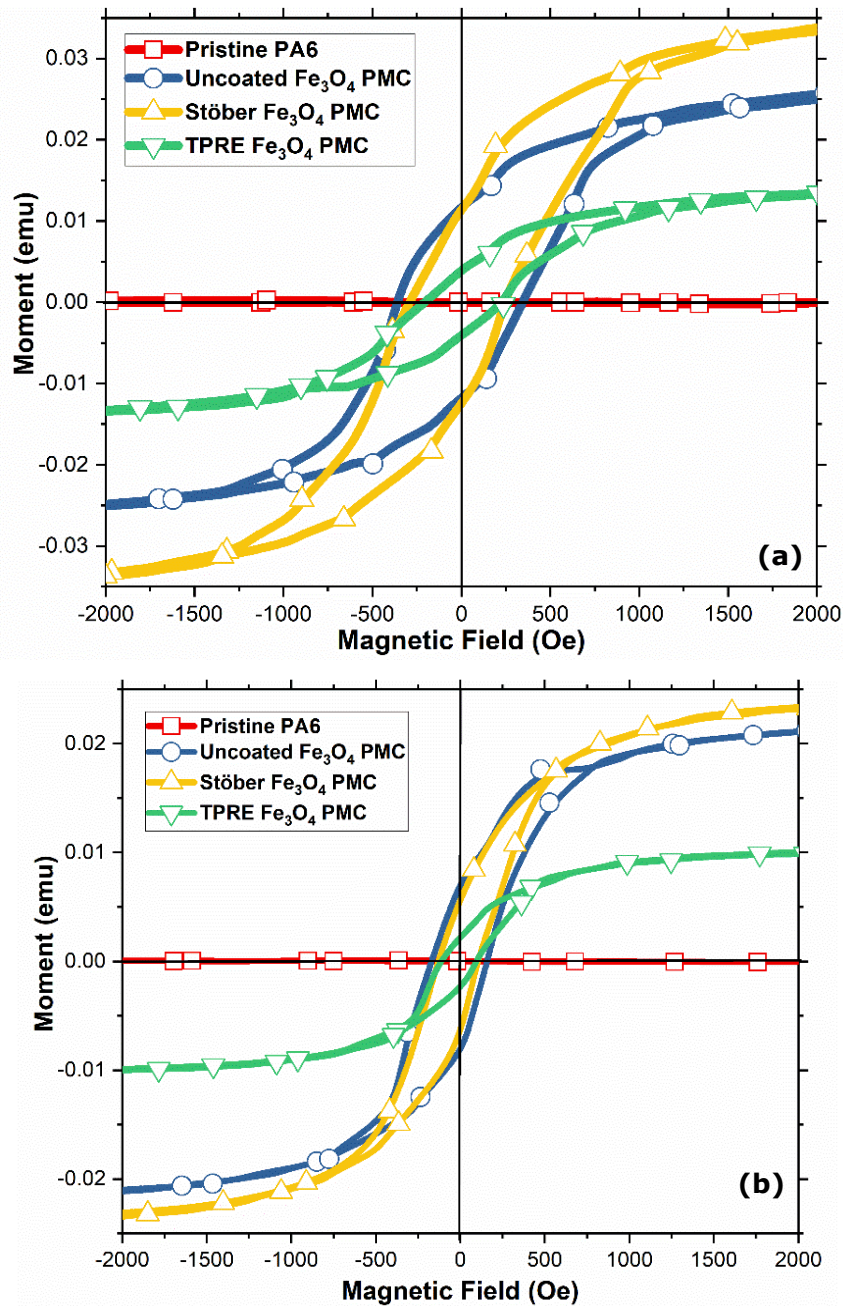


Figure 5.16. Magnetisation hysteresis loops for the Pristine PA6 sample, sample with uncoated MNPs and samples with varying percentages of silica coatings (Stöber and TPRE) on the MNPs at (a) 100 K and (b) 400 K

The magnetic (SQUID) measurements at 100K (Fig. 5.16 (a)) showed a magnetic moment ratio of 0% for *Pristine PA6 Sample* and 46%, 38%, and 31% for *Uncoated-Fe₃O₄ PMC*, *Stöber-Fe₃O₄ PMC* and *TPRE-Fe₃O₄ PMC Samples*, respectively. Further,

measurements taken after increasing temperature to 400 K (Fig. 5.16 (b)), showed the expected reduction in the values for M_r/M_s ratio. And here the values of magnetic moment ratio are 30%, 28%, and 23% for *Uncoated-Fe₃O₄ PMC*, *Stöber-Fe₃O₄ PMC* and *TPRE-Fe₃O₄ PMC Samples*, respectively. The observance of the wide hysteresis loop at lower temperature (100 K) as compared to that at higher temperature (400 K) hints towards the superparamagnetic behaviour induced in the designed PMC (210). The coercivity of all PMC samples had a value between 220-360 Oe and 110-170 Oe at temperatures of 100 K and 400 K, respectively. The noted results are summarised in Table 5.8 & 5.9 below.

Table 5.8: Summarised magnetic results at 100 K for Pristine PA6 sample, sample with uncoated MNPs and samples with varying percentages of silica coatings (Stöber and TPRE) on the MNPs.

Sample	Coercivity (H_c) (Oe)	Magnetic Remanence (M_r) (emu/g)	Magnetic Saturation (M_s) (emu/g)	Magnetic Moment Ratio (M_r/M_s) (%)
Pristine PA6	0	0	0	0
Uncoated-Fe ₃ O ₄ PMC	360	117 × 10 ⁻⁴	253 × 10 ⁻⁴	46 ± 7
Stöber- Fe ₃ O ₄ PMC	268	126 × 10 ⁻⁴	336 × 10 ⁻⁴	37 ± 3
TPRE- Fe ₃ O ₄ PMC	220	42 × 10 ⁻⁴	135 × 10 ⁻⁴	31 ± 5

Table 5.9: Summarised magnetic results at 400 K for Pristine PA6 sample, sample with uncoated MNPs and samples with varying percentages of silica coatings (Stöber and TPRE) on the MNPs.

Sample	Coercivity (H_c) (Oe)	Magnetic Remanence (M_r) (emu/g)	Magnetic Saturation (M_s) (emu/g)	Magnetic Moment Ratio (M_r/M_s) (%)
Pristine PA6	0	0	0	0
Uncoated-Fe ₃ O ₄ PMC	169	82 × 10 ⁻⁴	211 × 10 ⁻⁴	29 ± 6
Stöber- Fe ₃ O ₄ PMC	114	66 × 10 ⁻⁴	233 × 10 ⁻⁴	28 ± 3
TPRE- Fe ₃ O ₄ PMC	109	23 × 10 ⁻⁴	99 × 10 ⁻⁴	23 ± 4

Though, *TPRE-Fe₃O₄ PMC Sample* was proving better than other samples in the characterisations until now, but herein the major setback in terms of its lowest magnetic moment ratio has been observed. This is obviously due to the thick silica layer formed on

the MNPs surfaces, which suppresses their magnetisation by manifold as compared to the *Stöber-Fe₃O₄* MNPs.

5.3.5.2 OA-functionalised samples

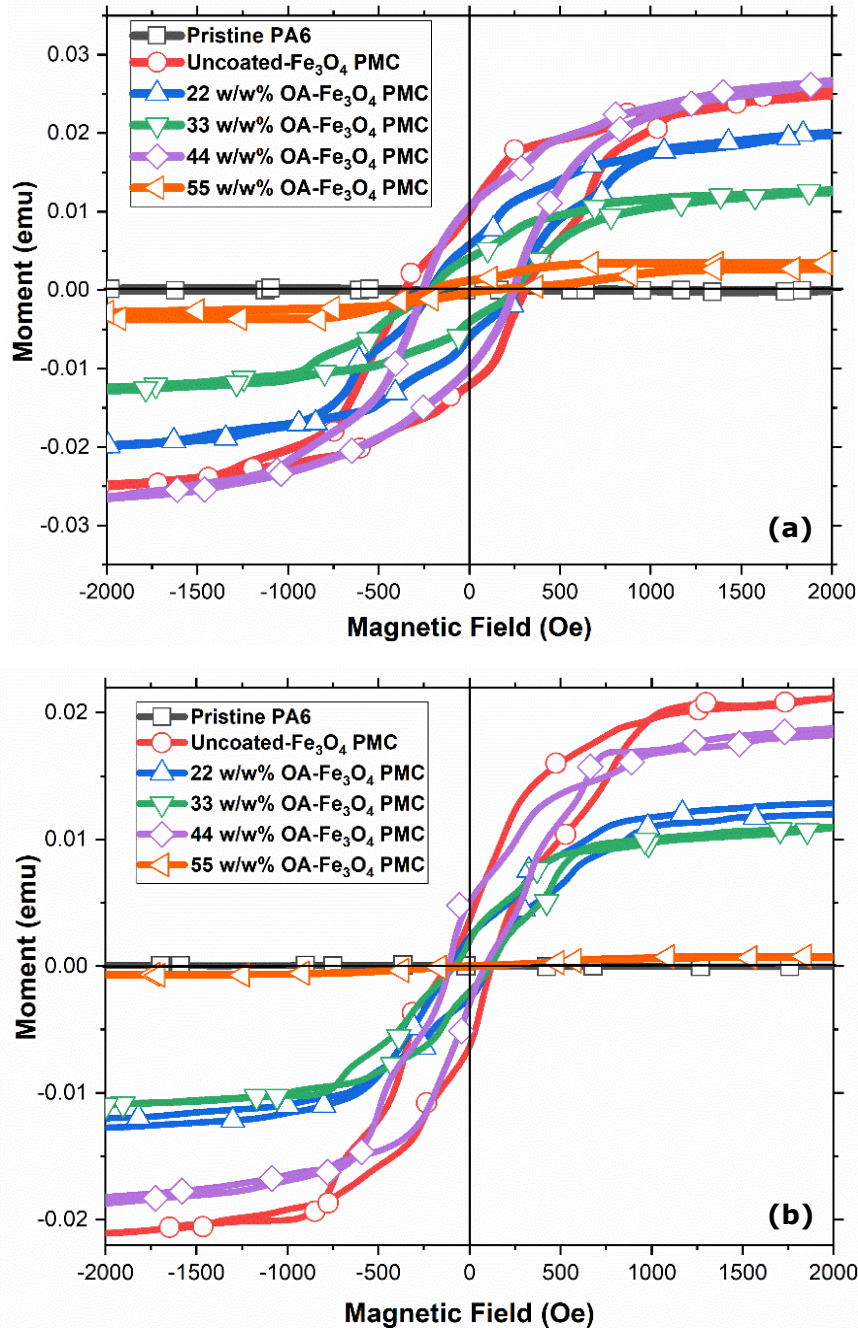


Figure 5.17. Magnetisation hysteresis loops for the Pristine PA6 sample, sample with uncoated MNPs and samples with varying percentages of OA loading on the MNPs at (a) 100 K and (b) 400 K.

The magnetic properties of the synthesised samples were assessed by magnetization curves at 100 K and 400 K temperatures. The hysteresis loops of all PMC samples were found to be similar as paramagnetic material. However, the variation in the magnetic properties due to dispersion state of MNPs resulting from the variation in OA loading is clearly distinguishable in Fig. 5.17 (a) and (b). On application of homogeneous magnetic field of 50000 Oe, (full scale plots included in Appendix D) the PMC shows a magnetic moment ratio (M_r/M_s) of remanence magnetisation (M_r) to saturation (M_s) of 0% and 46% for *Pristine PA6 and Uncoated-Fe₃O₄ PMC sample*, respectively. The ratio values were found to be 32%, 33%, 40% and 57% for 22-55 w/w % OA-Fe₃O₄ PMC Samples respectively at 100 K. After increasing temperature to 400 K, the values for M_r/M_s ratio were seen to be reduced (except for pristine sample) to 30% for uncoated MNPs sample, and 24%, 24%, 28% and 31% for 22-55 w/w % OA-Fe₃O₄ PMC Samples, respectively. Though the highest value observed for 44 w/w % OA-Fe₃O₄ PMC Sample (even higher than *Uncoated-Fe₃O₄ PMC sample*) is clearly distinctive indication of the uneven dispersion and agglomeration observed at higher OA loading, as observed in TEM and SAXS results. The M_r/M_s ratio for the 55 w/w % OA-Fe₃O₄ PMC Sample coating was found to be lowest amongst all PMC Samples which could be attributed to thicker coating owing to higher OA loading, as seen in similar studies (127,138). Despite of agglomeration was found in 55 w/w % OA-Fe₃O₄ PMC Sample, the organic material (OA) created a thick enough interphase between polymer matrix and MNP agglomerates to cause a reduction in overall magnetic properties. The observance of the larger coercive force in the hysteresis loop at lower temperature (100 K) as compared to that at higher temperature (400 K) confirms the paramagnetic behaviour of the designed PMCs (221). The hysteresis loops of all the synthesised PMCs revealed symmetric behaviour similar to that of ferromagnetic materials (222), confirming suitability of the synthesised PMCs for magnetic applications (67), especially for stimuli-based self-healing. Independent of the MNPs weight percentage in PMCs, the coercivity of all PMC samples (except pristine sample that showed zero magnetisation) took a value between 270-310 Oe and 110-120

O_e at temperatures of 100 K and 400 K, respectively. The noted results are summarised in Table 5.10 & 5.11 below.

Table 5.10: Summarised magnetic results at 100 K for Pristine PA6 sample, PMC sample with uncoated MNPs and PMC samples with varying percentages of OA loading on the MNPs.

Sample	Coercivity (H _c) (Oe)	Magnetic Remanence (M _r) (emu/g)	Magnetic Saturation (M _s) (emu/g)	Magnetic Moment Ratio (M _r /M _s) (%)
Pristine PA6	0	0	0	0
Uncoated-Fe ₃ O ₄ PMC	360	117 × 10 ⁻⁴	253 × 10 ⁻⁴	46 ± 7
22 w/w% OA-Fe ₃ O ₄ PMC	244	63 × 10 ⁻⁴	200 × 10 ⁻⁴	31 ± 4
33 w/w% OA-Fe ₃ O ₄ PMC	258	42 × 10 ⁻⁴	128 × 10 ⁻⁴	32 ± 3
44 w/w% OA-Fe ₃ O ₄ PMC	252	105 × 10 ⁻⁴	266 × 10 ⁻⁴	39 ± 5
55 w/w% OA-Fe ₃ O ₄ PMC	362	27 × 10 ⁻⁴	47 × 10 ⁻⁴	57 ± 12

Table 5.11: Summarised magnetic results at 400 K for Pristine PA6 sample, PMC sample with uncoated MNPs and PMC samples with varying percentages of OA loading on the MNPs.

Sample	Coercivity (H _c) (Oe)	Magnetic Remanence (M _r) (emu/g)	Magnetic Saturation (M _s) (emu/g)	Magnetic Moment Ratio (M _r /M _s) (%)
Pristine PA6	0	0	0	0
Uncoated-Fe ₃ O ₄ PMC	169	82 × 10 ⁻⁴	211 × 10 ⁻⁴	29 ± 6
22 w/w% OA-Fe ₃ O ₄ PMC	116	29 × 10 ⁻⁴	120 × 10 ⁻⁴	24 ± 3
33 w/w% OA-Fe ₃ O ₄ PMC	110	24 × 10 ⁻⁴	100 × 10 ⁻⁴	24 ± 3
44 w/w% OA-Fe ₃ O ₄ PMC	101	51 × 10 ⁻⁴	183 × 10 ⁻⁴	27 ± 5
55 w/w% OA-Fe ₃ O ₄ PMC	102	3 × 10 ⁻⁴	9 × 10 ⁻⁴	30 ± 9

In Fig. 5.17 (a) and (b), the hysteresis loop shows small coercive force with increase in OA loadings on MNPs suggesting transition from hard to soft magnetic behaviour of the PMCs. In summary, the values of saturation and remanence magnetisation of the magnetic moment ratio of PMCs as seen in Fig. 5.17 (a) and (b) were found to be increasing gradually with the amount of OA loading on the MNP coating, except for 55 w/w% OA-Fe₃O₄ PMC Sample which showed very high increment in 100K measurement.

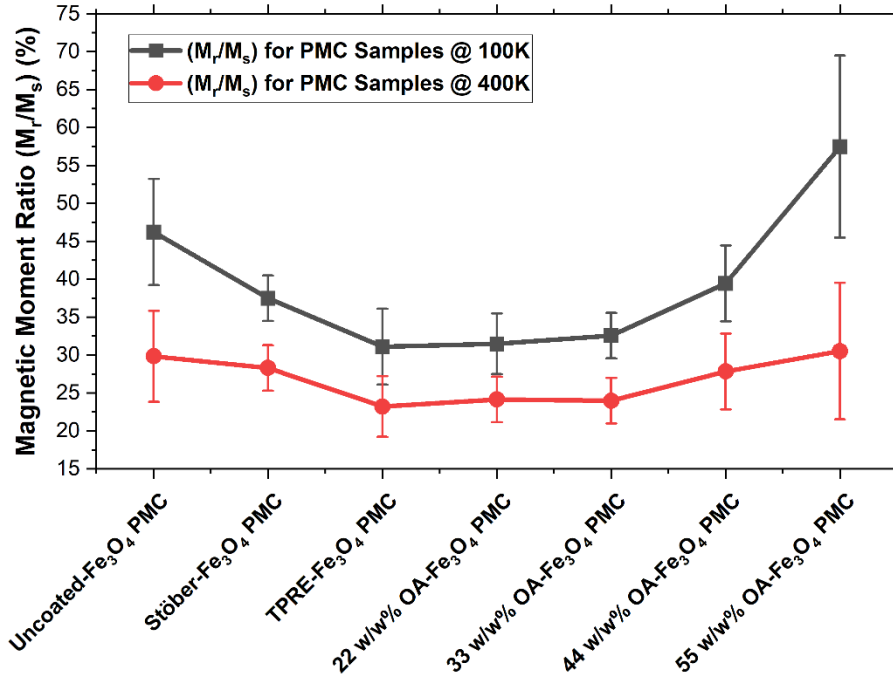


Figure 5. 18. Summarised comparison plot of the magnetic moment ratio (M_r/M_s) both at 100K and 400K for PMC samples with uncoated MNPs and samples with varying percentages of silica and OA loading on the MNPs.

Even though 55 w/w% OA- Fe_3O_4 PMC Sample showed highest M_r/M_s ratio but 22 w/w% OA- Fe_3O_4 PMC Sample showed improved dispersion of MNPs, which will prevent localized pyrolysis of the PMC during stimuli-based self-healing. The overall comparison of the characterisation results for all the prepared samples are done in the following section 5.4, and a suitable candidate material is selected for making the composite sandwich samples and to test the self-healing capability in GFRP composites.

5.4 Corelation of Dispersion State with Other Key

Findings

The onset of crystallization temperature steadily increases with the increase in OA content, indicating that the MNPs are acting as heterogenous nucleation agents in PA6 matrix and hence the higher crystallization rate than the pristine PA6. Moreover, the decreased melting peak can attribute to the decreased crystal size observed in XRD

(223,224). The DSC and XRD results confirmed that 22 w/w % OA-Fe₃O₄ PMC Sample showed highest degree of crystallinity and smallest crystallite size, respectively. As discussed in Section 5.2.3, the DSC and XRD results imply that 22 w/w% OA-Fe₃O₄ PMC Sample will have highest tensile strength and lowest melting temperature. The key results considered for selecting the appropriate PMC for the composite sample preparation, to be tested for self-healing application is summarised in Table 5.12 below.

Table 5.12: Summary of key findings from all the characterisation results.

Sample	Melting Temperature T_m (°C)	Degree of Crystallinity (%)	Crystallite size (nm)	Magnetic Moment Ratio (M_r/M_s) @ 100K (%)	Interaction Radius from the Simulated Model (IR) (nm)	Key Findings
Uncoated-Fe ₃ O ₄ PMC	213 ± 2	47 ± 2	42 ± 4	46 ± 7	265 ± 87	High crystallite size & melting temperature, very low degree of crystallinity and possibility of pyrolysis.
Stöber-Fe ₃ O ₄ PMC	212 ± 2	44 ± 4	36 ± 4	37 ± 3	166 ± 58	Low crystallite size and high melting temperature but lowest degree of crystallinity; lower magnetic response.
TPRE-Fe ₃ O ₄ PMC	210 ± 2	46 ± 3	33 ± 2	31 ± 5	129 ± 50	Low crystallite size but high melting temperature and lower degree of crystallinity; least magnetic response.
22 w/w% OA-Fe ₃ O ₄ PMC	200 ± 3	56 ± 4	30 ± 3	31 ± 4	142 ± 52	Lowest crystallite size & melting temperature, with highest degree of crystallinity. Least possibility of pyrolysis and

						maximum magnetic response.
33 w/w% OA-Fe ₃ O ₄ PMC	206 ± 3	49 ± 6	36 ± 4	32 ± 3	189 ± 82	Moderate crystallite size, melting temperature and degree of crystallinity. Slight possibility of pyrolysis and low magnetic response.
44 w/w% OA-Fe ₃ O ₄ PMC	207 ± 2	49 ± 3	48 ± 11	39 ± 5	188 ± 104	Highest crystallite size, melting temperature and lower degree of crystallinity. Highest pyrolysis and magnetic response.
55 w/w% OA-Fe ₃ O ₄ PMC	208 ± 2	42 ± 2	32 ± 13	67 ± 12	173 ± 67	Low crystallite size & degree of crystallinity and high melting temperature. Possibility of pyrolysis and least magnetic response.

Additionally, the magnetic properties of 22 w/w % OA-Fe₃O₄ PMC Sample is relatively higher than all other PMC samples. As seen in Table 5.12, the 22 w/w% OA-Fe₃O₄ PMC Sample was chosen for self-healing application as it will interact strongly with external electromagnetic field, melt at lower temperature, and provide highest tensile strength. 44 w/w% OA-Fe₃O₄ PMC Sample was not chosen despite of its higher magnetic properties than 22 w/w% OA-Fe₃O₄ PMC Sample to avoid localized pyrolysis due to the uneven dispersion and agglomeration concerns. Though Stöber-Fe₃O₄ PMC Sample showed almost similar IR values as that of the 22 w/w% OA-Fe₃O₄ PMC Sample but since it did not perform much better in other characterisation results, hence it was not the suitable choice. During cooling-heating cycle through multiple self-healing, the interactions between molecules impart the capability of adhesion using directional interactions that dictate the mechanical properties of a material (225), hence the degree of crystallinity, crystallite size and the thermal response of 22 w/w% OA-Fe₃O₄ PMC Sample is more favourable for the application than other samples. Also, the longer aliphatic coating of OA reduces the cluster stability and hence can result in increased self-healing efficiency (225,226).

Chapter Conclusion: This chapter discusses the characterisation results of the synthesised polymer nanocomposite samples with the functionalised MNPs. Herein, the FTIR and DSC characterisation gave the insights upon the chemical and thermal stability (degree of crystallinity). Further, the TEM, SAXS and XRD characterisations were utilised to assess the dispersion state of the MNPs, and the resulting data was fed to the developed MATLAB code for generating a simulated model. The simulated model gave the 3D representation of the MNPs dispersion state and their interaction radius. The SQUID measurements gave the magnetic moment ratio (Mr/Ms) at 100K and 400K comparison plot of the PMC samples with uncoated MNPs and samples with varying percentages of silica and OA loading on the MNPs. The overall characterisation results

comparison showed that the degree of crystallinity, crystallite size, interaction radius, and the magnetic & thermal response of 22 w/w% OA-Fe₃O₄ PMC Sample is more favourable for the composite stimuli based self-healing application than all other samples.

6. COMPOSITE STRUCTURE APPLICATION

In this chapter the composite dog bone sample preparation using the selected PMC is discussed. The standard GFRP dog bone composite samples are developed by sandwiching two PMC films between three layers of GFRP tapes. Further, the dog bone samples with and without damage, are tensile tested to determine the strength recovery after self-healing. The self-healing efficiency is calculated and presented based on the repetitive cycle of testing.

6.1 Materials

Glass fibre tape (PA6) with 0.18 mm thickness was purchased from Vitcas, and the synthesized polymer nanocomposite was used for composite sample preparation.

6.2 Standard Dog bone Sample Preparation

The composite dog bone samples were prepared using a fabricated metal die (details in Appendix E), prepared based on the composite sample testing specimen guidelines (227), dimensions of which are mentioned in Fig. 6.1.

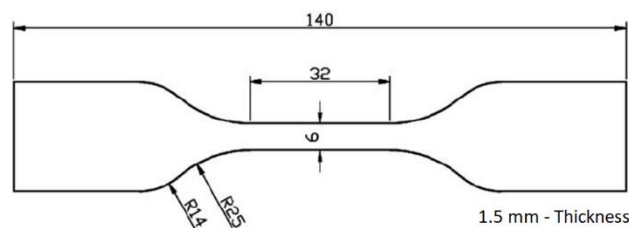


Figure 6.1. Tensile testing specimen dimensions, with grip length 30 mm and the specimen width 25 mm.

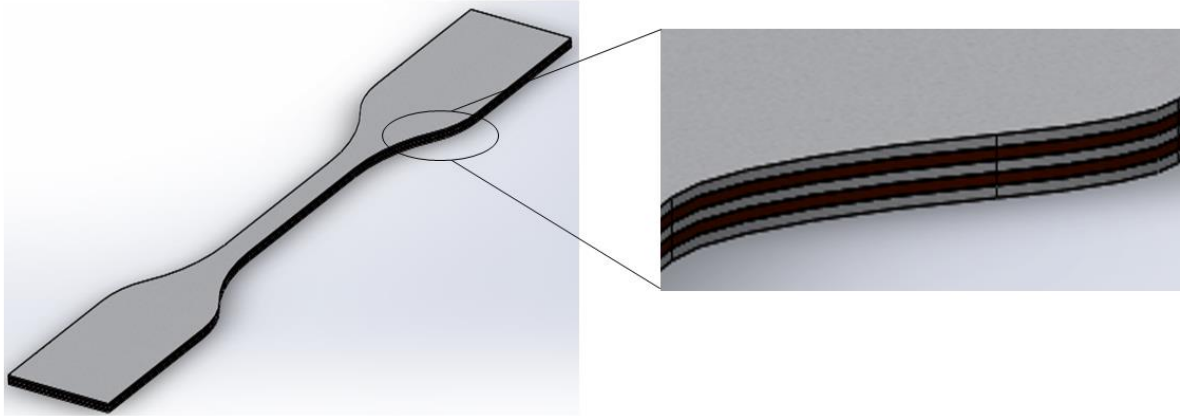


Figure 6.2. Standard dog bone samples prepared, showing different layers of the composite sample in CAD representation. (Arrangement of the layers are shown more clearly in the inset image; wherein the grey layer represents the Glass Fibre Tape, and the dark layer is the nanocomposite film.)

The virgin samples were prepared using three glass fibre tapes placed together with PMC film in between as represented in Fig. 6.2, and similarly the cracked-virgin sample was made but with an induced crack. The crack was induced as a thorough damage of the two outermost glass fibre tapes as a central snip of 2mm width, using a Stanley knife. The glass fibre tape was cleaned using mild acidic solution and ultrasound radiation to make its surface contaminant free allowing its enhanced bonding to PMC. The tape placement was done using hot gun (rating 50 KW) as a means of melting the PMC and setting it between the clean glass fibre tapes. All the samples were made to the size of standard 'dog-bone' specimen for composite testing. An example of the prepared samples without and with the induced crack are shown in Fig. 6.3.

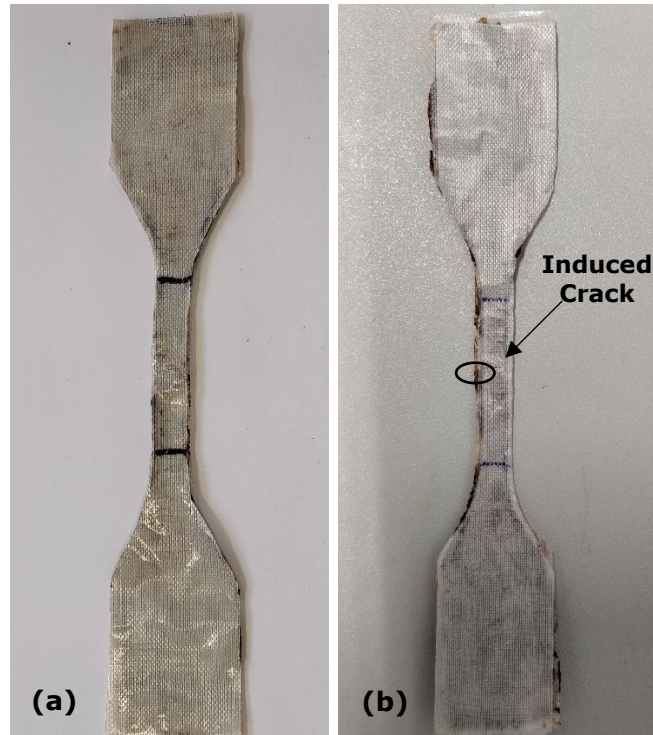


Figure 6.3. An example of the prepared samples (a) without and (b) with the induced crack.

6.3 Tensile testing and Self-Healing

6.3.1 Tensile Test Characterisation Method

Tensile testing with five test specimens was carried out using Instron 1195 universal tensile testing machine (UTM) according to ASTM D638, with a full-scale load cell range set to 50 kN. The crack on the specimen was created such that the applied tensile load direction was perpendicular to crack. It represented most onerous scenario. The standard 'dog-bone' specimen was used for measuring the desired stress-strain response. The crosshead displacement rate was set to vary at a rate of 0.5 mm/min. The stopping criteria for the test was fixed at 50% change in the maximum load capacity, and allowable length extension of 20 mm and change of width up to 3mm.

The composite GFRP tapes were self-healed after successive crack propagation, as the method followed in references (49,228), by microwave induction stimuli at 2.45 GHz for 30 seconds at 900W using a commercial microwave oven. After 30 s, the PMC film between GFRP tapes is melted at the crack location and the liquid PMC fills the crack.

After cooling at room temperature, the healed samples are tensile tested. The sample was not mechanically compressed after healing.

6.3.2 Results and Discussion

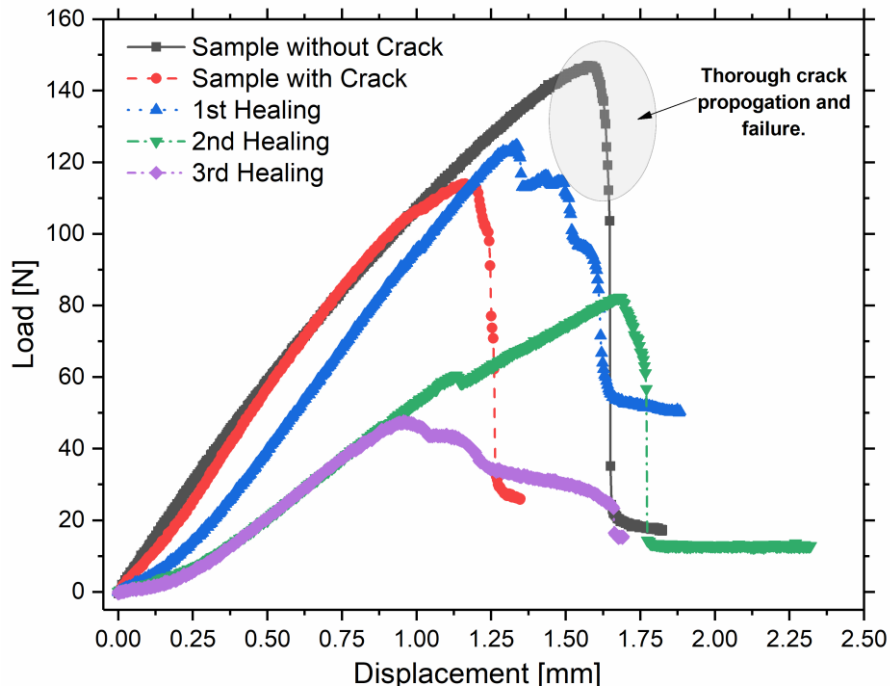


Figure 6.4. Load-displacement curves measured during tensile testing of virgin sample without and with crack, and the subsequent healings.

The tensile tests were conducted to determine the tensile strength of the multi-layered GFRP- PMC composite sample (Fig. 6.3). Tensile load was applied to multi-layered GFRP- PMC composite dog bone, here referred as “virgin sample”, to obtain relation of applied load to elongation (Fig. 6.4). Obtained results show an initial linear deformation region, followed by a small non-linear plastic deformation and final failure. As observed in Fig. 6.4, the maximum load sustained by the virgin sample before final break-up was 150 N. At maximum load, the crack on the sample started developing and brought about a loss of the storage modulus as a sudden drop in the load was witnessed (inset image shows the initial breakage, leading to the initiation of crack propagation and failure at the peak load). Adding extra layers did not increase the tensile strength of the virgin sample, and the maximum tensile stress was found to be comparable with that of the commercially

available Vitcas (in as bought condition) glass fibres composite tape (229). The early-stage crack initiation followed by the fibre failure was observed (Fig. 6.5 black curve); this is the usual phenomenon observed in the failure of the glass fibre composites (230).

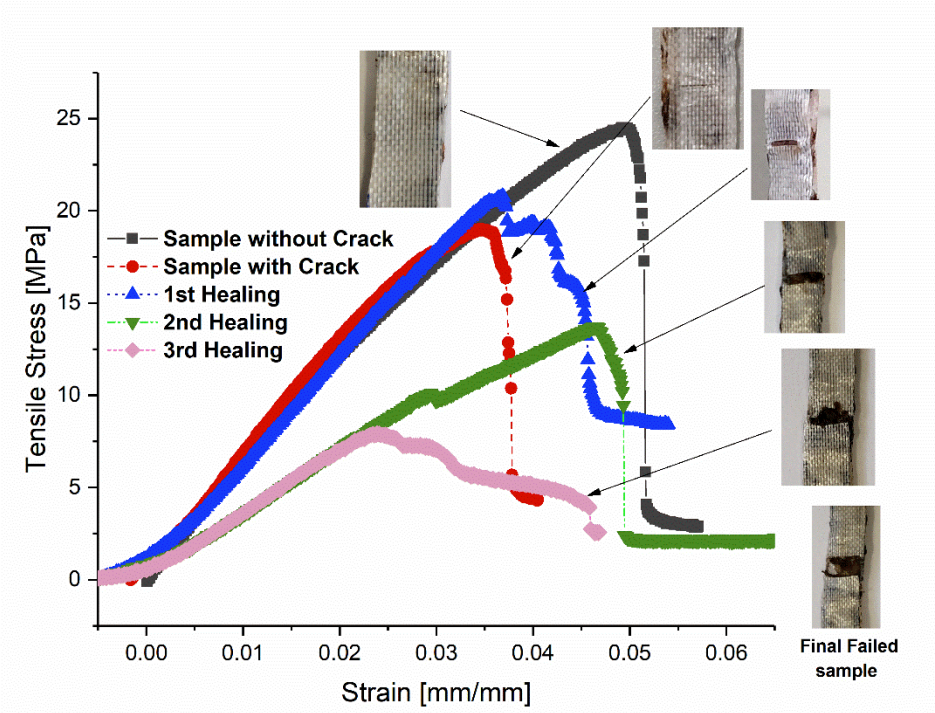


Figure 6.5. Stress-Strain curves measured during tensile testing of virgin sample without and with crack, and the subsequent healings.

In comparison to virgin sample, the cracked virgin sample showed reduction of 24% in its elongation and 21% in its tensile strength, which is evident in Fig. 6.5 (red dashed curve as compared to the black curve). Corresponding maximum tensile load of cracked virgin sample was found to be 114.04 N, dropped from the 150 N of virgin sample. After self-healing, the maximum tensile load of the sample was recovered but it was not as high as the virgin sample. Secondly, the failure of the healed sample was different than the one observed in virgin samples. Unlike virgin sample, the healed sampled failure was gradual and stepwise and the drop in tensile strength was prominent after each drop as it is manifested in blue curve of Fig. 6.5.

6.4 Determination of Self-Healing Efficiency

The self-healing is effective in regaining the strength of the composite sample. The maximum tensile stress of the sample improved by approximately 10% after 1st healing compared to tensile strength of the cracked virgin-sample. To compare the healing efficiency, the healing efficiency was defined as the ratio of the tensile strength of the healed sample to the original sample. The healing efficiency was calculated using the tensile test results for the subsequent healing following the reference equation (47). The response after each healing was compared with that of the virgin sample to make a clear distinction and test the viability of such composite materials in rendering the best outcome. The efficiencies based on strength recovery were calculated as $84 \pm 6\%$, $58 \pm 12\%$ and $34 \pm 15\%$ after first, second and third healing, respectively. Though the subsequent efficiencies are less after the first healing attempt, it's not only because of the lack of healing capability but because the sample itself is damaged in a way that can't be completely recovered, as is seen in the inset images in Fig. 6.5. This enunciates that this method of self-healing has a capability of improving the overall life of the structure by $\approx 175\%$, based on recovery efficiency. These efficiencies were observed for three out of five samples that were tested, hence giving a certainty of 60%. Until now there have been many concepts of self-healing for structural application, few of the relevant reported results with the lowest to highest efficiencies are summarised in Table 6.1.

Table 6.1: Some concepts of self-healing composites proposed for structural applications.

Techniques	Matrix/Filler Combination	Reported Efficiency	References	Limitations
1. Micro-encapsulation	Epon 828 with Carbon Fibre	38% & 66%	(28)	Requires a definite volume of catalyst loading; acts only on successful
	Epon 862 with glass fabric	68% & 78%	(29)	
	Epon 862 with E-glass	100%	(30)	

				rupture of the microcapsule.
2. Hollow Glass fibres (HGF)	Epoxy with HGF	5%	(33)	An alternative to microcapsules, but with similar limitations
	Epoxy with H-glass	19.3%	(34)	
	Epon 828 with E-glass	62%	(35)	
	Epoxy with hexcel	83.2%	(36)	
	Epoxy with HGF	129%	(37)	
3. Vascular	Epoxy with E-glass	40%	(40)	Similar to hollow fibres, only that it has a continue external supply network of healing agent,
	Epoxy with E-glass	67-74%	(41)	
	Epoxy with hexcel	96-99%	(42)	
4. Reversible Covalent bond	Mendomer with carbon fibre	92-94%	(45)	Reversible crosslinks are activated upon heating, but they are limited with low temperature resistance
5. Supramolecular interactions	Reverlink with E-glass	100%	(46,47)	Based on non-covalent interactions, but result in poor mechanical performance
6. Polymer blends	Epon 828 with E-glass	30%	(48,49)	Thermoplastic phase is dispersed within a thermoset host to facilitate crack healing, but the compatibility of two is a major concern and such healing is also
	Epon 828 with E-glass	94.9%	(50,51)	
	Epoxy with carbon fibre	156%	(52,53)	

				induced with gas pockets
--	--	--	--	--------------------------

Though these methods have shown satisfying results, but they lack in the case of homogeneous response; like if the crack is not activating the flow of healing agent, as it may happen if the crack is induced in the midst of microcapsule or hollow fibre or vascular network. Similarly, the methods have certain limitations as listed in Table 4; but the method proposed herein effectively deals with these issues and is not at all complex in fabrication. Since the MNPs are uniformly dispersed hence the GFRP composites can respond to stimuli anywhere, and repetitively without any conflict. And the efficiency of 1st self-healing (84%) is well comparable to other concepts proposed until now; and not only that, as mentioned earlier structural-monitoring capabilities if combined with self-healing can prove economically phenomenal. Though, the recovery of the tensile modulus/strength decreases drastically on the third healing, but theoretically the overall recovery ($\approx 175\%$) is still quite a useful improvement.

The proposed methods showed ability to heal the crack irrespective of its location on the surface area of the component. As PMC film is beneath every millimetre of the composite tape, the defect on the surface of the composite can be repaired repetitively by activating the flow of healing agent (designed magnetic PMC), which may not be the case in other methods.

Chapter Conclusion: This chapter discusses the results of the composite dogbone sample testing, prepared with the elected 22 w/w% OA- Fe_3O_4 PMC Sample. The sample was subjected to tensile testing after subsequent stimuli-based healing. The healing efficiency attained is $\approx 175\%$, over three cycles of subsequent healing. The method of microwave stimuli-based healing was presented with a representative sample in lab-based setup representing structural use case.

7. CONCLUSION AND FUTURE SCOPE

7.1 Conclusion

Fibre-reinforced polymer (FRP) composites are finding extensive use in the offshore industry. The products such as composite modules, spoolable pipes and pressure vessels are now manufactured using FRP for light-weighting and better management of the stress and strains resulting from the environmental loads. The challenge of accessing deep-water fields and other places has led to development of hybrid flexible riser consisting of metallic and thermoplastic composite layers (Figure 2.9 in Chapter-2). The composite section of the flexible or spoolable pipe also uses either carbon or glass fibre thermoplastic tapes, as they provide high damage and impact tolerance as well as chemical and solvent resistance combined with unlimited shelf life, low storage costs, weldability and recyclability. However, the major benefit of using thermoplastic is that it does not require an autoclave for manufacturing a large component. Majority of components used in offshore industry are very large and it is difficult to process them in an autoclave. With the methods such as automated tape placement, the kilometre-long quality composite pipes with well-consolidated layers are manufactured. Moreover, the cost and processing time is also very less.

Enhancing the access of offshore industries including renewables to the high technology composites requires reduction in cost through increase in reliability, dependable life and material performance. A small increase in reliability of the composite materials results into higher productivity of many offshore operations such as a typical subsea tie-back projects. Often these GRFP products are susceptible to scratches, cracks, and punctures, which can result in dangerous spillages, safety hazards, or simply loss of productivity. Although the strength and stiffness of anisotropic composite materials can be attuned accurately to withstand the expected loads, this may result in a structure less tolerant to damage in certain areas. As seen in computed tomography images in Figure 2.10 (a) and

(b) in Chapter 2, the layered thermoplastic composite structure can develop safety critical defects at considerably lower load. Furthermore, this early onset of the defects initiates the development of large transverse cracks until the entire component fails. Many other failure modes for composites in safety critical applications exist and can cause sudden failures, however, it all starts with micro-cracking of the composite matrix. As discussed in Chapter-3, microscale failure such as cracks occurs at an early stage of operation it is crucial to identify and repair critical micrometre scale defects early on. However, it is difficult to detect micron size delamination and therefore, if autonomous material healing is carried out at regular interval, the damage tolerance and productivity of the material can be improved significantly, and it will result in increased reliability by avoiding sudden catastrophic structural failures.

In Chapter-2, literature on the multiple methods of self-healing of composites and in particular through application of stimuli or on susceptible damage have been cited and discussed. Most methods are related to healing the epoxy based composite materials where liquid healing agents are incorporated into the structure using various methods. For example, a hollow fibre containing liquid healing agent can be 3D weaved into composite prepeg for mimicking veins in human body. Hollow fibre composite with 1 to 3% v/v fraction showed capability to arrest the crack propagation. In other self-healing strategy, the thermoplastic resin is combined with epoxy to heal the cracks in thermoset matrix composite through repetitive melting of thermoplastic. When hybrid polymer matrix in composites is heated, the thermoplastic filled the crack in epoxy. Some methods even use reversible bond in polymer and magnetic stimuli to recover the bonding strength of the polymer. Initial strength of such material is still limited for the structural application.

This work demonstrated a self-healing system for structural applications which can be operated remotely and integrated with sensing. As a part of this work, the basic component of such system, the self-healing multilayer tape consisting of a low melting temperature nanocomposite film sandwiched between high melting point thermoplastic

unidirectional fibre-reinforced prepreg or tape was prepared. The component made using these tapes can be exposed regularly to external stimuli to melt the PMC film and encourage liquid composite polymer to fill the microcracks through capillary action. The infiltration of viscous polymer in to the microcrack arrests the stress intensity at the tip which enhances fracture toughness by forming wedge shape film, capable of holding crack opening under maximum loading cycle condition. This process can hold back the crack propagation for significant time. Choice of stimuli can be magnetic field or microwave that can be applied remotely to FRP component. Together with crack-gap closing mechanism, the microwave source can be interfaced with electronic triggering mechanism to affect the self-healing in remotely located FRP components. Moreover, the healing can also be performed multiple times by applying micro-wave or magnetic stimuli.

In order to achieve efficient microwave induced melting of the polymer matrix in PMC, the uniform dispersion of MNP in polymer matrix is essential for such application. Increasing MNP loading reduces the inter-particle distances allowing formation of the agglomerates due to short range Van der Waals or hydrogen bonds. As in at air-liquid interface in bubbles, the particles tend to agglomerate at phase interfaces such as solid-solid, solid-liquid or air-liquid. Presence of MNP agglomerates in polymer matrix cause an uneven response to the applied stimulus; as the agglomerated particles region will absorb more stimulus energy and will melt the polymer excessively or undergo pyrolysis. Additionally, the dispersion also affects the size of crystal and degree of crystallinity of the polymer matrix in PMC. Low degree of crystallinity increases the melting temperature of PMC and the crystallite size affects the mechanical properties of the PMC. The dispersion also affects the magnetic properties of the PMC. In order to maintain lower melting temperature and better mechanical properties as well as to avoid pyrolysis, the PMC preparation was optimised to control the MNP dispersion. In Chapter-3, the variable silica (Stöber and TPPE) and hydrophobic oleic acid (22%, 33%, 44% and 55% w/w) coating was functionalised on the MNPs for assessing their effect on the magnetic

response and their resulting dispersion in the polymer matrix (Chapter-5) and therefore, optimizing all the properties including magnetic property of PMC. The silica and OA loading (w/w %) on the iron oxide MNPs was varied to determine the most suitable weight fraction for better dispersion of MNPs in PMC. The results related to dispersion, magnetic properties, degree of crystallinity and crystallite size, as are included to show the optimization of PMC in Chapter-5.

The concept of self-healing and its current state was discussed with a novel intent of applying it to thermoplastic structures using specially designed magnetically responsive PA-6 nanocomposite. To address the major issue of uniform dispersion arising with the synthesis of magnetic nanocomposites, two key steps were studied and implemented viz, functionalisation of the MNPs (Chapter-3) and in-situ polymerisation of the nanocomposite samples (Chapter-4). In surface modification of MNPs two approaches were implemented and characterised: silica functionalisation involving Stöber & microemulsion technique, and oleic acid functionalisation. The magnetic PA6 polymer nanocomposite samples were successfully synthesized using an anionic ring opening in-situ polymerisation approach, with optimised activator and initiator proportions for giving control over dispersion state of the functionalised MNPs and at the same time maintaining the required degree of crystallinity for ensuring the mechanical properties of a thermoplastic. These methods ensured improvements in the MNPs dispersion state in the base polymer matrix, which was characterised and compared for electing the best suitable PA-6 PMC for the composite sample preparation and subsequent self-healing study for damage tolerance.

This work reports the stimuli induced healing potential of the layered thermoplastic composite containing magnetic PMC film as healing agent (Figure 6.2 in Chapter-6). Firstly, the magnetic PA-6 polymer nanocomposite was synthesised by uniformly dispersing iron (III) oxide MNPs in polymer matrix. The in-situ ring opening polymerisation method was used for uniform dispersion of MNPs in PA-6 matrix. Subsequently, the PNC film of 0.2 mm was prepared for incorporation into layers of GFRP

composite, as seen in Figure 6.3 in Chapter-6. The standard GFRP dog bone composite samples were developed by sandwiching two PNC films between three layers of GFRP tapes. Secondly, the dog bone samples with and without damage, were tested to determine tensile strength before and after healing.

Notably, this is a first report on method capable of self-healing large structures made using fibre reinforced thermoplastic tape placement. Though many self-healing concepts for FRP composites have been proposed until now, but still their commercial application has not been tested yet (47). In this study, the concept of self-healing to enhance the life cycle through damage control of thermoplastic fibre reinforced tape layered composites for onshore and offshore structures is presented. The designed PMC was optimised for effective dispersion and physical properties and the 22 w/w% OA sample suits best for the structural bonding of the GFRP composites, acting as a consolidation. Consequently, the characterisation results supported the proposition well. The concept is tested using a multilayer dog bone sample and is shown to recover 84% of original strength in the first healing cycle. The concept of self-healing and its seamless integration method was presented in detail. Which resulted in renewed efficacy of the composite structure with the healing efficiencies of 84%, 58%, and 34% for subsequent healings as compared to that of a cracked virgin-sample. Furthermore, the overall strength of the structure can be improved at least by $\approx 175\%$ with 60% certainty using this scheme, and it is conveniently applicable to upgrade the existing practices.

7.2 Future Scope

There are variable scopes or opportunities wherein the current work can be implemented with slight modifications or further developments. Some of the scopes are discussed as follows:

7.2.1 Underwater Self-Healing Capability

The presented work could only demonstrate the use of microwave stimuli for self-healing, because the actual intended electromagnetic stimulus couldn't be utilised due to the working coil capacity limitation. The original idea of involving EM waves would be most suitable to have as this can widely address the issue of implementing the healing and even sensing technique under water, which is a critical issue for microwaves, because microwave's do not work in aqueous media. The development of a high-capacity electromagnetic induction coil can be considered; that can effectively address the stimuli generation for a significant amount of time which can bring about the melt-response of the PMC.

7.2.2 Remote Structural Health Monitoring

To extend this work further, the same setup of the prepared composite sample with the electromagnetic stimuli capability can be used for damage detection or automated structural health monitoring. Since the PMC absorbs the incident stimuli, it can be used to capture the thermal gradient upon incident thermal stimulus. The thermographic gradient can be used to compare a healthy and damaged component for defect or damage identification. Considering the fact, that any damage will expose the PMC layer, thereby allowing differential stimulus absorption in that region. Since, this method can operate as a standalone setup with infrared or thermographic cameras mounted, or even with the involvement of robotic drones the stimulus application and thermographic image capturing can be done for difficult to access regions. This can be a potential achievement, considering the need for offshore structural health monitoring. The current

setup can be modified easily, if the required thermography mounting can be coupled with the stimuli generating source.

7.2.3 Self-healing Insulation Materials for HVDC Cables

The capacity of offshore wind parks and subsea oil/gas processing facilities are expanding in size and require improved solutions for reliably transmitting large amounts of electric power using a smart energy system. The core of the upcoming smart energy system demands accelerated improvements in the transmission and distribution capacities of direct current based high voltage (HVDC) cables. With currently available offshore HVDC technology, the cost overruns and maintenance issues are frequent and many reports suggest that 80% of wind farm insurance claims in European continent have been cable-related. Development of the material for the long-distance transmission cables is no longer in focus, conversely, the development of materials for MVDC cables has come under intense focus.

The new insulating material should not allow the formation of electrical treeing and space charge concentration, which is a major cause of the complete breakdown and subsequently, damage to the polymer matrix. Space charges are accumulated electrons/holes and charges (cation or anion) on the surface of the material causing the inhomogeneous distribution of the electric field. Excessive charge accumulation can lead to electric treeing and damage the material. Controlling the space charge formation is key to the development of the new materials. Prepared PMC nanocomposite by addition of the metal oxide nanoparticles to the polymer matrix can enhance the insulating property by trapping the electrons at the interface of the nanoparticles. And in this case Fe_3O_4 MNPs can be the easily sourced and cheaper alternative for preparing the insulating nanocomposite layer. And with the PMC's self-healing capability, even if any damages are caused by the electric treeing, those can be easily reversed. This can present the feasibility of long-term deployment of HVDC cables as a viable solution.

7.2.4 PMC for Microscale Magnetic Components

Micro and nanoelectronics are getting very much in demand, namely micro inductors and micro transformer components are especially getting extensively utilised. The developed PMC materials of this thesis work, having varied dielectric, electric and magnetic response can be directly utilised for such effective component developments. The major future study can be then focussed on the optimal design process for varying geometries of devices e.g., V groove, planar, 2D spiral and 3D solenoid for the developed components. With the main challenge of being able to optimise their power density for DC-to-DC converters. And the ideal parameters of study being resistivity, relative permittivity, hysteresis, etc. The optimisation of design of such materials would be very useful for this application area; with research outputs directed towards the design, fabrication, and characterisation in terms of thin film & thick film deposition of magnetic materials with the variable geometries.

7.2.5 Hydrogen Generation with Functionalised MNPs

The potential of using nanoparticles for hydrogen production has been proven to give better efficiency for green hydrogen production. Green hydrogen, which is mainly produced by water electrolysis using renewable electricity, is one of the levers that will speed up the transition to a carbon neutral future. Specifically, the involvement of magnetic nanoparticles has shown higher efficacy for hydrogen production. These magnetic nanoparticles can be functionalised by selective photocatalytic moieties for photocatalytic hydrogen generation and even the photocatalysts can be recycled by magnetic force for repeated hydrogen generation. The functionalisation of the nanoparticles can also act as a reactive interface/medium for innovative methodology of hydrogen production through water splitting over Fe_3O_4 pellet at low temperature ($T = 300\text{ }^\circ\text{C}$, possible with solar power alone). The generation capacity at low temperature can be tuned by employing the effect of magnetic field and electric power. Since the interface created by the functionalisation involved on the nanoparticles surface dictates

their magnetic and electrical response, creating engineered interface can further improve the hydrogen generation performance and even their recyclability for repeated generation. The effect of variable interfaces in terms of the selective chemical moiety and the variable surface structures are still an uncovered area, demanding immediate attention for improved green hydrogen generation and to make such technologies commercially scalable. Optimising the interface for renowned green hydrogen generation is the major research question within the existing innovative technologies.

REFERENCES

- (1) Wu DY, Meure S, Solomon D. Self-healing polymeric materials: A review of recent developments. *Progress in polymer science*. 2008; 33(5):479-522.
- (2) Osswald TA, Menges G. Material Science of Polymers for Engineers. Cincinnati, OH. 2003.
- (3) Blaiszik BJ, Kramer SL, Olugebefola SC, Moore JS, Sottos NR, White SR. Self-healing polymers and composites. *Annual review of materials research*. 2010; 40:179-211.
- (4) Mittal V. Barrier resistance generation in polymer nanocomposites. *Optimization of Polymer Nanocomposite Properties*. 2010; pp. 1-19.
- (5) Lau K, Sankar J, Hui D. Enhancement of the mechanical strength of polymer-based composite using carbon nanotubes. 1st ed. USA: CRC/Taylor & Francis; 2006. Chapter 14.
- (6) Dodds N, Jha V, Latto J and Finch D. Unbonded Flexible Pipe: Composite Reinforcement for Optimized Hybrid Design. Unbonded Flexible Pipe: Composite Reinforcement for Optimized Hybrid Design. *Proceedings of the Offshore Technology Conference: Offshore Technology Conference*; 2015.
- (7) Jha V, Latto J, Dodds N, Anderson TA, Finch D and Vermilyea M. Qualification of flexible fiber-reinforced pipe for 10,000-foot water depths. Qualification of flexible fiber-reinforced pipe for 10,000-foot water depths. *Proceedings of the Offshore Technology Conference: Offshore Technology Conference*; 2013.
- (8) Ghosh SK. Self-healing materials: fundamentals, design strategies, and applications. Wiley Online Library; 2009. p. 1-28.
- (9) Chen Y, Kushner AM, Williams GA, Guan Z. Multiphase design of autonomic self-healing thermoplastic elastomers. *Nature chemistry*. 2012; 4(6):467-472.
- (10) Lee JY, Buxton GA, Balazs AC. Using nanoparticles to create self-healing composites. *The Journal of chemical physics*. 2004; 121(11):5531-5540.
- (11) White SR, Sottos NR, Geubelle PH, Moore JS, Kessler MR, Sriram S, et al. Autonomic healing of polymer composites. *Nature*. 2001; 409(6822):794-797.
- (12) Chung C, Roh Y, Cho S, Kim J. Crack healing in polymeric materials via photochemical [2 + 2] cycloaddition. *Chemistry of Materials*. 2004; 16(21):3982-3984.
- (13) Kryger MJ, Ong MT, Odom SA, Sottos NR, White SR, Martinez TJ, et al. Masked cyanoacrylates unveiled by mechanical force. *Journal of the American Chemical Society*. 2010; 132(13):4558-4559.
- (14) Karthikeyan S, Sijbesma RP. Forcing a molecule's hand. *Nature chemistry*. 2010; 2(6):436-437.
- (15) Davis DA, Hamilton A, Yang J, Cremer LD, Van Gough D, Potisek SL, et al. Force-induced activation of covalent bonds in mechanoresponsive polymeric materials. *Nature*. 2009; 459(7243):68-72.
- (16) Garcia S, Fischer H. Self-healing polymer systems: properties, synthesis and applications. *Smart Polymers and their Applications*. : Elsevier; 2014. p. 271-298.
- (17) Fall RA. *Puncture reversal of polyethylene ionomers-mechanistic studies*. 2001; .
- (18) Scott TF, Schneider AD, Cook WD, Bowman CN. Photoinduced plasticity in cross-linked polymers. *Science (New York, N.Y.)*. 2005; 308(5728):1615-1617.

- (19) Tennyson AG, Wiggins KM, Bielawski CW. Mechanical activation of catalysts for C–C bond forming and anionic polymerization reactions from a single macromolecular reagent. *Journal of the American Chemical Society*. 2010; 132(46):16631-16636.
- (20) Guo W, Jia Y, Tian K, Xu Z, Jiao J, Li R, et al. UV-triggered self-healing of a single robust SiO₂ microcapsule based on cationic polymerization for potential application in aerospace coatings. *ACS applied materials & interfaces*. 2016; 8(32):21046-21054.
- (21) Ghosh B, Urban MW. Self-repairing oxetane-substituted chitosan polyurethane networks. *Science (New York, N.Y.)*. 2009; 323(5920):1458-1460.
- (22) Gao L, He J, Hu J, Wang C. Photoresponsive self-healing polymer composite with photoabsorbing hybrid microcapsules. *ACS applied materials & interfaces*. 2015; 7(45):25546-25552.
- (23) Xu G, Lu W, Feng X, Yu S. Self-assembly of organic–inorganic nanocomposites with nacre-like hierarchical structures. *Soft Matter*. 2011; 7(10):4828-4832.
- (24) Kamphaus JM, Rule JD, Moore JS, Sottos NR, White SR. A new self-healing epoxy with tungsten (VI) chloride catalyst. *Journal of the royal society interface*. 2008; 5(18):95-103.
- (25) Blaiszik B, Sottos N, White S. Nanocapsules for self-healing materials. *Composites Science and Technology*. 2008; 68(3-4):978-986.
- (26) Jin H, Mangun CL, Stradley DS, Moore JS, Sottos NR, White SR. Self-healing thermoset using encapsulated epoxy-amine healing chemistry. *Polymer*. 2012; 53(2):581-587.
- (27) Billiet S, Van Camp W, Hillewaere XK, Rahier H, Du Prez FE. Development of optimized autonomous self-healing systems for epoxy materials based on maleimide chemistry. *Polymer*. 2012; 53(12):2320-2326.
- (28) Kessler M, Sottos N, White S. Composites Part A: Appl. *Sci.Manuf.* 2003; 34(8):743.
- (29) Patel AJ, Sottos NR, Wetzel ED, White SR. Autonomic healing of low-velocity impact damage in fiber-reinforced composites. *Composites Part A: Applied Science and Manufacturing*. 2010; 41(3):360-368.
- (30) Moll JL, White SR, Sottos NR. A self-sealing fiber-reinforced composite. *Journal of Composite Materials*. 2010; 44(22):2573-2585.
- (31) Bond IP, Williams MGJ, Trask RS. Self-healing CFRP for aerospace applications. *16th*. 2007; .
- (32) Wu X, Rahman A, Zhou Z, Pelot DD, Sinha-Ray S, Chen B, et al. Electrospinning core-shell nanofibers for interfacial toughening and self-healing of carbon-fiber/epoxy composites. *Journal of Applied Polymer Science*. 2013; 129(3):1383-1393.
- (33) Bleay S, Loader C, Hawyes V, Humberstone L, Curtis P. A smart repair system for polymer matrix composites. *Composites Part A: Applied Science and Manufacturing*. 2001; 32(12):1767-1776.
- (34) Kling S, Czigány T. Damage detection and self-repair in hollow glass fiber fabric-reinforced epoxy composites via fiber filling. *Composites Science and Technology*. 2014; 99:82-88.
- (35) Zhu Y, Ye XJ, Rong MZ, Zhang MQ. Self-healing glass fiber/epoxy composites with polypropylene tubes containing self-pressurized epoxy and mercaptan healing agents. *Composites Science and Technology*. 2016; 135:146-152.
- (36) Williams G, Trask R, Bond I. A self-healing carbon fibre reinforced polymer for aerospace applications. *Composites Part A: Applied Science and Manufacturing*. 2007; 38(6):1525-1532.

- (37) Trask R, Bond I. Biomimetic self-healing of advanced composite structures using hollow glass fibres. *Smart Materials and Structures*. 2006; 15(3):704.
- (38) Fifo O, Ryan K, Basu B. Glass fibre polyester composite with in vivo vascular channel for use in self-healing. *Smart Materials and Structures*. 2014; 23(9):095017.
- (39) Kousourakis A, Mouritz A. The effect of self-healing hollow fibres on the mechanical properties of polymer composites. *Smart Materials and Structures*. 2010; 19(8):085021.
- (40) Williams H, Trask R, Bond I. Self-healing sandwich panels: restoration of compressive strength after impact. *Composites Science and Technology*. 2008; 68(15-16):3171-3177.
- (41) Luterbacher R, Trask R, Bond I. Static and fatigue tensile properties of cross-ply laminates containing vasculature for self-healing applications. *Smart Materials and Structures*. 2015; 25(1):015003.
- (42) Norris CJ, Meadway GJ, O'Sullivan MJ, Bond IP, Trask RS. Self-healing fibre reinforced composites via a bioinspired vasculature. *Advanced Functional Materials*. 2011; 21(19):3624-3633.
- (43) Murphy EB, Bolanos E, Schaffner-Hamann C, Wudl F, Nutt SR, Auad ML. Synthesis and characterization of a single-component thermally remendable polymer network: Staudinger and Stille revisited. *Macromolecules*. 2008; 41(14):5203-5209.
- (44) Chen X, Dam M, One K, Mal A. S, H.; Nutt, SR; Sheran, K.; Wudl, F. A thermally remendable cross-linked polymeric material. *Science*. 2002; 295:1698-1702.
- (45) Park JS, Kim HS, Hahn HT. Healing behavior of a matrix crack on a carbon fiber/mendomer composite. *Composites Science and Technology*. 2009; 69(7-8):1082-1087.
- (46) Sordo F, Michaud V. Processing and damage recovery of intrinsic self-healing glass fiber reinforced composites. *Smart Materials and Structures*. 2016; 25(8):084012.
- (47) Cohades A, Branfoot C, Rae S, Bond I, Michaud V. Progress in self-healing fiber-reinforced polymer composites. *Advanced Materials Interfaces*. 2018; 5(17):1800177.
- (48) Hayes S, Jones F, Marshiya K, Zhang W. A self-healing thermosetting composite material. *Composites Part A: Applied Science and Manufacturing*. 2007; 38(4):1116-1120.
- (49) Hayes S, Zhang W, Branthwaite M, Jones F. Self-healing of damage in fibre-reinforced polymer-matrix composites. *Journal of the Royal Society Interface*. 2007; 4(13):381-387.
- (50) Cohades A, Michaud V. Thermal mending in E-glass reinforced Poly (ϵ -caprolactone)/epoxy blends. *Composites Part A: Applied Science and Manufacturing*. 2017; 99:129-138.
- (51) Cohades A, Michaud V. Damage recovery after impact in E-glass reinforced poly (ϵ -caprolactone)/epoxy blends. *Composite Structures*. 2017; 180:439-447.
- (52) Pingkarawat K, Wang C, Varley RJ, Mouritz A. Effect of mendable polymer stitch density on the toughening and healing of delamination cracks in carbon-epoxy laminates. *Composites Part A: Applied Science and Manufacturing*. 2013; 50:22-30.
- (53) Pingkarawat K, Bhat T, Craze D, Wang C, Varley RJ, Mouritz A. Healing of carbon fibre-epoxy composites using thermoplastic additives. *Polymer Chemistry*. 2013; 4(18):5007-5015.
- (54) Li Y, Zhu J, Wei S, Ryu J, Wang Q, Sun L, et al. Poly (propylene) nanocomposites containing various carbon nanostructures. *Macromolecular Chemistry and Physics*. 2011; 212(22):2429-2438.

- (55) Zhang X, Yan X, Guo J, Liu Z, Jiang D, He Q, et al. Polypyrrole doped epoxy resin nanocomposites with enhanced mechanical properties and reduced flammability. *Journal of Materials Chemistry C*. 2015; 3(1):162-176.
- (56) Zhang X, He Q, Gu H, Colorado HA, Wei S, Guo Z. Flame-retardant electrical conductive nanopolymers based on bisphenol F epoxy resin reinforced with nano polyanilines. *ACS applied materials & interfaces*. 2013; 5(3):898-910.
- (57) Lak A. *Synthesis and Characterization of Magnetic Iron Oxide Nanoparticles*. Technical University of Braunschweig; 2013 .
- (58) Cullity BD, Graham CD. Introduction to Magnetic Materials. 2nd ed. NJ, USA: John Wiley & Sons; 2011. p. 361-365.
- (59) Leslie-Pelecky DL, Rieke RD. Magnetic properties of nanostructured materials. *Chemistry of materials*. 1996; 8(8):1770-1783.
- (60) Jeong U, Teng X, Wang Y, Yang H, Xia Y. Superparamagnetic colloids: controlled synthesis and niche applications. *Advanced Materials*. 2007; 19(1):33-60.
- (61) Panzarasa G, Soliveri G, Pifferi V. Tuning the electrochemical properties of silicon wafer by grafted-from micropatterned polymer brushes. *Journal of Materials Chemistry C*. 2016; 4(2):340-347.
- (62) Cobo Sánchez C, Wähländer M, Taylor N, Fogelström L, Malmström E. Novel Nanocomposites of Poly (lauryl methacrylate)-Grafted Al₂O₃ Nanoparticles in LDPE. *ACS applied materials & interfaces*. 2015; 7(46):25669-25678.
- (63) Krysiak E, Wypych-Puszkarcz A, Krysiak K, Nowaczyk G, Makrocka-Rydzik M, Jurga S, et al. Core-shell system based on titanium dioxide with elevated value of dielectric permittivity: Synthesis and characterization. *Synthetic Metals*. 2015; 209:150-157.
- (64) Joumaa N, Toussay P, Lansalot M, Elaissari A. Surface modification of iron oxide nanoparticles by a phosphate-based macromonomer and further encapsulation into submicrometer polystyrene particles by miniemulsion polymerization. *Journal of Polymer Science Part A: Polymer Chemistry*. 2008; 46(1):327-340.
- (65) Fiabane J, Prentice P, Pancholi K. High yielding microbubble production method. *BioMed Research International*. 2016; 2016.
- (66) Roth CB, Dutcher JR. Glass transition and chain mobility in thin polymer films. *Journal of Electroanalytical Chemistry*. 2005; 584(1):13-22.
- (67) Ahmed AS, Ramanujan RV. Curie temperature controlled self-healing magnet-polymer composites. *Journal of Materials Research*. 2015; 30(7):946-958.
- (68) Vijayaakumar R, Koltypin Y, Cohen YS, Cohen Y, Aurbach D, Palchik O, et al. Preparation of amorphous magnetite nanoparticles embedded in polyvinyl alcohol using ultrasound radiation. *Journal of Materials Chemistry*. 2000; 10(5):1125-1129.
- (69) Park S, Bernet N, De La Roche S, Hahn H. Processing of iron oxide-epoxy vinyl ester nanocomposites. *Journal of Composite Materials*. 2003; 37(5):465-476.
- (70) Hetti M, Lai WC, Tse CW, Cheung CK, Lee YF, Lai YM, et al. *Release film with enhanced mechanical properties and method in preparing thereof*. 2015; .
- (71) Lao S, Ho W, Ngyuen K and Koo J. Micro Structural Analysis of Nylon 11 Nanocomposites. Micro Structural Analysis of Nylon 11 Nanocomposites. *Proceedings of the 37th ISTC Conference*; 2005.
- (72) Koo JH, Pilato LA, Wissler GE. Polymer nanostructured materials for propulsion systems. *Journal of Spacecraft and Rockets*. 2007; 44(6):1250-1262.
- (73) Koo J, Pilato L, Wissler G, Lee A, Abusafieh A and Weispfenning J. Epoxy nanocomposites for carbon fiber reinforced polymer matrix composites. Epoxy

- nanocomposites for carbon fiber reinforced polymer matrix composites. *Proceedings of SAMPE Symposium, Covina, CA*; 2005.
- (74) Chen C. Virginia Tech; 2011 .
- (75) Chen Y, Zhou S, Yang H, Wu L. Structure and properties of polyurethane/nanosilica composites. *Journal of Applied Polymer Science*. 2005; 95(5):1032-1039.
- (76) Tang J, Wang Y, Liu H, Xia Y, Schneider B. Effect of processing on morphological structure of polyacrylonitrile matrix nano-ZnO composites. *Journal of Applied Polymer Science*. 2003; 90(4):1053-1057.
- (77) Ma D, Hugener TA, Siegel RW, Christerson A, Mårtensson E, Önnby C, et al. Influence of nanoparticle surface modification on the electrical behaviour of polyethylene nanocomposites. *Nanotechnology*. 2005; 16(6):724.
- (78) Usuki A, Kawasumi M, Kojima Y, Okada A, Kurauchi T. Synthesis and properties of diamine-modified nylon 6-clay hybrid. *Kobunshi ronbunshu (Tokyo)*. 1995; 52(7):440-444.
- (79) Spitalsky Z, Tsoukleri G, Tasis D, Krontiras C, Georga S, Galiotis C. High volume fraction carbon nanotube-epoxy composites. *Nanotechnology*. 2009; 20(40):405702.
- (80) Laurent S, Forge D, Port M, Roch A, Robic C, Vander Elst L, et al. Magnetic iron oxide nanoparticles: synthesis, stabilization, vectorization, physicochemical characterizations, and biological applications. *Chemical reviews*. 2008; 108(6):2064-2110.
- (81) Khodabakhshi K. *Anionic polymerisation of caprolactam: an approach to optimising the polymerisation condition to be used in the jetting process*. Loughborough University; 2011 .
- (82) Pop E, Mann D, Wang Q, Goodson K, Dai H. Thermal conductance of an individual single-wall carbon nanotube above room temperature. *Nano letters*. 2006; 6(1):96-100.
- (83) Jana SC, Jain S. Dispersion of nanofillers in high performance polymers using reactive solvents as processing aids. *Polymer*. 2001; 42(16):6897-6905.
- (84) Zhang B, Xie C, Hu J, Wang H, Gui Y. Novel 1-3 metal nanoparticle/polymer composites induced by hybrid external fields. *Composites Science and Technology*. 2006; 66(11-12):1558-1563.
- (85) Hussain F, Hojjati M, Okamoto M, Gorga RE. Polymer-matrix nanocomposites, processing, manufacturing, and application: an overview. *Journal of Composite Materials*. 2006; 40(17):1511-1575.
- (86) Zhang M, Singh RP. Mechanical reinforcement of unsaturated polyester by Al₂O₃ nanoparticles. *Materials Letters*. 2004; 58(3-4):408-412.
- (87) Solans C, Izquierdo P, Nolla J, Azemar N, Garcia-Celma MJ. Nano-emulsions. *Current opinion in colloid & interface science*. 2005; 10(3-4):102-110.
- (88) Hong R, Fischer NO, Emrick T, Rotello VM. Surface PEGylation and ligand exchange chemistry of FePt nanoparticles for biological applications. *Chemistry of materials*. 2005; 17(18):4617-4621.
- (89) Lu A, Salabas Ee, Schüth F. Magnetic nanoparticles: synthesis, protection, functionalization, and application. *Angewandte Chemie International Edition*. 2007; 46(8):1222-1244.
- (90) Liu X, Guan Y, Ma Z, Liu H. Surface modification and characterization of magnetic polymer nanospheres prepared by miniemulsion polymerization. *Langmuir*. 2004; 20(23):10278-10282.

- (91) Sperling RA, Parak WJ. Surface modification, functionalization and bioconjugation of colloidal inorganic nanoparticles. *Philosophical Transactions of the Royal Society A: Mathematical, Physical and Engineering Sciences*. 2010; 368(1915):1333-1383.
- (92) Ito A, Shinkai M, Honda H, Kobayashi T. Medical application of functionalized magnetic nanoparticles. *Journal of bioscience and bioengineering*. 2005; 100(1):1-11.
- (93) Ding H, Zhang Y, Wang S, Xu J, Xu S, Li G. Fe₃O₄@ SiO₂ core/shell nanoparticles: the silica coating regulations with a single core for different core sizes and shell thicknesses. *Chemistry of Materials*. 2012; 24(23):4572-4580.
- (94) Kobayashi Y, Horie M, Konno M, Rodríguez-González B, Liz-Marzán LM. Preparation and properties of silica-coated cobalt nanoparticles. *The Journal of Physical Chemistry B*. 2003; 107(30):7420-7425.
- (95) Ghosh Chaudhuri R, Paria S. Core/shell nanoparticles: classes, properties, synthesis mechanisms, characterization, and applications. *Chemical reviews*. 2012; 112(4):2373-2433.
- (96) Wu W, Wu Z, Yu T, Jiang C, Kim W. Recent progress on magnetic iron oxide nanoparticles: synthesis, surface functional strategies and biomedical applications. *Science and technology of advanced materials*. 2015; .
- (97) Reddy LH, Arias JL, Nicolas J, Couvreur P. Magnetic nanoparticles: design and characterization, toxicity and biocompatibility, pharmaceutical and biomedical applications. *Chemical reviews*. 2012; 112(11):5818-5878.
- (98) Palanisamy S, Wang Y. Superparamagnetic iron oxide nanoparticulate system: synthesis, targeting, drug delivery and therapy in cancer. *Dalton transactions*. 2019; 48(26):9490-9515.
- (99) Sobal NS, Hilgendorff M, Moehwald H, Giersig M, Spasova M, Radetic T, et al. Synthesis and structure of colloidal bimetallic nanocrystals: the non-alloying system Ag/Co. *Nano Letters*. 2002; 2(6):621-624.
- (100) Du M, Liu Q, Huang C, Qiu X. One-step synthesis of magnetically recyclable Co@BN core-shell nanocatalysts for catalytic reduction of nitroarenes. *RSC advances*. 2017; 7(56):35451-35459.
- (101) Mamani J, Costa-Filho A, Cornejo D, Vieira E, Gamarra L. Synthesis and characterization of magnetite nanoparticles coated with lauric acid. *Materials Characterization*. 2013; 81:28-36.
- (102) Ghazanfari MR, Kashefi M, Shams SF, Jaafari MR. Perspective of Fe₃O₄ nanoparticles role in biomedical applications. *Biochemistry research international*. 2016; 2016.
- (103) Boyer C, Whittaker MR, Bulmus V, Liu J, Davis TP. The design and utility of polymer-stabilized iron-oxide nanoparticles for nanomedicine applications. *NPG Asia Materials*. 2010; 2(1):23-30.
- (104) Mahmoudi M, Sant S, Wang B, Laurent S, Sen T. Superparamagnetic iron oxide nanoparticles (SPIONs): development, surface modification and applications in chemotherapy. *Advanced Drug Delivery Reviews*. 2011; 63(1-2):24-46.
- (105) Sun T, Zhang YS, Pang B, Hyun DC, Yang M, Xia Y. Engineered nanoparticles for drug delivery in cancer therapy. *Angewandte Chemie International Edition*. 2014; 53(46):12320-12364.
- (106) Sapsford KE, Algar WR, Berti L, Gemmill KB, Casey BJ, Oh E, et al. Functionalizing nanoparticles with biological molecules: developing chemistries that facilitate nanotechnology. *Chemical reviews*. 2013; 113(3):1904-2074.

- (107) Liu C, Sahoo SL, Tsao M. Acridine orange coated magnetic nanoparticles for nucleus labeling and DNA adsorption. *Colloids and Surfaces B: Biointerfaces*. 2014; 115:150-156.
- (108) Zhao H, Saatchi K, Häfeli UO. Preparation of biodegradable magnetic microspheres with poly (lactic acid)-coated magnetite. *Journal of Magnetism and Magnetic Materials*. 2009; 321(10):1356-1363.
- (109) Wang L, Neoh K, Kang E, Shuter B, Wang S. Biodegradable magnetic-fluorescent magnetite/poly (dl-lactic acid-co- α , β -malic acid) composite nanoparticles for stem cell labeling. *Biomaterials*. 2010; 31(13):3502-3511.
- (110) Zhang M, O'Connor CJ. Synthesis and Characterization of PMMA Coated Magnetite Nanocomposites by Emulsion Polymerization. *MRS Online Proceedings Library Archive*. 2007; 1032.
- (111) He N, Wang Z and Li S. DNA separation and amplification application of (Fe₃O₄/PMMA)/SiO₂ nanoparticles with core-shell structure. DNA separation and amplification application of (Fe₃O₄/PMMA)/SiO₂ nanoparticles with core-shell structure. *ABSTRACTS OF PAPERS OF THE AMERICAN CHEMICAL SOCIETY: AMER CHEMICAL SOC 1155 16TH ST, NW, WASHINGTON, DC 20036 USA*; 2006.
- (112) Vallooran JJ, Bolisetty S, Mezzenga R. Macroscopic alignment of lyotropic liquid crystals using magnetic nanoparticles. *Advanced Materials*. 2011; 23(34):3932-3937.
- (113) Ma Y, Wu S, Wu T, Chang Y, Hua M, Chen J. Magnetically targeted thrombolysis with recombinant tissue plasminogen activator bound to polyacrylic acid-coated nanoparticles. *Biomaterials*. 2009; 30(19):3343-3351.
- (114) Padwal P, Bandyopadhyaya R, Mehra S. Polyacrylic acid-coated iron oxide nanoparticles for targeting drug resistance in mycobacteria. *Langmuir*. 2014; 30(50):15266-15276.
- (115) Sun C, Veiseh O, Gunn J, Fang C, Hansen S, Lee D, et al. In vivo MRI detection of gliomas by chlorotoxin-conjugated superparamagnetic nanoprobe. *Small*. 2008; 4(3):372-379.
- (116) Lee H, Yu MK, Park S, Moon S, Min JJ, Jeong YY, et al. Thermally cross-linked superparamagnetic iron oxide nanoparticles: synthesis and application as a dual imaging probe for cancer in vivo. *Journal of the American Chemical Society*. 2007; 129(42):12739-12745.
- (117) Ito A, Hibino E, Kobayashi C, Terasaki H, Kagami H, Ueda M, et al. Construction and delivery of tissue-engineered human retinal pigment epithelial cell sheets, using magnetite nanoparticles and magnetic force. *Tissue engineering*. 2005; 11(3-4):489-496.
- (118) Răcuciu M, Creangă D, Airinei A. Citric-acid-coated magnetite nanoparticles for biological applications. *The European Physical Journal E*. 2006; 21(2):117-121.
- (119) De Sousa ME, Fernandez van Raap, Marcela B, Rivas PC, Mendoza Zelis P, Girardin P, Pasquevich GA, et al. Stability and relaxation mechanisms of citric acid coated magnetite nanoparticles for magnetic hyperthermia. *The Journal of Physical Chemistry C*. 2013; 117(10):5436-5445.
- (120) Cheraghpour E, Javadpour S, Mehdizadeh AR. Citrate capped superparamagnetic iron oxide nanoparticles used for hyperthermia therapy. 2012; .
- (121) Zaloga J, Janko C, Nowak J, Matuszak J, Knaup S, Eberbeck D, et al. Development of a lauric acid/albumin hybrid iron oxide nanoparticle system with improved biocompatibility. *International journal of nanomedicine*. 2014; 9:4847-4866.

- (122) Shete P, Patil R, Tiwale B, Pawar S. Water dispersible oleic acid-coated Fe₃O₄ nanoparticles for biomedical applications. *Journal of Magnetism and Magnetic Materials*. 2015; 377:406-410.
- (123) Talelli M, Rijcken CJ, Lammers T, Seevinck PR, Storm G, van Nostrum CF, et al. Superparamagnetic iron oxide nanoparticles encapsulated in biodegradable thermosensitive polymeric micelles: toward a targeted nanomedicine suitable for image-guided drug delivery. *Langmuir*. 2009; 25(4):2060-2067.
- (124) Huang C, Tang Z, Zhou Y, Zhou X, Jin Y, Li D, et al. Magnetic micelles as a potential platform for dual targeted drug delivery in cancer therapy. *International journal of pharmaceutics*. 2012; 429(1-2):113-122.
- (125) Li H, Yan K, Shang Y, Shrestha L, Liao R, Liu F, et al. Folate-bovine serum albumin functionalized polymeric micelles loaded with superparamagnetic iron oxide nanoparticles for tumor targeting and magnetic resonance imaging. *Acta biomaterialia*. 2015; 15:117-126.
- (126) Araya T, Kasahara K, Nishikawa S, Kimura H, Sone T, Nagae H, et al. Antitumor effects of inductive hyperthermia using magnetic ferucarbotran nanoparticles on human lung cancer xenografts in nude mice. *OncoTargets and therapy*. 2013; 6:237-242.
- (127) Sen T, Bruce IJ. Mesoporous silica-magnetite nanocomposites: fabrication, characterisation and applications in biosciences. *Microporous and Mesoporous Materials*. 2009; 120(3):246-251.
- (128) Souza K, Ardisson J, Sousa E. Study of mesoporous silica/magnetite systems in drug controlled release. *Journal of Materials Science: Materials in Medicine*. 2009; 20(2):507.
- (129) Qu L, Tie S. Mesoporous silica-coated superparamagnetic magnetite functionalized with CuO and its application as a desulfurizer. *Microporous and Mesoporous Materials*. 2009; 117(1-2):402-405.
- (130) Yang P, Quan Z, Hou Z, Li C, Kang X, Cheng Z, et al. A magnetic, luminescent and mesoporous core-shell structured composite material as drug carrier. *Biomaterials*. 2009; 30(27):4786-4795.
- (131) Kim J, Kim HS, Lee N, Kim T, Kim H, Yu T, et al. Multifunctional uniform nanoparticles composed of a magnetite nanocrystal core and a mesoporous silica shell for magnetic resonance and fluorescence imaging and for drug delivery. *Angewandte Chemie*. 2008; 120(44):8566-8569.
- (132) Sebastianelli A, Sen T, Bruce IJ. Extraction of DNA from soil using nanoparticles by magnetic bioseparation. *Letters in applied microbiology*. 2008; 46(4):488-491.
- (133) Zhao X, Shi Y, Wang T, Cai Y, Jiang G. Preparation of silica-magnetite nanoparticle mixed hemimicelle sorbents for extraction of several typical phenolic compounds from environmental water samples. *Journal of Chromatography A*. 2008; 1188(2):140-147.
- (134) Chiang C, Sung C, Chen C. Application of silica-magnetite nanocomposites to the isolation of ultrapure plasmid DNA from bacterial cells. *Journal of Magnetism and Magnetic Materials*. 2006; 305(2):483-490.
- (135) Duan H, Kuang M, Wang X, Wang YA, Mao H, Nie S. Reexamining the effects of particle size and surface chemistry on the magnetic properties of iron oxide nanocrystals: new insights into spin disorder and proton relaxivity. *The Journal of Physical Chemistry C*. 2008; 112(22):8127-8131.
- (136) LaConte LE, Nitin N, Zurkiya O, Caruntu D, O'Connor CJ, Hu X, et al. Coating thickness of magnetic iron oxide nanoparticles affects R₂ relaxivity. *Journal of Magnetic Resonance Imaging: An Official Journal of the International Society for Magnetic Resonance in Medicine*. 2007; 26(6):1634-1641.

- (137) Lopez JA, González F, Bonilla FA, Zambrano G, Gómez ME. Synthesis and characterization of Fe₃O₄ magnetic nanofluid. *Revista Latinoamericana de Metalurgia y Materiales*. 2010; 30(1):60-66.
- (138) Voit W, Kim D, Zapka W, Muhammed M, Rao K. Magnetic behavior of coated superparamagnetic iron oxide nanoparticles in ferrofluids. *MRS Online Proceedings Library Archive*. 2001; 676.
- (139) Sonmez M, Georgescu M, Alexandrescu L, Gurau D, Ficai A, Ficai D, et al. Synthesis and applications of Fe₃O₄/SiO₂ core-shell materials. *Current pharmaceutical design*. 2015; 21(37):5324-5335.
- (140) Stöber W, Fink A, Bohn E. Controlled growth of monodisperse silica spheres in the micron size range. *Journal of colloid and interface science*. 1968; 26(1):62-69.
- (141) Helmi Rashid Farimani M, Shahtahmassebi N, Rezaee Roknabadi M, Ghows N. Synthesis and study of structural and magnetic properties of superparamagnetic Fe₃O₄@SiO₂ core/shell nanocomposite for biomedical applications. *Nanomedicine Journal*. 2014; 1(2):71-78.
- (142) Narita A, Naka K, Chujo Y. Facile control of silica shell layer thickness on hydrophilic iron oxide nanoparticles via reverse micelle method. *Colloids and Surfaces A: Physicochemical and Engineering Aspects*. 2009; 336(1-3):46-56.
- (143) Lu C, Hung Y, Hsiao J, Yao M, Chung T, Lin Y, et al. Bifunctional magnetic silica nanoparticles for highly efficient human stem cell labeling. *Nano letters*. 2007; 7(1):149-154.
- (144) Van Ewijk G, Vroege G, Philipse A. Convenient preparation methods for magnetic colloids. *Journal of Magnetism and Magnetic Materials*. 1999; 201(1-3):31-33.
- (145) Deng Y, Wang C, Hu J, Yang W, Fu S. Investigation of formation of silica-coated magnetite nanoparticles via sol-gel approach. *Colloids and Surfaces A: Physicochemical and Engineering Aspects*. 2005; 262(1-3):87-93.
- (146) Barnakov YA, Yu MH, Rosenzweig Z. Manipulation of the magnetic properties of magnetite-silica nanocomposite materials by controlled stober synthesis. *Langmuir*. 2005; 21(16):7524-7527.
- (147) Gupta AK, Wells S. Surface-modified superparamagnetic nanoparticles for drug delivery: preparation, characterization, and cytotoxicity studies. *IEEE transactions on nanobioscience*. 2004; 3(1):66-73.
- (148) Santra S, Tapeç R, Theodoropoulou N, Dobson J, Hebard A, Tan W. Synthesis and characterization of silica-coated iron oxide nanoparticles in microemulsion: the effect of nonionic surfactants. *Langmuir*. 2001; 17(10):2900-2906.
- (149) Faraji M, Yamini Y, Rezaee M. Magnetic nanoparticles: synthesis, stabilization, functionalization, characterization, and applications. *Journal of the Iranian Chemical Society*. 2010; 7(1):1-37.
- (150) Wei S, Wang Q, Zhu J, Sun L, Lin H, Guo Z. Multifunctional composite core-shell nanoparticles. *Nanoscale*. 2011; 3(11):4474-4502.
- (151) Glover AL, Bennett JB, Pritchett JS, Nikles SM, Nikles DE, Nikles JA, et al. Magnetic heating of iron oxide nanoparticles and magnetic micelles for cancer therapy. *IEEE Transactions on Magnetics*. 2012; 49(1):231-235.
- (152) Xu Q, Liu Y, Su S, Li W, Chen C, Wu Y. Anti-tumor activity of paclitaxel through dual-targeting carrier of cyclic RGD and transferrin conjugated hyperbranched copolymer nanoparticles. *Biomaterials*. 2012; 33(5):1627-1639.
- (153) Su H, Liu Y, Wang D, Wu C, Xia C, Gong Q, et al. Amphiphilic starlike dextran wrapped superparamagnetic iron oxide nanoparticle clusters as effective magnetic resonance imaging probes. *Biomaterials*. 2013; 34(4):1193-1203.

- (154) Sun S, Zeng H, Robinson DB, Raoux S, Rice PM, Wang SX, et al. Monodisperse mfe₂o₄ (m= fe, co, mn) nanoparticles. *Journal of the American Chemical Society*. 2004; 126(1):273-279.
- (155) Ueda K, Yamada K, Nakai M, Matsuda T, Hosoda M, Tai K. Synthesis of high molecular weight nylon 6 by anionic polymerization of ε-caprolactam. *Polymer Journal*. 1996; 28(5):446-451.
- (156) Yeh J, Kuo J, Chen C. Adiabatic anionic polymerization of caprolactam in the presence of N-acylated caprolactam macroactivator: Kinetic study. *Journal of Applied Polymer Science*. 1993; 50(10):1671-1681.
- (157) Mateva R, Dencheva N. On the behavior of organophosphorus lactam derivatives during anionic polymerization of ε-caprolactam. *Journal of Polymer Science Part A: Polymer Chemistry*. 1992; 30(7):1449-1462.
- (158) Greenley R, Stauffer J, Kurz J. The kinetic equation for the initiated, anionic polymerization of η-caprolactam. *Macromolecules*. 1969; 2(6):561-567.
- (159) Barmi M, Assempour H, Nazockdast H. Preparation and Characterization of HMW PA 6 via Anionic Polymerization of ε-Caprolactam by Using a Mixture of Di- and Tri-functional Chain Initiators. *International Polymer Processing*. 2006; 21(3):230-238.
- (160) Malkin AY, Ivanova S, Frolov V, Ivanova A, Andrianova Z. Kinetics of anionic polymerization of lactams.(Solution of non-isothermal kinetic problems by the inverse method). *Polymer*. 1982; 23(12):1791-1800.
- (161) Bakkali-Hassani C, Tunc D, Roos K, Planes M, Lecomte P, Carlotti S. Simultaneous Anionic Ring-Opening and Condensation Reactions for the Synthesis of Aliphatic-N-Alkyl Aromatic Copolyamides. *Macromolecules*. 2017; 50(1):175-181.
- (162) Siesler HW. Infrared and Raman spectroscopy of polymers. *Practical spectroscopy*; v.4. 1980; .
- (163) Arimoto H. α-γ Transition of nylon 6. *Journal of Polymer Science Part A: General Papers*. 1964; 2(5):2283-2295.
- (164) Šebenda J, Kraliček J. Effect of imides on the alkaline polymerisation of caprolactam. *Collection of Czechoslovak Chemical Communications*. 1958; 23(4):766-767.
- (165) Aharoni SM. *n-Nylons: their synthesis, structure, and properties*. : Wiley-Blackwell; 1997.
- (166) Tabb D, Koenig J. Fourier transform infrared study of plasticized and unplasticized poly (vinyl chloride). *Macromolecules*. 1975; 8(6):929-934.
- (167) Willbourn A. Polymethylene and the structure of polyethylene: Study of short-chain branching, its nature and effects. *Journal of polymer science*. 1959; 34(127):569-597.
- (168) Lin S, Bulkin B, Pearce E. Epoxy resins. III. Application of fourier transform IR to degradation studies of epoxy systems. *Journal of Polymer Science: Polymer Chemistry Edition*. 1979; 17(10):3121-3148.
- (169) Woodbrey JC and Thementozzi Q. Characterization of stereochemical regulation in polypropylenes. Characterization of stereochemical regulation in polypropylenes. *Journal of Polymer Science Part C: Polymer Symposia*: Wiley Online Library; 1965. p. 113-136.
- (170) Blaine R. *Determination of polymer crystallinity by DSC.TA Instruments*. 2011; .
- (171) Instruments T. Estimation of Polymer Lifetime by TGA Decomposition Kinetics: Thermal Analysis Application Brief. 2007; .
- (172) Pfannmöller M, Kowalsky W, Schröder RR. Visualizing physical, electronic, and optical properties of organic photovoltaic cells. *Energy & Environmental Science*. 2013; 6(10):2871-2891.

- (173) van-Bavel SS, Sourty E, de With G, Loos J. Three-dimensional nanoscale organization of bulk heterojunction polymer solar cells. *Nano letters*. 2009; 9(2):507-513.
- (174) DeLongchamp DM, Kline RJ, Herzing A. Nanoscale structure measurements for polymer-fullerene photovoltaics. *Energy & Environmental Science*. 2012; 5(3):5980-5993.
- (175) Hedley GJ, Ruseckas A, Samuel ID. Light harvesting for organic photovoltaics. *Chemical reviews*. 2017; 117(2):796-837.
- (176) Pfannmoller M, Flugge H, Benner G, Wacker I, Sommer C, Hanselmann M, et al. Visualizing a homogeneous blend in bulk heterojunction polymer solar cells by analytical electron microscopy. *Nano letters*. 2011; 11(8):3099-3107.
- (177) Moon JS, Takacs CJ, Sun Y, Heeger AJ. Spontaneous formation of bulk heterojunction nanostructures: Multiple routes to equivalent morphologies. *Nano letters*. 2011; 11(3):1036-1039.
- (178) Schnablegger H, Singh Y, editors. *The SAXS guide: getting acquainted with the principles*. 4th ed. Austria: Anton Paar GmbH; 2017.
- (179) Willmott P. *An introduction to synchrotron radiation: techniques and applications*. : John Wiley & Sons; 2019.
- (180) Björn L. *Characterisation of Injection Moulded Polymer Materials using SAXS and WAXS*. 2018; .
- (181) Hino K, Shingai R, Morita T, Toku K, Hirano T, Yoshikawa H, et al. Size distribution of gold nanoparticles covered with thiol-terminated cyanobiphenyl-type liquid crystal molecules studied with small-angle X-ray scattering and TEM. *Chemical Physics Letters*. 2008; 460(1-3):173-177.
- (182) Piiadov V, Ares de Araújo E, Oliveira Neto M, Craievich AF, Polikarpov I. SAXSMoW 2.0: Online calculator of the molecular weight of proteins in dilute solution from experimental SAXS data measured on a relative scale. *Protein Science*. 2019; 28(2):454-463.
- (183) Speakman SA. Estimating crystallite size using XRD. *MIT Center for Materials Science and Engineering*. 2014; :03-08.
- (184) Sager RE. Quantum Design—a Brief History of D Company Successful in Superconductivity. 2010; .
- (185) Clarke J. SQUIDS: theory and practice. *The new superconducting electronics*. : Springer; 1993. p. 123-180.
- (186) Dodds N, Pancholi K, Jha V, Tariq SF and Latta J. In Situ Investigation of Microstructural Changes In Thermoplastic Composite Pipe under Compressive Load. In Situ Investigation of Microstructural Changes In Thermoplastic Composite Pipe under Compressive Load. *International Conference on Offshore Mechanics and Arctic Engineering*: American Society of Mechanical Engineers; 2014. p. V06AT04A040.
- (187) Stokes-Griffin C, Compston P. An inverse model for optimisation of laser heat flux distributions in an automated laser tape placement process for carbon-fibre/PEEK. *Composites Part A: Applied Science and Manufacturing*. 2016; 88:190-197.
- (188) Campelj S, Makovec D, Drogenik M. Preparation and properties of water-based magnetic fluids. *Journal of Physics: Condensed Matter*. 2008; 20(20):204101.
- (189) Iler KR. The chemistry of silica. *Solubility, Polymerization, Colloid and Surface Properties and Biochemistry of Silica*. 1979; .
- (190) Rades S, Hodoroaba V, Salge T, Wirth T, Lobera MP, Labrador RH, et al. High-resolution imaging with SEM/T-SEM, EDX and SAM as a combined methodical approach

for morphological and elemental analyses of single engineered nanoparticles. *Rsc Advances*. 2014; 4(91):49577-49587.

(191) Rezaei G, Naghipour A, Fakhri A. Catalytic performance studies of new Pd and Pt Schiff base complexes covalently immobilized on magnetite nanoparticles as the environmentally friendly and magnetically recoverable nanocatalyst in C–C cross coupling reactions. *Catalysis Letters*. 2018; 148(2):732-744.

(192) Gojny FH, Nastalczyk J, Roslaniec Z, Schulte K. Surface modified multi-walled carbon nanotubes in CNT/epoxy-composites. *Chemical physics letters*. 2003; 370(5-6):820-824.

(193) Liu L, Wagner HD. Rubbery and glassy epoxy resins reinforced with carbon nanotubes. *Composites Science and Technology*. 2005; 65(11-12):1861-1868.

(194) Velasco-Santos C, Martínez-Hernández AL, Fisher FT, Ruoff R, Castaño VM. Improvement of thermal and mechanical properties of carbon nanotube composites through chemical functionalization. *Chemistry of materials*. 2003; 15(23):4470-4475.

(195) Paiva M, Zhou B, Fernando K, Lin Y, Kennedy J, Sun Y. Mechanical and morphological characterization of polymer–carbon nanocomposites from functionalized carbon nanotubes. *Carbon*. 2004; 42(14):2849-2854.

(196) Coleman JN, Khan U, Gun'ko YK. Mechanical reinforcement of polymers using carbon nanotubes. *Advanced Materials*. 2006; 18(6):689-706.

(197) Balazs AC, Emrick T, Russell TP. Nanoparticle polymer composites: where two small worlds meet. *Science (New York, N.Y.)*. 2006; 314(5802):1107-1110.

(198) Ito H, Russell TP, Wignall G. Interactions in mixtures of poly (ethylene oxide) and poly (methyl methacrylate). *Macromolecules*. 1987; 20(9):2213-2220.

(199) Blaine RL. Thermal applications note. *Polymer Heats of Fusion*. 2002 .

(200) Braun E, Levin BC. Nylons: A review of the literature on products of combustion and toxicity. *Fire and Materials*. 1987; 11(2):71-88.

(201) Mottus EH, Hedrick RM, Butler JM, inventors. Anonymous *Preparation of polycaprolactam using n-acyl activators*. U.S. 1962 .

(202) Navale S, Khuspe G, Chougule M, Patil V. Camphor sulfonic acid doped PPy/ α -Fe₂O₃ hybrid nanocomposites as NO₂ sensors. *RSC Advances*. 2014; 4(53):27998-28004.

(203) Ngwuluka N. Application of in situ polymerization for design and development of oral drug delivery systems. *Aaps Pharmscitech*. 2010; 11(4):1603-1611.

(204) Pockett J. *Crystallinity in linear polyamides: a study using melt blending with small-molecule diluents*. University of South Australia; 2004 .

(205) Yang F, Zhao M, Zheng B, Xiao D, Wu L, Guo Y. Influence of pH on the fluorescence properties of graphene quantum dots using ozonation pre-oxide hydrothermal synthesis. *Journal of Materials Chemistry*. 2012; 22(48):25471-25479.

(206) Larkin P. IR and Raman spectra—Structure Correlations: Characteristic Group Frequencies. *Infrared and Raman spectroscopy*. 2011; :73-115.

(207) Harrats C, Groeninckx G. Features, questions and future challenges in layered silicates clay nanocomposites with semicrystalline polymer matrices. *Macromolecular Rapid Communications*. 2008; 29(1):14-26.

(208) Tunc D, Boucekif H, Améduri B, Jérôme C, Desbois P, Lecomte P, et al. Synthesis of aliphatic polyamide bearing fluorinated groups from ϵ -caprolactam and modified cyclic lysine. *European Polymer Journal*. 2015; 71:575-584.

(209) Thomas S, Rouxel D, Ponnamma D. *Spectroscopy of polymer Nanocomposites*. : William Andrew; 2016.

- (210) Doi M, Edwards SF. The theory of polymer dynamics. : oxford university press; 1988. p. 140-176.
- (211) Teixeira J. Small-angle scattering by fractal systems. *Journal of Applied Crystallography*. 1988; 21(6):781-785.
- (212) Porod G, Glatter O, Kratky O. Small angle X-ray scattering. by O.Glatter and O.Kratky, Academic Press, London. 1982; :17.
- (213) Scott C. *Nylon-6 information and properties*. [homepage on the Internet]. 2001 cited 2019 February/20]. Available from: <http://www.polymerprocessing.com/polymers/PA6.html>.
- (214) Rittigstein P, Torkelson JM. Polymer–nanoparticle interfacial interactions in polymer nanocomposites: confinement effects on glass transition temperature and suppression of physical aging. *Journal of Polymer Science Part B: Polymer Physics*. 2006; 44(20):2935-2943.
- (215) Rybníkář F, Geil P. Melting and recrystallization of PA-6/PA-66 blends. *Journal of Applied Polymer Science*. 1993; 49(7):1175-1188.
- (216) Pashaei S, Avval MM, Syed AA. Thermal degradation kinetics of nylon6/GF/crysnano nanoclay nanocomposites by TGA. *Chemical Industry and Chemical Engineering Quarterly/CICEQ*. 2011; 17(2):141-151.
- (217) Fornes T, Paul D. Crystallization behavior of nylon 6 nanocomposites. *Polymer*. 2003; 44(14):3945-3961.
- (218) Porter R. Macromolecular physics, volume 3—crystal melting, Bernhard Wunderlich. 1980; :363.
- (219) Navarro-Pardo F, Martínez-Barrera G, Martínez-Hernández A, Castaño V, Rivera-Armenta J, Medellín-Rodríguez F, et al. Effects on the thermo-mechanical and crystallinity properties of nylon 6, 6 electrospun fibres reinforced with one dimensional (1D) and two dimensional (2D) carbon. *Materials*. 2013; 6(8):3494-3513.
- (220) Pallon L, Hoang A, Pourrahimi A, Hedenqvist MS, Nilsson F, Gubanski S, et al. The impact of MgO nanoparticle interface in ultra-insulating polyethylene nanocomposites for high voltage DC cables. *Journal of Materials Chemistry A*. 2016; 4(22):8590-8601.
- (221) Barrera G, Tiberto P, Allia P, Bonelli B, Esposito S, Marocco A, et al. Magnetic Properties of Nanocomposites. *Applied Sciences*. 2019; 9(2):212.
- (222) Karna S, Mishra S, Gunapala E, Dubenko I, Malagareddy V, Marasinghe G, et al. Polymer assisted synthesis of FeNi nanoparticles. *arXiv preprint arXiv:1212.3566*. 2012; .
- (223) Cho J, Paul D. Nylon 6 nanocomposites by melt compounding. *Polymer*. 2001; 42(3):1083-1094.
- (224) Jimenez G, Ogata N, Kawai H, Ogihara T. Structure and thermal/mechanical properties of poly (ϵ -caprolactone)-clay blend. *Journal of Applied Polymer Science*. 1997; 64(11):2211-2220.
- (225) Mphahlele K, Ray SS, Kolesnikov A. Self-healing polymeric composite material design, failure analysis and future outlook: a review. *Polymers*. 2017; 9(10):535.
- (226) Guadagno L, Raimondo M, Naddeo C, Longo P, Mariconda A, Binder WH. Healing efficiency and dynamic mechanical properties of self-healing epoxy systems. *Smart Materials and Structures*. 2014; 23(4):045001.
- (227) Kanchanomai C. Time-dependent fracture toughness of fumed silica/epoxy nanocomposites. *Journal of Composite Materials*. 2012; 46(16):1973-1983.
- (228) Yuan Y, Rong M, Zhang M, Yang G, Zhao J. Self-healing of fatigue crack in epoxy materials with epoxy/mercaptan system. *Express Polymer Letters*. 2011; 5(1).

(229) Landesmann A, Seruti CA, Batista EdM. Mechanical Properties of Glass Fiber Reinforced Polymers Members for Structural Applications. *Materials Research*. 2015; 18(6):1372-1383.

(230) Singh J, Kumar M, Kumar S, Mohapatra S. Properties of glass-fiber hybrid composites: a review. *Polymer-Plastics Technology and Engineering*. 2017; 56(5):455-469.

APPENDIX A: MATLAB CODE

The important code blocks that were implemented for the simulated 3D magnetic polymer nanocomposite model generation are listed and briefly discussed herein.

A.1 Main code for taking the radius range and weight percent of the MNPs loading in the polymer matrix.

```
clc, clear
close all
Rmin=0.015; %Minimum Radius
Rmax=0.12; %Maximum Radius
R=[Rmin,Rmax]; %Radius Range
W_Per=1; %Sphere to Cube Weight Percentage
generate_np_2_Particles_with_IR_Single(R,W_Per)
```

A.2 Function for generating the random sized MNPs within the passed value of radius range, for randomly orienting the generated MNPs and calculating the interaction radius.

```
function IR = generate_np_2_Particles_with_IR_Single(ptRrange,ptWp)

ptRrange_low=ptRrange(1); ptRrange_high=ptRrange(2);

L = [0;1;1;0;0];
B = [0;0;1;1;0];
H = [0;0;0;0;0];
H2=H+1;
figure;
hold on;
plot3(L,B,H,'k');
plot3(L,B,H2,'k');

for k=1:length(L)-1
    plot3([L(k);L(k)], [B(k);B(k)], [0;1], 'k');
end

rhoC=920; %Density of the Polymer Matrix (Cube)
rhoS=6080; %Density of the MNPs
Vc=L(2)*B(3)*H2(1);
Wc=Vc*rhoC;
Ws=((ptWp/2)/100)*Wc;
Vs=Ws/rhoS;
```

```

ptRads(1)=ptRrange_low + (ptRrange_high-ptRrange_low).*rand(1,1);
ptsIn(1,1)=(L(1)+ptRads(1)) + ((L(2)-ptRads(1))-(L(1)+ptRads(1)))...
.*rand(1,1);
ptsIn(1,2)=(B(1)+ptRads(1)) + ((B(3)-ptRads(1))-(B(1)+ptRads(1)))...
.*rand(1,1);
ptsIn(1,3)=(H(1)+ptRads(1)) + ((H2(1)-ptRads(1))-(H(1)+ptRads(1)))...
.*rand(1,1);
Vst=(4*pi*(ptRads(1)^3)/3);
i=2;
err1=0; err2=0;
while err1==0
    while err2==0
        ptRads(i)=ptRrange_low + (ptRrange_high-ptRrange_low).*rand(1,1);
        ptsIn(i,1)=(L(1)+ptRads(i)) + ((L(2)-ptRads(i))-...
(L(1)+ptRads(i))).*rand(1,1);
        ptsIn(i,2)=(B(1)+ptRads(i)) + ((B(3)-ptRads(i))-...
(B(1)+ptRads(i))).*rand(1,1);
        ptsIn(i,3)=(H(1)+ptRads(i)) + ((H2(1)-ptRads(i))-...
(H(1)+ptRads(i))).*rand(1,1);
        for j=1:i-1
            D=sqrt(((ptsIn(i,1)-ptsIn(j,1))^2)+((ptsIn(i,2)...
-ptsIn(j,2))^2)+((ptsIn(i,3)-ptsIn(j,3))^2));
            Rt=ptRads(i)+ptRads(j);
            if D<Rt
                err2=0;
                break
            else
                err2=1;
            end
        end
    end
    err2=0;
    Vst=Vst+(4*pi*(ptRads(i)^3)/3);
    if Vst<Vs
        err1=0;
    else
        err1=1;
    end
    i=i+1;
end

```

A.3 Finally, the code plots the MNPs with the generated radius and their estimated centre coordinates.


```

[nPts, nDims] = size(ptsIn)
% Make a distance map from each point to all others, making sure
%pt A to A is infinite
distMap = sqrt(cell2mat(arrayfun(@(i) sum(bsxfun(@minus,ptsIn(i,:),...
    , ptsIn).^2,2),1:nPts,'UniformOutput',false)));
distMap(logical(eye(size(distMap)))) = inf;

% Measure the initial nearest neighbours, setting point radii
%to half that distance
[nnDists, nn] = min(distMap,[],1);
IR = nnDists;

% Any pairs of points that are nearest neighbour are "finalised"
%and cannot expand
finalisedMask = arrayfun(@(i) nn(nn(i))==i, 1:nPts);

% Other "open" points can expand one by one
while ~all(finalisedMask)
    openPtIds = find(~finalisedMask);
    % Find the distance from these points' circles to all other
    %circles, and get that smallest gap
    openDistMap = bsxfun(@minus, bsxfun(@minus, distMap(:, openPtIds)...
        , ptRads(openPtIds)), ptRads');
    openPtMinGap = min(openDistMap,[],1);
    % Take the smallest gap, expand that point's circle to close that
    %gap, finalise that point.
    [~,idx] = min(openPtMinGap);
    %ptRads(openPtIds(idx)) = ptRads(openPtIds(idx)) + openPtMinGap(idx);
    finalisedMask(openPtIds(idx)) = true;
end

```

APPENDIX B: INITIATOR & ACTIVATOR

VARIATION DATA

B.1 Varying proportion of initiator (EtMgBr)

Table B.1.1. Thermal properties of the Polymer from DSC – EtMgBr-10%

	Glass Transition Temperature (°C)	Crystallizing Temperature (°C)	Melt Peak Temperature (°C)	Enthalpy (J/g)	Crystallinity (%)
1 st Run	56.68	197.25	221.04	58.26	30.66315789
2 nd Run	58.32	202.71	217.22	56.35	29.65789474
3 rd Run	54.71	202.61	215.54	60.5	31.84210526
Cycle Run	59.76	201.71	212.76	57.06	30.03157895
Average	57.3675	201.07	216.64	58.0425	30.54868421

Table B.1.2. Thermal properties of the Polymer from DSC – EtMgBr-30%

	Glass Transition Temperature (°C)	Crystallizing Temperature (°C)	Melt Peak Temperature (°C)	Enthalpy (J/g)	Crystallinity (%)
1 st Run	59.78	192.79	215.03	63.04	33.17894737
2 nd Run	54.68	201.38	216.96	70.58	37.14736842
3 rd Run	57.89	202.59	216.31	64.81	34.11052632
Cycle Run	51.68	192.7	215.34	62.82	33.06315789
Average	56.0075	197.365	215.91	65.3125	34.375

Table B.1.3. Thermal properties of the Polymer from DSC – EtMgBr-50%

	Glass Transition Temperature (°C)	Crystallizing Temperature (°C)	Melt Peak Temperature (°C)	Enthalpy (J/g)	Crystallinity (%)
1 st Run	59.87	189.9	214.66	89.91	47.32105263
2 nd Run	53.54	198.56	213.8	92.92	48.90526316
3 rd Run	58.97	188.48	210.43	93.61	49.26842105
Cycle Run	52.68	184.33	213.92	91.25	48.02631579
Average	56.265	190.3175	213.2025	91.9225	48.38026316

Table B.1.4. Thermal properties of the Polymer from DSC – EtMgBr-70%

	Glass Transition Temperature (°C)	Crystallizing Temperature (°C)	Melt Peak Temperature (°C)	Enthalpy (J/g)	Crystallinity (%)
1 st Run	54.23	163.89	215.89	90.76	47.76842105
2 nd Run	58.75	170.86	216.74	83.48	43.93684211
3 rd Run	52.56	175.45	215.25	89.02	46.85263158
Cycle Run	57.98	187.89	213.76	86.17	45.35263158
Average	55.88	174.5225	215.41	87.3575	45.97763158

Table B.1.5. Thermal properties of the Polymer from DSC – EtMgBr-100%

	Glass Transition Temperature (°C)	Crystallizing Temperature (°C)	Melt Peak Temperature (°C)	Enthalpy (J/g)	Crystallinity (%)
1 st Run	51.76	175.68	211.9	82.41	43.37368421
2 nd Run	54.82	187.89	216.96	80.93	42.59473684
3 rd Run	53.45	165.83	213.53	78.52	41.32631579
Cycle Run	51.82	160.58	206.12	74.84	39.38947368
Average	52.9625	172.495	212.1275	79.175	41.67105263

B.2 Varying proportion of activator (NACL)

Table B.2.1. Thermal properties of the Polymer from DSC – NACL-10%

	Glass Transition Temperature (°C)	Crystallizing Temperature (°C)	Melt Peak Temperature (°C)	Enthalpy (J/g)	Crystallinity (%)
1 st Run	51.67	185.62	220.06	74.83	39.38421053
2 nd Run	53.68	175.34	215.52	59.63	31.38421053
3 rd Run	52.89	176.64	218.92	83.33	43.85789474
Cycle Run	54.58	182.42	216.84	82.58	43.46315789
Average	53.205	180.005	217.835	75.0925	39.52236842

Table B.2.2. Thermal properties of the Polymer from DSC – NACL-30%

	Glass Transition Temperature (°C)	Crystallizing Temperature (°C)	Melt Peak Temperature (°C)	Enthalpy (J/g)	Crystallinity (%)
1 st Run	51.45	175.68	217.37	93.01	48.95263158
2 nd Run	53.21	175.89	216.18	92.49	48.67894737
3 rd Run	56.73	174.68	216.38	90.68	47.72631579
Cycle Run	55.47	175.68	215.51	94.38	49.67368421
Average	54.215	175.4825	216.36	92.64	48.75789474

Table B.2.3. Thermal properties of the Polymer from DSC – NACL-50%

	Glass Transition Temperature (°C)	Crystallizing Temperature (°C)	Melt Peak Temperature (°C)	Enthalpy (J/g)	Crystallinity (%)
1 st Run	49.65	174.56	216.52	88.74	46.70526316
2 nd Run	52.64	162.68	214.06	96.06	50.55789474
3 rd Run	53.79	179.89	215.42	94.56	49.76842105
Cycle Run	52.58	175.48	214.21	86.78	45.67368421
Average	52.165	173.1525	215.0525	91.535	48.17631579

Table B.2.4. Thermal properties of the Polymer from DSC – NACL 70%.

	Glass Transition Temperature (°C)	Crystallizing Temperature (°C)	Melt Peak Temperature (°C)	Enthalpy (J/g)	Crystallinity (%)
1 st Run	55.67	184.42	214.17	80.67	42.45789474
2 nd Run	51.49	186.57	215.15	75.58	39.77894737
3 rd Run	53.38	187.89	214.58	79.15	41.65789474
Cycle Run	52.87	186.78	213.66	79.63	41.91052632
Average	53.3525	186.415	214.39	78.7575	41.45131579

Table B.2.5. Thermal properties of the Polymer from DSC – NACL 100%.

	Glass Transition Temperature (°C)	Crystallizing Temperature (°C)	Melt Peak Temperature (°C)	Enthalpy (J/g)	Crystallinity (%)
1 st Run	51.68	163.89	212.38	72.17	31.37826087
2 nd Run	53.18	187.24	213.29	72.76	31.63478261
3 rd Run	54.92	188.39	213.2	74.66	32.46086957
Cycle Run	52.68	186.78	212.46	73.98	32.16521739
Average	53.115	181.575	212.8325	73.3925	31.90978261

B.3 Varying proportion of initiator (EtMgBr) and activator (NACL) both

Table B.3.1. Thermal properties of the Polymer from DSC – initiator (EtMgBr) and activator (NACL) both 10%.

	Glass Transition Temperature (°C)	Crystallizing Temperature (°C)	Melt Peak Temperature (°C)	Enthalpy (J/g)	Crystallinity (%)
1 st Run	53.64	91.34	172.08	48.26	25.4
2 nd Run	52.42	109.45	148.15	24.36	12.82105263
3 rd Run	53.97	112.1	175.85	47.95	25.23684211
Cycle Run	54.21	125.67	192.66	32.96	17.34736842
Average	53.56	109.64	172.185	38.3825	20.20131579

Table B.3.2. Thermal properties of the Polymer from DSC – initiator (EtMgBr) and activator (NACL) both 30%.

	Glass Transition Temperature (°C)	Crystallizing Temperature (°C)	Melt Peak Temperature (°C)	Enthalpy (J/g)	Crystallinity (%)
1 st Run	49.68	178.98	210.69	71.22	37.48421053
2 nd Run	53.21	182.16	211.96	63.02	33.16842105
3 rd Run	51.34	180.61	210.01	68.3	35.94736842
Cycle Run	53.55	189.98	214.79	58.59	30.83684211
Average	51.945	182.9325	211.8625	65.2825	34.35921053

Table B.3.3. Thermal properties of the Polymer from DSC – initiator (EtMgBr) and activator (NACL) both 50%.

	Glass Transition Temperature (°C)	Crystallizing Temperature (°C)	Melt Peak Temperature (°C)	Enthalpy (J/g)	Crystallinity (%)
1 st Run	55.61	177.38	214.77	88.73	46.7
2 nd Run	51.34	181.68	214.2	91.24	48.02105263
3 rd Run	53.27	178.92	217.15	93.16	49.03157895
Cycle Run	51.64	150.67	209.95	91.73	48.27894737
Average	52.965	172.1625	214.0175	91.215	48.00789474

Table B.3.4. Thermal properties of the Polymer from DSC – initiator (EtMgBr) and activator (NAACL) both 70%.

	Glass Transition Temperature (°C)	Crystallizing Temperature (°C)	Melt Peak Temperature (°C)	Enthalpy (J/g)	Crystallinity (%)
1 st Run	54.52	173.88	211.7	79.34	41.75789474
2 nd Run	53.21	168.55	209.03	81.79	43.04736842
3 rd Run	57.66	163.42	205.73	83.32	43.85263158
Cycle Run	52.45	162.48	206.06	81.94	43.12631579
Average	54.46	167.0825	208.13	81.5975	42.94605263

Table B.3.5. Thermal properties of the Polymer from DSC – initiator (EtMgBr) and activator (NAACL) both 100%.

	Glass Transition Temperature (°C)	Crystallizing Temperature (°C)	Melt Peak Temperature (°C)	Enthalpy (J/g)	Crystallinity (%)
1 st Run	59.13	188.89	212.23	66.74	35.12631579
2 nd Run	52.46	165.68	205.53	64	33.68421053
3 rd Run	53.46	173.68	203.79	59.12	31.11578947
Cycle Run	51.67	156.89	205.54	68.61	36.11052632
Average	54.18	171.285	206.7725	64.6175	34.00921053

APPENDIX C: SIMULATED MODELS GENERATED

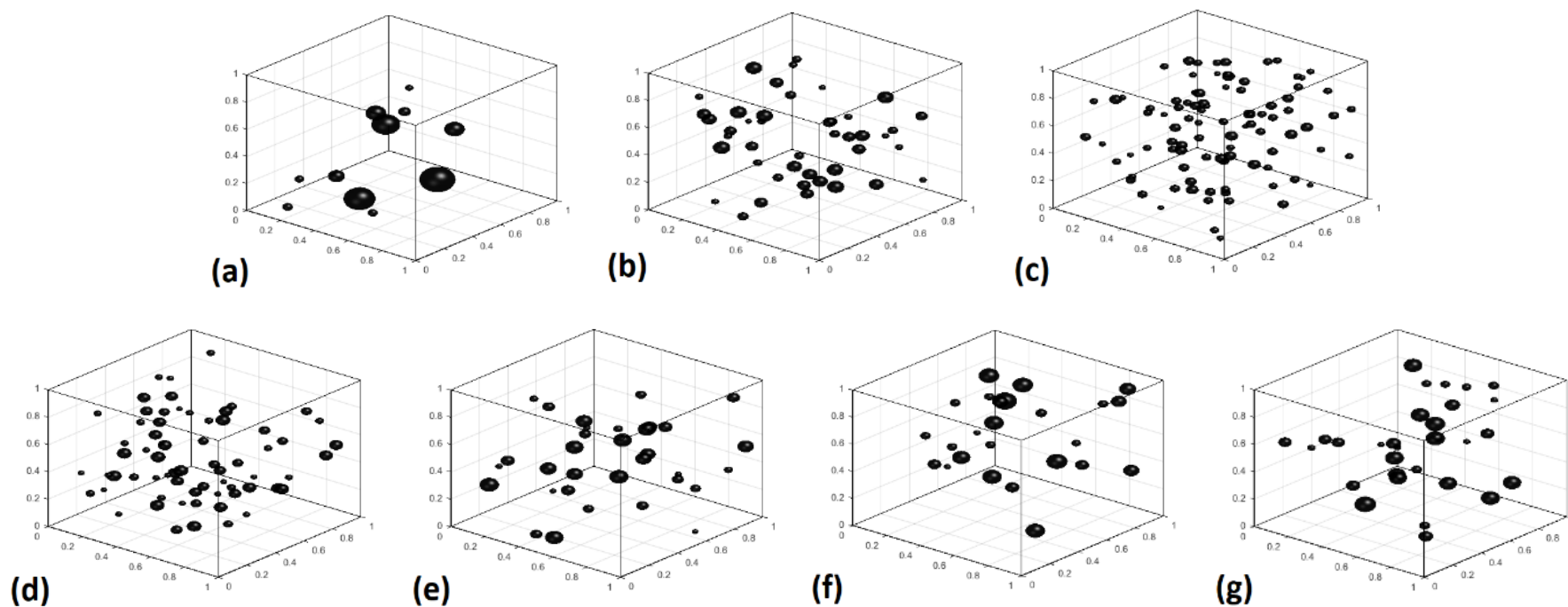


Figure C.1. Simulated model representation of the synthesised PMC samples (1 cubic micron size) for (a) Uncoated- Fe_3O_4 PMC; samples with varying proportions of silica coatings i.e. (b) Stöber- Fe_3O_4 PMC & (c) TPRE- Fe_3O_4 PMC; and samples with varying percentages of OA loading on the MNPs viz. (d) 22 w/w% OA- Fe_3O_4 PMC, (e) 33 w/w% OA- Fe_3O_4 PMC, (f) 44 w/w% OA- Fe_3O_4 PMC, and (g) 55 w/w% OA- Fe_3O_4 PMC. (Herein, solid Black spheres represent Fe_3O_4 MNPs or agglomerates.)

The values of the interaction radius (IR) generated by the designed MATLAB® code

Table C.1. Interaction radius values as calculated by the MATLAB® code for the simulated model of each sample type.

Sample	Minimum Interaction Radius (nm)	Maximum Interaction Radius (nm)	Average Interaction Radius (nm)	Standard Deviation (nm)
Uncoated-Fe ₃ O ₄ PMC	190	475	265	87
Stöber-Fe ₃ O ₄ PMC	80	346	166	58
TPRE-Fe ₃ O ₄ PMC	54	267	129	50
22 w/w% OA-Fe ₃ O ₄ PMC	77	345	142	52
33 w/w% OA-Fe ₃ O ₄ PMC	65	413	189	82
44 w/w% OA-Fe ₃ O ₄ PMC	63	498	188	104
55 w/w% OA-Fe ₃ O ₄ PMC	82	307	173	67

APPENDIX D: EDX & MAGNETIC MEASUREMENTS

Table : Elemental quantitative analysis results for all the functionalised MNP samples.

Samples	Element (Weight %)				
	C	O	Si	S	Fe
Uncoated-Fe ₃ O ₄ MNPs	26.81	20.42	-	0.19	28.15
Stöber-Fe ₃ O ₄ MNPs	24.84	18.77	1.20	-	27.27
TPRE-Fe ₃ O ₄ MNPs	22.43	20.70	5.82	0.17	26.94
22 w/w% OA-Fe ₃ O ₄ MNPs	27.73	21.50	-	-	26.58
33 w/w% OA-Fe ₃ O ₄ MNPs	28.66	22.49	-	-	27.58
44 w/w% OA-Fe ₃ O ₄ MNPs	29.84	24.59	-	-	26.21
55 w/w% OA-Fe ₃ O ₄ MNPs	30.57	26.81	-	-	25.15

Though the quantitative analysis was run for the elemental study in terms of weight% (W%) and also the atomic% (A%), the weight% data was more relevant to compare with the functionalisation loading of each type.

Full scale plots of induced magnetisation i.e. magnetic moment as a function of applied magnetic field, showing the associated hysteresis loops in inset figures at (a) 100 K and (b) 400 K temperatures.

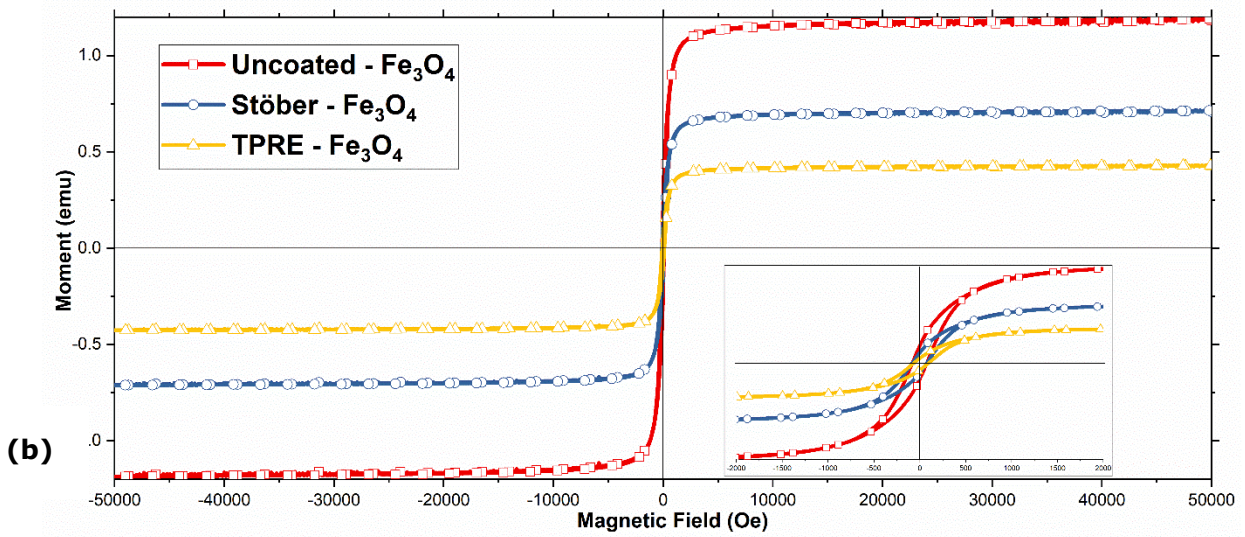
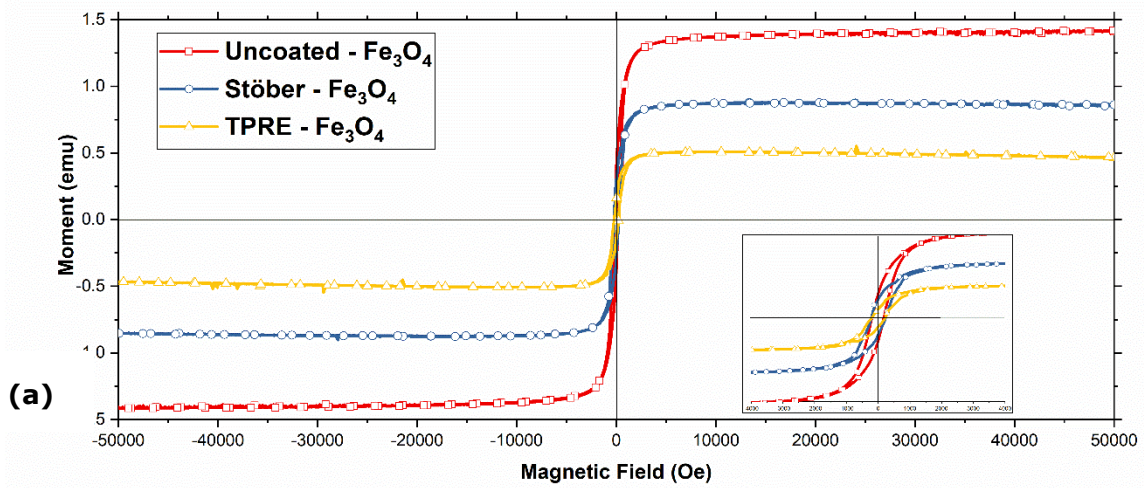


Figure D.1. Full scale plots of induced magnetisation (Magnetic moment as a function of applied magnetic field) and the associated hysteresis loops shown in inset figures for the uncoated MNPs and MNPs functionalised by Stöber and TPRE method, measured at (a) 100 K and (b) 400 K temperatures.

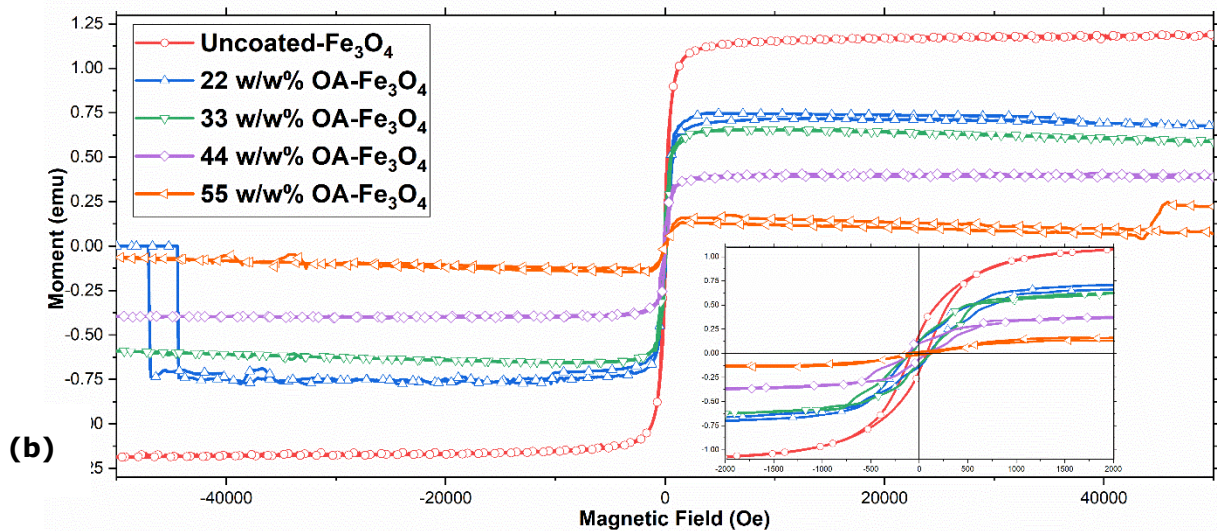
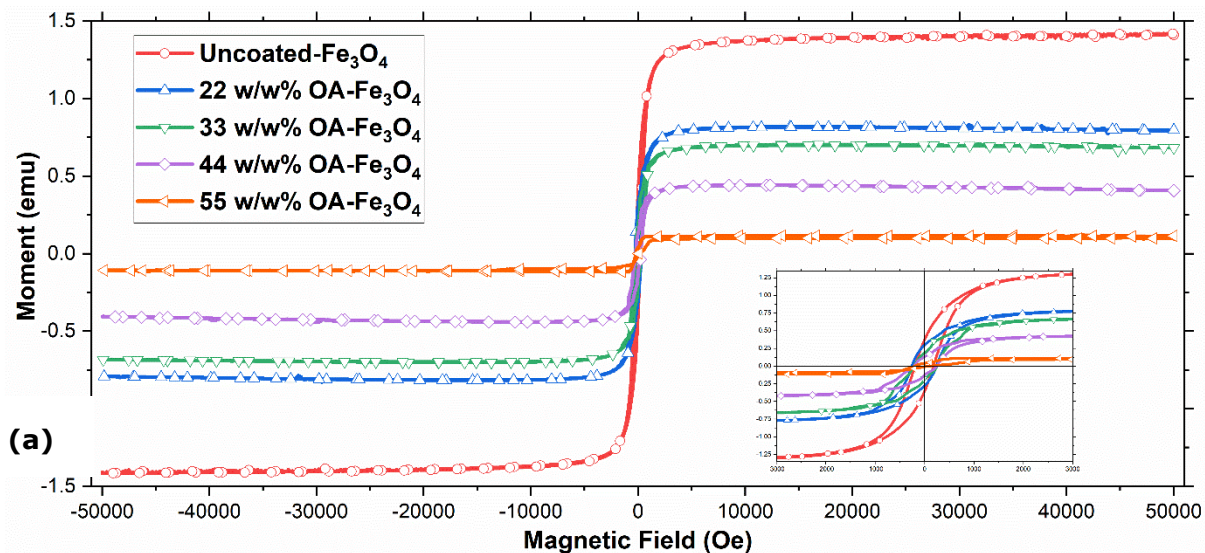


Figure D.2. Full scale plots of induced magnetisation (Magnetic moment as a function of applied magnetic field) and the associated hysteresis loops shown in inset figures for the uncoated MNPs and MNPs functionalised by oleic acid variations, measured at (a) 100 K and (b) 400 K temperatures.

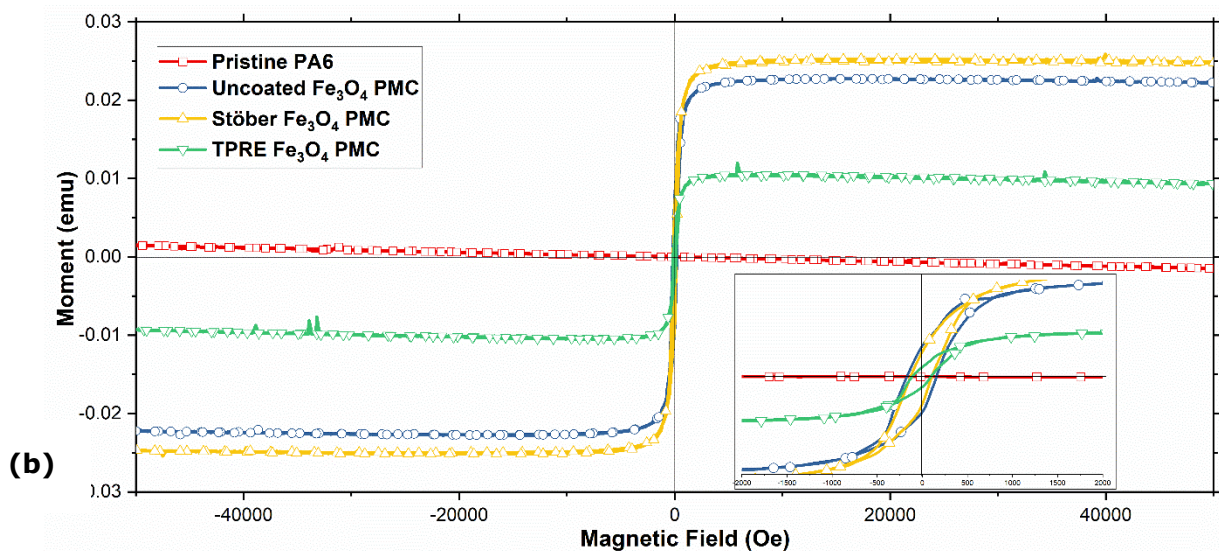
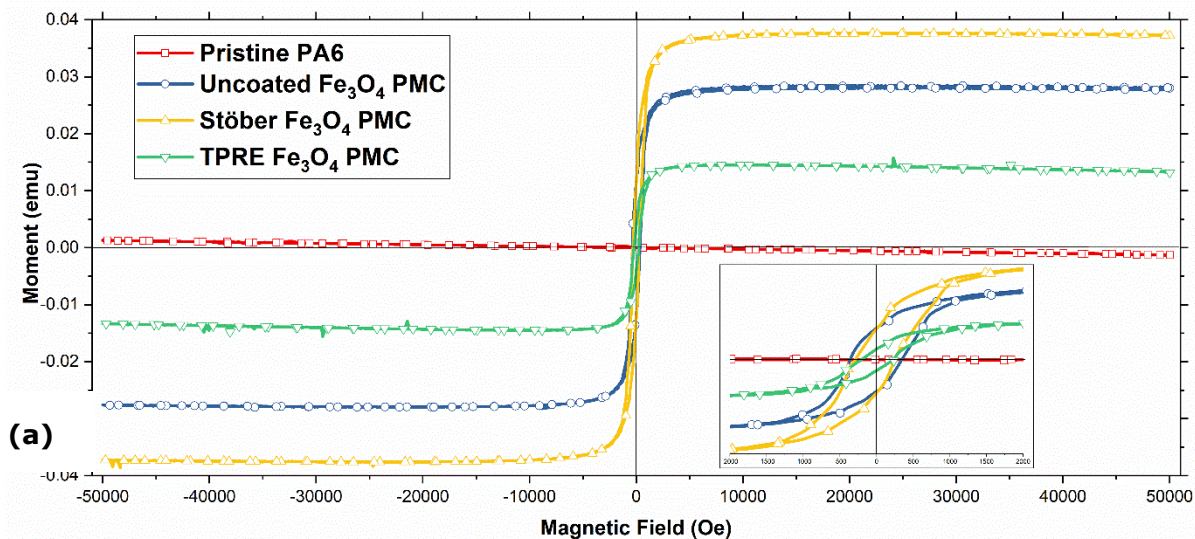


Figure D.3. Full scale plots of induced magnetisation (Magnetic moment as a function of applied magnetic field) and the associated hysteresis loops shown in inset figures for the various PMC samples (pristine, uncoated, Stöber and TPRE functionalised MNPs samples) measured at (a) 100 K and (b) 400 K temperatures.

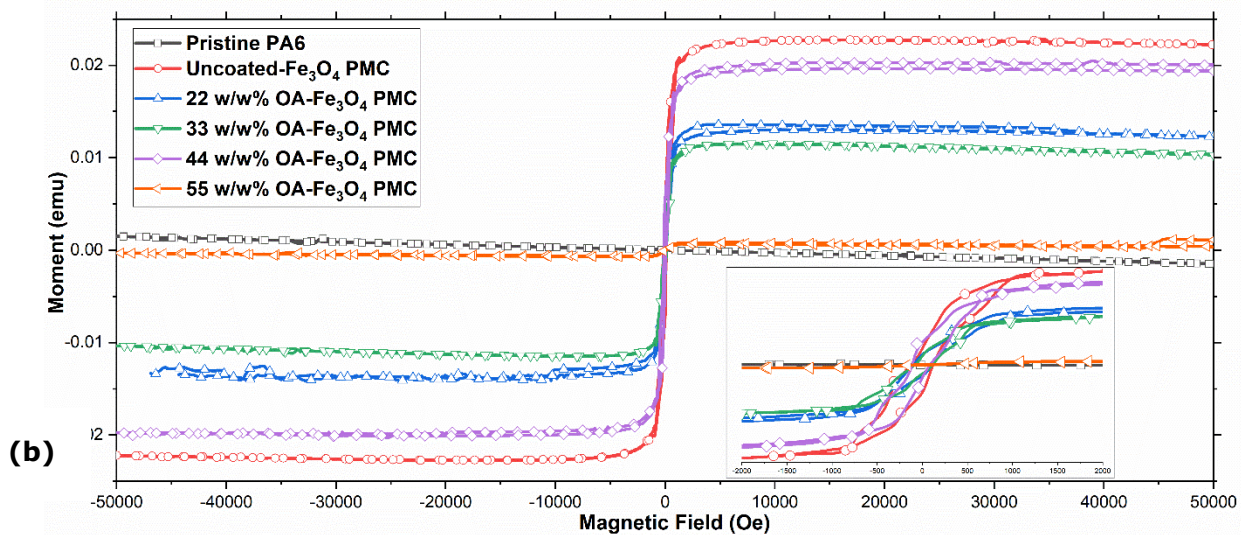
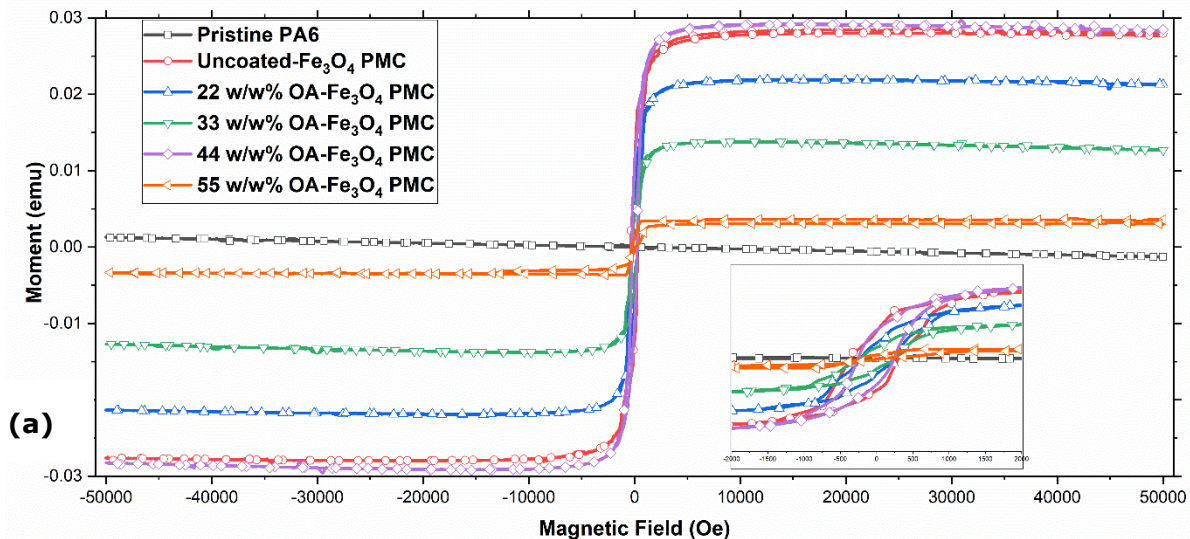


Figure D.4. Full scale plots of induced magnetisation (Magnetic moment as a function of applied magnetic field) and the associated hysteresis loops shown in inset figures for the various PMC samples (pristine, uncoated and oleic acid variations functionalised MNPs samples) measured at (a) 100 K and (b) 400 K temperatures.

APPENDIX E: COMPOSITE SAMPLE PREPARATION

For the composite dog bone sample preparations, required for the tensile testing and self-healing capability evaluation, there was a need to fabricate a metal-die so that all the samples can be prepared in exact similar manner. This practice will avoid any error inclusion due to the manufacturing aspect of the composite samples. Firstly, the CAD model was prepared in Solidworks® CAD package, it is shown in Fig. E.1 below. This ensured that the tolerances of all the mating parts were appropriately allocated and matched with each other by motion simulation of the die assembly. It also was used to create all the production drawings needed for the CNC fabrication process.

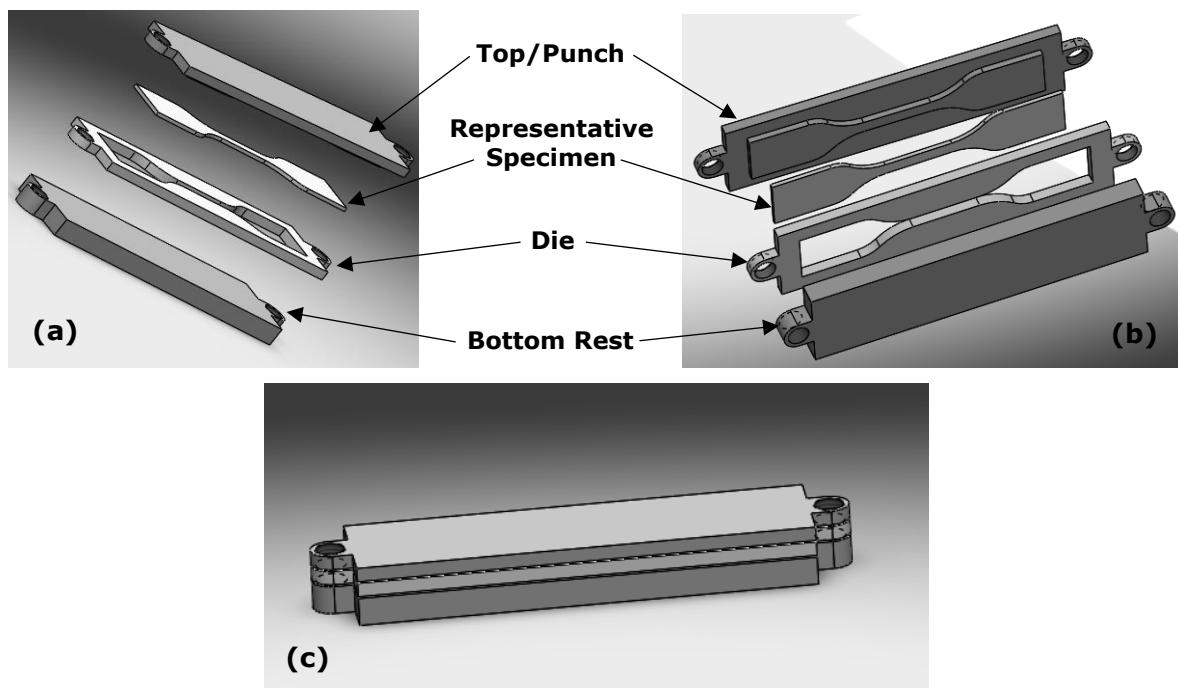
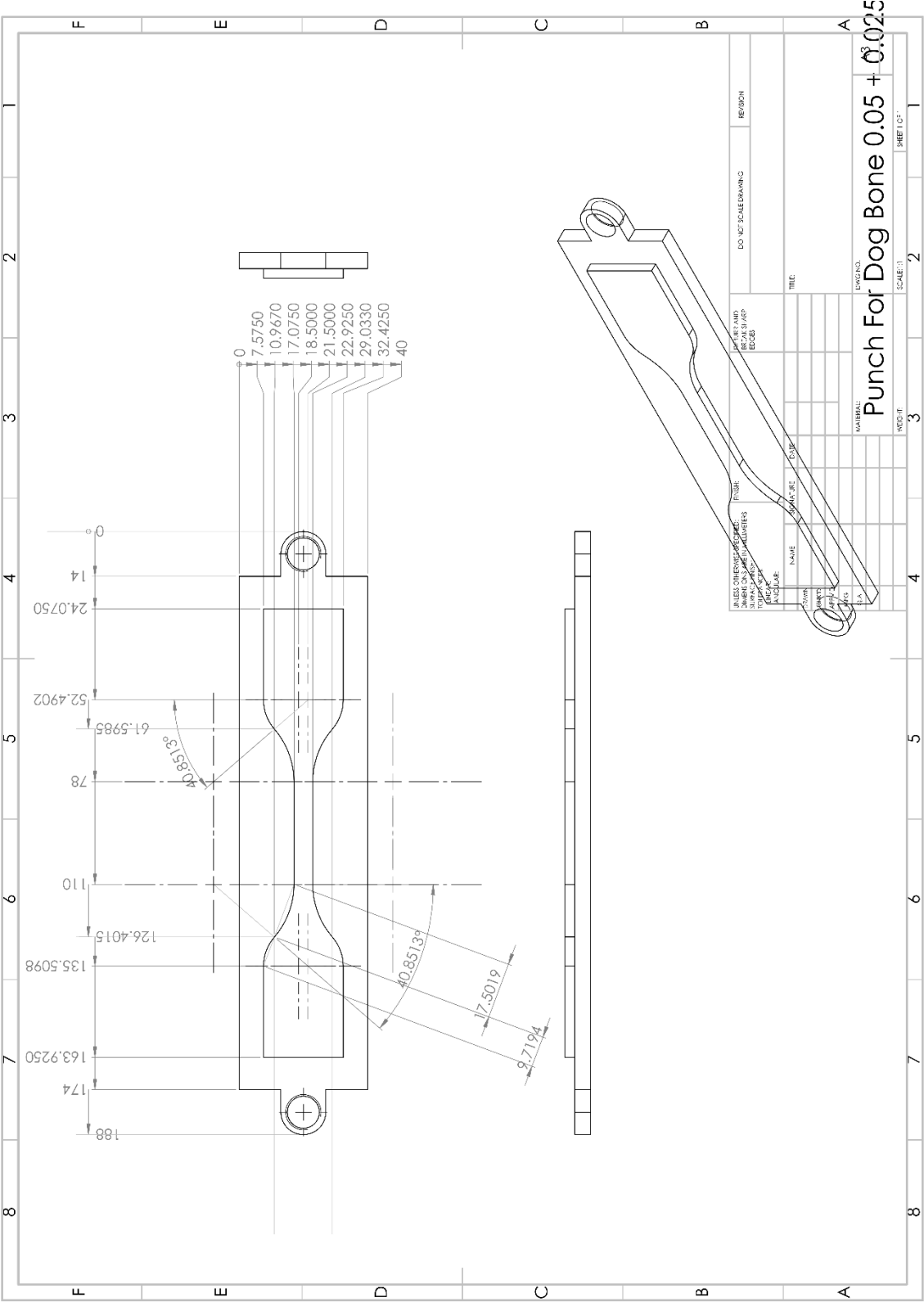


Figure E.1. CAD model of the die setup: (a) & (b) Exploded view of the entire setup and (c) assembled view.

Various production sheets generated using the CAD model are attached as follows for any reference:



The final finished metal die fabricated for the composite dog bone sample preparations is as follow:



Figure E.5. Upper and middle portions of the metal die fabricated for composite dog bone sample preparations.